Author:
Atkinson, George S

Title:
Quantum Metrology with Bright Squeezed Light

Quantum Metrology with Bright Squeezed Light

Author:

GEORGE ATKINSON

School of Physics
UNIVERSITY OF BRISTOL

A dissertation submitted to the University of Bristol in accordance with the requirements for award of the degree of DOCTOR OF PHILOSOPHY in the Faculty of Science.

AUGUST 2021

Word count: Thirty Thousand

Abstract

The noise of any measurement is fundamentally constrained by the laws of quantum mechanics, and this has significant implications for the development of sensors and measuring devices which are essential tools in science and engineering. In quantum metrology, the properties of quantum states of light are used to reduce measurement noise below the limit allowed by classical physics. In this thesis, we explore the application of squeezed states of light for improving precision and sensitivity in optical measurements.

Squeezed states are particularly versatile quantum states because they may be produced with high optical power, which makes them suitable for a range of optical applications. We begin by describing the development of a source of high power squeezed light, which utilised the Kerr effect in photonic crystal fibre. This approach allows us to generate quantum noise reduction at visible wavelengths.

We then investigate the precision improvement that may be attained by using squeezed light to reduce the noise of measurements in the frequency domain. We develop theory which shows that an improvement in the measured signal-to-noise ratio by applying squeezing does not necessarily correspond to a precision improvement, due to the effect of classical noise on the variance of the signal. Our theoretical model is used to identify the conditions required for squeezing to provide a precision improvement for the detection of amplitude modulation, and this is experimentally verified using our squeezed light source.

Finally, we develop a new method of optical loss estimation which provides enhanced precision by using squeezed light. This approach employs a novel technique for the cancellation of classical noise, which enables an experimental demonstration 8 orders of magnitude above the power limitations of previous demonstrations of quantum enhanced loss estimation. We anticipate that this approach will find application in imaging and spectroscopy.

ACKNOWLEDGEMENTS

My first thanks go to my supervisor, Dr Jonathan Matthews, who has given me a huge amount of support and encouragement. I am extremely grateful for all his time and help with this project.

I have also been very lucky to have the support of many other researchers in QETLabs. In particular, I would like to thank Giacomo Ferranti, Euan Allen and Alex McMillan for all the help they have given me throughout my PhD, and for their constant enthusiasm and optimism. Thanks also to Cyril Torre, Jason Mueller, David Payne, Sabine Wollmann, and all the other members of our research group within QETLabs, which I have hugely enjoyed being a part of. I have also had the benefit of being a part of the Quantum Engineering CDT, and would like to give a mention to the rest of cohort 3: Will, Brian, Jorge, Ross, Konstantina, Joe, João, Rachel, Max, David and Giorgos. It has been great fun working alongside you all.

Thanks to my orchestra friends, especially Gareth, Tim, Anna, Alasdair and Diego, and to my family, for always being so supportive and encouraging.

Finally, thank you Rebekah for everything. You have been a constant source of love and laughter, and I could not have got here without you.

AUTHOR'S DECLARATION

I declare that the work in this dissertation was carried out in accordance with the requirements of the University's Regulations and Code of Practice for Research Degree Programmes and that it has not been submitted for any other academic award. Except where indicated by specific reference in the text, the work is the candidate's own work. Work done in collaboration with, or with the assistance of, others, is indicated as such. Any views expressed in the dissertation are those of the author.

SIGNED: ..... DATE: .....

Manuscripts and Presentations

Quantum Enhanced Precision Estimation of Transmission with Bright Squeezed Light, **G.S. Atkinson**, E. J. Allen, G. Ferranti, A. R. McMillan, J. C. F. Matthews,
Physical Review Applied, vol. 16, no. 4, pp. 044031, 2021.

Loss Estimation with continuous and discrete variable quantum light, **G.S. Atkinson**, E. J. Allen, G. Ferranti, A. R. McMillan, J. C. F. Matthews.
(Talk) SPIE Photonics West, Moscone Center, San Francisco, USA. 06/02/2020.

Fisher Information with Continuous Variable Quantum Resources, **G.S. Atkinson**, E. J. Allen, G. Ferranti, A. R. McMillan, J. C. F. Matthews.
(Poster) CLEO Europe, International Congress Center, Munich, Germany. 26/06/2019.

Fisher Information with Continuous Variable Quantum Resources, **G.S. Atkinson**, E. J. Allen, G. Ferranti, A. R. McMillan, J. C. F. Matthews.
(Poster) Quantum 2019, University of Turin, Turin, Italy. 29/05/2019.

Fisher Information with Continuous Variable Quantum Resources, **G.S. Atkinson**, E. J. Allen, G. Ferranti, A. R. McMillan, J. C. F. Matthews.
(Talk) Physics Postgraduate Conference, University of Bristol, Bristol, UK. 14/05/2019.

Fisher Information with Continuous Variable Quantum Resources, **G.S. Atkinson**, E. J. Allen, G. Ferranti, A. R. McMillan, J. C. F. Matthews.
(Poster) BQIT, M Shed, Bristol, UK. 1/04/2019.

Quantifying the Effects of Dispersion on Kerr Squeezed Light with Photonic Crystal Fibre, **G.S. Atkinson**, E. J. Allen, G. Ferranti, A. R. McMillan, J. C. F. Matthews.
(Poster) BQIT, M Shed, Bristol, UK. 19/04/2018.

List of Acronymns

AM	Amplitude Modulation
BS	Beamsplitter
CRB	Cramér-Rao Bound
CW	Continuous Wave
DC	Direct Current
DFT	Discrete Fourier Transform
ENB	Equivalent Noise Bandwidth
EOM	Electro-optic Modulator
FFT	Fast Fourier Transform
FM	Frequency Modulation
FWHM	Full-width at Half Maximum
GT	Glan-Taylor polariser
HWP	Half-wave Plate
IF	Intermediate Frequency
LO	Local Oscillator
PBS	Polarising Beamsplitter
PCF	Photonic Crystal Fibre
PD	Photodiode
PDC	Parametric Downconversion
PM	Powermeter
POVM	Positive Operator-valued Measure
QCRB	Quantum Cramér-Rao Bound
QNL	Quantum Noise Limit
QWP	Quarter-wave Plate
RBW	Resolution Bandwidth
SA	Spectrum Analyser
SNR	Signal-to-Noise Ratio
SQL	Standard Quantum Limit
VBW	Video Bandwidth

Table of Contents

List of Figures

Figure **Page**

CHAPTER 1

INTRODUCTION

Quantum metrology is concerned with the description of measurements according to the laws of quantum mechanics [4]. Since quantum theory is non-deterministic, the outcome of any measurement has some intrinsic uncertainty according to the properties of the quantum state used to probe the measured system. It is of fundamental interest to study the nature of this quantum noise [5].

A quantum description of measurements has also enabled new techniques for reducing noise beyond the bounds imposed by using classical probe states [6]. This has significant implications for science and technology, by allowing for improvements in current measurement capabilities, and the development of new measurement devices. Squeezed states of light, which have uncertainty reduced below the classical limit, have played an important role in these developments. For example, squeezed light has been applied to the detection of gravitational waves [7, 8], and in biological measurements [9, 10]. A particular advantage of squeezed light is that it may be generated with high optical power. Since the power of the probe sets a fundamental bound on the performance of an optical measurement, this makes squeezing a crucial resource in quantum metrology [11]. In this thesis, we develop a source of bright squeezed light, and use it to perform measurements with noise reduced below the classical limit. In particular, we focus on methods that allow for the enhancement of measurement precision with high probe power.

Chapter 2 consists of background material which covers relevant topics in quantum optics. This includes a description of some useful quantum states and operators, and common techniques for the detection of quantum states of light. We describe some relevant details of spectrum analysis, which is necessary in order to correctly interpret the results of the experimental measurements in this thesis. This chapter also includes a detailed description of

the noise characteristics of squeezed light, which will be useful for analysing the generated squeezing.

In Chapter 3, we describe the development of a source of bright, visible wavelength squeezed light using the Kerr effect in photonic crystal fibre (PCF). While the previous experiments which have used PCF to generate high power visible squeezed light have employed spectral filtering [12, 13], we use a nonlinear interferometer to generate the squeezing in this experiment. We therefore demonstrate the applicability of this technique at visible wavelengths, which was made possible due to the dispersion characteristics of the PCF. The chapter includes a review of the theory of squeezing via the Kerr interaction, and an overview of the various techniques that have used the Kerr interaction to generate squeezing. Results from a numerical simulation are discussed, which quantifies the squeezing that may be achieved given the characteristics of the PCF. We also provide a detailed characterisation of the source and detector. The results for the squeezing measurements demonstrate maximum of -1.3 dB quantum noise reduction, which is sufficient to demonstrate an improvement in the performance of optical measurements.

Chapter 4 reports on an experiment which demonstrates enhanced precision and sensitivity in the estimation of a modulated optical loss, using the squeezed light source described in Chapter 3. The precision of a measurement is determined by the variance of repeated estimates [14], whereas sensitivity corresponds to the minimum detectable signal [15]. Previous experimental work with bright squeezed light has focused on sensitivity enhancement [16, 10, 7, 8, 17]. In this chapter, we demonstrate that for frequency domain measurements, improvement of sensitivity is not sufficient to demonstrate a precision enhancement. This is due to the effect of excess low frequency optical noise being transferred to the measured signal, which can significantly increase the variance of the estimates. Our theoretical results allow us to identify the conditions required to achieve a precision improvement with bright squeezing, and this is experimentally demonstrated. This work corresponds to the first measurement of amplitude modulation which demonstrates an improvement in precision beyond the classical limit using high power squeezing.

In Chapter 5, we experimentally demonstrate a novel method for the estimation of a static loss with squeezed light, which enables an improvement in the measurement precision and sensitivity beyond the classical limit. Loss estimation is a crucial tool in optical metrology, and is central to techniques such as spectroscopy and imaging [18, 19]. However, due to the aforementioned excess low frequency noise, loss estimation using bright squeezing has so far only been discussed theoretically [20, 21], and experimental demonstrations of quantum enhanced precision in loss estimation have been limited to picowatts of optical power [22, 23]. Our approach uses high frequency path modulation to avoid low frequency noise, and allows for further suppression of classical noise by optical cancellation of common-mode signals. This demonstration constitutes an improvement of 8 orders

of magnitude beyond the power limitations of previous measurements of optical loss with quantum enhanced precision. The theoretical limits of precision with this strategy are discussed in relation to other methods of loss estimation, and we also present simulations which demonstrate the potential application of this approach to quantum imaging with bright squeezed light.

CHAPTER 2

BACKGROUND

This chapter introduces some key concepts and techniques relevant to the rest of this thesis. Section 2.1 reviews a quantum description of the electromagnetic field, and Section 2.2 describes the theory of photodetection and some common methods of detecting the quantum properties of light. In Section 2.3, the noise properties of squeezed light are discussed in more detail.

Statement of Work

This constitutes an introductory chapter and contains no new research material.

2.1 Quantum Optics

In this section, some theoretical concepts necessary for describing the quantum properties of the electromagnetic field will be presented. We will begin by introducing the modal decomposition of the electromagnetic field, and the quantum operators associated with these modes. An initial focus on single mode quantum states and operators will facilitate the description of some important quantum effects, and a discussion of useful representations of quantum states. We will then describe some features of multi-mode and continuous mode light, and optical devices which act on more than one mode.

2.1.1 The Electromagnetic Field

In the classical picture, light corresponds to an electromagnetic wave, and can be described by the electric and magnetic field amplitudes $\boldsymbol{E}$ and $\boldsymbol{B}$. The dynamical behaviour of these

fields in the presence of electric charges are governed by Maxwell's equations, which can be written as [24]

$$\nabla \cdot \boldsymbol{E} = \frac{\rho}{\epsilon_0}, \tag{2.1}$$

$$\nabla \cdot \boldsymbol{B} = 0, \tag{2.2}$$

$$\nabla \times \boldsymbol{E} = -\frac{\partial \boldsymbol{B}}{\partial t} \tag{2.3}$$

and

$$\nabla \times \boldsymbol{B} = \mu_0 \left(\boldsymbol{J} + \epsilon_0 \frac{\partial \boldsymbol{E}}{\partial t} \right). \tag{2.4}$$

Equations 2.2 and 2.3 express how the electric and magnetic fields are related to each other independently of the presence of charges and currents, while Equations 2.1 and 2.4 describe how the behaviour of the electric and magnetic fields are determined by the charge density ρ and the current density $\boldsymbol{J}$. The constants ϵ_0 and μ_0 are respectively the permittivity and permeability of the vacuum.

Equations 2.1-2.4 will be used to describe the propagation of light in a dielectric medium in Chapter 3. However, in the following, we consider for simplicity the case where light is propagating in a vacuum, i.e. where $\rho = 0$ and $\boldsymbol{J} = 0$. It is convenient to write the electromagnetic field in terms of the vector potential $\boldsymbol{A}$ and scalar potential ϕ, such that the electric and magnetic fields may be defined as

$$\boldsymbol{E} = -\nabla\phi - \frac{\partial \boldsymbol{A}}{\partial t} \qquad \text{and} \qquad \boldsymbol{B} = \nabla \times \boldsymbol{A}, \tag{2.5}$$

from which we can see that Equations 2.3 and 2.4 are satisfied. The fields obtained from Equation 2.5 are unchanged by the gauge transformation

$$\boldsymbol{A} \to \boldsymbol{A} + \nabla\chi, \qquad \phi \to \phi - \frac{\partial \chi}{\partial t}, \tag{2.6}$$

where χ is an arbitrary scalar field. We therefore choose the Coulomb gauge, defined by $\nabla \cdot \boldsymbol{A} = 0$, which is particularly useful in quantum optics. With this choice of gauge, it follows from Equation 2.1 that the scalar potential $\phi = 0$ in the absence of charges. Equation 2.4 can then be written as

$$\nabla^2 \boldsymbol{A} - \frac{1}{c^2} \frac{\partial^2 \boldsymbol{A}}{\partial t^2} = 0, \tag{2.7}$$

where $c = (\mu_0 \epsilon_0)^{-1/2}$ is the speed of light in a vacuum. Equation 2.7 can be used to describe the properties of electromagnetic fields propagating in free space, and is known as the electromagnetic wave equation [25].

2.1.2 Quantised Field Modes

Since Equation 2.7 is a linear differential equation, a general solution for $\boldsymbol{A}$ may be written as a superposition of possible solutions:

$$\boldsymbol{A} \equiv \boldsymbol{A}(\boldsymbol{r},t) = \sum_k A_k u_k(\boldsymbol{r},t), \tag{2.8}$$

where A_k defines the amplitude of each solution $u_k(\boldsymbol{r},t)$, for position vector $\boldsymbol{r}$ and time t. We refer to the solutions $u_k(\boldsymbol{r},t)$ as modes of the electromagnetic field. A common choice of mode basis is that of travelling plane wave solutions $u_k(\boldsymbol{r},t) = e^{i(\boldsymbol{k}.\boldsymbol{r}-\omega_k t)}$, where $\omega_k = c|\boldsymbol{k}|$, which form a complete and orthonormal mode basis. The vector potential can then be written as

$$\boldsymbol{A}(\boldsymbol{r},t) = \sum_k \left(\boldsymbol{A}_k e^{i(\boldsymbol{k}.\boldsymbol{r}-\omega_k t)} + \boldsymbol{A}_{-k} e^{i(\omega_k t - \boldsymbol{k}.\boldsymbol{r})} \right), \tag{2.9}$$

and we find that $\boldsymbol{A}_{-k} = \boldsymbol{A}_k^*$, since the values of $\boldsymbol{E}$ and $\boldsymbol{B}$ must correspond to real quantities. The electromagnetic field may be quantised by associating each monochromatic mode with an excitation of a quantum harmonic oscillator defined by the bosonic creation and annihilation operators $\hat{a}$ and $\hat{a}^\dagger$, which obey the bosonic commutation relations [26]

$$[\hat{a}_k, \hat{a}_{k'}^\dagger] = \delta_{k,k'} \qquad \text{and} \qquad [\hat{a}_k, \hat{a}_{k'}] = 0. \tag{2.10}$$

The quantised vector potential can then be defined as

$$\hat{\boldsymbol{A}} \equiv \hat{\boldsymbol{A}}(\boldsymbol{r},t) = \sum_k \left(\boldsymbol{A}_k \hat{a}_k e^{i(\boldsymbol{k}.\boldsymbol{r}-\omega_k t)} + \boldsymbol{A}_k^* \hat{a}_k^\dagger e^{i(\omega_k t - \boldsymbol{k}.\boldsymbol{r})} \right). \tag{2.11}$$

The expected value of the vector potential for a given quantum state $|\Psi\rangle$ then returns the classical value: $\boldsymbol{A} = \langle\Psi|\hat{\boldsymbol{A}}|\Psi\rangle$. The Hamiltonian in this mode basis can be defined as a sum of the Hamiltonians of each independent monochromatic mode [27]:

$$\hat{H} = \sum_\omega \hbar\omega \left(\hat{a}_\omega^\dagger \hat{a}_\omega + \frac{1}{2} \right), \tag{2.12}$$

where $\hbar$ is the reduced Planck constant. This corresponds to a system of decoupled quantum harmonic oscillators, where each excitation generated by the creation operator $\hat{a}_\omega^\dagger$ corresponds to a single photon with a well-defined frequency ω. The basis of travelling plane waves is particularly convenient for describing the behaviour of monochromatic modes, and many states of light can be approximated to behave like this, particularly in the case of continuous-wave collimated laser light with a mode-field diameter much larger than the scale of the wavelength of light [28]. However, in some cases, the propagation of light is more conveniently described by a more realistic set of modes. For example, the basis of Hermite-Gaussian modes provide a good description of laser beams propagating in free space, which can account for effects such as diffraction [29]. Also, light can be generated as

a train of optical pulses, which each contain a superposition of different frequency modes. Therefore, in order to allow for a quantum description of more general states of light, we consider the unitary transformation U applied to the set of modes $\boldsymbol{A}_k(\boldsymbol{r},t) = \boldsymbol{A}_k u_k(\boldsymbol{r},t)$:

$$\boldsymbol{A}_l(\boldsymbol{r},t) = \sum_k U_{l,k}\boldsymbol{A}_k(\boldsymbol{r},t) \qquad \text{and} \qquad \hat{a}_l^\dagger = \sum_k U_{l,k}\hat{a}_k^\dagger. \tag{2.13}$$

Given that the transformation is unitary, it follows that the new creation and annihilation operators still obey the bosonic commutation relations [28]. We can therefore define a number state of the mode l, $|n\rangle_l$, which is an eigenstate of the number operator $\hat{n}_l = \hat{a}_l^\dagger \hat{a}_l$:

$$\hat{n}_l |n\rangle_l = n_l |n\rangle_l , \tag{2.14}$$

where the eigenvalues n_l are the set of non-negative integers, and the eigenstates $|n\rangle_l$ form a complete and orthonormal basis. These number states, also known as Fock states, form a basis for the Hilbert space of the quantised radiation state in the mode l. The action of the creation and annihilation operators on the state $|n\rangle_l$ are summarised as:

$$\hat{a}_l^\dagger |n\rangle_l = \sqrt{n_l + 1}\,|n_l + 1\rangle_l , \tag{2.15}$$

$$\hat{a}_l |n\rangle_l = \sqrt{n_l}\,|n_l - 1\rangle_l \qquad \text{and} \tag{2.16}$$

$$\hat{a}_l |0\rangle_l = 0. \tag{2.17}$$

The creation operator $\hat{a}_l^\dagger$ therefore creates a photon in the mode defined by the function $u_l(\boldsymbol{r},t)$. While the unitarity of the transformation U ensures the bosonic commutation relations apply, this transformation in general will couple different frequency components. If this is the case, the functions $u_l(\boldsymbol{r},t)$ will no longer correspond to normal modes, and therefore the dynamics of the mode l cannot be considered independently from the other modes of the electromagnetic field. However, it is often the case that each new mode has a spectrum that is closely distributed around a central frequency ω_l. This case is referred to as the quasi-monochromatic approximation, and it can be shown that the resulting Hamiltonian can be approximated to have the same form as Equation 2.12, meaning that each mode can be considered an independent excitation of the electromagnetic field [30].

2.1.3 Single Mode Quantum Optics

Light can often be well described by a single mode of the electromagnetic field. It is therefore useful to consider the quantum states and operators that are used to describe light in a single mode. While there are many choices of basis in which an independent field mode can be excited, here the basis of monochromatic plane waves is used for simplicity. However, it is

worth noting that many of the results that are given here apply in an arbitrary orthonormal mode basis. The electric field for a single mode state can be written as

$$\hat{\boldsymbol{E}} = \boldsymbol{E}_k \hat{a}_k e^{i(\boldsymbol{k}.\boldsymbol{r}-\omega_k t)} + \boldsymbol{E}_k^* \hat{a}_k^\dagger e^{i(\omega_k t - \boldsymbol{k}.\boldsymbol{r})}. \tag{2.18}$$

Since we are only considering a single mode k, the index notation can be dropped, and the creation and annihilation operators can be denoted simply as $\hat{a}^\dagger$ and $\hat{a}$ respectively. Since the creation and annihilation operators are not Hermitian, they do not correspond to physically observable quantities. It is therefore often useful to define the quadrature operators:

$$\hat{x} = \frac{1}{\sqrt{2}}(\hat{a} + \hat{a}^\dagger) \qquad \text{and} \qquad \hat{p} = \frac{i}{\sqrt{2}}(\hat{a}^\dagger - \hat{a}), \tag{2.19}$$

which are Hermitian observables. The commutator of the pair of quadrature operators is given by

$$[\hat{x}, \hat{p}] = i, \tag{2.20}$$

which implies that $\hat{x}$ and $\hat{p}$ are canonically conjugate variables. An important result of the non-commutivity of the quadrature operators is the uncertainty relation:

$$\Delta x \Delta p \geq \frac{1}{2}, \tag{2.21}$$

where Δx and Δp are the standard deviations of the probability distributions corresponding to $\hat{x}$ and $\hat{p}$. States that saturate the bound $\Delta x \Delta p = \frac{1}{2}$ are known as minimum uncertainty states. The eigenstates of the quadrature operators are denoted $|x\rangle$ and $|p\rangle$, and obey the relations $\hat{x}|x\rangle = x|x\rangle$ and $\hat{p}|p\rangle = p|p\rangle$ for eigenvalues x and p. We can also transform into a rotated basis by applying the phase shift operator $\hat{U}(\theta) = e^{-i\theta\hat{n}}$. The action of $\hat{U}(\theta)$ on the annihilation operator is $\hat{U}(\theta)^\dagger \hat{a} \hat{U}(\theta) = \hat{a} e^{-i\theta}$. Using Equation 2.19, the quadrature amplitudes at an arbitrary phase θ are therefore given by

$$\hat{x}_\theta = \hat{U}(\theta)^\dagger \hat{x} \hat{U}(\theta) = \frac{1}{\sqrt{2}}\left(e^{i\theta}\hat{a}^\dagger + e^{-i\theta}\hat{a}\right) = \hat{x}\cos\theta + \hat{p}\sin\theta \tag{2.22}$$

and

$$\hat{p}_\theta = \hat{U}(\theta)^\dagger \hat{p} \hat{U}(\theta) = \frac{i}{\sqrt{2}}\left(e^{i\theta}\hat{a}^\dagger - e^{-i\theta}\hat{a}\right) = \hat{p}\cos\theta - \hat{x}\sin\theta. \tag{2.23}$$

By comparing Equations 2.22-2.23 to Equation 2.18, it is clear that $\hat{x}_\theta$ is directly proportional to the amplitude of the electric field at phase θ, and $\hat{p}_\theta$ is directly proportional to the amplitude of the electric field at phase $\theta + \pi/2$.

The quadrature operators can accordingly be used to define a phase space, i.e. a coordinate system where all possible states can be represented. However, due to the uncertainty

relation given by Equation 2.21, a quantum state must be described by a distribution in phase space, as opposed to a single point. One such distribution is called the Wigner function, and is defined by [27]

$$W(x,p) = \frac{1}{2\pi}\int_{-\infty}^{\infty} \left\langle x - \frac{y}{2}\right| \hat{\rho} \left| x + \frac{y}{2}\right\rangle e^{iyp} dy, \tag{2.24}$$

for a quantum state defined by density matrix $\hat{\rho}$. The Wigner function shares many of the properties of a joint probability distribution over x and p. For example, it is a normalised function:

$$\int_{-\infty}^{\infty}\int_{-\infty}^{\infty} W(x,p)dxdp = 1, \tag{2.25}$$

and the marginal distributions are given by integrating the Wigner function over the conjugate quadrature:

$$\int_{-\infty}^{\infty} W(x,p)dp = \langle x|\hat{\rho}|x\rangle = P(x), \qquad \text{and} \qquad \int_{-\infty}^{\infty} W(x,p)dx = \langle p|\hat{\rho}|p\rangle = P(p). \tag{2.26}$$

The marginal distributions are true probability distributions and correspond to the projection of $\hat{\rho}$ onto the quadrature states. For an arbitrary quadrature angle, the marginal distribution can be obtained by applying the phase shift operator to the Wigner function:

$$\int_{-\infty}^{\infty} W(x_\theta, p_\theta)dp_\theta = \langle x_\theta|\hat{\rho}|x_\theta\rangle = P(x_\theta). \tag{2.27}$$

This corresponds to the projection of the Wigner function onto the quadrature state $|x_\theta\rangle = \hat{U}(\theta)|x\rangle$. Therefore, while the Wigner function is not itself measurable as a result of the non-commutivity of the quadrature operators, it can be used to calculate the distributions corresponding to the measurement of an arbitrary field quadrature. An important property of the Wigner function is that is allows negative values of $W(x,p)$, and is therefore a quasi-probability distribution. The negativity of the Wigner function is associated with non-classical features of a quantum state [31]. However, there exist many classical and quantum states which do not have negative values of $W(x,p)$. For example, Gaussian states, which are defined by Gaussian distributed Wigner functions, must have a positive Wigner function. Coherent states and squeezed states are examples of Gaussian states, and will be discussed in further detail in Section 2.1.4. Other quasi-probability distributions that can be used to describe quantum states are the Husimi Q representation and the Glauber–Sudarshan P representation [32]. However, the Wigner function will be the distribution used to represent quantum states in this thesis.

2.1.4 Quantum States of Light

In this section, we describe some single-mode quantum states which will be used in the chapters that follow.

2.1.4.1 Photon Number States

From the description of the photon number state in Section 2.1.2, the single-mode number state $|n\rangle$ can be defined in a simplified notation as the eigenstate of the photon number operator $\hat{n} = \hat{a}^\dagger \hat{a}$:

$$\hat{n}\,|n\rangle = n\,|n\rangle\,. \tag{2.28}$$

Using Equation 2.15, the state $|n\rangle$ can then be written in terms of the vacuum state as

$$|n\rangle = \frac{(\hat{a}^\dagger)^n}{\sqrt{n!}}\,|0\rangle = \hat{N}(n)|0\rangle\,, \tag{2.29}$$

where we have defined the number state creation operator as

$$\hat{N}(n) = \frac{(\hat{a}^\dagger)^n}{\sqrt{n!}}. \tag{2.30}$$

From Equation 2.12, we can see that number states have a definite energy:

$$\langle n|\hat{H}\,|n\rangle = \hbar\omega\left(n+\frac{1}{2}\right) \qquad \text{and} \qquad \langle n|\hat{H}^2\,|n\rangle - \langle n|\hat{H}\,|n\rangle^2 = 0. \tag{2.31}$$

The expected value and variance of the quadrature operator x_θ can also be directly calculated as

$$\langle n|\hat{x}_\theta\,|n\rangle = 0 \qquad \text{and} \qquad \langle n|\hat{x}_\theta^2\,|n\rangle - \langle n|\hat{x}_\theta\,|n\rangle^2 = n+\frac{1}{2}, \tag{2.32}$$

which corresponds to a distribution centered on the origin, with a variance that is independent of the phase θ and scales with the energy of the state. We can infer from this that the mean value of the electric field for a number state is zero, and this behaviour is considerably different to that of a classical field, which oscillates at frequency ω. The Wigner function is [27]

$$W(x,p) = \frac{(-1)^n}{\pi} L_n[2(x^2+p^2)]e^{-x^2-p^2}, \tag{2.33}$$

where the function $L_n[\bullet]$ is the Laguerre polynomial, defined as

$$L_n[x] = \sum_{k=0}^{n}\binom{n}{k}\frac{(-1)^k}{k!}x^k, \tag{2.34}$$

for binomial coefficient

$$\binom{n}{k} = \frac{n!}{k!(n-k)!}. \tag{2.35}$$

For any number state, this Wigner function is symmetric about the origin, indicating that it always has a completely undefined phase. The Wigner function for a 3-photon number

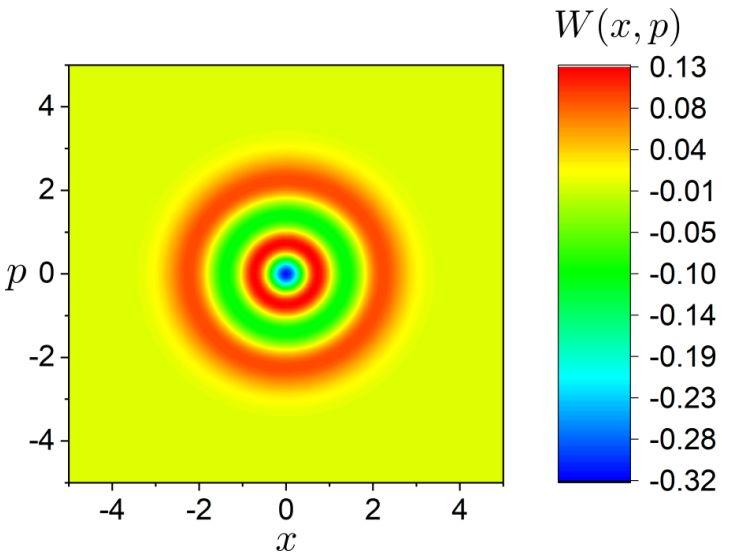

Figure 2.1: Wigner function of a 3-photon number state, $|3\rangle$.

state $|3\rangle$ is plotted in Figure 2.1. The highly non-classical nature of the photon number state is indicated by the regions of negativity in the Wigner function. The vacuum state $|0\rangle$ is a special case of the number state, and using Equation 2.33, the Wigner function of the vacuum state is

$$W(x,p) = \frac{e^{-x^2-p^2}}{\pi}. \tag{2.36}$$

This is a Gaussian probability distribution with a standard deviation of $1/\sqrt{2}$. From Equation 2.21, we can see that the vacuum state is a minimum uncertainty state.

2.1.4.2 Coherent States

The coherent state is defined as an eigenstate of the annihilation operator [26]:

$$\hat{a}\,|\alpha\rangle = \alpha\,|\alpha\rangle\,, \tag{2.37}$$

for complex amplitude α. It is useful for calculations to write this in the number basis, by using Equation 2.29 and Equation 2.37:

$$|\alpha\rangle = \sum_n^\infty |n\rangle\langle n|\alpha\rangle = \sum_n^\infty \frac{\alpha^n}{\sqrt{n!}}\langle 0|\alpha\rangle\,|n\rangle\,. \tag{2.38}$$

By substituting this expression into the normalisation condition $\langle\alpha|\alpha\rangle = 1$, and using the orthogonality of number states, it immediately follows that $e^{|\alpha|^2}|\langle 0|\alpha\rangle|^2 = 1$, and this gives

$$|\alpha\rangle = e^{-\frac{|\alpha|^2}{2}} \sum_n^\infty \frac{\alpha^n}{\sqrt{n!}}|n\rangle\,. \tag{2.39}$$

An important property of Equation 2.39 is that for two coherent states $|\alpha\rangle$ and $|\beta\rangle$, the overlap $|\langle\alpha|\beta\rangle|^2 = e^{-|\alpha-\beta|^2}$. Therefore, the coherent states do not form an orthonormal basis set. However, the overlap decays exponentially with distance, such that $|\alpha\rangle$ and $|\beta\rangle$ are approximately orthogonal if $|\alpha-\beta| \gg 1$. Equation 2.39 may also be written in terms of a unitary operation on the vacuum state as [26]

$$|\alpha\rangle = e^{\alpha\hat{a}^\dagger - \alpha^*\hat{a}}|0\rangle = D(\alpha)|0\rangle, \tag{2.40}$$

where the displacement operator $\hat{D}(\alpha)$ is defined as

$$\hat{D}(\alpha) = e^{\alpha\hat{a}^\dagger - \alpha^*\hat{a}}. \tag{2.41}$$

By considering the case of $\alpha = 0$, it is evident that the coherent state with $\alpha = 0$ is identical to the zero photon Fock state, and that both states can be equally considered as the vacuum state $|0\rangle$. The action of the displacement operator on the creation and annihilation operators are respectively:

$$\hat{D}(\alpha)^\dagger \hat{a}\hat{D}(\alpha) = \alpha + \hat{a} \qquad \text{and} \qquad \hat{D}(\alpha)^\dagger \hat{a}^\dagger \hat{D}(\alpha) = \alpha^* + \hat{a}^\dagger. \tag{2.42}$$

Therefore, for a coherent state with complex amplitude $\alpha = |\alpha|e^{i\theta}$, the expectation value and variance of the quadrature operators are given by

$$\langle\alpha|\hat{x}|\alpha\rangle = x_0 = \sqrt{2}|\alpha|\cos(\theta), \qquad \langle\alpha|\hat{x}^2|\alpha\rangle - \langle\alpha|\hat{x}|\alpha\rangle^2 = \frac{1}{2} \tag{2.43}$$

and

$$\langle\alpha|\hat{p}|\alpha\rangle = p_0 = \sqrt{2}|\alpha|\sin(\theta), \qquad \langle\alpha|\hat{p}^2|\alpha\rangle - \langle\alpha|\hat{p}|\alpha\rangle^2 = \frac{1}{2}. \tag{2.44}$$

From Equation 2.18, this implies that the mean value of the electric field oscillates with frequency ω. Furthermore, the quadrature noise becomes negligible in the limit $\alpha \gg 1$. Coherent states therefore closely resemble the behaviour of classical light predicted by Equation 2.9. It can also be shown that laser light can be considered as a coherent state excitation [26]. The photon number statistics are governed by the probability distribution

$$P(n) = |\langle n|\alpha\rangle|^2 = \frac{e^{\frac{-|\alpha|^2}{2}}|\alpha|^2}{\sqrt{n!}}, \tag{2.45}$$

which is a Poissonian distribution defined by a mean and variance of

$$\langle\alpha|\hat{n}|\alpha\rangle = |\alpha|^2 \qquad \text{and} \qquad \langle\alpha|\hat{n}^2|\alpha\rangle - \langle\alpha|\hat{n}|\alpha\rangle^2 = |\alpha|^2. \tag{2.46}$$

The Poisson distribution approaches a Gaussian distribution for large values of $\langle\hat{n}\rangle$, and the resulting photon number uncertainty of $\Delta n = \sqrt{n}$ is often referred to as shot noise. The Wigner function of a coherent state is given by [27]

$$W(x,p) = \frac{1}{\pi}e^{-(x-x_0)^2-(p-p_0)^2}. \tag{2.47}$$

Equation 2.47 describes a Gaussian minimum uncertainty state for all values of α, and corresponds to a vacuum state displaced from the origin by the distance $|\alpha|$. This is illustrated in Figure 2.2, in which the Wigner function for the coherent state $|\alpha\rangle$ is plotted for $\alpha = 0$ and $\alpha = 3e^{\frac{i\pi}{4}}$. It is evident that the quadrature noise distribution of the coherent state is independent of the amplitude α.

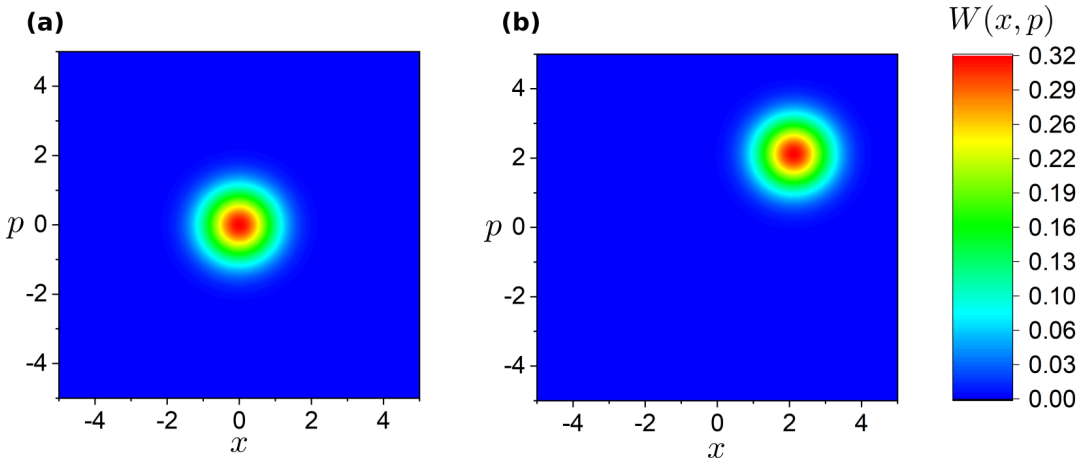

Figure 2.2: Wigner function of the coherent state, $|\alpha\rangle$, for (a) $\alpha = 0$ and (b) $\alpha = 3e^{\frac{i\pi}{4}}$.

2.1.4.3 Squeezed States

A squeezed state of light can be defined by the condition that for some phase angle θ, the uncertainty $\Delta\hat{x}_\theta < 1/\sqrt{2}$ [28]. From Equation 2.21, it is clear that there must be a corresponding increase in the uncertainty of the orthogonal $\hat{p}_\theta$ quadrature. A particularly useful example of squeezed light is provided by the squeezed coherent state, defined as

$$|\alpha, z\rangle = \hat{D}(\alpha)\hat{S}(z)|0\rangle\,, \tag{2.48}$$

where $\hat{D}(\alpha)$ is the displacement operator as defined in Equation 2.41, and $\hat{S}(z)$ is the squeezing operator:

$$\hat{S}(z) = e^{\frac{1}{2}(z^*\hat{a}^2 - z\hat{a}^{\dagger 2})} \qquad \text{and} \qquad z = re^{i\vartheta}, \tag{2.49}$$

for real r and ϑ. The action of the squeezing operator on the creation and annihilation operators is given by [26]

$$\hat{S}(z)^\dagger \hat{a}\hat{S}(z) = \hat{a}\cosh(r) - \hat{a}^\dagger e^{i\vartheta}\sinh(r) \qquad \text{and} \qquad \hat{S}(z)^\dagger \hat{a}^\dagger \hat{S}(z) = \hat{a}^\dagger \cosh(r) - \hat{a}e^{-i\vartheta}\sinh(r). \tag{2.50}$$

By using Equation 2.42, the action of the combined squeezing and displacement operators on the creation and annihilation operators can then be derived as

$$\hat{D}(\alpha)^\dagger \hat{S}(z)^\dagger \hat{a}\hat{S}(z)\hat{D}(\alpha) = \hat{a}\cosh(r) - \hat{a}^\dagger e^{i\vartheta}\sinh(r) + \alpha \tag{2.51}$$

and

$$\hat{D}(\alpha)^\dagger \hat{S}(z)^\dagger \hat{a}^\dagger \hat{S}(z)\hat{D}(\alpha) = \hat{a}^\dagger \cosh(r) - \hat{a}e^{-i\vartheta}\sinh(r) + \alpha^*. \tag{2.52}$$

This leads to the following eigenvalue equation for $|\alpha, z\rangle$:

$$(\hat{a}\cosh(r) + \hat{a}^\dagger e^{i\vartheta}\sinh(r))|\alpha, z\rangle = (\alpha\cosh(r) + \alpha^* e^{i\vartheta}\sinh(r))|\alpha, z\rangle. \tag{2.53}$$

Squeezed coherent states therefore tend towards quadrature eigenstates in the limit of infinite squeezing $r \to \infty$. For $\alpha = |\alpha|e^{i\theta}$, the quadrature expectation values and variances are given by

(2.54)

$$\langle\alpha, z|\hat{x}|\alpha, z\rangle = \sqrt{2}|\alpha|\cos(\theta), \qquad \langle\alpha, z|\hat{x}^2|\alpha, z\rangle - \langle\alpha, z|\hat{x}|\alpha, z\rangle^2 = \frac{1}{2}\left[e^{2r}\sin^2\left(\frac{\vartheta}{2}\right) + e^{-2r}\cos^2\left(\frac{\vartheta}{2}\right)\right]$$

and

(2.55)

$$\langle\alpha, z|\hat{p}|\alpha, z\rangle = \sqrt{2}|\alpha|\sin(\theta), \qquad \langle\alpha, z|\hat{p}^2|\alpha, z\rangle - \langle\alpha, z|\hat{p}|\alpha, z\rangle^2 = \frac{1}{2}\left[e^{2r}\cos^2\left(\frac{\vartheta}{2}\right) + e^{-2r}\sin^2\left(\frac{\vartheta}{2}\right)\right].$$

This implies that, while the mean value of the quadrature operators is identical to that of a coherent state, the uncertainty in each quadrature is dependant on the squeezing angle ϑ. For $r > 0$, the minimum and maximum uncertainty values are $e^r/\sqrt{2}$ and $e^{-r}/\sqrt{2}$ respectively, and can therefore be reduced below the uncertainty of the vacuum state $|0\rangle$. For the case that $r = 0$, the squeezed coherent state is identical to a coherent state. We note that for $\vartheta = 0$, $|\alpha, z\rangle$ is a minimum uncertainty state according to Equation 2.21. However, not all squeezed states are minimum uncertainty states, an example being the Kerr state, which will be discussed in Chapter 3.

The Wigner function of a general squeezed coherent state $|\alpha, z\rangle$ is given by [33]

$$W(x, p) = \frac{1}{\pi}e^{-e^{2r}\alpha_x^2 - e^{-2r}\alpha_y^2}, \tag{2.56}$$

where

$$\begin{aligned}\alpha_x &= (x - \Re(\alpha))\cos\left(\frac{\vartheta}{2}\right) + (y - \Im(\alpha))\sin\left(\frac{\vartheta}{2}\right),\\ \alpha_y &= -(x - \Re(\alpha))\sin\left(\frac{\vartheta}{2}\right) + (y - \Im(\alpha))\cos\left(\frac{\vartheta}{2}\right),\end{aligned} \tag{2.57}$$

with $\Re(\bullet)$ and $\Im(\bullet)$ corresponding to the real and imaginary parts respectively. In Figure 2.3, the Wigner function for a squeezed coherent state is plotted for $\alpha = 3e^{i\frac{\pi}{4}}$, $r = 0.5$ and $\vartheta = \frac{\pi}{2}$. Since $\vartheta = 2\theta$, the squeezing is oriented in the amplitude direction, and such a state is referred to as amplitude squeezed.

The contour of $W(x, p)$ corresponding to the uncertainty of the squeezed coherent state is an ellipse in phase space, i.e. the uncertainty is reduced in one quadrature at the expense

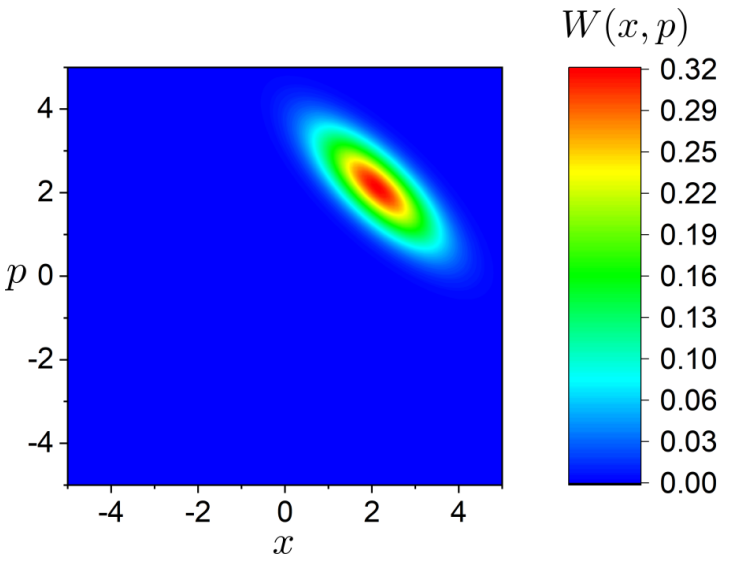

Figure 2.3: Wigner function for a squeezed coherent state with $\alpha = 3e^{i\frac{\pi}{4}}$, and $z = 0.5e^{i\frac{\pi}{2}}$.

of increased uncertainty in the orthogonal quadrature, and the corresponding probability distribution is non-classical [34]. For general ϑ, the orientation of this squeezing ellipse in quadrature space is given by the angle $\vartheta/2$, as indicated by Equations 2.54-2.55. The photon number statistics are given by

$$\langle \alpha, z | \hat{n} | \alpha, z \rangle = |\alpha|^2 + \sinh^2(r) \tag{2.58}$$

and

$$\begin{aligned} &\langle \alpha, z | \hat{n}^2 | \alpha, z \rangle - \langle \alpha, z | \hat{n} | \alpha, z \rangle^2 \\ &\quad = |\alpha|^2 \left(e^{2r} \sin^2 \left(\theta - \frac{1}{2}\vartheta \right) + e^{-2r} \cos^2 \left(\theta - \frac{1}{2}\vartheta \right) \right) + 2\sinh^2(r)\left(\sinh^2(r) + 1\right). \end{aligned} \tag{2.59}$$

This means that, for appropriate phase angles, the photon number statistics of squeezed coherent light can be sub-Poissonian, with a photon number uncertainty reduced to $\Delta n = e^{-r}\sqrt{n}$, below the shot noise limit of the coherent state. The minor axis of the uncertainty ellipse in this case is parallel to the direction of the complex amplitude α, and such a state is therefore amplitude squeezed. Conversely, a phase squeezed state has minimum uncertainty in the direction orthogonal to α.

In the case that $\alpha = 0$, the squeezed coherent state corresponds to a squeezed vacuum state $|z\rangle = \hat{S}(z)|0\rangle$. From Equations 2.54 and 2.55, it is clear that for squeezed vacuum, while the expectation values of the quadrature operators vanish, the quadrature variances are identical to that of a squeezed coherent state, and can therefore also be reduced below that of the vacuum state. For $r = 0$, the squeezed vacuum state $|z\rangle$ is reduced to the vacuum state $|0\rangle$. In general, it can be shown that, for some choice of ϑ, the application of the

squeezing operator $\hat{S}(z)$ to any quantum state defined by the density matrix $\hat{\rho}$ has the effect of reducing the quadrature uncertainty $\Delta\hat{x}$ by a factor of e^{-r} [34].

2.1.5 Multi-mode States and Operators

It is often the case that measurements in quantum optics require the description of more than one mode. In this section, some states and operators will be introduced that can be used to describe the behaviour of multi-mode light, and optical components that act on the Hilbert space of more than one mode.

2.1.5.1 Beamsplitters

A beamsplitter is an optical component that transmits and reflects incident light into two orthogonal spatial output modes. For the case that the properties of the beamsplitter are independent of the polarisation of incident light, i.e. for a non-polarising beamsplitter, the transformation of the two input modes defined by annihilation operators $\hat{a}$ and $\hat{b}$ are given by [26]

$$\begin{aligned} \hat{c} &= te^{i\phi_1}\hat{a} + re^{i\phi_2}\hat{b}, \\ \hat{d} &= re^{i\phi_3}\hat{a} + te^{i\phi_4}\hat{b}, \end{aligned} \tag{2.60}$$

where t, r, ϕ_1, ϕ_2, ϕ_3, $\phi_4 \in \Re$. The parameters r and t are respectively the reflection and transmission coefficients, and ϕ_n is the phase shift. This transformation is illustrated geometrically in Figure 2.4(a). Assuming that the transformations preserve the commutation relations, i.e. $[\hat{c},\hat{c}^\dagger] = [\hat{d},\hat{d}^\dagger] = 1$ and $[\hat{c},\hat{d}^\dagger] = 0$, the following conditions can be directly obtained:

$$r^2 + t^2 = 1 \qquad \text{and} \qquad \phi_1 + \phi_4 - \phi_2 - \phi_3 = \pi. \tag{2.61}$$

The values of $R = r^2$ and $T = t^2$ are known as the reflectance and transmittance, and define the average fraction of energy reflected and transmitted from the beamsplitter respectively. The ratio $R:T$ is often written as a percentage, such that for example a 90:10 beamsplitter is used to describe a beamsplitter with $r^2 = 0.9$ and $t^2 = 0.1$.

It is noted that, in order to preserve the commutation relations, the transformation given in Equation 2.60 must be used even if one of the input modes is empty, and therefore corresponds to a vacuum state. The coupling of vacuum fluctuations to non-classical light can have a significant effect on the noise characteristics of the quantum state. Equation 2.61 implies that there is some freedom in the choice of the phase shift of each component, and the correct phase shifts can be specified by considering the boundary conditions on the electromagnetic field at a partially reflective and transmissive surface. For example, light reflected by a medium with a higher refractive index than the one in which it is propagating

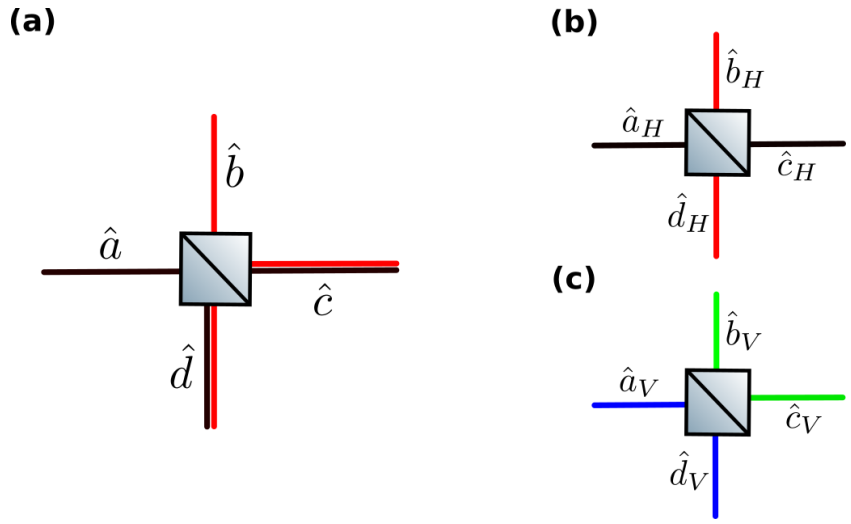

Figure 2.4: Geometrical illustration of the transformation for polarising and non-polarising beamsplitters, with input modes $\hat{a}, \hat{b}$ and output modes $\hat{c}, \hat{d}$. (a) Non-polarising beamsplitter. (b) Polarising beamsplitter, for horizontally polarised input light. (c) Polarising beamsplitter, for vertically polarised input light.

acquires a phase shift of π, while light reflected by a medium with a lower refractive index does not acquire a phase shift. Another important consequence of the conditions given in Equation 2.61 is that the total photon number is conserved:

$$\hat{n}_c + \hat{n}_d = \hat{c}^\dagger \hat{c} + \hat{d}^\dagger \hat{d} = (r^2 + t^2)(\hat{a}^\dagger \hat{a} + \hat{b}^\dagger \hat{b}) = \hat{n}_a + \hat{n}_b, \tag{2.62}$$

as expected for a lossless beamsplitter.

When considering an optical system with more than one mode, it is often convenient to use matrices to define transformations such as beamsplitter relations. Equation 2.60 can therefore be written as

$$\begin{bmatrix} \hat{c} \\ \hat{d} \end{bmatrix} = \begin{bmatrix} te^{i\phi_1} & re^{i\phi_2} \\ re^{i\phi_3} & te^{i\phi_4} \end{bmatrix} \begin{bmatrix} \hat{a} \\ \hat{b} \end{bmatrix}. \tag{2.63}$$

For example, in the case of a 90:10 beamsplitter, the transformation matrix B is given by

$$B = \begin{bmatrix} \sqrt{0.1} & \sqrt{0.9} \\ -\sqrt{0.9} & \sqrt{0.1} \end{bmatrix}. \tag{2.64}$$

It can be seen from this example that the π phase shift on the mode $\hat{a}$ upon reflection ensures that the matrix B is unitary. As discussed in Section 2.1.2, this is necessary since unitary transformations preserve the commutation relations.

Another commonly used beamsplitter in quantum optics experiments is the polarising beamsplitter, which reflects and transmits orthogonal polarisation components. This is a

four-mode transformation which can be written as

$$\begin{bmatrix} \hat{c}_H \\ \hat{d}_H \\ \hat{c}_V \\ \hat{d}_V \end{bmatrix} = \begin{bmatrix} 1 & 0 & 0 & 0 \\ 0 & 1 & 0 & 0 \\ 0 & 0 & 0 & 1 \\ 0 & 0 & 1 & 0 \end{bmatrix} \begin{bmatrix} \hat{a}_H \\ \hat{b}_H \\ \hat{a}_V \\ \hat{b}_V \end{bmatrix}. \tag{2.65}$$

As can be seen from Equation 2.65, the horizontally polarised component is always transmitted, while the vertically polarised component is reflected into the perpendicular spatial mode. This is illustrated in Figure 2.4(b)-(c). It can also be directly verified that this is a unitary and photon number conserving transformation. While polarising beamsplitters can equally be made to reflect horizontally polarised light and transmit vertically polarised light, the convention used in Equation 2.65 will be used in this thesis.

2.1.5.2 Waveplates

Other useful optical components include half-wave plates and quarter-wave plates. These devices act on a single spatial mode, and apply a relative phase shift between orthogonal polarisation components. We have seen that the action of the phase shift operator $U(\theta)$ on the annihilation operators gives $U(\theta)^\dagger \hat{a} U(\theta) = \hat{a} e^{-i\theta}$. Therefore, the action of a waveplate on the polarisation modes is given by

$$\begin{bmatrix} \hat{b}_H \\ \hat{b}_V \end{bmatrix} = \begin{bmatrix} 1 & 0 \\ 0 & e^{-i\theta} \end{bmatrix} \begin{bmatrix} \hat{a}_H \\ \hat{a}_V \end{bmatrix} = \begin{bmatrix} \hat{a}_H \\ \hat{a}_V e^{-i\theta} \end{bmatrix}. \tag{2.66}$$

Such a waveplate can be oriented at an arbitrary angle ϕ to the horizontal axis. The transformation can then be defined by a more general matrix $M(\theta, \phi)$:

$$\begin{aligned} M(\theta,\phi) &= \begin{bmatrix} \cos(\phi) & -\sin(\phi) \\ \sin(\phi) & \cos(\phi) \end{bmatrix} \begin{bmatrix} 1 & 0 \\ 0 & e^{-i\theta} \end{bmatrix} \begin{bmatrix} \cos(\phi) & \sin(\phi) \\ -\sin(\phi) & \cos(\phi) \end{bmatrix} \\ &= \begin{bmatrix} \cos^2(\phi) + e^{-i\theta}\sin^2(\phi) & \sin(\phi)\cos(\phi)(1-e^{-i\theta}) \\ \sin(\phi)\cos(\phi)(1-e^{-i\theta}) & \sin^2(\phi) + e^{-i\theta}\cos^2(\phi) \end{bmatrix}. \end{aligned} \tag{2.67}$$

For half-wave plates, $\theta = \pi$, and for quarter-wave plates, $\theta = \pi/2$. The effect of these devices can more easily be seen by writing the specific matrices:

$$M_{HWP}(\phi) = \begin{bmatrix} \cos(2\phi) & \sin(2\phi) \\ \sin(2\phi) & -\cos(2\phi) \end{bmatrix}, \qquad M_{QWP}(\phi) = \begin{bmatrix} \cos^2(\phi) - i\sin^2(\phi) & \sin(\phi)\cos(\phi)(1+i) \\ \sin(\phi)\cos(\phi)(1+i) & \sin^2(\phi) - i\cos^2(\phi) \end{bmatrix}. \tag{2.68}$$

Half-wave plates accordingly rotate the polarisation direction of incident light, while quarter-wave plates alter the ellipticity of the incident light, and can therefore be used to transform between linear and circular polarisation states.

2.1.5.3 Continuous Mode Light

In Section 2.1.2, the electromagnetic field operators were described in terms of a sum of frequency modes. Implicit in this description was the assumption of a finite quantisation cavity, of volume V, which ensures that only a discrete set of frequencies are supported. To describe real experiments, it is often useful take the limit of a quantisation axis which extends infinitely in the z direction, while retaining the assumption that the field is confined to a finite area A perpendicular to this axis. In this case, a continuous spectrum of frequencies are allowed, and therefore the summation of Equation 2.11 can be replaced by an integral. The conversion between discrete and continuous variable notation gives [26]

$$\sum_k \to \frac{1}{\Delta\omega}\int d\omega, \qquad \delta_{k,k'} \to \Delta\omega\delta(\omega-\omega'), \tag{2.69}$$

where the spacing of frequency modes $\Delta\omega \to 0$ in the limit of an infinite quantisation axis. The bosonic creation and annihilation operators are related by

$$\hat{a}_k \to \sqrt{\Delta\omega}\hat{a}(\omega) \qquad \text{and} \qquad \hat{a}_k^\dagger \to \sqrt{\Delta\omega}\hat{a}(\omega)^\dagger, \tag{2.70}$$

which means that the commutation relations are maintained:

$$[\hat{a}(\omega),\hat{a}(\omega')^\dagger] = \delta(\omega-\omega') \qquad \text{and} \qquad [\hat{a}(\omega),\hat{a}(\omega')] = 0. \tag{2.71}$$

Therefore, the continuous mode field operators can be treated much the same as the discrete mode counterparts. However, since a single mode of the continuum has zero measure, it is necessary to use the single particle representation for continuous mode Fock states, by labelling the frequency of each excitation explicitly. With this notation, an n-photon Fock state is written in terms of the vacuum state as

$$|\omega_1,\omega_2...,\omega_n\rangle = \frac{1}{\sqrt{n!}}\hat{a}(\omega_n)^\dagger...\hat{a}(\omega_1)^\dagger|0\rangle\,. \tag{2.72}$$

With the condition that $\hat{a}(\omega)|0\rangle = 0$, the action of the creation and annihilation operators on a continuous mode Fock state are then given by [34]

$$\hat{a}(\omega)^\dagger|\omega_1,...,\omega_n\rangle = \sqrt{1+n}\,|\omega,\omega_1...,\omega_n\rangle \tag{2.73}$$

and

$$\hat{a}(\omega)|\omega_1,...,\omega_n\rangle = \frac{1}{\sqrt{n}}\sum_i^n \delta(\omega-\omega_i)|\omega_1,...,\omega_{i-1},\omega_{i+1},...,\omega_n\rangle\,. \tag{2.74}$$

Orthogonality in the continuous mode basis is given by the expression:

$$\langle\omega'_m,...,\omega'_1|\omega_1,...,\omega_n\rangle = \delta_{nm}\frac{1}{n!}\sum_N \delta(\omega_1-\omega'_1)\delta(\omega_2-\omega'_2)... \tag{2.75}$$

where the summation is taken over the $n!$ possible pairings of the different frequency modes. Given the complexity of the above notation, it is often useful to transform into a discrete mode basis by [35]

$$\hat{b}_i^\dagger = \int \phi_i(\omega)\hat{a}(\omega)^\dagger d\omega, \tag{2.76}$$

which may be compared to the equivalent transformation between discrete mode bases given in Equation 2.13. Provided that the functions $\phi_i(\omega)$ form an orthonormal basis set, the resulting mode operators $\hat{b}_i$ satisfy the discrete mode commutation relations. This approach can for example be used to define a Fock space where each excitation corresponds to a single photon wavepacket distributed over a range of frequencies.

Another useful feature of the continuous mode basis is that, assuming the bandwidth of the field excitation is much smaller that its central frequency, it is possible to define the time domain creation and annihilation operators, which are related to the frequency domain annihilation operators by Fourier transform [26]:

$$\hat{a}(t) = \int_{-\infty}^{\infty} \hat{a}(\omega)e^{-i\omega t}d\omega, \qquad \hat{a}(\omega) = \int_{-\infty}^{\infty} \hat{a}(t)e^{i\omega t}dt. \tag{2.77}$$

It follows from Equation 2.71 that such time domain operators also have an associated commutation relation:

$$[\hat{a}(t), \hat{a}(t')^\dagger] = \delta(t - t'). \tag{2.78}$$

The photon number operator can be written as a function of either time or frequency as

$$\hat{n} = \int \hat{a}(\omega)^\dagger \hat{a}(\omega)d\omega = \int \hat{a}(t)^\dagger \hat{a}(t)dt. \tag{2.79}$$

We will see that the use of the continuous mode operators will play an important role in describing the propagation of pulsed light, and in the theory of photodetection.

2.1.6 Fluctuation Analysis of Quantum States

When considering the time evolution of quantum fields, it is often useful to separate the annihilation operator into the classical mean-field component $\langle \hat{A}(t) \rangle$ and the quantum fluctuation operator $\hat{a}(t)$ [36]:

$$\hat{A}(t) = \langle \hat{A}(t) \rangle + \hat{a}(t) = \alpha(t) + \hat{a}(t). \tag{2.80}$$

Here, $\hat{A}(t)$ is the annihilation operator evolved according to the Heisenberg picture, and $\hat{a}(t)$ governs the quantum fluctuations. It is noted that $\langle \hat{A}(t) \rangle$ is still in general a function of time, since the expectation value is taken on the vacuum state $|0\rangle$ and so does not average over stochastic or deterministic variations in the coherent amplitude $\alpha(t)$.

As a simple example, we can consider that for a quasi-monochromatic coherent state, we have $\alpha(t) = \alpha$, where $|\alpha|^2$ is the average photon flux per unit time. The total number of photons integrated over a duration T is given by

$$\hat{n} = \int_0^T \hat{A}(t)^\dagger \hat{A}(t) dt = \int_0^T \left(\alpha^* + \hat{a}(t)^\dagger\right)\left(\alpha + \hat{a}(t)\right) dt \\ = |\alpha|^2 T + \int_0^T \left(\alpha^* \hat{a}(t) + \alpha \hat{a}(t)^\dagger + \hat{a}(t)^\dagger \hat{a}(t)\right) dt, \tag{2.81}$$

where $\hat{a}(t)$ is just the time domain bosonic annihilation operator as defined in Equation 2.77. This gives a photon number mean and variance of

$$\langle \hat{n} \rangle = |\alpha|^2 T \qquad \text{and} \qquad \langle \hat{n}^2 \rangle - \langle \hat{n} \rangle^2 = \int_0^T \int_0^T |\alpha|^2 \langle \hat{a}(t) \hat{a}(t')^\dagger \rangle dt dt' = |\alpha|^2 T, \tag{2.82}$$

as expected from Equation 2.46. In Section 2.2, this approach will provide a useful means of analysing photodetection techniques.

2.2 Photodetection

In order to describe in more detail how the quantum states discussed in Section 2.1 relate to experimentally measured quantities, it is necessary to introduce the theory of photodetection. Here, we will focus on photodiode measurements, which will be the method of detection used in Chapters 3-5.

2.2.1 Direct Detection

A photodiode is a semiconducting device which generates free electrons when photons are absorbed, allowing a current to flow which is proportional to the number of detected photons [37]. We can therefore introduce a photocurrent operator:

$$\hat{i}(t) = q\hat{n}(t) = q\hat{A}(t)^\dagger \hat{A}(t), \tag{2.83}$$

where q is the electron charge, and this corresponds to the instantaneous photocurrent generated from an ideal detector. Direct detection refers to the measurement strategy whereby a quantum state is measured directly by a single photodiode, and can therefore be used to perform photon number measurements of a quantum state. This is illustrated in Figure 2.5. A photodetector typically consists of a photodiode connected to an electronic circuit which amplifies the voltage of the measured signal, such that it can be analysed by a measurement device such as a spectrum analyser or oscilloscope.

Since not all photons that reach the photodiode will be absorbed, the quantum efficiency η is used to characterise the ratio of generated electrons to incident photons. This effect

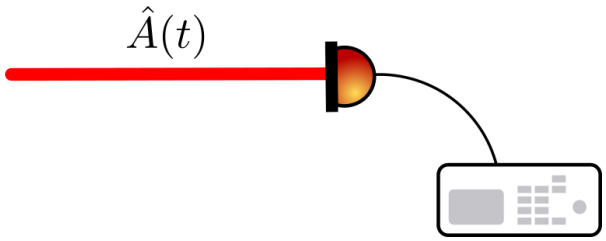

Figure 2.5: Direct detection of a quantum state of light. It is assumed that the active area of the photodiode is larger than the cross-sectional area of the mode function of the detected light. The photocurrent is analysed on a measuring device such as a spectrum analyser or oscilloscope.

can be accounted for by modelling the detector as a perfect efficiency photodiode preceded by a beamsplitter with transmission coefficient $t = \sqrt{\eta}$ [26]. Another feature of imperfect detectors is the electronic noise, which can be described by the addition of a stochastic noise term to the measured photocurrent. Writing the annihilation operator as $\hat{A}(t) = |\alpha(t)|e^{i\theta} + \hat{a}(t)$, the photocurrent operator can be approximated as

$$\hat{i}(t) \approx q\left(|\alpha(t)|^2 + \sqrt{2}|\alpha(t)|\hat{x}_\theta(t)\right), \tag{2.84}$$

where it is assumed that the term quadratic in the annihilation operators is negligible, and electronic noise has been neglected. The quadrature operator $\hat{x}_\theta(t)$, as defined in Equation 2.22, corresponds to the quantum amplitude fluctuations of $\hat{A}(t)$.

2.2.2 Homodyne Detection

Another commonly used detection technique is homodyne detection, which enables the measurement of arbitrary quadrature components of an optical field [38]. This scheme is shown in Figure 2.6 and involves the interference of a signal field $\hat{A}_s(t)$ to be measured with a phase shifted reference field $\hat{A}_{LO}(t)e^{-i\phi}$, known as the local oscillator (LO), on a 50:50 beamsplitter (BS). The two output modes of the beamsplitter are measured on separate photodiodes, and the quadrature measurement is achieved by taking the electronic subtraction of the two photocurrents. The phase ϕ can be controlled by a phase shifter applied to the LO before the 50:50 beamsplitter. The output of each mode of the beamsplitter can then be written as

$$\hat{A}_1(t) = \frac{1}{\sqrt{2}}(\hat{A}_s(t) + \hat{A}_{LO}(t)e^{-i\phi}), \qquad \hat{A}_2(t) = \frac{1}{\sqrt{2}}(\hat{A}_s(t) - \hat{A}_{LO}(t)e^{-i\phi}). \tag{2.85}$$

This results is a value for the photon number operator measured at each detector of

$$\hat{n}_1(t) = \frac{1}{2}(\hat{A}_s^\dagger(t)\hat{A}_s(t) + \hat{A}_{LO}^\dagger(t)\hat{A}_{LO}(t) + \hat{A}_s^\dagger(t)\hat{A}_{LO}(t)e^{-i\phi} + \hat{A}_{LO}^\dagger(t)\hat{A}_s(t)e^{i\phi}) \tag{2.86}$$

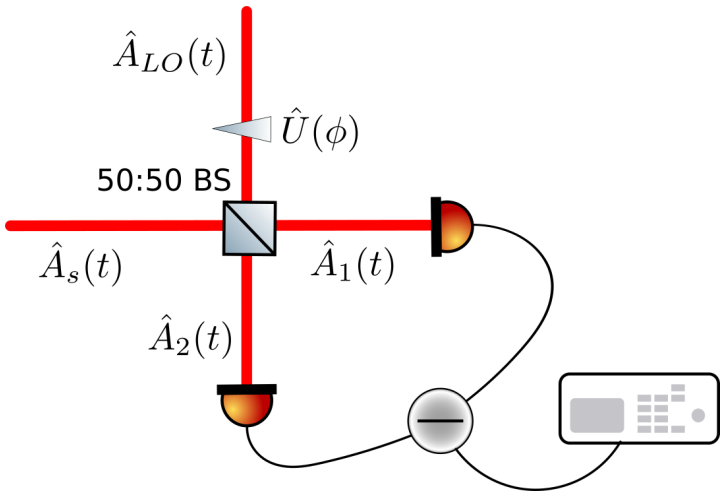

Figure 2.6: Homodyne detection of a quantum state of light. The signal beam and local oscillator typically come from the same source, in order that the local oscillator can provide a constant phase reference.

and

$$\hat{n}_2(t) = \frac{1}{2}(\hat{A}_s^\dagger(t)\hat{A}_s(t) + \hat{A}_{LO}^\dagger(t)\hat{A}_{LO}(t) - \hat{A}_s^\dagger(t)\hat{A}_{LO}(t)e^{-i\phi} - \hat{A}_{LO}^\dagger(t)\hat{A}_s(t)e^{i\phi}). \tag{2.87}$$

The subtraction photocurrent is therefore

$$\hat{i}_-(t) = q(\hat{n}_1(t) - \hat{n}_2(t)) = q(\hat{A}_s^\dagger(t)\hat{A}_{LO}(t)e^{-i\phi} + \hat{A}_{LO}^\dagger(t)\hat{A}_s(t)e^{i\phi}). \tag{2.88}$$

If the LO is a bright coherent state, it may be written as $\hat{A}_{LO}(t) = |\alpha_{LO}|e^{i\theta_{LO}} + \hat{a}_{LO}(t)$, where $\hat{a}_{LO}(t)$ is the ordinary bosonic annihilation operator. Furthermore, if the local oscillator is sufficiently bright compared to the signal field ($|\alpha_{LO}| \gg \langle \hat{A}_s(t) \rangle$), then the quantum fluctuations on the LO may be neglected, resulting in

$$\hat{i}_-(t) = q|\alpha_{LO}|\left(e^{\theta_{LO}-\phi}\hat{A}_s^\dagger(t) + e^{\phi-\theta_{LO}}\hat{A}_s(t)\right) = \sqrt{2}q|\alpha_{LO}|\hat{x}_{s,\theta}(t), \tag{2.89}$$

where $\hat{x}_{s,\theta}$ is the quadrature amplitude of the signal field at phase $\theta = \theta_{LO} - \phi$, as defined in Equation 2.22. This means that quadrature measurements of the signal field can be taken at arbitrary phases θ by scanning the phase shift ϕ applied to the LO. An advantage of this strategy is that, in the strong LO limit, the detected photocurrent is insensitive to noise on the LO beam [39]. Furthermore, given that the difference photocurrent is proportional to the amplitude of the LO, arbitrarily small signals can be measured by increasing the power of the local oscillator. By repeated measurements on identical copies of quantum states at different phase angles, this strategy can be used to reconstruct the Wigner function of an arbitrary single mode quantum state, in a process called homodyne tomography [40].

2.2.3 Self-Homodyne Detection

A variation of the homodyne detection technique described above is self-homodyne detection, which is also referred to as balanced detection. In this case, the local oscillator beam is removed, and both the addition and subtraction photocurrents are measured, as shown in Figure 2.7. The signal field may be separated into the mean field and fluctuating com-

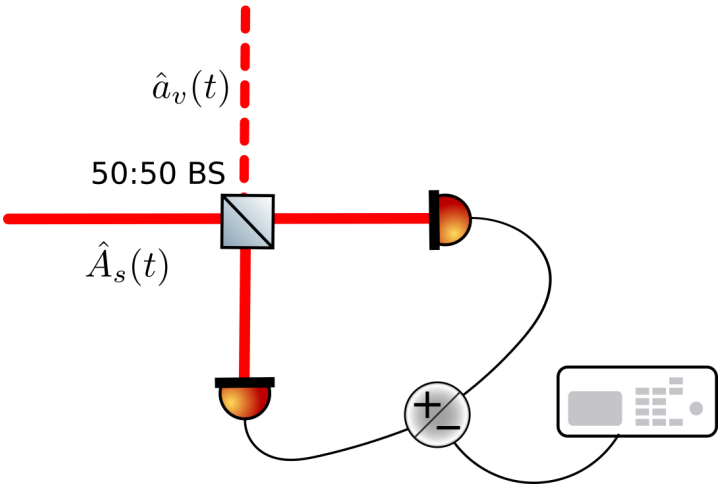

Figure 2.7: Self-homodyne detection of a quantum state of light. The removal of the local oscillator means that only the amplitude quadrature is measured, as in direct detection. The dashed line indicates a vacuum port.

ponents as $\hat{A}_s(t) = |\alpha|e^{i\theta} + \hat{a}_s(t)$, and the LO is replaced by the vacuum state $\hat{a}_v(t)$. From Equation 2.86-2.87, the addition and subtraction photocurrents are then respectively

$$\hat{i}_+(t) \approx q\left(|\alpha|^2 + \sqrt{2}|\alpha|\hat{x}_{s,\theta}(t)\right) \tag{2.90}$$

and

$$\hat{i}_-(t) = \sqrt{2}q|\alpha|\hat{x}_{v,\theta}(t). \tag{2.91}$$

By using the noise of the subtraction photocurrent as a reference, this measurement therefore enables a direct comparison of the amplitude noise of the quantum state $\hat{A}_s(t)$ relative to the vacuum noise [36]. This can be used to measure the squeezing of bright amplitude squeezed light, as discussed in Section 2.3.2.

For homodyne and self-homodyne detection, transimpedance-amplified balanced photodetectors are often used [41]. These devices consist of two photodiodes connected in series, such that the difference photocurrent is amplified. In the case of self-homodyne detection, the addition photocurrent can be measured by sending all the light to one of the two photodiodes.

2.2.4 Spectral Analysis of Photocurrents

We have seen in Sections 2.2.1-2.2.3 how the time domain photocurrent relates to the quantum fluctuations of the measured light for these detection strategies. In practise, it is also necessary to consider the low frequency classical noise due to the optical field and the detection electronics. In the case of homodyne detection, there is significant cancellation of low frequency optical noise in the subtraction photocurrent, since classical laser intensity fluctuations will be correlated between the photodiodes. Therefore, for a detector with sufficiently low electronic noise, time domain measurements of quantum noise can be achieved [42]. However, in this thesis, we will be primarily concerned with direct measurements of a quantum field, as described in Section 2.2.1. In this case, frequency domain measurements are necessary to avoid the effect of classical fluctuations in the detected light [36]. This can be achieved either by taking the Fourier transform of time domain data acquired with an oscilloscope, or by measuring the spectral components of the photocurrent directly using an electronic spectrum analyser (SA). In this section, some relevant details of spectrum analyser measurements will be discussed.

An SA is an electronic device which measures the power spectrum of a voltage source. Most modern spectrum analysers operate using the heterodyne principle, and the operation of such a spectrum analyser is outlined is as follows, based on the description in [43]. A block diagram illustrating the operation a heterodyne spectrum analyser is shown in Figure 2.8. The input signal is mixed with a local oscillator, which shifts the frequency com-

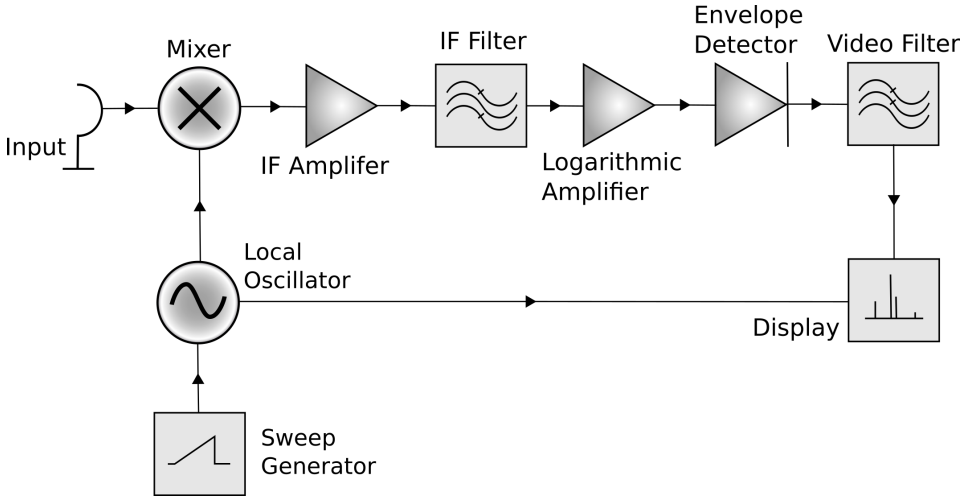

Figure 2.8: Block diagram of a spectrum analyser (SA) operating on the heterodyne principle.

ponents of the signal, and the resulting signal is amplified. The intermediate frequency (IF) filter is then used to select a frequency component of the signal. The IF filter has a fixed frequency, so the frequency of the local oscillator must be tuned in order to select differ-

ent frequency components of the signal. The 3 dB bandwidth of the IF filter is known as the resolution bandwidth (RBW), and determines the frequency resolution of the displayed noise spectrum. Following the IF filter, the signal is logarithmically amplified, which enables the detection of signals with a large dynamic range. The envelope detector outputs a voltage corresponding to the amplitude of the selected frequency component. The low-pass video filter then reduces the fluctuations in the voltage from the envelope detector, effectively averaging the measured signal. The bandwidth of the video filter is called the video bandwidth (VBW), and for values of VBW<RBW, the video filter reduces the fluctuations on the measured signal. Analog-to-digital converters are used to digitise the measured signal before it is displayed, and each measured sample of the spectral noise power can therefore be a result of further processing on multiple data points. For the measurements discussed in this thesis, the spectrum analyser was set to sample mode, which means only one sample is used for each data point, and avoids additional complexity involved in analysing the effect of further digital processing on the statistics of the measured data.

The measured power in a $\pm B/2$ frequency interval around the detection frequency Ω can be defined as

$$p_\Omega = 2R \left| \int_{-\infty}^{\infty} H(\nu)\hat{i}(\nu)d\nu \right|^2, \tag{2.92}$$

where R is the resistance of the measurement device, $H(\nu)$ is the response function of the IF filter, and the factor of 2 comes from the integration over positive and negative frequencies. The spectral photocurrent $\hat{i}(\nu)$ is related to the time domain photocurrent $\hat{i}(t)$ by Fourier transform:

$$\hat{i}(\nu) = \int_{-\infty}^{\infty} \hat{i}(t)e^{-2\pi i\nu t}dt. \tag{2.93}$$

The function $H(\nu)$ is typically Gaussian distributed. While a rectangular filter function would be ideal, the transient response of such a filter would significantly limit the speed of the measurement. Nonetheless, when theoretically modelling the spectral noise power, a rectangular filter function can often be assumed. In this case, Equation 2.92 reduces to

$$p_\Omega = 2R \left| \int_{\Omega-\frac{B}{2}}^{\Omega+\frac{B}{2}} \hat{i}(\nu)d\nu \right|^2. \tag{2.94}$$

It is important to note that Equation 2.94 differs from an often quoted definition of the power in a frequency band, $p_\Omega = 2R\int_{\Omega-\frac{B}{2}}^{\Omega+\frac{B}{2}} |i(\nu)|^2 d\nu$ [36]. The reason for the definition used here is that measuring devices such as spectrum analysers and oscilloscopes are fundamentally voltage detectors, and therefore the displayed power level is computed from the voltage measured in a given frequency range. This means that the integration of the photocurrent density effectively occurs before taking the absolute square. While the average value $\langle p_\Omega \rangle$

typically does not significantly differ between these definitions, Var(p_Ω) does. Since much of the analysis presented in this thesis will relate to the variance of the spectral power, Equation 2.94 will be used as a definition for p_Ω throughout.

In order to extract useful information from spectrum analyser measurements, it is often necessary to make relative measurements between different spectral features. For example, if the signal has a single harmonic component at a sideband frequency, signal-to-noise ratio (SNR) measurements can be used to gain information about the properties of the detected light. However, it is necessary to account for some of the electronic processing of the spectrum analyser to correctly interpret the results of such measurements. When the video filter averages the output of the logarithmic amplifier, the power p_Ω is determined from square of the average voltage, where the average voltage is a result of logarithmic voltage measurements. The resulting power can differ from that which would be obtained by computing the average of a series of power measurements, if the voltage does not have a Gaussian probability distribution [44]. This is because the average of the log is not necessarily the same as the log of the average. This is the case for noise measurements, which follow a Rayleigh distribution, and results in an under-response of 2.51 dB in the measured power of broadband noise. This means that a correction factor of 2.51 dB must be added to noise measurements to obtain a true estimate of the noise power. The voltage of CW signals is typically Gaussian distributed, and therefore this correction factor does not apply.

Another important consideration when analysing noise measurements relates to the equivalent noise bandwidth (ENB), which defines the width of a rectangular filter which would measure the same p_Ω in response to white noise as a Gaussian filter with a RBW of B. The ratio between the ENB and the RBW is 1.056 (0.24 dB). Therefore, if the assumption of a rectangular is made when analysing the spectral noise power, 0.24 dB must be subtracted from the measured noise power to correct for this difference [44].

So far we have discussed the additional considerations required when analysing the average power values measured by a spectrum analyser. In this thesis, the behaviour of the variance of such measurements will also play an important role. Therefore, it is useful to discuss the effect that video filtering has on the variance spectrum analyser measurements. As outlined above, the function of the video filter is to reduce the variance of the power measurements, and we will therefore introduce the factor ε, which corresponds to the variance reduction factor due to video averaging. The bandwidth of the envelope modulation noise resulting from these power fluctuations is approximately half the effective noise bandwidth of the RBW filter, and the noise bandwidth of the video filter is typically a factor of $\pi/2$ greater than the VBW [44]. The value of ε results from the ratio of these two bandwidths, and is therefore

$$\varepsilon = \frac{\pi B_V}{1.056 B}. \tag{2.95}$$

It should be noted that modern spectrum analysers are not restricted to using the heterodyne principle described above, and can also output a power spectrum by digitising the time domain data and performing the fast Fourier transform (FFT) to measure the spectral noise power [45]. The same process would be required if using an oscilloscope for this measurement. An advantage of FFT analysers is that, whereas heterodyne analysers require an individual measurement at each frequency, FFT analysers can output the spectral noise power for a range of frequencies using a single measurement of integration time $t = 1/B$, where B is the frequency resolution. However, FFT analysers are limited by the sample rate of the analog-to-digital converter, and therefore are more suitable for measurements of low frequency signals. Many of the measurements in this thesis will be performed using a spectrum analyser operating in heterodyne mode, due to the high measurement frequencies and RBW. Nonetheless, Equation 2.94 may be used to analyse the spectral noise power for both FFT and heterodyne spectrum analysis. In the case of FFT analysers, the variance reduction factor equivalent to that in Equation 2.95 simply corresponds to the inverse of the number of averages used to compute each estimate of p_Ω. Many of the spectrum analyser measurements in this thesis will only be taken at a single frequency, for example when monitoring the power of a signal over time. The spectrum analyser setting corresponding to such time-domain measurements of a single frequency component is referred to as zero-span mode. In this case, the speed advantage of FFT analysers measuring over a wide frequency range does not apply, making heterodyne analysers ideal for this type of measurement.

2.3 Measurements of Squeezed Light

The focus of this thesis is the application of bright squeezed light to high precision measurements. Therefore, in this section, some of the concepts introduced so far will be used to describe measurements of squeezed light in more detail. In particular, we will discuss the detection of broadband amplitude squeezed light, accounting for the low frequency noise typically observed in real experiments.

2.3.1 Squeezed Light in the Frequency Domain

We first consider the single mode squeezing operator defined in Equation 2.49. In the basis of continuous frequency modes, the squeezing operator can be generalised as [46]

$$\hat{S}(\xi) = e^{\frac{1}{2}(\hat{P}(\xi) - \hat{P}(\xi)^\dagger)}, \tag{2.96}$$

where the operator

$$\hat{P}(\xi) = \int\int \xi(\omega, \omega')\hat{a}(\omega)\hat{a}(\omega')d\omega d\omega' \tag{2.97}$$

is known as the continuous mode photon pair annihilation operator. A special case of the function $\xi(\omega,\omega')$ is given by

$$\xi(\omega,\omega') = z(\omega)\delta(\omega+\omega'-2\omega_p), \qquad 0 \leq \omega,\omega' \leq 2\omega_p. \tag{2.98}$$

This corresponds to the nonlinear process of four-wave mixing, whereby a pair of photons is created from two pump photons of frequency ω_p [47]. The resulting photon pair creation operator is

$$\hat{P}(\xi)^\dagger = \int z(\omega)\hat{a}(\omega)^\dagger \hat{a}(2\omega_p-\omega)^\dagger d\omega. \tag{2.99}$$

By writing $z(\nu) = r(\nu)e^{i\vartheta(\nu)}$, where $\nu = \omega - \omega_p$ is the distance from the pump frequency, the action of the corresponding squeezing operator $\hat{S}(\xi)$ on the creation and annihilation operators is then given by [48]

$$\hat{a}_\xi(\nu) = \hat{S}(\xi)^\dagger \hat{a}(\nu)\hat{S}(\xi) = \hat{a}(\nu)\cosh(r(\nu)) - \hat{a}(-\nu)^\dagger e^{i\vartheta(\nu)}\sinh(r(\nu)) \tag{2.100}$$

and

$$\hat{a}_\xi(\nu)^\dagger = \hat{S}(\xi)^\dagger \hat{a}(\nu)^\dagger \hat{S}(\xi) = \hat{a}(\nu)^\dagger\cosh(r(\nu)) - \hat{a}(-\nu)e^{-i\vartheta(\nu)}\sinh(r(\nu)). \tag{2.101}$$

Comparing Equations 2.100-2.101 to Equation 2.50, we can see that the effect of such a squeezing operation on the vacuum state is to introduce correlations between pairs of frequency modes centered on the pump frequency. Using Equation 2.76, we can transform into the basis of discrete temporal modes:

$$\hat{b} = \int \phi(\omega)^* \hat{a}_\xi(\omega) d\omega. \tag{2.102}$$

It follows that the annihilation operator for a single temporal mode of the continuous mode squeezed state defined by Equation 2.98 is [49]

$$\hat{b}_\xi = \hat{b}\cosh(r) - \hat{b}^\dagger e^{i\vartheta}\sinh(r), \tag{2.103}$$

which is an ideal single mode squeezed state. Here we have assumed that the function $\phi(\nu)$ is sufficiently narrowband that the squeezing parameters $r(\nu)$ and $\vartheta(\nu)$ may be assumed to be constant. The connection between single mode squeezing in the time domain and continuous mode squeezing between pairs of frequency modes will be useful for analysing the detection of single mode squeezed light in the frequency domain.

2.3.2 Characterising the Noise Properties of Squeezed Light

We now consider self-homodyne of amplitude squeezed light in the frequency domain. As for Equation 2.80, the annihilation operator of the amplitude squeezed state can be written as

$$\hat{A}_s(t) = |\alpha(t)|e^{i\theta} + \hat{a}_s(t). \tag{2.104}$$

The classical amplitude $|\alpha(t)|$ is treated here as a stochastic variable, and can be denoted $|\alpha(t)| = \alpha + \zeta(t)\alpha$, where $\langle|\alpha(t)|\rangle = \alpha$ and $\zeta(t)$ is a noise term with $\langle\zeta(t)\rangle = 0$, which arises from the low frequency classical noise of the laser. By neglecting terms quadratic in the creation/annihilation operators as in Equation 2.84, the addition and subtraction photocurrent are respectively:

$$\hat{i}_+(t) = q\left(|\alpha(t)|^2 + \sqrt{2}|\alpha(t)|\hat{x}_{s,\theta}(t) + n_e(t)\right), \tag{2.105}$$

and

$$\hat{i}_-(t) = q\left(\sqrt{2}|\alpha(t)|\hat{x}_{v,\theta}(t) + n_e(t)\right), \tag{2.106}$$

where $n_e(t)$ is the dark count rate from electronic noise, and $\hat{x}_{s,\theta}(t)$ and $\hat{x}_{v,\theta}(t)$ respectively are the quadrature operators for the squeezed state and the vacuum state. The spectral photocurrent density for the addition photocurrent is then given by

$$\hat{i}_+(\nu) = q\left[I(\nu) + \sqrt{2}\int \alpha(\mu)\hat{x}_{s,\theta}(\nu-\mu)d\mu\right], \tag{2.107}$$

where $\int \equiv \int_{-\infty}^{\infty}$, and $I(\nu)$ is the Fourier transform of the classical component:

$$I(\nu) = \int \left(|\alpha(t)|^2 + n_e(t)\right)e^{-2\pi i\nu t}dt. \tag{2.108}$$

Also, the Fourier transform of the quadrature operator is

$$\hat{x}_{s,\theta}(\nu) = \int \hat{x}_{s,\theta}(t)e^{-2\pi i\nu t}dt = \frac{1}{\sqrt{2}}\left[\hat{a}_s(-\nu)^\dagger e^{i\theta} + \hat{a}_s(\nu)e^{-i\theta}\right]. \tag{2.109}$$

For amplitude squeezed light, $\hat{a}_s(\nu)$ has the form of Equation 2.100 with $z(\nu) = re^{2i\theta}$, where the phase $\vartheta = 2\theta$ ensures the squeezing is oriented in the amplitude direction. The frequency dependence of the classical amplitude of the light is defined by

$$\alpha(\nu) = \int |\alpha(t)|e^{-2\pi i\nu t}dt = \alpha\delta(\nu) + \alpha h(\nu), \tag{2.110}$$

where $h(\nu) = \int \zeta(t)e^{-2\pi i\nu t}dt$ describes the frequency dependence of the classical amplitude noise. It also follows from Equation 2.108 that

$$I(\nu) = \alpha^2\left(\delta(\nu) + 2h(\nu) + \int h(\mu)h(\nu-\mu)d\mu\right) + n_e(\nu). \tag{2.111}$$

It is now possible to analyse the case of a spectrum analyser measurement at frequency Ω. For a resolution bandwidth of B, the detected power is the average value $\langle p_\Omega\rangle$, where p_Ω is given by Equation 2.94. From Equations 2.107-2.111, and writing $\int_{\Omega-\frac{B}{2}}^{\Omega+\frac{B}{2}} \equiv \int^{\Omega}$, this results

in

$$\langle p_\Omega^+ \rangle = 2R \left\langle \left| \int^\Omega \hat{i}_+(\nu) d\nu \right|^2 \right\rangle \tag{2.112}$$

$$= 2q^2 R \left[\left\langle \left| \int^\Omega I(\nu) d\nu \right|^2 \right\rangle + 2 \left\langle \int^\Omega \int^\Omega \int\int \alpha(\mu)^* \alpha(\overline{\mu}) \hat{x}_{s,\theta}(\nu-\mu)^\dagger \hat{x}_{s,\theta}(\overline{\nu}-\overline{\mu}) d\mu d\overline{\mu} d\nu d\overline{\nu} \right\rangle \right]$$

$$= 2q^2 R \left[4\alpha^4 \left\langle \left| \int^\Omega h(\nu) d\nu \right|^2 \right\rangle + \left\langle \left| \int^\Omega n_e(\nu) d\nu \right|^2 \right\rangle + \alpha^2 B e^{-2r} \right],$$

where the expectation value has been evaluated on the vacuum state, and terms involving the expectation value of a single quadrature operator have been neglected due to the orthogonality condition of Equation 2.75. The factor of e^{-2r} on the last term demonstrates that the detected light is in fact amplitude squeezed. The classical and electronic noise terms give independent contributions since they are uncorrelated, and hence have a random phase relationship. This is sometimes referred to as adding noise in quadrature [36]. The power resulting from the subtraction photocurrent equivalently results in

$$\langle p_\Omega^- \rangle = 2q^2 R \left[\left\langle \left| \int^\Omega n_e(\nu) d\nu \right|^2 \right\rangle + \alpha^2 B \right]. \tag{2.113}$$

The noise of the subtraction photocurrent therefore gives a reliable measure of the combined optical shot noise and electronic noise even in the presence of excess laser amplitude noise. In order to estimate the squeezing, it is therefore necessary to ensure that $\langle p_\Omega^+ \rangle = \langle p_\Omega^- \rangle$ when $r = 0$, i.e. that the classical noise due to $\zeta(t)$ is negligible at the detection frequency. If the measured power due to electronic noise alone is $\langle p_E \rangle$, then the squeezing parameter $\Phi = e^{-2r}$ may be directly inferred by

$$\Phi = \frac{\langle p_\Omega^+ \rangle - \langle p_\Omega^E \rangle}{\langle p_\Omega^- \rangle - \langle p_\Omega^E \rangle}. \tag{2.114}$$

This strategy is used to characterise the generated squeezing in Chapter 3. The degree of squeezing is often quoted in decibels, as

$$\Phi_{dB} = 10 \log_{10}(\Phi). \tag{2.115}$$

Throughout this thesis, experimentally measured squeezing values will accordingly be quoted in decibels, with the dB subscript used to distinguish between the linear and logarithmic units.

2.3.3 Effect of Loss on Squeezing

A final property of squeezed light which is useful to briefly discuss is the effect of loss on squeezing. Optical loss on a mode $\hat{A}$, defined by transmittance η, can in general be modelled by a beamsplitter with transmission and reflection coefficients $t = \sqrt{\eta}$ and $r = \sqrt{1-\eta}$

respectively [50]. Using Equation 2.60, we can therefore write the mode $\hat{A}'$ after the loss as

$$\hat{A}' = \sqrt{\eta}\hat{A} + \sqrt{1-\eta}\hat{a}, \tag{2.116}$$

where the coupled mode $\hat{a}$ is in the vacuum state. As discussed in Section 2.1.5.1, this description ensures that the commutation relations are conserved. If the mode $\hat{A}$ corresponds to a squeezed state, it follows directly from Equation 2.116 that the squeezing parameter on the output of the loss is given by [36]

$$\Phi' = \eta\Phi + 1 - \eta, \qquad \text{or} \qquad 1 - \Phi' = \eta(1-\Phi). \tag{2.117}$$

Therefore, the measured noise suppression $1-\Phi'$ reduces linearly with the applied loss. Squeezed coherent states therefore tend towards coherent states as loss is applied. This effect can significantly limit the degree of squeezing observed.

CHAPTER 3

VISIBLE WAVELENGTH KERR SQUEEZING WITH PHOTONIC CRYSTAL FIBRE

3.1 Introduction

By allowing for reduced quantum noise in an optical field, squeezed light provides a key resource for investigations of fundamental physics [5, 51], and applications of quantum information processing [52, 53, 54] and quantum metrology [9, 55, 8]. This has led to a significant amount of work in the generation and optimisation of squeezed light [56]. Any method of generating quantum squeezing must involve a process which results in correlations between the fluctuations of the field quadratures. Three of the most common methods of generating squeezed light are parametric downconversion (PDC) [2], four-wave mixing [57] and the Kerr effect [58]. Unlike the former two approaches, squeezing via the Kerr interaction is inherently phase matched, which allows for flexibility in the wavelength of the probe light. Additionally, it relies on the $\chi^{(3)}$ nonlinear interaction, meaning it is necessary to use materials with inversion symmetry, such as optical fibre, for which the $\chi^{(2)}$ interaction vanishes. The possibility of using materials such as optical fibre lends a significant flexibility to the approach of Kerr squeezing, and means that it does not require a cavity to enhance the strength of the interaction. As well as simplifying the experimental requirements, the lack of a cavity means that the bandwidth of squeezing is only limited by the optical bandwidth, rather than the bandwidth of the cavity [59]. These features mean that utilising the Kerr effect is a robust and flexible approach, which has routinely been used for the generation of squeezed light [60, 59, 61].

The Kerr interaction requires high optical powers to reach sufficient nonlinearity. This

is commonly achieved by using ultrashort pulses, for which high peak powers can be propagated in optical fibre without generating unwanted nonlinear effects [60, 62]. However, this requires careful control of the pulses, since dispersion can act to spread out the pulse and therefore reduce the nonlinearity. Control of pulse spreading may be achieved by generating optical solitons, where the nonlinearity and dispersion are perfectly balanced [59, 63]. However, the conditions required to generate solitons in standard single-mode fibres place significant constraints on experimental parameters such as fibre length, wavelength and optical power. In order to avoid the limitations of standard single mode fibre, photonic crystal fibre (PCF) may be used, in which a periodical microstructure arrangement of material may be used to guide the light [64, 12, 65, 66, 67]. This enables the pulses to be confined in a much smaller core size, leading to significantly higher nonlinearities, and therefore lower minimum power requirements. It also has the advantage that the dispersion characteristics may be tailored by the fibre structure, allowing for squeezing at a larger span of wavelengths. This means that squeezing via the Kerr effect is applicable to a wide range of measurements, and is particularly well suited for biological measurements, which often require shorter wavelengths due other measurement constraints such as fluorescence spectra and imaging resolution [68, 69]. Bright Kerr amplitude squeezing using PCF has previously been achieved at visible wavelengths via spectral filtering [12, 13]. However, the squeezing that may be achieved by this approach is significantly limited by the loss applied by the spectral filter [70]. Therefore, we use PCF to generate Kerr amplitude squeezing at visible wavelengths in an nonlinear interferometer configuration. This work provides the first demonstration of amplitude squeezing with a nonlinear interferometer using PCF at visible wavelengths.

This chapter is structured as follows. Section 3.2 describes the theory of Kerr squeezing and Section 3.3 reviews previous approaches of generating Kerr squeezed light. In Section 3.4 we describe a numerical simulation which is used to quantify the predicted level of squeezing of our setup. Section 3.5 provides a characterisation of important experimental parameters of the source and detector. In Section 3.6, experimental results are presented for Kerr squeezing, alongside results from the numerical simulation, providing insight into potential future directions for improving the level of generated squeezing. Section 3.7 concludes the chapter.

Statement of Work

Sections 3.2-3.4 contain introductory material only. The dispersion measurement setup was originally built by Alex McMillan. The custom-built balanced detector was fabricated by Francesco Raffaelli and assembled by myself. The photonic crystal fibre was fabricated at the University of Bath by William Wadsworth. The source and detector characterisation

described in Section 3.5 was carried out by myself, and the experimental work described in Section 3.5 was completed by myself. The work presented in this chapter corresponds to the development of the first squeezed light source at the University of Bristol.

3.2 Theory of Kerr Squeezing

3.2.1 The Optical Kerr Effect

The optical Kerr interaction in general describes the parametric coupling of two optical fields of frequencies ω_1 and ω_2 via the $\chi^{(3)}$ nonlinearity, where the frequencies of the coupled fields following the interaction are unchanged. In the case of a strong incident beam of frequency ω_0, the field can couple to itself via the Kerr interaction, and for linearly polarised light this degenerate process is described by the electric polarisation [26]:

$$\boldsymbol{P} = \epsilon_0 \chi \boldsymbol{E} = \epsilon_0 \left(\chi^{(1)} + 3\chi^{(3)} |\boldsymbol{E}|^2 \right) \boldsymbol{E}, \tag{3.1}$$

where χ is the electric susceptibility of the medium. This process will be referred to here as the Kerr effect, and corresponds to a special case of degenerate four-wave mixing. Here, we have assumed that there is a negligible $\chi^{(2)}$, which is true of materials with inversion symmetry, such as optical fibre. If $\chi^{(1)}$ and $\chi^{(3)}$ are real, the polarisation of the medium does not generate absorption, and the effect of the nonlinear susceptibility is purely to modify the refractive index n. Converting between the electric field and the intensity I (power per unit area), we find

$$n = \sqrt{1+\chi} \approx n_0 + n_2 I, \tag{3.2}$$

where $n_0 = \sqrt{1+\chi^{(1)}}$ is the linear refractive index and $n_2 = 3\chi^{(3)}/4n_0^2\epsilon_0 c$ is the nonlinear refractive index. The effect of nonlinear refraction is to generate intensity dependence on the phase of the light. For a wavepacket propagating a distance L with wave vector β_0, the additional nonlinear phase shift acquired due to the Kerr nonlinearity is given by [71]

$$\phi_{NL} = \beta_0 L n_2 I = \gamma L \langle P \rangle, \tag{3.3}$$

for an average power $\langle P \rangle$ confined in an area A, with the nonlinear coefficient $\gamma = \omega_0 n_2 / cA$. Ultrashort pulses with high peak power have been shown to allow significant nonlinearity to be achieved in silica optical fibres [72]. However, the resulting time-dependence of the nonlinear phase across the pulse duration leads to a chirping effect in the instantaneous frequency, and broadening of the optical spectrum. Careful consideration of the combined effects of dispersion and nonlinear spectral broadening are therefore required to find optimal properties for pulsed squeezed light generation. The expression for the electric polarisation

given in Equation 3.1 strictly only applies to a medium with an instantaneous response [73]. To analyse the effects of dispersion in pulsed light, it is necessary to relax this assumption and account for the frequency dependence of the linear susceptibility.

3.2.2 Nonlinear Pulse Propagation

We will now consider in more detail the effect of the nonlinear refractive index on pulsed light propagating in a dispersive Kerr medium. We begin by considering the propagation of an optical field in a dielectric material according to Maxwell's equations. Firstly, from Equation 2.3 and 2.4, we may write

$$\nabla \times \nabla \times \boldsymbol{E} = -\mu_0 \left(\frac{\partial \boldsymbol{J}}{\partial t} + \epsilon_0 \frac{\partial^2 \boldsymbol{E}}{\partial t^2} \right). \tag{3.4}$$

For dielectric materials such as optical fibre, it is assumed that there are no free charges, and for a non-magnetic dielectric material, the current density can then be defined as $J = \frac{\partial P}{\partial t}$ [74]. We can also write $\rho = 0$, and from Equation 2.1 this gives $\nabla \cdot \boldsymbol{E} = 0$, and therefore $\nabla \times \nabla \times \boldsymbol{E} = \nabla(\nabla \cdot \boldsymbol{E}) - \nabla^2 \boldsymbol{E} = -\nabla^2 \boldsymbol{E}$. Equation 3.4 then becomes

$$\nabla^2 \boldsymbol{E} = \frac{1}{c^2} \frac{\partial^2 \boldsymbol{E}}{\partial t^2} + \mu_0 \frac{\partial^2 \boldsymbol{P}}{\partial t^2}. \tag{3.5}$$

It is useful to consider solutions of Equation 3.5 in the form of quasi-monochromatic plane waves with central frequency ω_0, propagating along the z direction:

$$\boldsymbol{E}(\boldsymbol{r}, t) = \frac{1}{2} [\hat{\boldsymbol{E}}(z,t) e^{-i(\omega_0 t - \beta_0 z)} + \hat{\boldsymbol{E}}(z,t)^* e^{i(\omega_0 t - \beta_0 z)}], \tag{3.6}$$

where $\hat{\boldsymbol{E}}(z,t)$ defines the slowly-varying envelope of the wavepacket, and β_0 is the wave vector. The assumption that the field is quasi-monochromatic implies that the envelope function $\hat{\boldsymbol{E}}(z,t)$ has a small spectral width $\Delta\omega$ such that $\Delta\omega/\omega_0 \ll 1$. We can also separate the linear and non-linear parts of the electric polarisation as $\boldsymbol{P}(\boldsymbol{r},t) = \boldsymbol{P}_L(\boldsymbol{r},t) + \boldsymbol{P}_{NL}(\boldsymbol{r},t)$, where [73]

$$\boldsymbol{P}_L(\boldsymbol{r},t) = \epsilon_0 \int_{-\infty}^{\infty} \chi^{(1)}(t-t') \boldsymbol{E}(\boldsymbol{r},t') dt' \tag{3.7}$$

and

$$\boldsymbol{P}_{NL}(\boldsymbol{r},t) = 3\epsilon_0 \chi^{(3)} |\boldsymbol{E}(\boldsymbol{r},t)|^2 \boldsymbol{E}(\boldsymbol{r},t) = \epsilon_0 \epsilon_{NL} \boldsymbol{E}(\boldsymbol{r},t). \tag{3.8}$$

Here we have used the adiabatic approximation, whereby variations in the pulse envelope are assumed to be much slower than the relaxation time of the nonlinear polarisation induced by the optical field, which justifies removing the frequency dependence from the third-order susceptibility [74]. The quantity $\epsilon_{NL} = 3\chi^{(3)} |\boldsymbol{E}(\boldsymbol{r},t)|^2$ may then be treated as

time-independent given the slowly-varying envelope approximation and the perturbative nature of $\boldsymbol{P}_{NL}$. We can write the polarisation components $\boldsymbol{P}_L(\boldsymbol{r},t)$ and $\boldsymbol{P}_{NL}(\boldsymbol{r},t)$ as

$$\boldsymbol{P}_L(\boldsymbol{r},t) = \frac{1}{2}[\hat{\boldsymbol{P}}_L(z,t)e^{-i(\omega_0 t-\beta_0 z)} + \hat{\boldsymbol{P}}_L(z,t)^* e^{i(\omega_0 t-\beta_0 z)}] \tag{3.9}$$

and

$$\boldsymbol{P}_{NL}(\boldsymbol{r},t) = \frac{1}{2}[\hat{\boldsymbol{P}}_{NL}(z,t)e^{-i(\omega_0 t-\beta_0 z)} + \hat{\boldsymbol{P}}_{NL}(z,t)^* e^{i(\omega_0 t-\beta_0 z)}]. \tag{3.10}$$

In order to find an equation for the envelope function $\hat{\boldsymbol{E}}(z,t)$, it is useful to work in the frequency domain. We therefore consider the Fourier transform of the envelope function:

$$\hat{\boldsymbol{E}}(z,\omega-\omega_0) = \int_{-\infty}^{\infty} \hat{\boldsymbol{E}}(z,t)e^{i(\omega-\omega_0)t}dt. \tag{3.11}$$

By using the definitions of $\boldsymbol{P}_L(\boldsymbol{r},t)$ and $\boldsymbol{P}_{NL}(\boldsymbol{r},t)$ in terms of the electric field, substituting the solutions given by equations 3.6-3.10 into Equation 3.5, and taking the Fourier transform, we then obtain the equation:

$$2i\beta_0\frac{\partial\hat{\boldsymbol{E}}(z,\omega-\omega_0)}{\partial z} + \beta_0^2(\chi^{(1)}(\omega)+\epsilon_{NL})\hat{\boldsymbol{E}}(z,\omega-\omega_0) = 0, \tag{3.12}$$

where we have made use of both the quasi-monochromatic assumption ($\Delta\omega/\omega_0 \ll 1$) and the slowly-varying envelope approximation ($\partial^2\hat{\boldsymbol{E}}(z,t)/\partial t^2 \ll 1$). We can then define the complex, frequency dependent wavevector in terms of the linear susceptibility $\chi^{(1)}(\omega)$ as

$$\tilde{\beta} = \sqrt{1+\chi^{(1)}(\omega)}\beta_0 = \beta(\omega)+\Delta\beta, \tag{3.13}$$

where $\beta(\omega)$ is the real part of the wavevector, and $\Delta\beta = i\tilde{\alpha}/2$ is the imaginary part of the wavevector, for absorption coefficient $\tilde{\alpha}$. Since $\Delta\beta$ constitutes a small perturbation of the wavevector, it is possible to neglect the frequency dependence in the attenuation given by $\Delta\beta$. We can Taylor expand $\beta(\omega)$ about the central frequency component:

$$\beta(\omega) = \beta_0 + (\omega-\omega_0)\frac{d\beta(\omega)}{d\omega}\bigg|_{\omega=\omega_0} + \frac{1}{2}(\omega-\omega_0)^2\frac{d^2\beta(\omega)}{d\omega^2}\bigg|_{\omega=\omega_0}, \tag{3.14}$$

and associate $\beta_1 = \frac{d\beta(\omega)}{d\omega}\Big|_{\omega=\omega_0}$ with the group velocity and $\beta_2 = \frac{d^2\beta(\omega)}{d\omega^2}\Big|_{\omega=\omega_0}$ with the group velocity dispersion. Then, by substituting Equation 3.13 into Equation 3.12, and taking the inverse Fourier transform, we obtain

$$\frac{\partial\hat{\boldsymbol{E}}(z,t)}{\partial z} + \beta_1\frac{\partial\hat{\boldsymbol{E}}(z,t)}{\partial t} + \frac{1}{2}i\beta_2\frac{\partial^2\hat{\boldsymbol{E}}(z,t)}{\partial t^2} + \frac{\tilde{\alpha}}{2}\hat{\boldsymbol{E}}(z,t) = \frac{i\epsilon_{NL}\beta_0\hat{\boldsymbol{E}}(z,t)}{2}, \tag{3.15}$$

where we have replaced the $(\omega-\omega_0)$ terms with the differential operator $i(\partial/\partial t)$ in the last step. Equation 3.15 is known as the nonlinear Schrodinger equation [71], and describes the

propagation of light in an nonlinear, lossy and dispersive medium. It may be written in a more convenient form by using the coordinate frame travelling at the group velocity in the z direction with the transformation $\xi = t - \beta_1 z$, which gives

$$\frac{\partial \hat{\boldsymbol{E}}(z,\xi)}{\partial z} + \frac{1}{2} i \beta_2 \frac{\partial^2 \hat{\boldsymbol{E}}(z,\xi)}{\partial \xi^2} + \frac{\tilde{\alpha}}{2} \hat{\boldsymbol{E}}(z,\xi) = \frac{i \epsilon_{NL} \beta_0 \hat{\boldsymbol{E}}(z,\xi)}{2}. \tag{3.16}$$

This equation will be used for the simulation of pulsed squeezed light in PCF. An important special case of Equation 3.16 is where the effects of nonlinearity and dispersion perfectly balance, such that, for $\tilde{\alpha} = 0$, the envelope $\hat{\boldsymbol{E}}(z,\xi)$ stays unchanged with propagation distance z. Such a solution of the propagation equation is known as a fundamental soliton. It is also possible to find solutions of Equation 3.16 where the envelope changes periodically with propagation distance, and these solutions are known as higher-order solitons. The conditions required for solitons are given by pulses for which the power has a time dependence of $P(\xi) \approx P_0 \operatorname{sech}^2(\xi/1.76 T_{FWHM})$ and which satisfy integer solutions of the equation [71]

$$N^2 \approx \frac{\gamma P_0 T_{FWHM}^2}{3.11 |\beta_2|}, \tag{3.17}$$

where P_0 is the peak power and T_{FWHM} is the full-width at half-maximum of the initial pulse. The case of $N = 1$ corresponds to the fundamental soliton, and higher values of N correspond to the conditions required for higher order solitons. While for simplicity we have considered the infinite plane wave case in the derivation of the nonlinear Schrodinger equation presented here, an identical result may be derived for the particular case of light propagating in the optical modes of a fibre [71].

3.2.3 Quantum Noise in a Kerr Medium

In order to analyse the effect of the Kerr interaction on the noise of a coherent state, we will consider Equation 3.16 in the case of zero-dispersion $\beta_2 = 0$ and zero loss $\tilde{\alpha} = 0$. This gives

$$\frac{\partial \hat{\boldsymbol{E}}(z,\xi)}{\partial z} = \frac{i \epsilon_{NL} \beta_0 \hat{\boldsymbol{E}}(z,\xi)}{2}, \tag{3.18}$$

with the solution

$$\hat{\boldsymbol{E}}(z,\xi) = \hat{\boldsymbol{E}}(0,\xi) e^{i z \beta_0 \epsilon_{NL}/2}. \tag{3.19}$$

It is important to emphasise that this solution assumes negligible loss, such that ϵ_{NL} is a constant of motion. By converting between the electric field operator and the bosonic annihilation operator notation, the effect of the propagation of a single temporal mode in a Kerr medium may be written as [75]

$$\hat{a}_K = e^{i \kappa \hat{a}^\dagger \hat{a}} \hat{a} = \hat{U}_K^\dagger \hat{a} \hat{U}_K, \tag{3.20}$$

where $\kappa = \gamma\hbar\omega z$ and we have introduced the unitary operator $\hat{U}_K = e^{i\hat{H}_K}$ governed by the Kerr Hamiltonian $\hat{H}_K = \frac{\kappa}{2}\hat{a}^{\dagger 2}\hat{a}^2 = \frac{\kappa}{2}\hat{n}(\hat{n}-1)$ for photon number operator $\hat{n}$. With this Hamiltonian, it is now possible to analyse the effect of Kerr evolution for an initial coherent state $|\alpha\rangle$ [76]:

$$|K\rangle = \hat{U}_K|\alpha_0\rangle = e^{i\frac{\kappa}{2}\hat{n}(\hat{n}-1)}|\alpha_0\rangle = e^{\frac{-|\alpha_0|^2}{2}}\sum_{n=0}^{\infty}\frac{\alpha_0^n}{\sqrt{n!}}e^{i\frac{\kappa}{2}n(n-1)}|n\rangle. \tag{3.21}$$

An intuitive way to see the effect of this evolution on the noise statistics of the coherent state is to plot the Wigner function of the final Kerr state, which is given by [77]

$$W(x,y) = \frac{e^{-|\alpha_0|^2-2|\alpha|^2}}{\pi}\sum_{m,n=0}^{\infty}\frac{\alpha_0^m\alpha_0^{*n}}{m!n!}e^{-i\frac{\kappa}{2}(m^2-n^2)}H_{m,n}(2\alpha^*,2\alpha), \tag{3.22}$$

where $\alpha = x+iy$ and $H_{m,n}(z,z^*)$ is the complex Hermite polynomial, which can be defined by [78]

$$H_{m,n}(z,z^*) = \sum_{k=0}^{m\wedge n}(-1)^k k!\binom{m}{k}\binom{n}{k}z^{m-k}(z^*)^{n-k}. \tag{3.23}$$

The Wigner function for an initial coherent state $|\alpha_0\rangle$ with $\alpha_0 = 3$ and the corresponding Kerr state for $\kappa = 0.08$ are shown in Figure 3.1. The effect of the nonlinear phase shift is that the higher amplitude components of the distribution are shifted in phase more than the lower amplitude components, leading to the crescent shaped distribution shown. The result is that the fluctuations in a range of quadrature components are reduced below the that of the vacuum state, i.e. the Kerr state is squeezed. We also observe from the marked circles centered on the origin that the photon number fluctuations of the state are unchanged following the nonlinear phase shift, which illustrates the photon number preserving nature of the Kerr effect. The non-classical nature of the Kerr state is indicated by the negative regions of the Wigner function.

To analyse the amount of squeezing that results from the Kerr effect, it is useful to consider a geometrical picture, where the uncertainty of the initial coherent state is given by contours of the Wigner function in Cartesian coordinates centered on the coherent state as

$$\begin{aligned} x_\alpha &= \frac{1}{2\sqrt{2}}\cos\xi, \\ y_\alpha &= \frac{1}{2\sqrt{2}}\sin\xi. \end{aligned} \tag{3.24}$$

Writing the annihilation operator for the coherent state in the form $\hat{a} = \alpha+\delta\hat{a}$, and assuming a bright field $|\alpha| \gg 1$, Equation 3.20 can then be written as [79]

$$\hat{a}_K = e^{i\kappa|\alpha+\frac{1}{2\sqrt{2}}e^{i\xi}|^2}\left(\alpha+\frac{1}{2\sqrt{2}}e^{i\xi}\right) \approx e^{i\kappa\alpha^2}\left(\alpha+\frac{1}{2\sqrt{2}}e^{i\xi}+\frac{1}{\sqrt{2}}i\kappa\alpha^2\cos(\xi)\right), \tag{3.25}$$

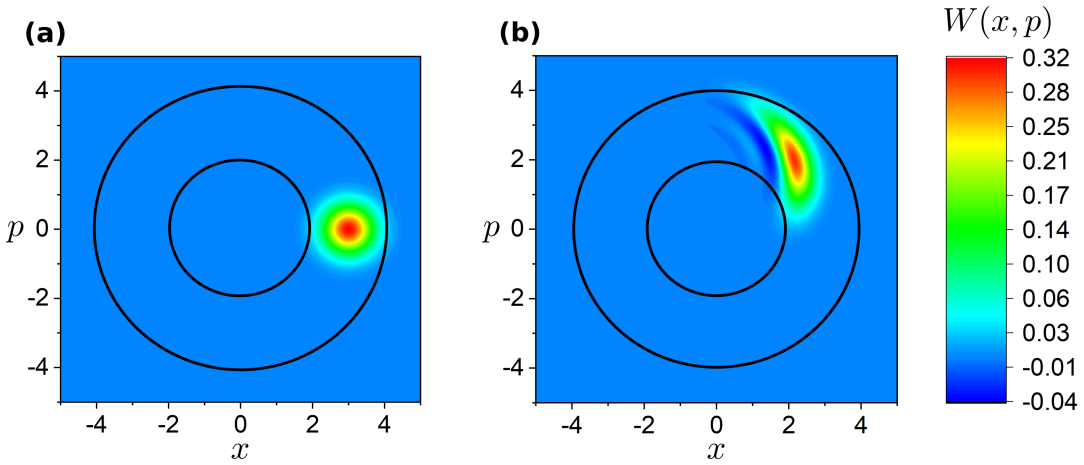

Figure 3.1: Plots showing the evolution of the Wigner function of a coherent state in a Kerr medium. (a) Wigner function of an initial coherent state with $\alpha_0 = 3$. (b) Corresponding Kerr state for $\kappa = 0.08$. The black circles indicate contours of constant amplitude, illustrating the photon number conserving nature of the Kerr effect.

where the exponent is expressed as the first two terms of a Taylor expansion. Writing the equation of the noise contour in Cartesian coordinates as before gives

$$x_K = \frac{1}{2\sqrt{2}}\cos(\xi), \qquad y_K = \frac{1}{2\sqrt{2}}\sin(\xi) + \frac{1}{\sqrt{2}}\kappa\alpha^2\cos(\xi), \tag{3.26}$$

which is the equation for an ellipse, with $x_K^2 + (y_K - 2\kappa\alpha^2 x_K)^2 = \frac{1}{8}$. In this case, the squeezing ellipse corresponds to that of an ideal minimum uncertainty squeezed state, with major and minor axes respectively given by lengths [26]:

$$\frac{1}{\sqrt{2}}e^{r} = \sqrt{\frac{1}{2} + \theta_K^2 + \theta_K\sqrt{1+\theta_K^2}}, \qquad \frac{1}{\sqrt{2}}e^{-r} = \sqrt{\frac{1}{2} + \theta_K^2 - \theta_K\sqrt{1+\theta_K^2}}, \tag{3.27}$$

for the squeezing parameter r, where $\theta_K = \kappa\alpha^2$. It is therefore possible to define the field variance of the Kerr state at an arbitrary phase angle θ as [80]

$$\langle K|\hat{x}_\theta^2|K\rangle - \langle K|\hat{x}_\theta|K\rangle^2 \approx \frac{1}{2}\left[e^{2r}\sin^2\left(\theta - \frac{\nu}{2}\right) + e^{-2r}\cos^2\left(\theta - \frac{\nu}{2}\right)\right], \tag{3.28}$$

where $\nu/2$ is the angle of the minor axis of the squeezing ellipse. We therefore see that for a coherent state with $|\alpha|^2 \gg 1$, the generated quadrature squeezing increases monotonically with the applied nonlinear phase shift.

3.3 Observing Kerr Squeezing

Since the Kerr state is itself not photon number squeezed, it is not possible to distinguish the Kerr state from a coherent state by direct detection alone. As described in Chapter 2, homodyne detection provides a means of measuring the quantum noise distribution of an optical signal at arbitrary phase angles. However, as discussed in Section 2.2.2, homodyne detection requires that the power of the signal is negligible compared to the power of the local oscillator [39]. This is typically difficult to achieve with a Kerr state, since achieving sufficient nonlinearity requires high powers that will be difficult to surpass with the local oscillator. Therefore, a number of alternative strategies have been developed to measure the reduced quantum noise of the Kerr state.

One such strategy is to place the $\chi^{(3)}$ medium in both arms of a balanced interferometer. It was shown by Shirisaki and Haus that the interference of two identical Kerr states leads to squeezed vacuum on one of the outputs of the interferometer, which may be measured by homodyne detection [81]. This may be achieved in a Sagnac configuration, whereby the initial coherent state is split by a beamsplitter into two counterpropagating beams, and after passing through the same $\chi^{(3)}$ material, the interference of these beams on the output of the original beamsplitter results in the squeezed vacuum state [59, 60, 62, 63]. This strategy has the advantage that both Kerr states should be identical, resulting in high interferometric stability and visibility [58], and therefore a robust method of generating squeezing.

An additional complexity of observing squeezed vacuum is the requirement of a local oscillator which is phase locked to the squeezed vacuum state. For the detection of amplitude squeezed light, a simple intensity measurement is sufficient to detect the reduction in quantum noise. Therefore, it is desirable to have the ability to use the Kerr effect to generate amplitude squeezing, and two common methods have been used to achieve this. One method involves spectral filtering of high-order solitons [82, 83, 13], which can be understood as follows. High-order solitons have energy greater than that of the fundamental soliton, and have a temporal and spectral envelope which varies periodically as it propagates. Because of the energy dependence of the periodic spectral broadening, it is possible to engineer the properties of the system such that amplitude fluctuations above the average value lead to increased spectral broadening. In this case, spectral filtering of the broadened pulse leads to increased loss, which counteracts the initial amplitude fluctuation. The opposite effect occurs for fluctuations below the average value, and this leads to amplitude squeezing of the output state. A significant limitation of this method is that the loss applied by the filter imposes a limit on the squeezing that may be produced [70]. Furthermore, the collimation of the filtered beam is experimentally challenging [12].

Another method of generating amplitude squeezing is by placing the $\chi^{(3)}$ material in

an asymmetric interferometer [84]. As for squeezed vacuum generation, this can be implemented in a Sagnac configuration [1, 61]. If the splitting ratio is approximately 90:10, the stronger 90% reflected light experiences a significant nonlinear phase shift, and acquires the quantum noise distribution of a Kerr state. The weaker auxiliary 10% transmitted light only acquires a slight nonlinear phase shift and remains approximately coherent. Upon interference of the two beams on the output of the beamsplitter, the coherent part acts to displace the Kerr state in phase space, such that it becomes amplitude squeezed. This may also be achieved by using a polarisation interferometer to attain more flexibility in the splitting ratio and relative phase of the Kerr phase-shifted light and the auxiliary light, which allows for further optimisation [58, 85]. Polarisation interferometers have also been used to generate polarisation squeezing using a similar approach [86]. However, the use of a polarisation interferometer requires that the Kerr squeezed beam and the displacement beam propagate co-linearly through the fibre with orthogonal polarisations. Therefore, a delay must be applied to the auxillary pulses to compensate for the birefringence in the optical fibre. An intuitive explanation for the process of squeezing in an asymmetric interferometer configuration is that interference of the two fields generates intensity dependence of the output state on the nonlinear phase shift θ_K, which is itself dependent on the power of light passed through the $\chi^{(3)}$ medium. Therefore, an amplitude fluctuation above the average value leads to an increase in θ_K, which for particular power levels acts to reduce the intensity of the output light, therefore suppressing the amplitude fluctuation. Amplitude fluctuations below the average value lead to a similar cancellation effect, and this gives rise to amplitude squeezing on the output of the interferometer. We can therefore see similarities with the example of Kerr squeezing by spectral filtering, whereby fluctuations in the nonlinear phase act to suppress fluctuations in amplitude. The method of generating Kerr squeezing by using an asymmetric Sagnac interferometer is the experimental implementation used here. This method will therefore be the focus for the remainder of this section, and will be discussed in more detail in Section 3.5 and 3.6.

The earliest experiments to generate Kerr amplitude squeezing used bright CW light [87]. However, it was discovered that the squeezing in this case became limited by guided acoustic wave Brillouin scattering, which is caused by the photon-phonon interactions in the fibre. With pulsed light, the required Kerr nonlinearity could be achieved without generating such unwanted effects [60], and this has become a common approach for achieving Kerr squeezing. The highest Kerr squeezing measured to date is 6.1 dB, which was achieved by using 480 fs pulses [62]. A further advantage of using pulsed light is that the saturation level of detection systems is typically determined by the average optical power, rather than the peak power. Using ultra-short pulses then places a lower constraint on the saturation power of the detector. With pulsed light, long interaction lengths may still be required to generate the required Kerr nonlinearity in single-mode fibre, and this can lead to sig-

nificant pulse spreading over distance in the fibre, which is detrimental to the generated squeezing [88]. One approach to avoid this is to apply anomalous dispersion to the initial pulses [58], compensating for any normal dispersion in the Kerr medium. The anomalous dispersion can for example be provided by a prism pair [89]. Alternatively, solitons can be used such that the pulse maintains its envelope during propagation [1, 61, 90]. Another approach is to use PCF [65], which generally has a smaller core size than single-mode fibre, and therefore typically requires a shorter interaction length. This allows for greater flexibility in the wavelength of the squeezing, since the dispersion properties of PCF may be engineered by careful design of fibre structure. Our approach will be to use PCF in an asymmetric Kerr interferometer to generate amplitude squeezing at visible wavelengths. In future work, PCF may be used to generate solitons in this configuration, which are typically limited to the short-wavelength infrared region when using standard single-mode fibre. It has been shown that the squeezing of optical solitons in a lossless medium is fundamentally limited by Raman noise [91], where the high optical intensity results in the inelastic scattering of photons. However, we will show that optical loss and the dispersive properties of the fibre are the dominant limiting factors of the squeezing generated in this experiment.

3.4 Numerical Simulation

In the case of optical solitons, it has been shown that an analytical expression for the squeezing generated in a Kerr medium may be obtained [92]. However, for more general levels of dispersion, no such analytical result exists. Therefore, a numerical simulation is used to analyse the predicted squeezing using the PCF in this case. In the absence of loss, Equation 3.16 may be written in terms of the quantised amplitude $\hat{U}$:

$$\frac{\partial \hat{U}}{\partial z} = -\frac{i\beta_2}{2}\frac{\partial^2 \hat{U}}{\partial \xi^2} + i\kappa\left|\hat{U}\right|^2\hat{U}, \tag{3.29}$$

where $\hat{U}$ corresponds to the annihilation operator evolved according to the Heisenberg picture. It is possible to write $\hat{U} = U + \hat{u}$, where $U = \langle\hat{U}\rangle$ corresponds to the classical amplitude, and $\hat{u}$ corresponds to the fluctuating quantum amplitude. From Equation 3.29, the propagation equation for the classical part U may then be obtained by simply neglecting the quantum terms, and U may then be solved numerically using the split-step method [71]. In this method, dispersion and nonlinearity are assumed independent for small propagation distances, and are alternately applied. To describe this algorithm, the pulse must first be discretised in terms of propagation distance and time, such that $U_j(n)$ corresponds to the classical amplitude of the envelope with the time step labelled by the integer j and the propagation distance labelled by the integer n. Here, each time step is separated by an interval Δt, and each propagation distance is separated by the interval Δz. The two alternate steps

of the split-step method may then be written as [71]

$$\begin{aligned} &1. \quad U_j(n+1) = e^{i\gamma\hbar\omega|U_j(n)|^2\Delta z} U_j(n) \\ &2. \quad U_j(n+1) = \mathrm{DFT}^{-1}\left[e^{i\frac{\beta_2}{2}\omega_j^2\Delta z}\mathrm{DFT}[U_j(n+1)]\right], \end{aligned} \tag{3.30}$$

where DFT denotes the discrete Fourier transform, and $\omega_j = 2\pi j/N\Delta t$, where the pulse is divided into a total of N discrete time steps.

The discretised propagation equation for the quantum amplitude operator may then be obtained by cancelling the classical terms from Equation 3.29, which results in [88]

$$\begin{aligned} \hat{u}_j(n+1) = &\left[1 + 2i\gamma\hbar\omega\Delta z\left|U_j(n)\right|^2\right]\hat{u}_j(n) + i\hbar\omega\gamma\Delta z\left|U_j(n)\right|^2\hat{u}_j^\dagger(n) \\ &+ i\Delta z\mathrm{DFT}^{-1}\left[\omega_j^2\frac{\beta_2}{2}\mathrm{DFT}[\hat{u}_j(n)]\right], \end{aligned} \tag{3.31}$$

where the terms higher than first-order in $\hat{u}$ have been neglected. Equivalently, this may be written in terms of the bosonic creation and annihilation operators corresponding to the time mode k, $\hat{a}_k^\dagger$ and $\hat{a}_k$, as

$$\hat{u}_j(n) = \sum_k [\mu_{jk}(n)\hat{a}_k + \nu_{jk}(n)\hat{a}_k^\dagger], \tag{3.32}$$

where

$$\begin{aligned} \mu_{jk}(n+1) = &\left[1 + 2i\gamma\hbar\omega\Delta z\left|U_j(n)\right|^2\right]\mu_{jk}(n) + i\hbar\omega\gamma\Delta z\left|U_j(n)\right|^2\nu_{jk}^*(n) \\ &+ i\Delta z\mathrm{DFT}^{-1}\left[\omega_j^2\frac{\beta_2}{2}\mathrm{DFT}[\mu_{jk}(n)]\right], \end{aligned} \tag{3.33}$$

and

$$\begin{aligned} \nu_{jk}(n+1) = &\left[1 + 2i\gamma\hbar\omega\Delta z\left|U_j(n)\right|^2\right]\nu_{jk}(n) + i\hbar\omega\gamma\Delta z\left|U_j(n)\right|^2\mu_{jk}^*(n) \\ &+ i\Delta z\mathrm{DFT}^{-1}\left[\omega_j^2\frac{\beta_2}{2}\mathrm{DFT}[\nu_{jk}(n)]\right]. \end{aligned} \tag{3.34}$$

Additionally, since we are interested in analysing the case where the pulse is initially described by a coherent state, we can assume that each time mode of $\hat{u}$ is initially in the vacuum state, giving the initial conditions $\mu_{jk}(0) = \delta_{jk}$ and $\nu_{jk}(0) = 0$. This means that, by numerically propagating the matrices μ_{jk} and ν_{jk}, the noise properties of the final state can be found. Consider the nonlinear interferometer shown in Figure 3.2, with states $\hat{U}'$ and $\hat{U}''$ propagating through a Kerr medium, and interfering on the output of BS2, resulting in the state $\hat{U}'''$. It may been shown that if BS2 has reflection coefficient R and transmission coefficient T, the squeezing parameter Φ of the output state $\hat{U}''' = U''' + \hat{u}'''$ when measured by direct detection is given by [64]

$$\Phi = R\sum_{m=1}^{N}\left|\sum_{j=1}^{N}\left|U_j'''\right|\left(\mu_{jm}'e^{-i\theta_j} + \nu_{jm}'e^{i\theta_j}\right)\right|^2 + T\sum_{m=1}^{N}\left|\sum_{j=1}^{N}\left|U_j'''\right|\left(\mu_{jm}''e^{-i\theta_j} + \nu_{jm}''e^{i\theta_j}\right)\right|^2, \tag{3.35}$$

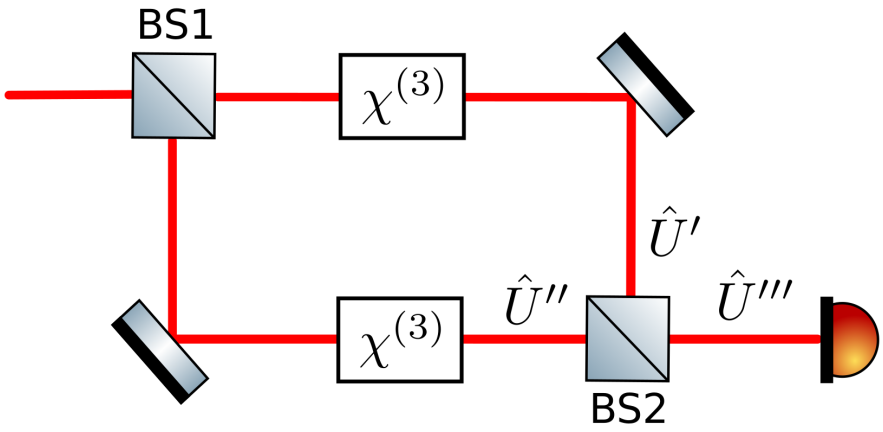

Figure 3.2: Schematic diagram of a nonlinear interferometer. BS1 and BS2 are beamsplitters with arbitrary reflection and transmission coefficients.

where θ_j corresponds to the phase of U_j, the evolution matrices μ'_{jm} and ν'_{jm} correspond to the state $\hat{U}'$, and the matrices μ''_{jm} and ν''_{jm} correspond to the state $\hat{U}''$. This result is equivalent to that which would be obtained for a nonlinear interferometer in the Sagnac configuration, as described in Section 3.3. Equation 3.35 will therefore be used for the simulation of the squeezing generated by the PCF in this experiment.

3.5 Source and Detector Characterisation

3.5.1 Dispersion

As we have discussed, the dispersion of the optical fibre used to generate squeezing may have a significant effect on the generated squeezing. In order to analyse the effects of the dispersion of the PCF used in this experiment, an interferometric measurement of dispersion was first carried out, using a Spectra Physics Mai Tai Ti:Sapphire laser, which is used for all the optical measurements in this thesis.

A schematic diagram of the dispersion measurement setup is shown in Figure 3.3. Linearly polarised light is split between two paths at the first polarising beamsplitter (PBS1). One path is coupled into a 0.17 m length of PCF, and the half-wave plate HWP2 rotates the polarisation of this light to be on axis with the fibre, such that it maintains linear polarisation on the output, while HWP3 rotates the polarisation of this light back to its original state. The other path is subject to an adjustable delay. The two paths are recombined on a second polarising beamsplitter PBS2, and the adjustable mirror may be scanned until the the pulses overlap on the output. HWP4 is used to rotate the combined polarisation state such that interference may be measured at the powermeter (PM) after PBS3. This is

achieved by plotting the output power as a function of path length, and adjusting the mirror until an interference pattern is observed.

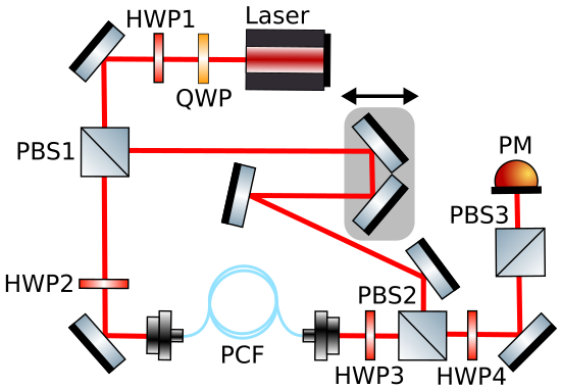

Figure 3.3: Experimental diagram of the interferometric dispersion measurement setup.

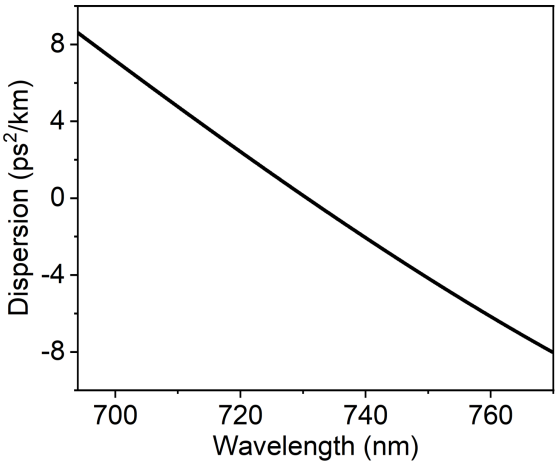

Figure 3.4: Measured dispersion parameter β_2 at a range of wavelengths between 694 – 770 nm.

Due to the group velocity dispersion of the fibre, different wavelengths of light will propagate in the fibre with different group velocities. Therefore, the temporal separation of the pulses will depend on the wavelength of the light. We may consider the time difference, $\Delta\tau$, that corresponds to the difference in propagation time of two different spectral components:

$$\Delta\tau = \left| \frac{L}{v_{g1}} - \frac{L}{v_{g2}} \right| \tag{3.36}$$

for a fibre of length L, and light with group velocities v_{g1} and v_{g2} at frequencies ω_1 and ω_2 respectively. For frequencies that are closely separated by a frequency difference $\Delta\omega$, we can then write

$$\begin{aligned} \Delta\tau = \left| L \left(\frac{\partial\beta}{\partial\omega}\bigg|_{\omega=\omega_1} - \frac{\partial\beta}{\partial\omega}\bigg|_{\omega=\omega_2} \right) \right| &= \left| L \left(\frac{\partial\beta}{\partial\omega}\bigg|_{\omega=\omega_2} + \frac{\partial}{\partial\omega}\left(\frac{\partial\beta}{\partial\omega}\bigg|_{\omega=\omega_0} \right) \Delta\omega - \frac{\partial\beta}{\partial\omega}\bigg|_{\omega=\omega_2} \right) \right| \\ &= \left| L \frac{\partial^2\beta}{\partial\omega^2}\bigg|_{\omega_0} \Delta\omega \right|, \end{aligned} \tag{3.37}$$

where ω_0 is the average frequency across the span $\Delta\omega$. By recording the mirror position at the centre of the interference pattern for a range of wavelengths, each position can be converted into a time value τ for light travelling at speed $c = 3 \times 10^8$ m/s. Then, from Equation 3.37, by taking the gradient of the resulting data, $\partial\tau/\partial\omega$, we can infer the group velocity dispersion using [93]

$$\frac{\partial^2\beta}{\partial\omega^2} = \frac{1}{L}\frac{\partial\tau}{\partial\omega}. \tag{3.38}$$

This is plotted in Figure 3.4, and shows a zero-dispersion value at 730 nm, which is in agreement with the approximate value provided by the manufacturer of the PCF.

3.5.2 Nonlinearity Coefficient

Another parameter which must be found in order to simulate the squeezing generated from the PCF is the nonlinearity coefficient γ. In order to characterise γ, we will analyse the effect of the Kerr nonlinearity on the optical spectrum of a typical laser pulse. We consider again Equation 3.29, for the case of negligible dispersion $\beta_2 \approx 0$. Although the analytical solution for the propagation equation in this case relies on the assumption that $|\hat{U}|^2$ is independent of propagation distance, it is important to note that since the optical power varies across the duration of the pulse, $|\hat{U}|^2$ typically depends strongly on ξ. This leads to a time dependence of the nonlinear phase $\phi_{NL}(\xi)$. The instantaneous frequency relative to the carrier is then given by $\omega(\xi) - \omega_0 = \frac{\partial \phi_{NL}(\xi)}{\partial \xi}$. As the pulse propagates through the nonlinear medium, this leads to the generation of new frequency components, broadening the optical spectrum [74]. Figure 3.5 illustrates the effect of this broadening on the power spectrum of 100 fs pulses from the Ti:Sapphire laser propagating through $L = 1.22$ m of PCF. This measurement was taken using 0.6 mW of average power, which is equivalent to ≈ 75 W peak power for the 80 MHz repetition rate. The central wavelength was 730 nm, which corresponds to the measured zero-dispersion wavelength of the PCF. This broadening

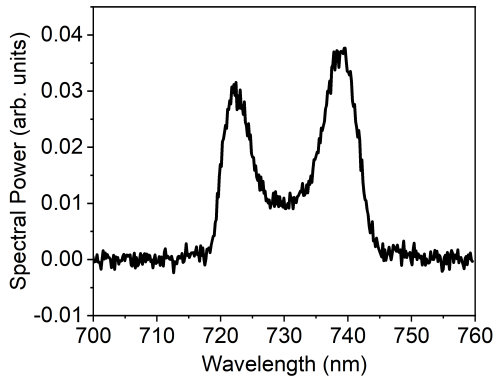

Figure 3.5: Experimentally measured optical spectrum from a pulse train with 75 W peak power after propagating through a $L = 1.22$ m length of PCF.

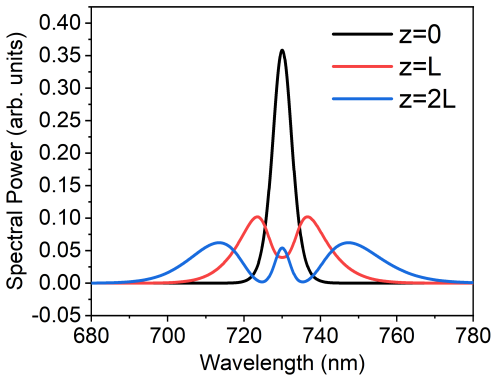

Figure 3.6: Simulation of the power spectrum of a pulse with a peak power of 75 W propagating through various lengths of PCF with nonlinearity $\gamma = 0.04$ W^{-1}m^{-1}.

effect may also be simulated classically using Equation 3.30, and Figure 3.6 shows the simulated power spectrum of a pulse with the same properties and a nonlinearity coefficient of $\gamma = 0.04$ W^{-1}m^{-1}. This value of γ was chosen since it gives the best agreement by visual

comparison with the experimental data shown in Figure 3.5. Therefore $\gamma = 0.04$ W^{-1}m^{-1} will be used for the simulations of squeezing in this chapter. The slight asymmetry in Figure 3.5 is expected due to the effect of third-order dispersion, which becomes important close to the zero-dispersion wavelength [71].

3.5.3 Detection Efficiency

In order to obtain information about the detected optical power from electronic measurements, it is crucial to properly characterise the detection efficiency. Due to the strong dependence of the degree of squeezing on optical loss, obtaining a precise measurement of the detection efficiency is also important in estimating the generated squeezing from the measured squeezing. The two photodetectors used for measurements in this thesis are transimpedance-amplified balanced detectors, which amplify the subtraction photocurrent of two photodiodes. As discussed in Section 2.2.3, the addition photocurrent for self-homodyne detection can be measured by sending all the light to one photodiode.

The electrical response of a detector to light is often quantified by the responsivity R, which is defined as the generated current I as a fraction of the detected power P, and is related to the detection efficiency η by [94]

$$R = \frac{I}{P} = \frac{\eta q}{\hbar \omega}, \tag{3.39}$$

for light with carrier angular frequency ω. Here, the generated current I can be obtained from a voltage measurement V by using Ohm's law according to the value of the gain resistance R_G: $I = V/R_G$. Results of measured voltage as a function of optical power incident on each photodiode are plotted for a Thorlabs PDB440A(-AC) detector and a custom-built detector in Figures 3.7 and 3.8, for wavelengths of 740 nm and 760 nm respectively.

The gradients of these plots were used to calculate the responsivity by using values of $R_G = 1.2$ kΩ for the custom-built detector and $R_G = 18.9$ kΩ for the Thorlabs detector. By using Equation 3.39, this resulted in an estimate of $\eta = 0.555 \pm 0.002$ and $\eta = 0.836 \pm 0.003$ respectively, with the errors calculated from the fitting data. The higher efficiency of the Thorlabs detector means that this is used for the majority of the sensing experiments in this thesis. However, the custom-built detector has a significantly higher saturation power, meaning it is useful for measurements of squeezing which used shorter lengths of PCF, and therefore require higher power levels to generate sufficient nonlinearity for squeezing.

3.5.4 Shot Noise Clearance

Since classical laser noise and electronic noise generally dominate over quantum optical noise at low frequencies, MHz of electronic bandwidth is typically required to observe shot

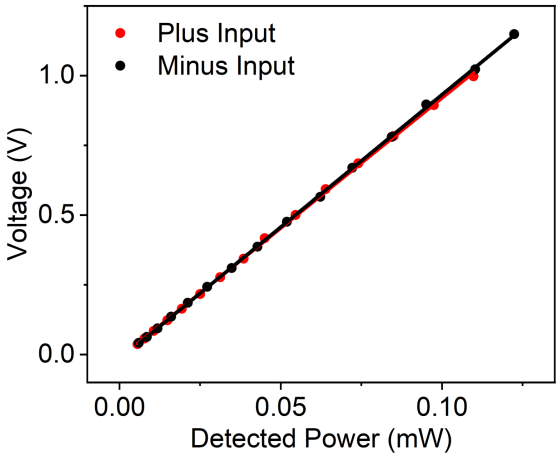

Figure 3.7: Voltage as a function of detected optical power for the Thorlabs PDB440A(-AC) balanced detector.

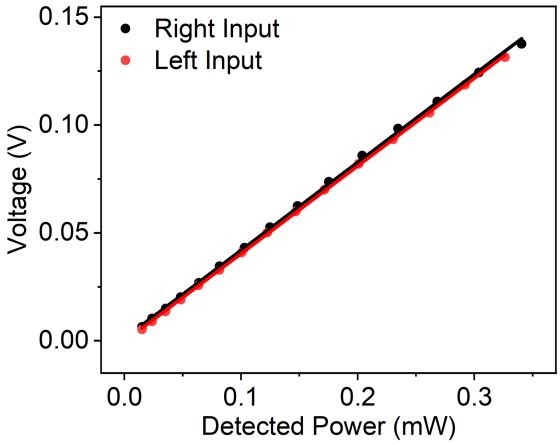

Figure 3.8: Voltage as a function of detected optical power for the custom-built balanced detector.

noise limited behaviour and therefore the effect of squeezing. Transimpedance-amplified photodetectors are also affected by broadband electronic noise [95], so it is important to verify that the shot noise of the laser may be observed over this broadband electronic noise.

To confirm that this is the case, the noise power of the detector upon illumination was compared with the noise power with the laser blocked. This is plotted in Figure 3.9 for the Thorlabs detector and Figure 3.10 for the custom-built detector. We also distinguish here between the shot noise level and the laser noise level, where the optical shot noise is measured by sending an equal amount of light to both photodiodes, and the laser noise level by sending all the light to a single photodiode, as discussed in Section 2.2.3. The electronic

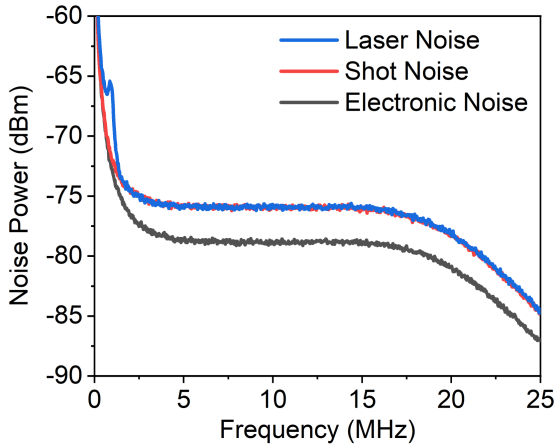

Figure 3.9: Noise power spectrum of the Thorlabs PDB440A(-AC) balanced detector, for 0.1 mW of average optical power.

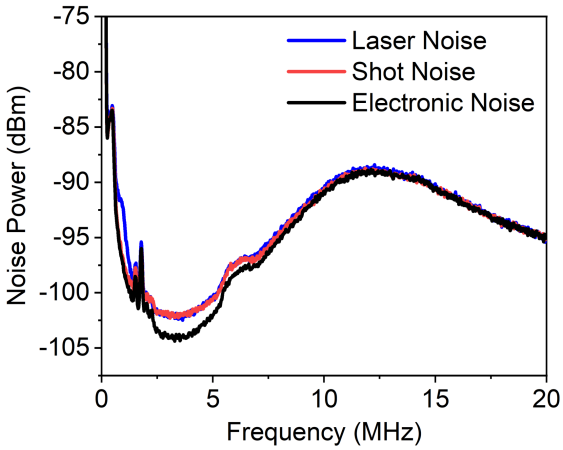

Figure 3.10: Noise power spectrum of the custom-built balanced detector, for 0.4 mW of average optical power.

noise properties of the detector may then be quantified by the shot noise clearance, which corresponds to the ratio between the shot noise power and the electronic noise power [95]. From Figure 3.9, we observe 3 dB of shot noise clearance at 10 MHz, with 0.1 mW of optical power. The results in Figure 3.10 exhibit a significant amount of electronic noise over the bandwidth of the detector. However, the electronic noise reaches a minimum at around 3 MHz, where 2 dB of shot noise clearance is observed for a power of 0.4 mW. This data indicates that the laser light is shot noise limited above $\gtrsim 2$ MHz, and in Figure 3.9 we observe the frequency independence of the shot noise, as expected from Equation 2.113 of Chapter 2.

In order to verify that the scaling of this noise corresponds to the expected behaviour for a coherent state, a measurement of the optical noise power as a function of the detected optical power for the Thorlabs and custom-built detector are plotted in Figures 3.11 and 3.12 respectively, where each measurement was taken in a frequency band with significant shot noise clearance. Here, the noise power corresponding to the detected optical signal has been

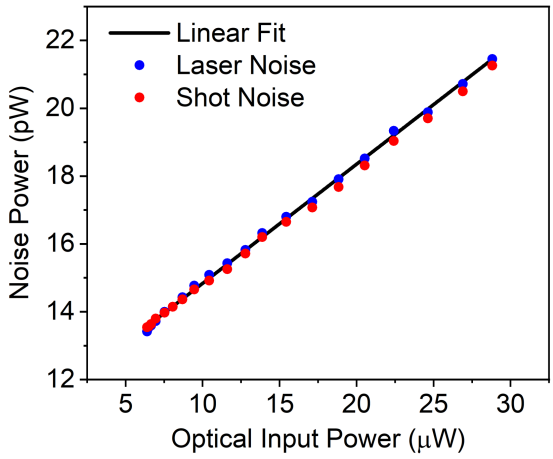

Figure 3.11: Noise power of the Thorlabs PDB440A(-AC) balanced detector at 10 MHz as a function of detected power.

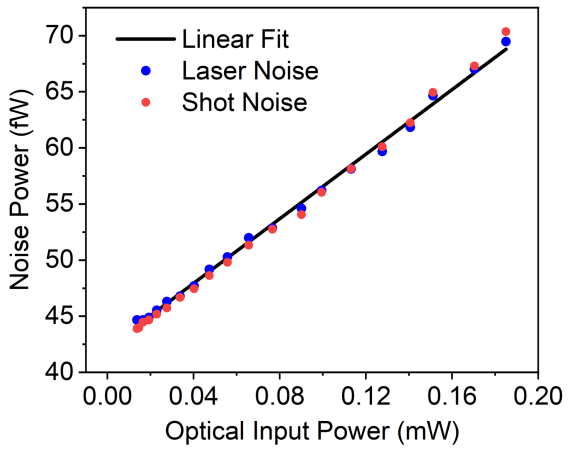

Figure 3.12: Noise power of the custom-built balanced detector at 3 MHz as a function of detected power.

calculated by subtracting the electronic noise power from the total measured noise power. These graphs demonstrate the expected linear scaling between variance and power from Equation 2.113 of Chapter 2, and an R-square value of 0.999 and 0.997 are obtained for a linear fitting of Figures 3.11 and 3.12 respectively. This is in contrast to the quadratic scaling of the variance which would be observed if the laser light was dominated by classical intensity fluctuations [96]. We can therefore conclude that the laser light is limited by optical shot noise in this frequency bandwidth.

3.6 Experimental Implementation

Using the simulation described in Section 3.4 and characterisation data from Section 3.5, it is possible to analyse the predicted squeezing using different lengths of fibre, to find the optimal parameters for squeezing in this case. A value for the nonlinear phase shift of $\phi_{NL} \approx \pi$ has been shown to be sufficient for the generation of significantly squeezed light [92]. It is therefore useful to analyse the squeezing at fibre lengths that give $\phi_{NL} = \pi$ for powers that are sufficiently less than the saturation power of the detector used. We first consider the custom-built detector, which saturates at ~ 5 mW average power. Using Equation 3.3 with $\gamma = 0.04$ W^{-1}m^{-1} and a fibre length of $L = 1.22$ m, we find that a phase shift of $\phi_{NL} = \pi$ occurs at $P_0 = 64$ W peak power, which is 0.5 mW of average power for the 80 MHz repetition rate, and may therefore be measured with this detector. Since the Thorlabs detector saturates at ~ 0.4 mW of average power, a longer length of fibre must be used to measure sufficient nonlinearity without saturating this detector. We analyse the case for the ~ 14 m reel of PCF. Using Equation 3.3, the power required for $L = 14$ m is $P_0 = 5.6$ W (0.05 mW average power), which can be measured using the Thorlabs detector.

Due to effects such as third-order dispersion and Raman scattering, it is often not possible to create perfect fundamental solitons [71]. However, the use of anomalous dispersion to counteract the effects of pulse envelope distortion has been shown to be useful for squeezed light generation even without generating perfect solitons [88]. We can use the numerical methods described in Section 3.4 for the 90:10 Kerr interferometer to simulate the squeezing in the anomalous dispersion regime for the above lengths of fibre. Results for these simulations are shown in Figure 3.13 and 3.14 for $L = 14$ m and $L = 1.22$ m respectively. In

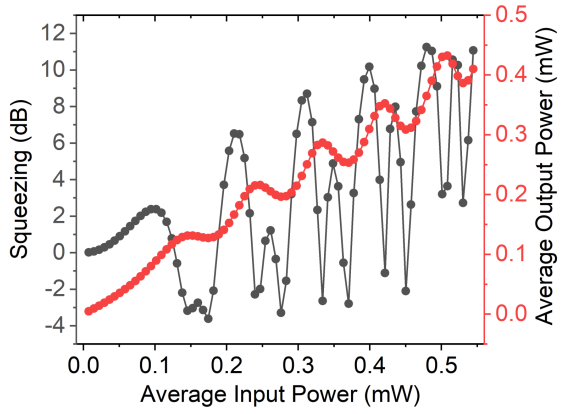

Figure 3.13: Simulated squeezing as a function of average input power from the 14 m reel of fibre, for $\beta_2 = -2$ps^2/km and $\gamma = 0.04$ W^{-1}m^{-1}.

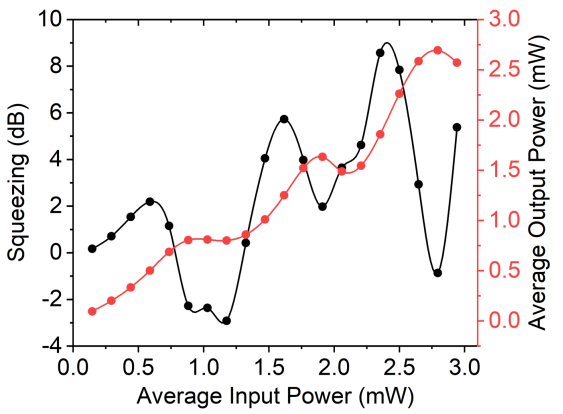

Figure 3.14: Simulated squeezing as a function of average input power from the 1.22 m reel of fibre, for $\beta_2 = -6$ps^2/km and $\gamma = 0.04$ W^{-1}m^{-1}.

Figure 3.13, the results are plotted for $\beta_2 = -2\text{ps}^2/\text{km}$, which was found to be optimal. The results in Figure 3.14 correspond to an optimal value of $\beta_2 = -6\text{ps}^2/\text{km}$. In each plot, the red line represents the simulated classical output power versus input power to the interferometer, and the black line is the simulated squeezing parameter Φ_{dB} as a function of input power. The observed oscillations in the output power are expected due to the dependence of the phase ϕ_{NL} on the optical power. We also observe oscillations in Φ_{dB}, since squeezing is observed for particular values of ϕ_{NL}, which varies periodically. This simulation provides a useful heuristic picture of amplitude squeezing using this method, since the stationary points of the oscillations in output power coincide with squeezing, while regions of sharply increasing or decreasing output power coincide with antisqueezing. Qualitatively, we expect this to be the case, since, on a stationary point in output power, fluctuations in the power of the input light become suppressed on the output of the interferometer, leading to amplitude squeezing, while the opposite effect occurs for antisqueezing.

The optimal values found for the dispersion parameter given above can be used to motivate the range of wavelengths tested when optimising squeezing in this experiment. A schematic of the experimental setup is shown in Figure 3.15. 100 fs pulses from the Spectra

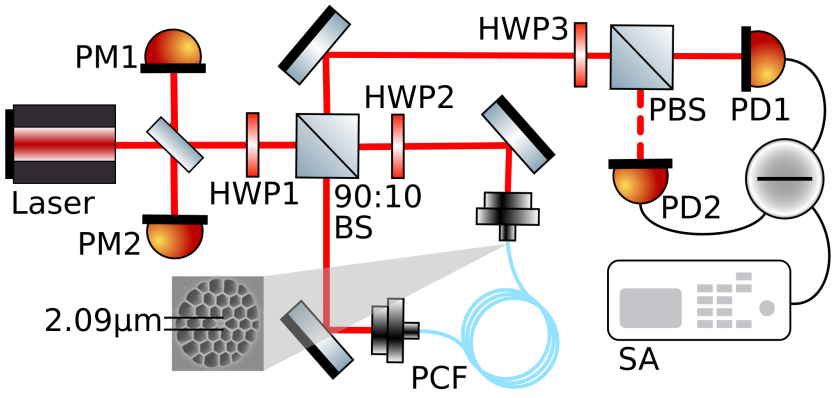

Figure 3.15: Diagram of the experimental setup used for squeezed light generation. Interference of the 90% reflected Kerr phase shifted light with the 10% transmitted light leads to amplitude squeezing on the output of the interferometer, which can be measured by direct detection at PD1. The dashed line indicates that the path to PD2 is unused for the detection of squeezed light, and this port is only used for the calibration of shot noise from the balanced subtraction of the photocurrents from PD1 and PD2.

Physics Mai Tai Ti:Sapphire laser are coupled into the asymmetric nonlinear interferometer, which has a splitting ratio of 90:10. Half-wave plates HWP1 and HWP2 are used to match the polarisation of the light with one of the main axes of the PCF, such that the light output from the fibre is approximately linearly polarised. The effect of nonlinear interference at the 90:10 beamsplitter was monitored by measuring the optical power of the light backpropagated from the interferometer at powermeter PM1 and by measuring the noise

power of the light at PD1. The shot noise level was calibrated by measuring the noise power of the subtraction photocurrent of PD1 and PD2.

Experimental results from this setup are shown in Figures 3.16 and 3.17 for the 14 m and 1.22 m length of fibre respectively. The red curves show the power of the backpropa-

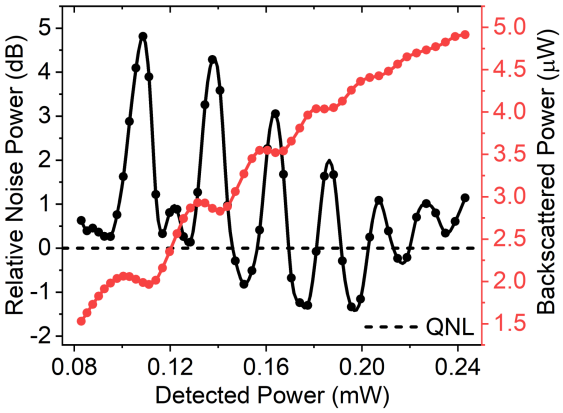

Figure 3.16: Squeezing results from the 14 m reel of PCF, for λ = 740 nm. The noise power is measured at a frequency of 10 MHz.

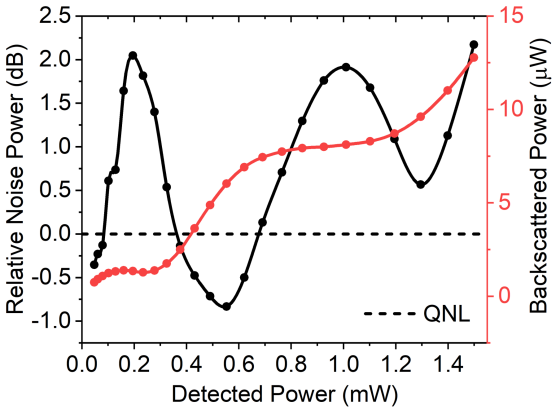

Figure 3.17: Squeezing results from the 1.22 m length of PCF, for λ = 760 nm. The noise power is measured at a frequency of 3 MHz.

gated light at PM1 versus the detected power, which is calibrated from a measurement at PM2. The black curves represent the measured squeezing parameter in dB, Φ_{dB}, as a function of detected power, and the dashed lines correspond to the quantum noise limit. The squeezing parameter is calculated using Equations 2.114-2.115 of Chapter 2. Since regions of sharply increasing backpropagated power correspond to plateaus in the power propagated towards PD1, we expect from the previous discussion that plateaus in backpropagated power will coincide with antisqueezing, while regions with a steep slope in backpropagated power will coincide with squeezing, and this behaviour is indeed observed. A maximum of -0.8 dB of squeezing is observed in the 1.22 m length of fibre, while -1.3 dB is observed in the 14 m reel. We also find an optimal wavelength of 760 nm for the L = 1.22 m and 740 nm for L = 14 m reel, which agrees with the optimal dispersion parameters predicted by the simulation. However, while the simulation predicts soliton-like behaviour for a wide range of the power values used, significant spectral distortion is observed experimentally, as shown in Figure 3.18 for the 14 m reel and Figure 3.19 for the 1.22 m length of fibre. A possible reason for the distortion observed in the optical spectra shown in Figures 3.18-3.19 is the effect of third-order dispersion [71]. By degrading the interference of the pulses on the 90:10 beamsplitter, this is likely to place a significant limit on the squeezing that may be generated with this PCF [88]. While third-order dispersion may be incorporated into the simulation, interferometric instability in the dispersion measurement meant that

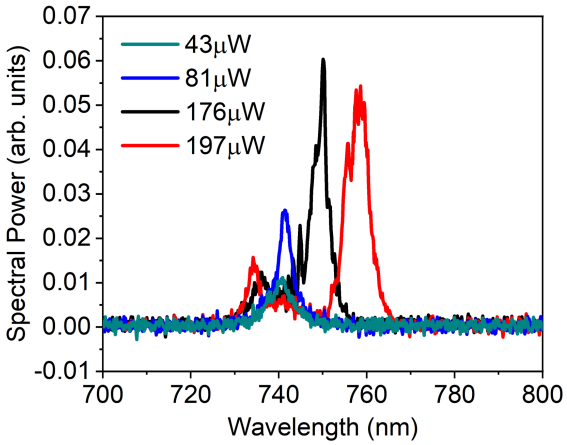

Figure 3.18: Experimentally measured optical spectrum for a range of detected powers for the 14 m reel of PCF, at $\lambda = 740$ nm.

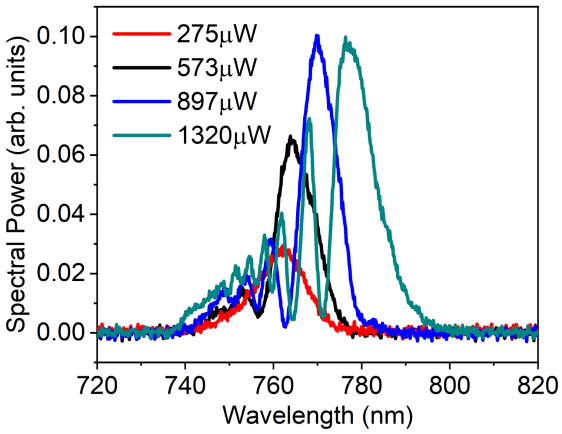

Figure 3.19: Experimentally measured optical spectrum for a range of detected powers for the 1.22 m reel of PCF, at $\lambda = 760$ nm.

it was difficult to obtain a precise estimate of β_3 for this experiment. An additional reason for the discrepancy between the simulated and measured squeezing values may be due to the Raman effect [88, 91].

3.7 Conclusion

This chapter provides a numerical and experimental study of amplitude squeezing via the optical Kerr effect with PCF. Our work complements previous studies of squeezing in microstructured fibre, and shows that significant squeezing can be achieved using this approach at visible wavelengths by engineering the dispersion properties of the fibre. The approach of using an asymmetric interferometer provides an advantage over previous demonstrations of bright visible squeezing via the Kerr effect in PCF [12], since there is no requirement for filtering of the squeezed light. While single mode fibre was used to generate high power photon number squeezing at visible wavelengths in [58], the use of PCF here means that there is no requirement for additional dispersion compensation. In Section 3.6, we demonstrated a maximum of -1.3 dB of measured squeezing, which corresponds to -1.6 dB when corrected for the detection efficiency of $\eta = 0.836$. The numerical simulation showed good qualitative agreement with the experimental results, and was consistent with the optimal wavelengths found for squeezing in each fibre length due to the second-order dispersion.

There are a number of reasons for the lack of exact numerical agreement between the simulation and experimental results. Firstly, there is some uncertainty in experimental

parameters such as the nonlinearity coefficient γ and the pulse duration T_0. Furthermore, while we would expect to see soliton-like behaviour at around the wavelengths used for the measurement, this was not observed experimentally. This suggests higher-order effects such as third-order dispersion may act to degrade the squeezing observed in this case, since even small values of third-order dispersion may have a significant effect on the stability of optical solitons. This indicates a promising route to improving the generated squeezing in future experiments using PCF, by engineering the fibre structure to flatten the dispersion curve, such that it is possible to obtain negligible β_3 for finite β_2. Another effect that may have limited the squeezing obtained in this experiment is Raman scattering, which has been shown to be significant in previous fibre squeezing measurements [91]. However, this is more challenging to overcome, with the only known approach being cryogenic cooling of the optical fibre.

The degree of squeezing demonstrated here is nonetheless sufficient for the application of this source to significantly reduce the noise of optical measurements. In the following chapters, this squeezed light source will be used to experimentally investigate high-power quantum precision-enhancement in optical metrology.

CHAPTER 4

QUANTUM ENHANCED PRECISION ESTIMATION OF AMPLITUDE MODULATION

4.1 Introduction

The performance of any optical measurement is fundamentally limited by quantum fluctuations in the probe and the measurement device. When coherent laser light is used as a probe, the optical fluctuations are due to shot noise, arising from the Poisson distributed photon number distribution of the coherent state [26]. In some cases, noise contributions from other classical sources, such as detection electronics or excess laser noise, can be reduced such that the optical shot noise determines the uncertainty in the measured observable [97]. This defines the quantum noise limit (QNL) for classical optics, which is characterised by a $1/\sqrt{N}$ scaling in error, for a probe containing N photons [98]. Therefore, by increasing the intensity of the probe beam, or measuring for longer periods of time, it is possible in general to reduce the effect of shot noise on the measurement. It is also possible to reduce the error by strengthening the interaction between the probe and sample via multiple passes [99, 100] or optimising sample length [101]. However, there can often exist restrictions on the total optical exposure, the measurement time, and sample properties [102, 103]. By using non-classical states of light, the fluctuations in the probe beam may be significantly reduced relative to that of a coherent state, thus providing a way to perform 'sub-shot-noise' parameter estimation per photon in the probe [6, 104].

The QNL defines the best precision achievable without the use of quantum correlations for a given apparatus and photon number [9]. This is distinguished from the standard quantum limit (SQL), which defines a measurement-independent limit to the precision that may

be achieved using a minimum uncertainty state of a given photon number, without quantum resources [98]. Here, we will use the QNL to describe the theoretical limit of precision with classical light, since by accounting for experimental parameters such as detection efficiency, the QNL allows for a more intuitive description of the precision improvement by using non-classical light. As we have seen in Chapter 2, squeezed states can have uncertainty below the QNL, and therefore provide a suitable resource for quantum metrology. Squeezed states of light may also be produced with arbitrary intensity using coherent laser light [105]. This makes squeezed light a uniquely practical probe state for improving the performance of optical techniques beyond the QNL.

The ability of a measurement to estimate a parameter may be characterised by both precision and sensitivity. The precision is determined by the variance of repeated estimates [14], and therefore depends on the fluctuations in the measured signal. Sensitivity is defined as the smallest possible signal that may be observed [15], and therefore only depends on the signal-to-noise ratio (SNR). Sub-shot-noise measurements using bright squeezed light have so far been driven by improvements in sensitivity beyond the QNL, and this has been applied to optical techniques such as spectroscopy [16, 106, 107, 108, 109], light microscopy [10, 110], gravitational wave detection [7, 8], optical magnetometry [17], and a range of other optical techniques [111, 112, 9, 113, 114]. However, we will show that observing enhanced sensitivity is not sufficient to show enhanced precision. Demonstrations of transmission measurements with precision beyond the QNL have been limited to $\sim$ pW of probe power [23, 115]. This restricts the practical applicability compared to using classical laser light, since classical measurements are often able to reach much higher levels of power. To attain a precision improvement using bright squeezed light as a probe, the variance of the measured signal must be dominated by quantum noise. In this chapter, we develop a theoretical model which can be used to calculate the variance of signals measured in the frequency domain. This model is used to determine the conditions required to obtain both precision and sensitivity enhancement beyond the QNL in the estimation of a modulated optical loss using bright amplitude squeezed light, which is experimentally demonstrated. This corresponds to the first observation of enhanced precision in the estimation of amplitude modulation (AM) using high power amplitude squeezed light.

In Section 4.2, we begin by introducing the theory of Fisher information [116], which will be used to quantify the precision improvement of our measurement using squeezed light. In Section 4.3, we derive the Fisher information for the loss parameter measured in this experiment, and show that a quantum advantage in precision is attainable under certain conditions. Section 4.4 shows the experimental results for the AM measurement and Section 4.5 concludes the chapter.

4.2 Parameter Estimation and the Cramér-Rao Bound

The purpose of any measurement is to estimate a parameter θ, or set of parameters $\boldsymbol{\theta} = \{\theta_1, \theta_2, ...\}$, based on a set of data $\boldsymbol{x} = \{x_1, x_2, ...\}$. The problem of parameter estimation is to define a measurement strategy which maximises the information about θ contained in $\boldsymbol{x}$, and an estimator $\hat{\theta}(\boldsymbol{x})$ which maximises the amount of information about θ that may be extracted from $\boldsymbol{x}$ [117]. The caret in this context indicates that $\hat{\eta}$ is an estimator, as opposed to an operator. We will first discuss some desirable properties of estimators.

Two key properties which determine the performance of an estimator are the variance and the bias. Intuitively, the variance describes how close the set of estimates are, on average, to the expected value of the estimates. The bias is the difference between the expected value of the estimator and the true value of the parameter. These properties quantify the error in the estimation procedure. In order to define these quantities more formally, we can specify a probability distribution $f(x|\theta)$ which describes the likelihood of observing the outcome x, given the parameter θ. This is known as the likelihood function. The bias is then given by [118]

$$\text{Bias}_\theta(\hat{\theta}) = \mathbb{E}_{f(\boldsymbol{x}|\theta)}(\hat{\theta}) - \theta. \tag{4.1}$$

Here, $\mathbb{E}_{\boldsymbol{x}|\theta}(\hat{\theta})$ is known as the expectation value of $\hat{\theta}$, and can be given as $\mathbb{E}_{\boldsymbol{x}|\theta}(\hat{\theta}) = \int_{\mathbb{X}} \hat{\theta}(x) f(x|\theta) dx$ when x is a continuous parameter, where $\mathbb{X}$ is the domain of the estimator $\hat{\theta}$. For a discrete parameter x this integral is replaced with a summation. In the ideal case the bias will be zero, such that on average, $\hat{\theta} = \theta$. The variance of an estimator is defined by [116]

$$\text{Var}_\theta(\hat{\theta}) = \mathbb{E}_{f(\boldsymbol{x}|\theta)}[(\hat{\theta} - \mathbb{E}_{f(\boldsymbol{x}|\theta)}[\hat{\theta}])^2]. \tag{4.2}$$

A desirable property of an estimator is to have the minimum variance, such that the uncertainty in the estimated values is small. In order to minimise the error due to both the bias and the variance, an optimal estimator can be defined as one which minimises a quantity called the mean squared error, defined as [116]

$$\text{MSE}_\theta(\hat{\theta}) = \mathbb{E}_{f(\boldsymbol{x}|\theta)}[(\hat{\theta} - \theta)^2], \tag{4.3}$$

which can equivalently be expressed as

$$\text{MSE}_\theta(\hat{\theta}) = \text{Var}_\theta(\hat{\theta}) + \text{Bias}_\theta(\hat{\theta})^2. \tag{4.4}$$

The mean squared error provides a useful characterisation of the estimator performance in both classical and quantum estimation theory [119]. However, due to the bias term, estimators which minimise the mean squared error typically depend on the value of the true parameter θ and are therefore not realisable in practise. A common approach is to require that the bias is zero, and find an estimator which minimises the variance.

4.2.1 Fisher Information

In order to determine whether an estimator has minimum variance, it is necessary to find a lower bound on the variance of any unbiased estimator. Such a bound is called the Cramér-Rao bound (CRB), and is expressed as [120]

$$\mathrm{Var}_\theta(\hat{\theta}) \geq \frac{1}{\mathcal{F}(\theta)}, \tag{4.5}$$

where $\mathcal{F}(\theta)$ is the Fisher information of the parameter θ. The precision of a measurement is given by the inverse of the variance, and therefore the CRB sets a bound on the maximum achievable precision of the measurement, for any estimator $\hat{\theta}$. If an unbiased estimator saturates the CRB for all θ, it is known as an efficient estimator. The Fisher information may be written in terms of the likelihood function as [116]

$$\mathcal{F}(\theta) = \mathbb{E}_{f(x)}\left[\left(\frac{\partial}{\partial\theta}\log(f(x|\theta))\right)^2\right]. \tag{4.6}$$

Intuitively, the Fisher information describes how sharply peaked the likelihood function is. For a narrow likelihood distribution, the data $\boldsymbol{x}$ is highly dependent on θ, and therefore contains more information about θ than a more broadly peaked $f(x|\theta)$. The distribution $f(x|\theta)$ is directly determined by the choice of measurement. Therefore, in order to optimise the estimation procedure, a first step is to choose a measurement procedure for which the corresponding $f(x|\theta)$ maximises the Fisher information. Then, an unbiased estimator is required which minimises $\mathrm{Var}_\theta(\hat{\theta})$, and in the optimal case saturates the CRB.

4.2.2 Quantum Fisher Information

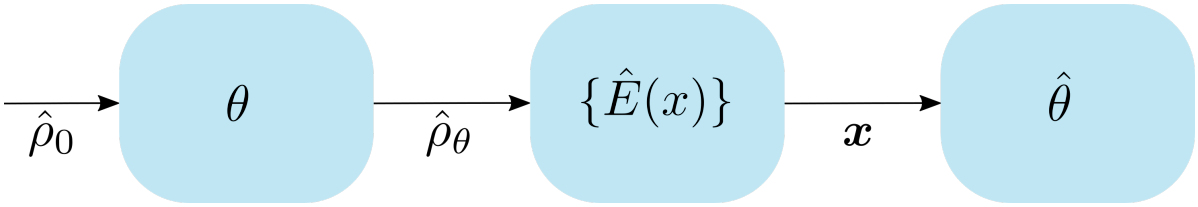

Figure 4.1: General quantum parameter estimation procedure illustrated by the interaction of an initial state $\hat{\rho}_0$ with a system described by the parameter θ. The final state $\hat{\rho}_\theta$ is subjected to the POVM $\{\hat{E}(x)\}$ and the measurement outcomes $\boldsymbol{x}$ are described by the distribution $f(x|\theta) = \mathrm{Tr}[\hat{E}(x)\hat{\rho}_\theta]$. The estimator $\hat{\theta}$ is then computed based on the data $\boldsymbol{x}$.

In quantum estimation theory, finding the optimal quantum measurement strategy may be a highly non-trivial task. It is therefore useful to consider the bound on the variance as a result of optimising over all possible quantum measurements. Such a bound is given

by the quantum Fisher information $\mathcal{F}_Q(\theta)$, and leads to the quantum Cramér-Rao bound (QCRB) [121]:

$$\mathrm{Var}_\theta(\hat{\theta}) \geq \frac{1}{\mathcal{F}(\theta)} \geq \frac{1}{\mathcal{F}_Q(\theta)}. \tag{4.7}$$

$\mathcal{F}_Q(\theta)$ therefore corresponds to the maximum possible value of $\mathcal{F}(\theta)$, where this bound is only saturated in the case that $\mathcal{F}(\theta)$ is evaluated for the optimal measurement strategy. A general quantum measurement strategy is shown in Figure 4.1. An initial quantum state given by the density operator $\hat{\rho}_0$ is allowed to interact with a system, where some property of this system is described by the parameter θ. The interaction of $\hat{\rho}_0$ with the system generates some dependence of the state on θ, which is now given by $\hat{\rho}_\theta$. A measurement of the state $\hat{\rho}_\theta$ can be described by the set of operators $\{\hat{E}(x)\}$ acting on $\hat{\rho}_\theta$ known as a positive operator-valued measure (POVM) [122]. Here, x denotes the measurement outcome, and the elements $\hat{E}(x)$ must be positive semi-definite and satisfy $\int \hat{E}(x)dx = \mathbb{1}$, where $\mathbb{1}$ is the identity operator. The probability distribution of the measurement data are described by the Born rule: $f(x|\theta) = \mathrm{Tr}[\hat{E}(x)\hat{\rho}_\theta]$. The POVM formalism may then be used to compute $\mathcal{F}(\theta)$ according to 4.6. The quantum Fisher information $\mathcal{F}_Q(\theta)$ corresponds to the maximum value of $\mathcal{F}(\theta)$ over all POVMs. For an initial pure state $\rho_0 = |\Psi\rangle\langle\Psi|$, transforming under unitary evolution $\hat{U}(\theta) = e^{i\hat{H}(\theta)}$, $\mathcal{F}_Q(\theta)$ may be written as [123]

$$\mathcal{F}_Q(\theta) = 4(\langle\Psi|\hat{H}(\theta)^2|\Psi\rangle - \langle\Psi|\hat{H}(\theta)|\Psi\rangle^2). \tag{4.8}$$

The quantum Fisher information then depends only on the initial state $\hat{\rho}_0$ and the Hamiltonian $\hat{H}(\theta)$ generating translations in θ. Therefore, by careful consideration of the probe state and interaction, $\mathcal{F}_Q(\theta)$ may be maximised. For mixed initial states or non-unitary processes, it is often the case that an analytic expression for $\mathcal{F}_Q(\theta)$ cannot be obtained. In such cases, it is however often possible to find an upper bound for $\mathcal{F}_Q(\theta)$ [124]. Minimisation of $\mathrm{Var}_\theta(\hat{\theta})$ for an unbiased estimator $\hat{\theta}$ then yields an optimal quantum estimation strategy.

4.3 Estimation of a Modulated Loss with Squeezed Light

4.3.1 Theoretical Model

The parameter estimated in this experiment is the modulation index, δ_m, which corresponds to a fractional modulation in optical loss [125]. This may be expressed as $\delta_m = (P - P')/P$, where P and P' are the maximum and minimum output power due to modulation, as illustrated by Figure 4.2. By observing the power oscillations in the time domain, it may be possible to directly measure δ_m from P and P'. However, typical laser sources and

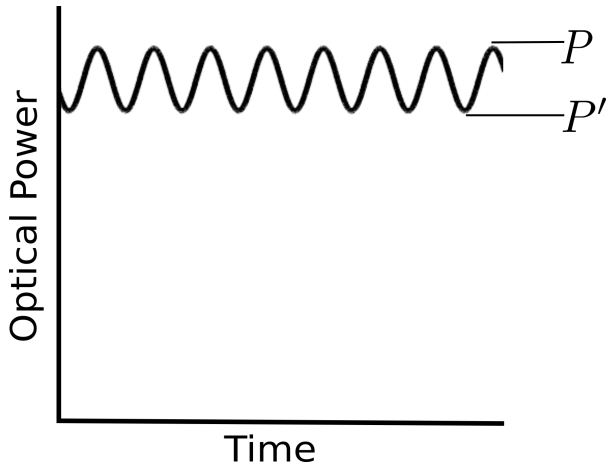

Figure 4.2: Illustration of the effect of AM on the time dependence of optical power.

detectors are only shot noise limited in the MHz frequency regime. Therefore, by making a frequency domain measurement of the optical power around the modulation frequency, we can infer a value of δ_m without integrating over any low frequency classical noise. Provided that the modulation frequency Ω is in a shot noise limited bandwidth, squeezed light may then be used to estimate a value of δ_m with sensitivity beyond the QNL. However, we show that sub-QNL sensitivity is not a sufficient condition to enhance precision. In this section, we define an estimator for δ_m in terms of the measured spectral noise power, and discuss the experimental conditions that must be satisfied in order to attain a precision improvement in δ_m by using amplitude squeezed light as a probe. While estimation of the modulation index is itself of limited application, the detection of modulated signals has played a crucial role in both classical and quantum optical metrology [126, 110, 10]. The analysis discussed here provides a general methodology which may be directly translated into such applications.

For a modulation frequency Ω, the process of sinusoidal AM generates two optical sidebands at $\pm\Omega$ from the carrier frequency. Upon photodetection, this leads to a single electronic sideband in the spectral noise power at frequency Ω, which contains information about δ_m. An estimator for δ_m is derived from the optical SNR using a similar approach to Xiao et al. [127], which used homodyne detection. For direct photodetection of AM in a shot noise limited bandwidth around Ω, we may write the SNR as $\delta_{SNR} = \langle p_s \rangle / \langle p_n \rangle$, where $\langle p_s \rangle$ is the average signal component of the generated electronic power at frequency Ω and $\langle p_n \rangle$ is the average electronic power due to the optical noise. The assumption of a weakly modulated carrier ($\delta_m \ll 1$) means that we can consider that the loss applied by the EOM has a negligible effect on both the squeezing parameter Φ and the average optical power on the output of the EOM. Therefore, for an optical power of P on the input of the EOM, the average (DC) measured photocurrent may be expressed as $i_0 = q\eta_q P(1-(\delta_m/2))/\hbar\omega \approx q\eta_q P/\hbar\omega$, for a photodiode efficiency of η_q and light with a carrier wave of angular frequency ω. By

calculating the expected values for the signal and noise, we may then write δ_{SNR} as

$$\delta_{SNR} = \frac{\langle p_s \rangle}{\langle p_n \rangle} \approx \frac{\delta_m^2 i_0}{4q\Phi B}, \tag{4.9}$$

for a resolution bandwidth of B (see Appendix A.1). From Equation 4.9, we can define an estimator for the modulation index as

$$\hat{\delta}_m = \sqrt{\frac{4q\Phi B \hat{\delta}_{SNR}}{i_0}}, \tag{4.10}$$

where

$$\hat{\delta}_{SNR} = \frac{p_\Omega - p_N}{p_N - p_E} \quad \text{and} \quad i_0 = \frac{q\eta_q \langle P \rangle}{\hbar\omega}. \tag{4.11}$$

The carets on $\hat{\delta}_m$ and $\hat{\delta}_{SNR}$ indicate that these are estimators. Here, p_Ω, p_N and p_E are the measured spectral noise powers of the electronic sideband, the optical noise floor and the electronic noise floor respectively. $\langle P \rangle$ is the average detected optical power, and both $\langle P \rangle$ and p_N may be precalibrated with high precision. The dependence of $\hat{\delta}_m$ on the optical noise is then contained in the measurement of p_Ω.

For an input resistance of R to the measuring device (e.g. spectrum analyser or oscilloscope), we can define the power of the electronic sideband as

$$p_\Omega = 2R|\hat{i}_\Omega|^2, \tag{4.12}$$

where $\hat{i}_\Omega$ is the photocurrent in the frequency bin centered on Ω. By considering power fluctuations due to quantum optical noise, low frequency classical optical noise, and electronic noise, the variance of the signal power is found to be

$$\mathrm{Var}(p_\Omega) = \langle p_\Omega^2 \rangle - \langle p_\Omega \rangle^2 \approx \frac{R^2}{M}\left[2q\delta_m^2 i_0^3 \Phi B + 4\delta_m^4 i_0^4 \mathrm{Var}(\Re[\mathcal{H}]) + 4q^2\delta_m^2 i_0^2 \mathrm{Var}(\Re[\mathcal{N}]) \right] \tag{4.13}$$

(see Appendix A.2). $\Re[\bullet]$ corresponds to the real part, $\mathcal{H}$ is the DC component of the classical relative amplitude noise from the laser and modulator, $\mathcal{N}$ is the component of electronic noise in the $\pm B$ frequency interval around Ω, and M is the number of spectral averages. The dependence of $\mathrm{Var}(p_\Omega)$ on $\mathcal{H}$ is due to classical noise being transferred from the carrier to the optical sidebands upon modulation. We assume here that the variance of the optical noise due to the classical intensity fluctuations scales quadratically with optical power, as expected for technical laser noise [96]. In order to quantify the advantage in precision which may be obtained by using squeezed light, we analyse the Fisher information on the modulation index, $\mathcal{F}(\delta_m)$. Given that we use an amplitude squeezed state to perform an amplitude measurement, the classical Fisher information saturates the quantum Cramér-Rao bound [128]. Therefore, directly evaluating the classical Fisher information provides a

bound on any quantum strategy. For our measurement strategy, and assuming $\alpha \gg 1$, $\hat{\delta}_{SNR}$ is normally distributed and we can define $\mathcal{F}(\delta_{SNR})$ according to [129]

$$\mathcal{F}(\delta_{SNR}) = \frac{1}{\mathrm{Var}(\hat{\delta}_{SNR})} = \left[\left(\frac{\partial\langle\hat{\delta}_{SNR}\rangle}{\partial\langle p_\Omega\rangle}\right)^2 \mathrm{Var}(p_\Omega)\right]^{-1}. \tag{4.14}$$

$\mathcal{F}(\delta_m)$ can be obtained from $\mathcal{F}(\delta_{SNR})$ by using [129]

$$\mathcal{F}(\delta_m) = \left(\frac{\partial\delta_{SNR}}{\partial\delta_m}\right)^2 \mathcal{F}(\delta_{SNR}). \tag{4.15}$$

We find that $\mathrm{Var}(\Re[\mathcal{N}])$ contributes negligibly to $\mathcal{F}(\delta_m)$, and from Equation 4.10-4.15, this leads to

$$\mathcal{F}(\delta_m) \approx M\left[\frac{2q\Phi B}{i_0} + 4\delta_m^2 \mathrm{Var}(\Re[\mathcal{H}])\right]^{-1}. \tag{4.16}$$

The quantum advantage is then the ratio $\mathcal{Q}(\delta_m)$ between the values of $\mathcal{F}(\delta_m)$ for a squeezed ($\Phi < 1$) and coherent ($\Phi = 1$) state. The variance of $\hat{\delta}_m$ can be obtained by standard error propagation. We find

$$\mathrm{Var}(\hat{\delta}_m) = \left(\frac{\partial\langle\hat{\delta}_m\rangle}{\partial\langle p_\Omega\rangle}\right)^2 \mathrm{Var}(p_\Omega) = \frac{1}{\mathcal{F}(\delta_m)}. \tag{4.17}$$

Therefore, $\hat{\delta}_m$ is an efficient estimator. We also find that, in the limit of weak AM, $\langle\hat{\delta}_m\rangle = \delta_m$, meaning our estimator is unbiased.

The Fisher information per detected photon may be defined as $\mathcal{F}'(\delta_m) = \mathcal{F}(\delta_m)/\langle N\rangle$, where $\langle N\rangle = i_0/qB$ is the number of photons detected in the measurement time B^{-1}. Using Equation 4.16, this gives

$$F'(\delta_m) = M\left[2\Phi + 4\delta_m^2\langle N\rangle \mathrm{Var}(\Re[\mathcal{H}])\right]^{-1}. \tag{4.18}$$

A graph illustrating the dependence of $\mathcal{F}'(\delta_m)$ on the RBW is shown in Figure 4.3 for a typical laser source which is quantum noise limited at Ω (solid line) and various levels of squeezing (dashed lines), with all other parameters fixed. We find that, for sufficiently high RBWs, squeezing provides sub-QNL precision in estimating δ_m. This can be seen from Equation 4.16, since for $2q\Phi B/i_0 \gg 4\delta_m^2 \mathrm{Var}(\Re[\mathcal{H}])$, quantum noise limits the precision of the measurement, and we find $\mathcal{Q}(\delta_m) \to \mathcal{Q}_{opt}$, where

$$\mathcal{Q}_{opt} = \frac{1}{\Phi}. \tag{4.19}$$

Given that all the information on the parameter δ_m is contained at the modulation frequency Ω, this model suggests a practically achievable quantum advantage in precision is possible, per photon in the probe.

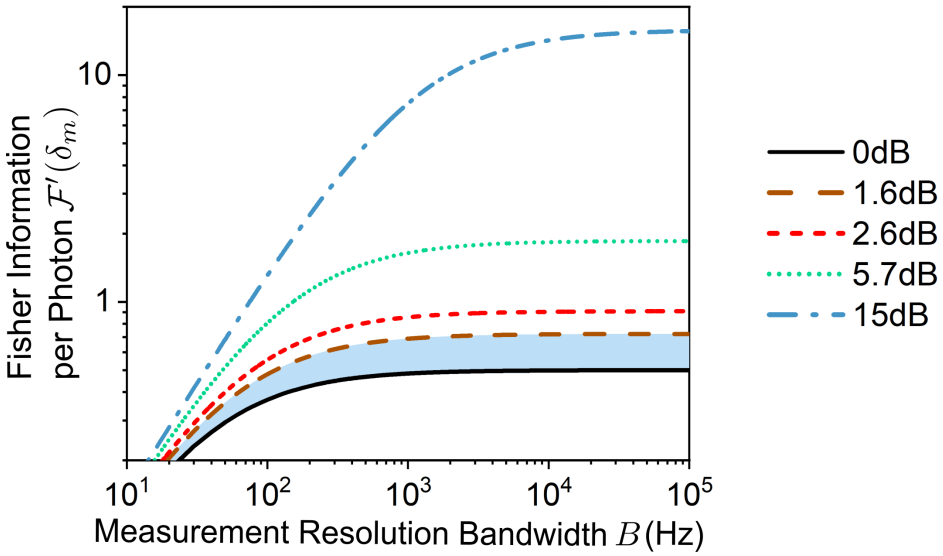

Figure 4.3: Theoretical model of the Fisher information per detected photon $\mathcal{F}'(\delta_m)$, using Equation 4.18. This is plotted for typical laser light which is quantum noise limited at Ω (solid line) and squeezed light (dashed lines): -1.6 dB and -2.6 dB are the measured and inferred generated squeezing levels in our experiment, -5.7 dB is amplitude squeezing previously achieved using an asymmetric Kerr interferometer [1] and -15 dB is the highest measured squeezing to date [2]. For each plot, $P = 0.2$ mW, $\lambda = 740$ nm, $\eta_q = 1$, $\delta_m = 1 \times 10^{-4}$ and $\mathrm{Var}(\Re[\mathcal{H}]) = 1 \times 10^{-5}$.

4.3.2 Simulation

In order to verify the theoretical model described in 4.3.1, a simulation of the generated photocurrent was implemented. The photocurrent was discretised in the time domain, and given by

$$i(t_n) = q\left(|\alpha(t_n)|^2 + \sigma(t_n)\right), \tag{4.20}$$

where $t_n = n/f_s$ is the time at sample n, for a sample rate of f_s. $\alpha(t_n)$ corresponds to the discretised classical amplitude from Equation A.2, where the stochastic classical noise function $\zeta(t_n)$ is defined such that it has a spectral amplitude which is proportional to $1/k^2$ for frequency index k. This ensures that the classical noise is negligible at high frequencies ~ 10 MHz surrounding the modulation frequency. The function $\sigma(t_n)$ describes the quantum optical noise and follows a Normal distribution with variance $\mathrm{Var}(\sigma(t_n)) = \Phi N f_s$, for N detected photons per second. This definition follows since N/f_s photons are detected in a time interval $1/f_s$, which leads to a quantum noise contribution of $\sqrt{\Phi N/f_s}$ photons in this measurement interval, following Poisson statistics. The count rate of photons from quantum noise is therefore given by $\sqrt{\Phi N f_s}$ photons per second. By implementing the Fast Fourier

Transform (FFT) algorithm, we can then compute the power in the kth frequency bin as

$$p(\nu_k) = \frac{2R}{N_s^2}|i(\nu_k)|^2 \tag{4.21}$$

for $k > 1$, where $i(\nu_k)$ is the discrete Fourier transform of the time domain photocurrent. Here, $\nu_k = kB$, where $B = N_s f_s$ and N_s is the total number of samples. Figure 4.4 shows the simulated power spectrum $p(\nu_k)$ in the frequency domain surrounding the modulation frequency $\Omega = 10$ MHz, for $R = 50$ Ohms, $\alpha^2 = 1 \times 10^{15}$, $f_s = 100$ MHz, $B = 10$ kHz and $\Phi = 1$. By sampling the SNR from the simulated power spectrum, $\hat{\delta}_m$ may be estimated, and this is plotted for a range of δ_m in Figure 4.5. This shows agreement between the estimated and true modulation index for low δ_m. However, for $\delta_m \gtrsim 0.02$, there is a bias in the estimation, which increases with δ_m. This is due to the discrepancy between the value of $\langle P \rangle$ used in the estimation according to Equation 4.11 and the true value of $\langle P \rangle$ when AM is applied.

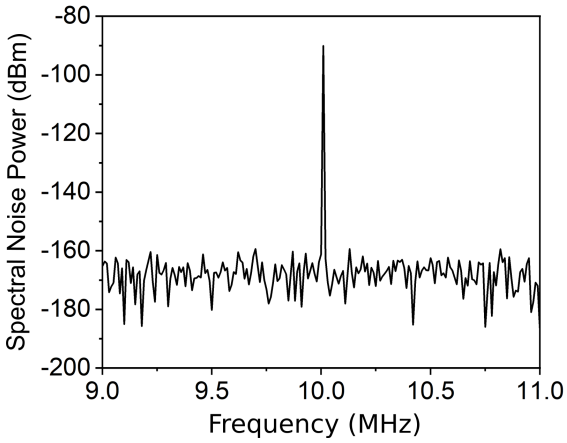

Figure 4.4: Simulated spectral noise power $p(\nu_k)$ around the modulation frequency.

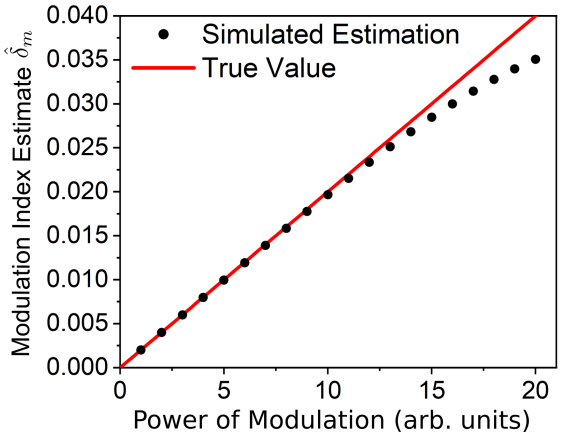

Figure 4.5: Simulated estimation and true value of the modulation index for a range of modulation depths.

Figure 4.6 shows a comparison of the simulated $\mathrm{Var}(p_\Omega)$ with the theoretical value predicted from Equation A.32 of Appendix A.2. This demonstrates good numerical agreement, and illustrates that classical noise dominates the variance of the measured signal at high δ_m, since $\mathrm{Var}(p_\Omega)$ diverges from the QNL above $\delta_m \gtrsim 0.002$. This behaviour is expected, since the amplitude the measured signal must be small for quantum effects to dominate, due to the difference in the scaling of classical and quantum noise with the number of measured photons. These results suggest a limit in the amount of power that can be measured with quantum limited precision, due to low frequency classical noise on the optical probe. However, by efficiently encoding information on the measured signal, quantum limited precision may be achieved with high power quantum probes. In the case of this measurement, all the measured signal photons contribute to the estimation, and quantum limited precision is possible for small δ_m.

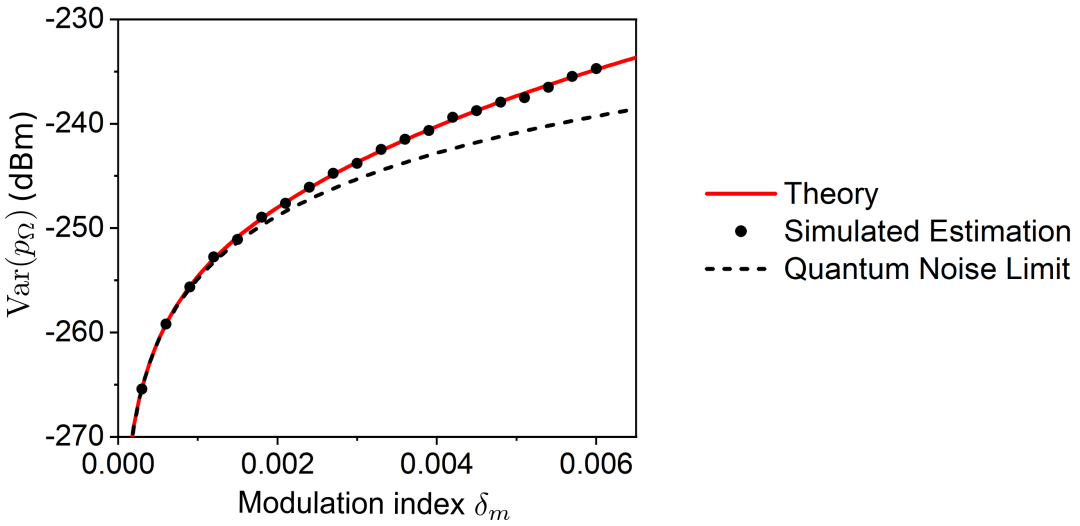

Figure 4.6: Variance of the peak power of the sideband. The black data points correspond to the variance of the simulated noise power $p(v_\Omega)$, while the solid and dashed curves are theoretical values taken using Equation A.32 of Appendix A.2.

4.4 Experimental Implementation

For the measurement, we used the source of amplitude squeezed light described in Chapter 3. Here, the squeezed light is generated using 14 m of photonic crystal fibre (PCF), and the average optical power of the output state is 0.2 mW, which equates to 25 W of peak power. This probe is launched into a modulating sample, in this case implemented using a Thorlabs EO-AM-NR-C1 electro-optic modulator (EOM), which modulates the polarisation of the light. Passing this light through a polarising beamsplitter (PBS) produces weak AM, and generates optical sidebands at a distance $\pm\Omega$ from the carrier frequency. It is necessary to verify that the classical amplitude of the light on the output of the PBS is in fact sinusoidally amplitude modulated at frequency Ω, as described by Equation A.2 in Appendix A.1. Therefore, a more detailed analysis of the action of the EOM on the classical amplitude is provided in Appendix A.3. The resulting state is measured with direct detection, by collecting all the light on a single photodiode of a Thorlabs PDB440A(-AC) balanced amplified photodetector. The balanced subtraction photocurrent is used to calibrate the shot noise level. A Rohde & Schwarz FPC1000 spectrum analyser (SA) is used for measurement of the spectral noise power. A diagram of the experimental setup is shown in Figure 4.7. Also shown are illustrations of the behaviour of the spectral noise power of an initial laser input (a), where the noise characteristics at Ω initially approximate that of a coherent state $|\alpha\rangle$ and so quantum noise dominates the power fluctuations. The light is subsequently squeezed in amplitude (b) and then modulated in amplitude (c). The insets show the ideal evolution of the state at $\pm\Omega$ for an initial coherent state $|\alpha\rangle$. The final state

is amplitude squeezed with an average photon number of $\langle \hat{n}(\pm\Omega)\rangle = \delta_m |\alpha|^2/2$.

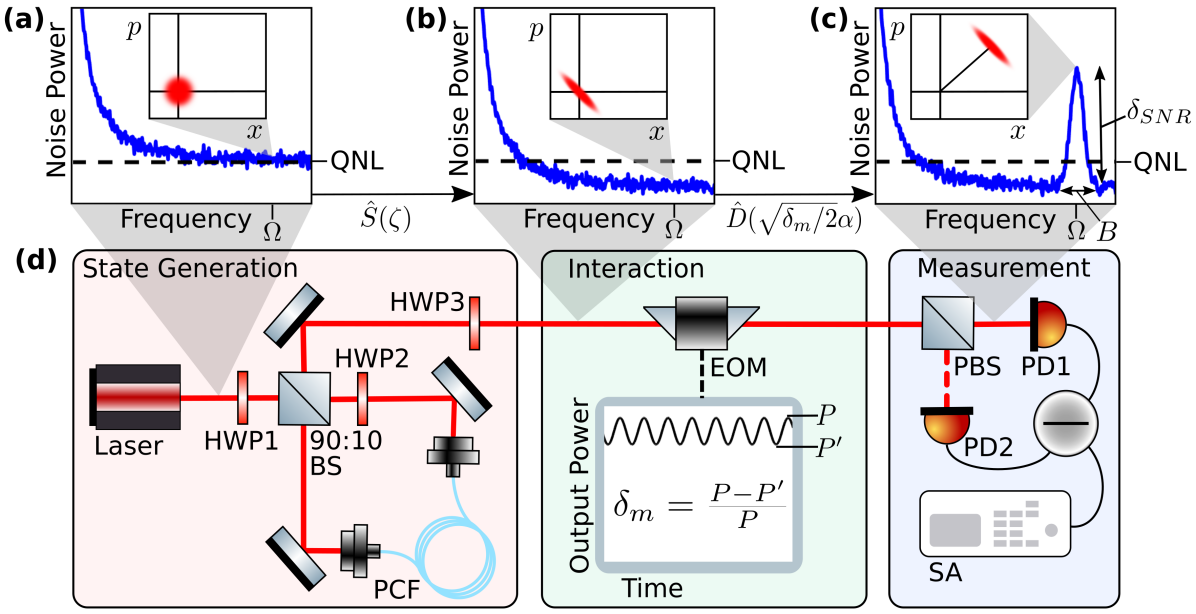

Figure 4.7: Experimental setup, showing expected behaviour for laser light. (a-c) Plots of spectral noise power illustrating the effect of amplitude squeezing and modulation on a typical laser source, with the quadrature diagrams showing a coherent state defined by $\hat{x}$, $\hat{p}$ at $\pm\Omega$. (d) Schematic of the experiment. A pulsed laser at 740 nm propagates into the Sagnac interferometer for squeezed state generation. A birefringent photonic crystal fibre (PCF) provides the nonlinear medium for Kerr squeezing. The electro-optic modulator (EOM) combined with the polarising beamsplitter (PBS) are used to generate AM, which is measured on a spectrum analyser (SA).

One condition that is required for the theoretical model to accurately describe the observations is that the RBW must be significantly larger than the optical linewidth of the generated sidebands. This means that the width of the measured electronic sideband must be limited by the RBW. If this condition is satisfied, then the theoretical description of the optical sidebands as delta functions is justified. This was experimentally verified by measuring the full width at half maximum (FWHM) of the detected electronic sideband as a function of B. These results are shown in Figure 4.8, and fitting a line to the data resulted in the equation: $FWHM = 0.991B + 0.023$. This demonstrates the expected linear scaling, since the width of the electronic sideband is approximately equal to the RBW. The error bars in Figure 4.8 are smaller than the data points. The optical linewidth of the sidebands was measured to be < 1 Hz, lower than the smallest resolvable frequency width of the SA.

Figure 4.9 shows the spectral noise power traces of amplitude modulated squeezed light and antisqueezed light, with the corresponding shot noise level. The blue trace corresponds to -1.2 dB of amplitude squeezing, and the red trace corresponds to 2.7 dB of antisqueezing.

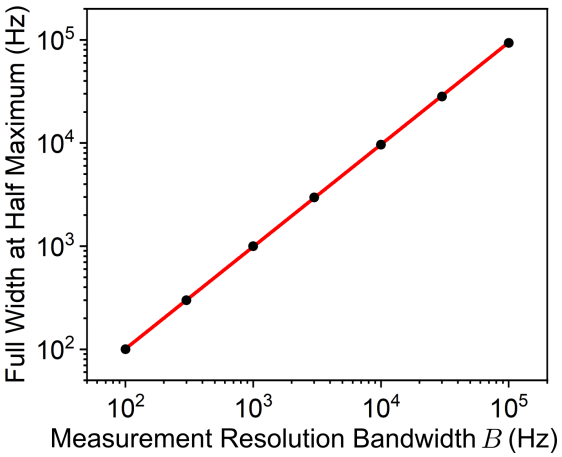

Figure 4.8: Scaling of FWHM of the electronic sideband with the RBW.

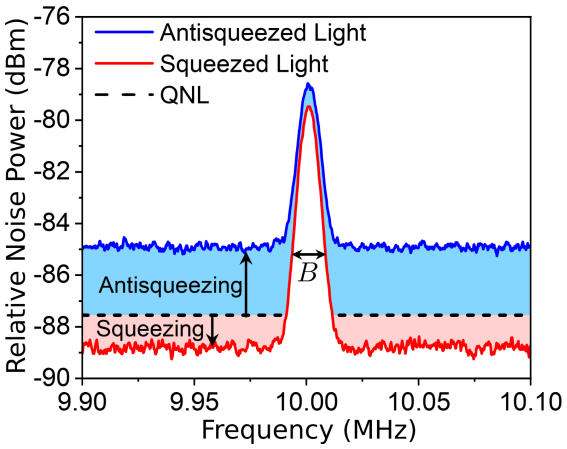

Figure 4.9: 10 MHz AM measured by direct detection. The red trace corresponds to −1.2 dB of squeezing, and the blue trace to 2.7 dB of antisqueezing.

The traces for squeezing and antisqueezing are corrected for the difference in the respective shot noise levels by subtracting the difference between the shot noise level corresponding to each trace and the average shot noise level. The electronic noise has also been subtracted from each trace. The RBW is $B = 10$ kHz, and the frequency separation of trace points in Figure 4.9 is smaller than the RBW since the trace is a result of multiple samples within each RBW interval. These results demonstrate enhanced sensitivity to measurements of AM due to the amplitude squeezing, as already shown in [127].

In order to compare experimental measurement noise to that predicted from Equation 4.17, it is necessary to determine the value of M. As described in Section 2.2.4, for a heterodyne spectrum analyser, the VBW filter performs a smoothing of the detected power, which reduces the variance by a factor ε [44]. This is equivalent to the effect of spectral averaging, and we can therefore write $M = 1/\varepsilon$, giving

$$M = \frac{1.056B}{\pi B_V}. \tag{4.22}$$

A constant ratio of $B/B_V = 100$ was used for data collection, which results in $M = 33.6$.

Measurements of $\mathrm{Var}(\hat{\delta}_m)$ as a function of detected power and $\hat{\delta}_m$ are plotted in Figure 4.10 and Figure 4.11 respectively. In Figure 4.10, numerical agreement is observed between the experimental data and the QNL, where the QNL corresponds to Equation 4.17 for $\mathrm{Var}(\Re[\mathcal{H}]) = 0$. This is possible since for the high RBW ($B = 30$ kHz) and low modulation index ($\hat{\delta}_m = 2\times10^{-4}$) used, quantum noise dominates the variance of the measurement. The slight divergence between the theory and experiment at low powers is likely due to the contribution of electronic noise, which becomes greater when the detected photocurrent is

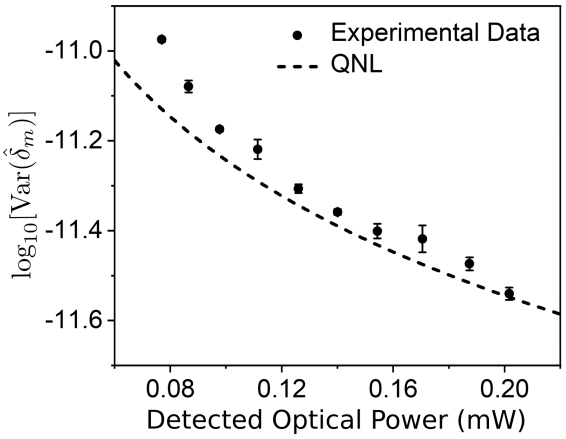

Figure 4.10: Measured variance of the modulation index as a function of detected power.

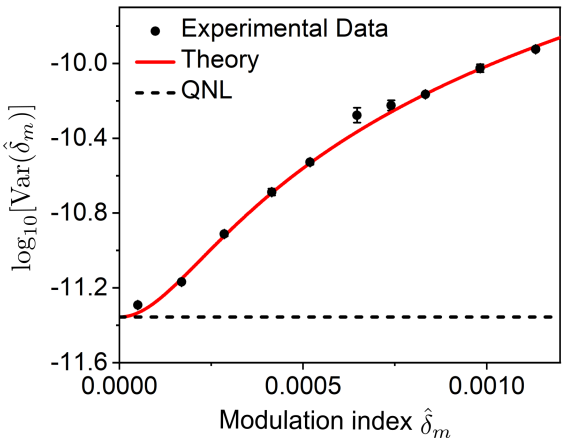

Figure 4.11: Measured variance of the modulation index as a function of $\hat{\delta}_m$.

small. The theoretical fitting in Figure 4.11 corresponds to Equation 4.17 where $\mathrm{Var}(\Re[\mathcal{H}])$ is used as a fitting parameter, and this gives $\mathrm{Var}(\Re[\mathcal{H}]) = 2.3 \pm 0.4 \times 10^{-5}$ with an R-square value of $R_s = 0.996$. Figure 4.11 demonstrates significant divergence from the QNL for high modulation indices, which supports the results from theory and simulation shown in Figure 4.6.

We have seen that under certain conditions it is possible to reach the QNL in the estimation of $\hat{\delta}_m$. Therefore, by varying Φ from antisqueezing to squeezing, it is expected that a quantum advantage in precision may be observed when $\Phi < 1$. From Equation 4.17, we know that $\mathrm{Var}(\hat{\delta}_m)$ is proportional to Φ and inversely proportional to $\langle P \rangle$. However, the profile of squeezing with optical power is such that the shift in power is negligible across the range of squeezing values $[-1.6, 2.7]$ dB of this measurement. Therefore, $\mathrm{Var}(\hat{\delta}_m)$ scales linearly with Φ. By fitting the data for $\mathrm{Var}(\hat{\delta}_m)$ to a linear function, we infer the measured quantum advantage using

$$\mathcal{Q}(\hat{\delta}_m) = \frac{\mathrm{Var}(\hat{\delta}_m)_{QNL}}{\mathrm{Var}(\hat{\delta}_m)_{\Phi}}, \tag{4.23}$$

where $\mathrm{Var}(\hat{\delta}_m)_{QNL}$ is the variance of the modulation index for coherent light inferred from the fitting, and $\mathrm{Var}(\hat{\delta}_m)_{\Phi}$ corresponds to the measured variance in the modulation index for the squeezing parameter Φ. Figure 4.12 shows results for $\mathcal{Q}(\hat{\delta}_m)$ at a range of different levels of squeezing, measured with a 100 kHz RBW. The value of δ_m had a small experimental drift which varied between $\delta_m = [0.8, 1.0] \times 10^{-4}$ over the duration of the measurements. The large RBW means that classical noise contributes negligibly to $\mathrm{Var}(\hat{\delta}_m)$, and the measurement saturates the optimal quantum bound $\mathcal{Q}_{opt}$ given by Equation 4.19 (red curve). A quantum advantage of $\mathcal{Q}(\hat{\delta}_m) = 1.44 \pm 0.09$ is observed with -1.6 dB of squeezing, in agree-

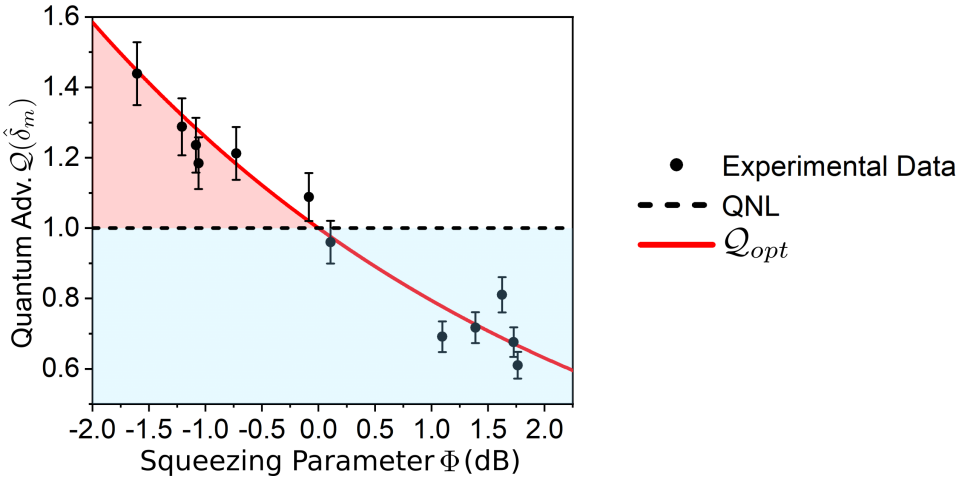

Figure 4.12: Measured quantum advantage in precision of estimated δ_m, $\mathcal{Q}(\hat{\delta}_m)$, for a range of squeezing levels. The red line corresponds to $\mathcal{Q}_{opt}$.

ment with $\mathcal{Q}_{opt} = 1.45$. We therefore demonstrate sub-shot-noise precision in the estimation of δ_m using bright squeezed light. Each measurement of $\mathrm{Var}(\hat{\delta}_m)_\Phi$ is taken from 50 samples of $\hat{\delta}_m$. In Figure 4.12, the error bars indicate the standard deviations over 236 variance measurements.

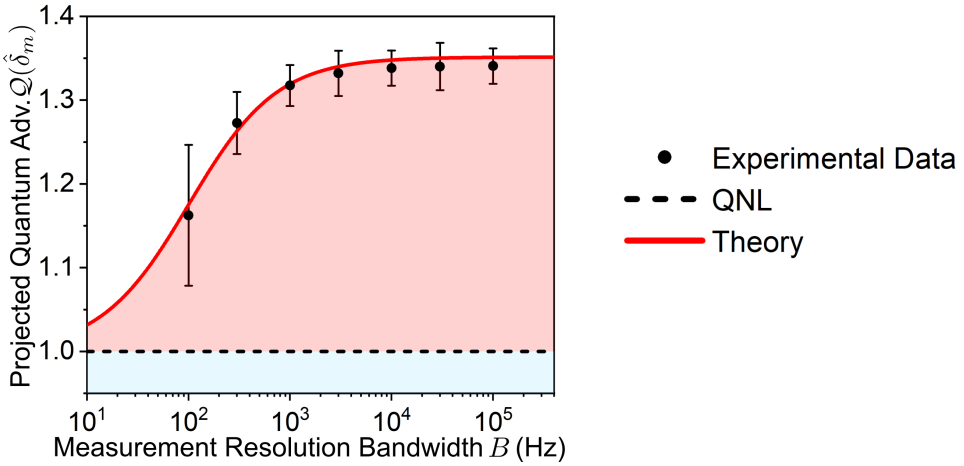

Figure 4.13: Projected $\mathcal{Q}(\hat{\delta}_m)$ for a range of RBWs B, for an average level of -1.3 dB squeezing.

We may also infer the quantum advantage for an arbitrary Φ from the linear fitting of $\mathrm{Var}(\hat{\delta}_m)_\Phi$ with Φ. By doing this for a range of RBWs, we can plot the dependence of $\mathcal{Q}(\hat{\delta}_m)$ on B for $\Phi = -1.3$ dB, which corresponds to the average maximum squeezing value. These results are shown in Figure 4.13, with $\mathrm{Var}(\Re[\mathcal{H}])$ used as a fitting parameter, which gives $\mathrm{Var}(\Re[\mathcal{H}]) = 7 \pm 1 \times 10^{-6}$. The R squared value for this fitting is $R^2 = 0.89$. We demonstrate

sub-QNL precision down to $B = 100$ Hz, with the decreasing $\mathcal{Q}(\hat{\delta}_m)$ at low B due to the increasing relative classical noise contribution. The maximum quantum advantage observed here is $\mathcal{Q}(\hat{\delta}_m) = 1.34 \pm 0.07$, which again closely agrees with the the optimal $\mathcal{Q}_{opt} = 1.35$ for the average squeezing parameter of $\Phi = 0.74$. In Figure 4.13, the error bars were derived from the standard deviations over 10 evaluations of the quantum advantage from separate fittings to the data, where each fitting curve was based on an average of 23 variance measurements for each Φ. The bounds on the quantum advantage for this measurement are determined directly by the squeezing value, and therefore by improving the measured squeezing, significant further enhancement is possible. Optical losses cause a significant degradation in measured squeezing, and we measure a detection efficiency of $\eta_q = 0.84$ and an optical efficiency between the output of the interferometer and the detector of $\eta_{opt} = 0.81$. The maximum squeezing value of -1.6 dB corresponds to -2.6 dB of generated amplitude squeezing, accounting for these additional losses.

4.5 Conclusion

The work presented in this chapter constitutes the first study of enhanced-precision spectral estimation with bright squeezed states of light in the presence of classical laser noise. The only known previous experimental demonstration of enhanced precision estimation with bright squeezed light was found in [9], which shows both sensitivity and precision improvement in particle tracking, and corresponds to a phase measurement. However, our work provides a more detailed analysis by developing a theoretical model for the expected measurement precision, which shows agreement with experiment. Such a quantitative study of precision estimation with squeezed light has been seen before using squeezed vacuum states for phase estimation in [130, 131]. The work shown in this chapter likewise included analysis of the estimator variance for a measurement of AM, using high power amplitude squeezed states of light.

In Section 4.3, the theoretical model was derived for the Fisher information on the modulation index of a modulated optical loss, $\mathcal{F}(\delta_m)$, measured by direct detection at the frequency of the generated optical sideband. We showed that amplitude squeezed states allow us to extract a higher $\mathcal{F}(\delta_m)$ per detected photon. The quantum advantage was found to depend on the generated squeezing, the RBW and the classical laser noise. The amount of low frequency classical noise transferred to the optical sidebands increases with the amplitude of the measured signal. We therefore show that for measurements of high power optical signals, sub-QNL sensitivity does not necessarily imply sub-QNL precision.

In Section 4.4, we presented an experimental demonstration of this estimation procedure. This verified the theoretical model, showing up to a 44% quantum advantage in precision in the estimation of the modulation index, per detected photon. This general demon-

stration motivates applications in areas such as spectroscopy [132] and imaging [133], where precision may determine the performance of the measurement, which can be improved by using squeezed light. Further to this, the theoretical model for the variance of the spectral noise power may be directly applicable to measurements such as Raman spectroscopy [134, 10], which involve the detection of a modulated signal using a high power squeezed probe. Our measurement utilised amplitude squeezed light of 0.2 mW average optical power (25 W peak power) as a probe. This power is comparable to the photon dose required to induce a photophobic response in living cells [103], therefore indicating this technique's relevance to biological measurements. This work opens the way to performing measurements that compete with the optical powers of current classical techniques, but have superior precision and sensitivity beyond the classical limit.

CHAPTER 5

QUANTUM ENHANCED ESTIMATION OF STATIC LOSS WITH BRIGHT SQUEEZED LIGHT

5.1 Introduction

Loss estimation is a ubiquitous tool in optical metrology, and forms the basis of spectroscopy [18] and imaging [19]. It therefore has wide-ranging applicability across science and engineering [19, 135, 136, 137, 138, 139]. Loss estimation is also a particularly simple means of extracting information from a sample, since it involves only direct intensity measurements and therefore does not require phase sensitive detection. However, when the measured loss is small, or when there are restrictions in the probe power or measurement duration, optical noise is a key limiting factor in the performance of such measurements [97]. The loss parameter δ is defined by $\langle P\rangle_{out} = (1-\delta)\langle P\rangle_{in}$, where $\langle P\rangle_{out}$ and $\langle P\rangle_{in}$ are the average optical power before and after the sample respectively. The quantum noise limit for loss estimation is given by $\mathrm{Var}(\delta) = [(1-\delta)/\langle N\rangle]^{1/2}$ [22], for $\langle N\rangle$ average photons in the probe. In the previous chapters, we have shown how squeezed light may be used to reduce the noise of an optical probe below the quantum noise limit. Amplitude squeezing may be used to reduce the optical noise while maintaining the bright intensity of laser light. As discussed in Chapter 4, the probe power sets a bound on the measurement precision, which means that bright amplitude squeezed light is an ideal resource for loss estimation [21].

The quantum noise limit represents a fundamental limit to the precision of loss estimation using classical light. However, unlike in the case of a modulated loss measurement described in Chapter 4, there are many experimental challenges associated with encoding a static loss as an AC signal in a shot noise limited bandwidth. Therefore, measurements of

optical loss are often constrained by excess low frequency classical noise due to the laser or the detection electronics [140, 141].

One approach for reaching the quantum noise limit in the case of molecular absorption measurements is frequency modulation (FM) spectroscopy [126]. This involves modulating the frequency of the laser across the absorption feature of the sample, such that the wavelength modulation is converted into amplitude modulation, which can be detected by a direct intensity measurement. The generated signal at the frequency of modulation is proportional to the sample absorption. Since lasers can be frequency modulated at ~MHz, this allows for an estimation of the absorption which avoids low frequency noise, and therefore high sensitivities can be achieved using this method. However, it also requires a narrow absorption feature for full modulation, which significantly limits its use in more general applications of loss estimation.

Another method which can be used for imaging and spectroscopy is spatial modulation. In this approach, the position of a sample is modulated in and out of the path of a tightly focused laser beam [142]. This is typically achieved by mounting the sample on a piezoelectric stage which is driven with a sinusoidal voltage, but it is also possible to modulate the laser beam. This generates intensity modulation, which can be used to infer the sample absorption. As for FM spectroscopy, the modulation allows for low frequency noise to be significantly avoided. However, the frequency of modulation is commonly limited to ~kHz, which means that this approach is typically still limited by excess classical noise [143]. Furthermore, this strategy is restricted to the detection of nanoparticles [144].

An alternative to such modulation-based techniques is balanced detection of the DC photocurrent [97], whereby the photocurrent measured by two photodiodes is slightly unbalanced by the presence of an absorbing sample. The resulting DC signal can be used to obtain an estimate of the sample absorption. In this case, the excess laser noise is correlated between the two detectors, and this is referred to as common-mode noise. This means that there is significant cancellation of classical noise in the subtraction photocurrent, as described in Section 2.3.2. This technique has enabled imaging of single molecules with sensitivity approaching the quantum noise limit [19]. A significant challenge in this approach is achieving sufficient rejection of common-mode noise, and minimising electronic noise in order to obtain quantum noise limited behaviour at DC.

Photon counting experiments have enabled transmission estimation [23] and imaging [133] with precision surpassing the quantum noise limit. This is typically achieved by using a non-degenerate photon pair source to generate pairs of photons in two separate spatial modes, referred to as the signal and idler beams. The detection of a signal photon is then used to indicate the presence of an idler photon. By placing the sample in the path of the idler beam, and using photon counting devices for timing the arrival of detected photons, a transmission estimate can be obtained by comparing the number of signal and idler

photons detected coincidentally with the total number of detected signal photons. While this approach has allowed for significant quantum precision enhancement [22], such measurements are limited to picowatts of optical power, which restricts the practical applicability of this technique as discussed in Chapter 4.

In this chapter, we describe an experiment which can be used to measure a static optical loss with precision and sensitivity beyond the quantum noise limit using bright amplitude squeezed light. This novel approach enables cancellation of excess laser noise, and allows for detection at MHz frequencies by using resonantly enhanced amplitude modulation. While loss estimation with high power squeezed light has been the subject of theoretical studies [20, 21], the experiment presented here corresponds to the first measurement of a static loss with enhanced precision using amplitude squeezed light. This measurement represents an improvement of 8 orders of magnitude beyond the power limitations of previous measurements of optical loss with quantum enhanced precision [23, 22]. In Section 5.2, we give an overview of theoretical limits in the precision of loss estimation. In Section 5.3, we derive the Fisher information of the measured loss parameter. Section 5.4 describes the experimental scheme and the results obtained for the loss measurement. Section 5.5 concludes the chapter.

Statement of Work

The simulation presented in Figure 5.11 was based on code written by Euan Allen, and analysis of the imaging simulations accordingly resulted from discussions with Euan Allen, Giacomo Ferranti, Alex McMillan and Jonathan Matthews.

5.2 Quantum Limits in Loss Estimation

5.2.1 Direct Detection

Here we will present an analysis of the Fisher information on a transmission parameter $\eta = 1-\delta$ for absorption δ, comparing the strategy of direct detection for laser light with and without the presence of excess laser intensity fluctuations. In the case of an ideal coherent state of initial amplitude $\hat{A}_0(t) = \alpha e^{i\theta} + \hat{a}(t)$, the quantum field amplitude after the transmission η can be written as $\hat{A}(t) = \sqrt{\eta}\alpha e^{i\theta} + \hat{b}(t)$, where $\hat{b}(t) = \sqrt{\eta}\hat{c}(t) + \sqrt{1-\eta}\hat{d}(t)$ for bosonic annihilation operators $\hat{c}(t)$ and $\hat{d}(t)$. Here, we have modelled the loss as a beamsplitter, with $\hat{c}(t)$ corresponding to the transmitted quantum fluctuations of the probe light, and $\hat{d}(t)$ the coupled vacuum mode. A schematic illustrating this strategy is shown in Figure 5.1.

An estimate of η is provided by comparing the DC voltage generated from the photocurrent with and without the presence of the sample, denoted V' and V respectively. Following a similar approach to Section 4.3, here in the time domain, we can write the measured

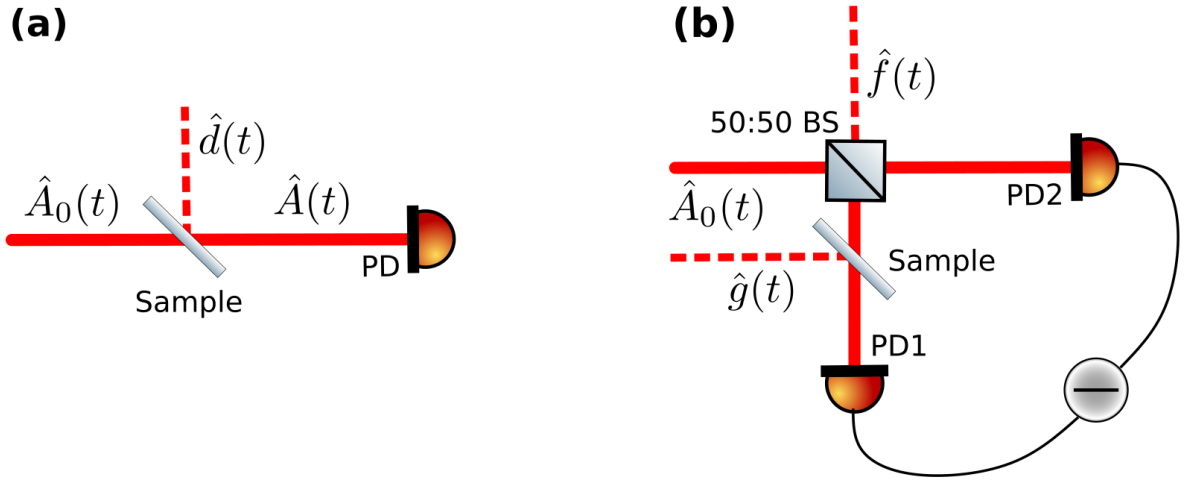

Figure 5.1: Diagrams showing the strategies of direct detection (a) and balanced detection (b) for estimating optical loss. The dashed lines indicate vacuum ports.

voltage U in terms of the photocurrent $\hat{i}(t)$ as

$$U = \frac{R}{T}\int_0^T \hat{i}(t)dt, \tag{5.1}$$

for a measurement over a time interval T, using a measuring device with resistance R. The time domain photocurrent for the detected light after propagating through the sample can be written as

$$\hat{i}(t) = q\hat{A}(t)^\dagger \hat{A}(t) \approx q\left(\eta\alpha^2 + \sqrt{\eta}\alpha\left[\hat{b}(t)e^{-i\theta} + \hat{b}(t)^\dagger e^{i\theta}\right]\right), \tag{5.2}$$

where terms quadratic in the creation/annihilation operators have been neglected. The resulting expected values of the measured voltages are $\langle V'\rangle = qR\eta\alpha^2$ with the sample and $\langle V\rangle = qR\alpha^2$ without the sample. The transmission estimate $\hat{\eta}$ is then given by

$$\hat{\eta} = \frac{V'}{V}, \tag{5.3}$$

where the caret indicates that $\hat{\eta}$ is an estimator. We can also assume that the value of V can be precalibrated with high precision. The variance of the measured voltage with the sample in place is

$$\begin{aligned}\mathrm{Var}(V') = \langle V'^2\rangle - \langle V'\rangle^2 &= \frac{R^2}{T^2}\int_0^T\int_0^T \langle \hat{i}(t)\hat{i}(t')\rangle dtdt' - \frac{R^2}{T^2}\int_0^T\int_0^T \langle \hat{i}(t)\rangle\langle \hat{i}(t')\rangle dtdt' \\ &= \frac{q^2R^2\eta\alpha^2}{T^2}\int_0^T\int_0^T \langle \hat{b}(t)\hat{b}(t')e^{-2i\theta} + \hat{b}(t)\hat{b}(t')^\dagger + \hat{b}(t)^\dagger\hat{b}(t') + \hat{b}(t)^\dagger\hat{b}(t')^\dagger e^{2i\theta}\rangle dtdt' \\ &= \frac{q^2R^2\eta\alpha^2}{T^2}\int_0^T\int_0^T \delta(t-t')dtdt' = \frac{q^2R^2\eta\alpha^2}{T}.\end{aligned} \tag{5.4}$$

For large photon numbers, the statistics of the measured voltage are normally distributed, and the Fisher information on the voltage saturates the Cramér-Rao bound [129]: $\mathcal{F}(V') = \mathrm{Var}(V')^{-1}$. Therefore, the Fisher information on the transmission parameter, $\mathcal{F}(\eta)$, can be calculated:

$$\mathcal{F}(\eta) = \left(\frac{\partial\langle V'\rangle}{\partial\eta}\right)^2 \mathcal{F}(V') = \left(\frac{\partial\langle V'\rangle}{\partial\eta}\right)^2 \frac{1}{\mathrm{Var}(V')} = \frac{T\alpha^2}{\eta} = \frac{\langle N\rangle}{\eta}, \tag{5.5}$$

where $\langle N\rangle = T\alpha^2$ corresponds to the number of photons detected in time T. As expected, this bound is identical to the quantum Fisher information on a loss parameter for a coherent state [128], meaning direct detection is an optimal measurement strategy for loss estimation in the absence of excess laser noise.

We now relax the assumption of an ideal coherent state, and include a classical amplitude noise term $\zeta(t)$. The quantum amplitude can then be written as $\hat{A}(t) = (1+\zeta(t))\sqrt{\eta}\alpha e^{i\theta} + \hat{b}(t)$. In this case, we obtain the following expression for $\hat{i}(t)$:

$$\hat{i}(t) = q\hat{A}(t)^\dagger\hat{A}(t) \approx q\left(\eta\alpha^2 + \sqrt{\eta}\alpha\left[\hat{b}(t)e^{-i\theta} + \hat{b}(t)^\dagger e^{i\theta}\right]\right) + 2\eta\alpha^2\zeta(t). \tag{5.6}$$

The variance of the voltage measurement then gives the result:

$$\mathrm{Var}(V') = \langle V'^2\rangle - \langle V'\rangle^2 = \frac{q^2R^2\eta\alpha^2}{T} + \frac{4\alpha^4\eta^2R^2}{T^2}\int_0^T\int_0^T \langle\zeta(t)\zeta(t')\rangle dt dt'. \tag{5.7}$$

For a typical laser, the second term of this expression will dominate due to the slow intensity fluctuations [96], and therefore direct detection will no longer saturate the bound given by Equation 5.5.

5.2.2 Balanced Detection

Due to the effect of classical intensity fluctuations discussed in Section 5.2.1, direct detection does not provide an optimal strategy for transmission estimation using classically-noisy laser light. However, a strategy that may be used to overcome these intensity fluctuations is balanced detection [145]. Here, the optical power is evenly split between two photodiodes, and the sample is placed in the path to one of the photodiodes. A differential measurement of the photocurrent of the two photodiodes is then made. Since the classical intensity fluctuations are correlated between the two detectors, this strategy can reject a significant fraction of the excess laser noise in the limit of small losses ($\delta \ll 1$). Furthermore, by using a transimpedance-amplified balanced photodetector, the electronic subtraction of the photocurrents occurs before amplification, meaning that it is not necessary to precisely match the electronic properties of two separate amplifiers [95]. We label the photocurrents generated by photodiodes PD1 and PD2 as $\hat{i}_1(t)$ and $\hat{i}_2(t)$ respectively, with the sample placed in the path of PD1 as illustrated in Figure 5.1. Writing the quantum amplitude of the state

before the 50:50 beamsplitter as $\hat{A}(t) = \alpha e^{i\theta} + \hat{e}(t)$, the photocurrent measured by the two detectors are:

$$\hat{i}_1(t) = \frac{\alpha^2}{2} + \sqrt{\frac{1}{2}}\alpha\hat{b}(t)e^{-i\theta} + \sqrt{\frac{1}{2}}\alpha\hat{b}(t)^\dagger e^{i\theta} + \alpha^2\zeta(t), \tag{5.8}$$

$$\hat{i}_2(t) = \frac{\eta\alpha^2}{2} + \sqrt{\frac{\eta}{2}}\alpha\hat{c}(t)e^{-i\theta} + \sqrt{\frac{\eta}{2}}\alpha\hat{c}(t)^\dagger e^{i\theta} + \eta\alpha^2\zeta(t). \tag{5.9}$$

In this case, we can denote the quantum amplitudes as $\hat{b}(t) = \sqrt{1/2}\left(\hat{e}(t) + \hat{f}(t)\right)$ and $\hat{c}(t) = \sqrt{\eta/2}\left(\hat{e}(t) - \hat{f}(t)\right) - \sqrt{1-\eta}\hat{g}(t)$, where $\hat{f}(t)$ and $\hat{g}(t)$ correspond to the vacuum fluctuations coupled from the 50:50 beamsplitter and the applied loss respectively. This results in a difference photocurrent of

$$\hat{i}_-(t) = (1-\eta)\frac{\alpha^2}{2} + \frac{\alpha e^{-i\theta}}{\sqrt{2}}\left(\hat{b}(t) - \sqrt{\eta}\hat{c}(t)\right) + \frac{\alpha e^{i\theta}}{\sqrt{2}}\left(\hat{b}(t)^\dagger - \sqrt{\eta}\hat{c}(t)^\dagger\right) + (1-\eta)\alpha^2\zeta(t). \tag{5.10}$$

The resulting expectation value of the subtraction voltage with the sample in place is $\langle V_-\rangle = qR\alpha^2(1-\eta)/2$, as compared the total voltage of $\langle V\rangle = qR\alpha^2$. Therefore, an estimator for the transmission parameter may be written as

$$\hat{\eta} = \frac{V - 2V_-}{V}. \tag{5.11}$$

The variance of the voltage resulting from the subtraction photocurrent, V_-, is

$$\begin{aligned}\mathrm{Var}(V_-) = \langle V_-^2\rangle - \langle V_-\rangle^2 &= \frac{R^2}{T^2}\int_0^T\int_0^T \langle\hat{i}_-(t)\hat{i}_-(t')\rangle dt dt' - \frac{R^2}{T^2}\int_0^T\int_0^T \langle\hat{i}_-(t)\rangle\langle\hat{i}_-(t')\rangle dt dt' \\ &= \frac{q^2R^2(1-\eta)^2\alpha^4}{T^2}\int_0^T\int_0^T \langle\zeta(t)\zeta(t')\rangle dt dt' + \frac{q^2R^2\alpha^2(1+\eta)}{2T}.\end{aligned} \tag{5.12}$$

In the case that the loss of the sample is small ($\delta = 1-\eta \ll 1$), the classical noise term in Equation 5.12 is negligible in comparison to the quantum noise term, resulting in

$$\mathrm{Var}(V_-) \approx \frac{q^2R^2\alpha^2}{T}, \tag{5.13}$$

as expected due to voltage fluctuations from optical shot noise. As before, it may be assumed that V can be precalibrated with high precision. The resulting Fisher information in the case of balanced detection of a small optical loss is

$$\mathcal{F}(\eta) = \left(\frac{\partial\langle V_-\rangle}{\partial\eta}\right)^2\mathcal{F}(V_-) = \left(\frac{\partial\langle V_-\rangle}{\partial\eta}\right)^2\frac{1}{\mathrm{Var}(V_-)} \approx \frac{\langle N\rangle}{4}. \tag{5.14}$$

This result is expected since half of the measured light does not interact with the sample. Therefore, as well as the effective number of probe photons being halved, there is a shot noise contribution from the light measured by both detectors, leading to the factor of 4 difference to the Fisher information obtained with direct detection using a coherent state.

5.3 Estimation of a Static Loss with Squeezed Light

While balanced detection is a useful method for detecting an optical loss using laser light, there are some significant limitations with this measurement strategy. Firstly, it requires shot noise limited behaviour at DC, which is technically challenging due to the high electronic noise typically observed at low frequencies. This makes balanced detection particularly difficult when using low probe powers (μW) [97], where the shot noise clearance is significantly reduced. It also relies on the detector having a high common mode rejection ratio, in order for excess laser noise not to be amplified by the detection electronics. Furthermore, this strategy is fundamentally limited by shot noise, since, as discussed in Section 2.3.2, any noise reduction due to quantum correlations such as squeezing is removed when measuring the subtraction photocurrent. While strategies such as wavelength modulation [126] or spatial modulation of the sample [142] overcome these problems of low frequency noise, they typically demand very specific properties of the sample. Absorption measurements using wavelength modulation, for example, require the sample to have a narrow absorption feature. In the case of spatial modulation strategies, the diameter of the sample must be much smaller than the wavelength of the light [142]. This motivates the need for a measurement strategy which avoids the effects of low frequency electronic noise and classical intensity fluctuations, and for which bright squeezed light may provide a precision advantage, but which does not place such restrictions on the measured sample. In this section, such a scheme is proposed, which employs path modulation of amplitude squeezed light.

For this strategy, amplitude modulation is required in order to encode information on the static transmission parameter η in a shot noise limited bandwidth. By using a modulator which is resonantly enhanced to allow $\delta_m = 1$, the maximum amount of power is transferred to the signal. Resonant modulators use an LC circuit with a fixed resonant frequency to significantly reduce the voltage required for full modulation. However, as discussed in Chapter 4, a direct measurement of a fully amplitude modulated signal will be dominated by the intensity noise transferred to the sideband. Here, amplitude modulated light on both output ports of a PBS is recombined by using a second PBS, before being measured by direct detection, as shown in Figure 5.2. A sample of transmission η is placed on one of the output ports of PBS1. Since the amplitude modulation generated on each output of PBS1 will be π out of phase, the modulation of the combined signal will cancel out when $\eta = 1$. When $\eta < 1$, the imbalance in the modulation due to the loss generates a signal in the measured photocurrent at the modulation frequency. This scheme essentially corresponds to a modulation of the path of the probe light between the two ports of PBS1. However, in contrast to the spatial modulation scheme described in Section 5.1, this does not require mechanical modulation of the sample position, and can therefore achieve much higher modulation frequencies. Similarly to balanced detection, the contribution of laser

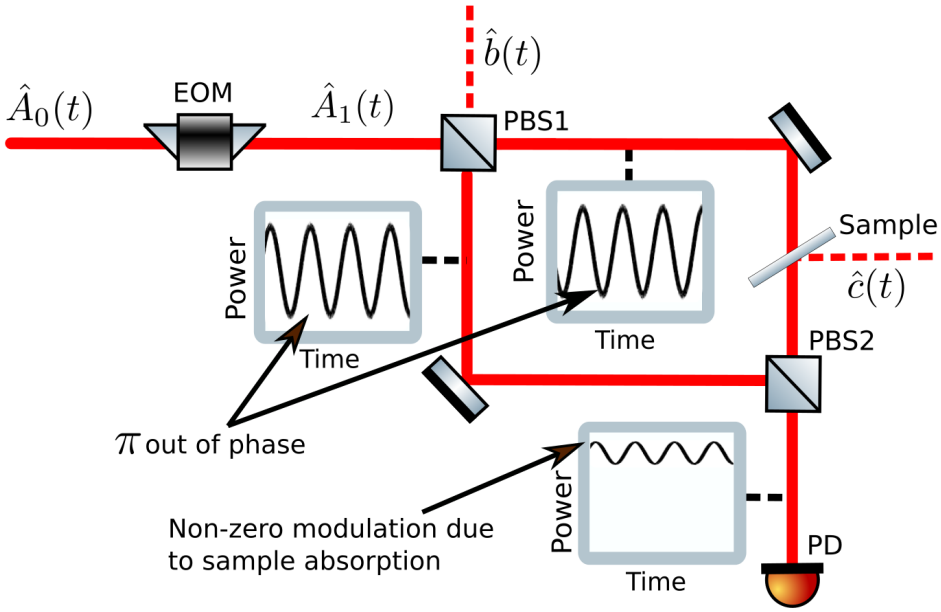

Figure 5.2: Schematic of the quantum enhanced loss estimation measurement. The electro-optic modulator (EOM) fully modulates the polarisation of the amplitude squeezed state $\hat{A}_0(t)$, which leads to path modulation between the two output ports of PBS1. With a sample placed before PBS2, the loss causes an imbalance in the modulation. This generates a signal at the modulation frequency which is proportional to the applied loss, and is detected by the photodiode (PD). The dashed lines indicate vacuum ports.

intensity noise to the variance of this signal will be negligible if the applied loss is small. Furthermore, if the input state is amplitude squeezed, the squeezing is not significantly degraded by the modulation for a small loss. Therefore, amplitude squeezing may be used to enhance the precision of the transmission estimate. In Appendix B.1, the signal-to-noise ratio of the measured photocurrent is shown to be

$$\delta_{SNR} = \frac{i_0 \delta_m^2 (1-\eta)^2}{16 q \Phi B}, \tag{5.15}$$

for DC photocurrent i_0, modulation index δ_m, squeezing parameter Φ, and resolution bandwidth B. From Equation 5.15, the estimator for the transmission of the sample can then be written as

$$\hat{\eta} = 1 - \sqrt{\frac{16 q \Phi B \hat{\delta}_{SNR}}{i_0 \delta_m^2}}, \tag{5.16}$$

where $\hat{\delta}_{SNR}$ and i_0 can be estimated according to Equation 4.11 in Chapter 4, and the values of δ_m, $\langle P \rangle$ and p_N may all be precalibrated. In Appendix B.2, the variance of the

power of the electronic sideband for M spectral averages is derived to be

(5.17)
$$\mathrm{Var}(p_\Omega) \approx \frac{R^2}{M}\left[\frac{1}{2}q\delta_m^2(1-\eta)^2 i_0^3 \Phi B + \frac{1}{4}\delta_m^4(1-\eta)^4 i_0^4 \mathrm{Var}(\Re[\mathcal{H}]) + q^2\delta_m^2(1-\eta)^2 i_0^2 \mathrm{Var}(\Re[\mathcal{N}])\right].$$

The Fisher information on the transmission parameter can then be derived from

$$\mathcal{F}(\eta) = \left(\frac{\partial \delta_{SNR}}{\partial \eta}\right)^2 \mathcal{F}(\delta_{SNR}), \tag{5.18}$$

where $\mathcal{F}(\delta_{SNR})$ can be obtained using Equation 4.14 as before. Neglecting the electronic noise term, this gives the result:

$$\mathcal{F}(\eta) = M\left[\frac{8q\Phi B}{i_0\delta_m^2} + 4(1-\eta)^2\mathrm{Var}(\Re[\mathcal{H}])\right]^{-1}. \tag{5.19}$$

We note that both Equation 5.16 and Equation 5.19 rely on the assumption that the applied loss is small, i.e. $\delta \ll 1$, such that the effect of the loss on the quantum fluctuations can be neglected. In the limit that the classical noise term in Equation 5.19 may also be neglected, Equation 5.19 can be written as

$$\mathcal{F}(\eta) = \frac{M\langle N\rangle \delta_m^2}{8\Phi}, \tag{5.20}$$

where $\langle N\rangle$ is the average number of detected photons in the measurement time B^{-1}. With no squeezing, full modulation and no spectral averaging, this is a factor of 2 lower than the bound for balanced detection, since the DC signal is not measured. We can also define the Fisher information per photon incident on the sample $\mathcal{F}'(\eta) = \mathcal{F}(\eta)/\langle N_s\rangle$, where $\langle N_s\rangle = \langle N\rangle/2$ is the average number of photons propagating through the sample in the measurement time B^{-1}. This is a useful metric since the number of photons is often limited by optical power which the sample can be exposed to. Using Equation 5.20, assuming full modulation and no spectral averaging, this gives $\mathcal{F}'(\eta) = 1/4\Phi$. We can compare this to the result of $\mathcal{F}'(\eta) = 1/\Phi$ obtained for a squeezed coherent state, using direct detection. Due to the low frequency noise observed on realistic sources of bright squeezed light, we can conclude that our measurement strategy provides a practical means of detecting an optical loss, using amplitude squeezed light as a probe.

The variance of the estimate $\hat{\eta}$ using this strategy can also be derived as

$$\mathrm{Var}(\hat{\eta}) = \left(\frac{\partial\langle\hat{\eta}\rangle}{\partial\langle p_\Omega\rangle}\right)^2 \mathrm{Var}(p_\Omega) = \frac{1}{F(\eta)}. \tag{5.21}$$

The estimator therefore corresponds to a minimum-variance estimator for this measurement strategy.

In Figure 5.3, $\mathcal{F}(\eta)$ is plotted as a function of the applied modulation depth. The solid black curve corresponds to Equation 5.20, for $i_0 = 0.2$ mA, $\Phi = 1$, and $B = 1$ MHz. The

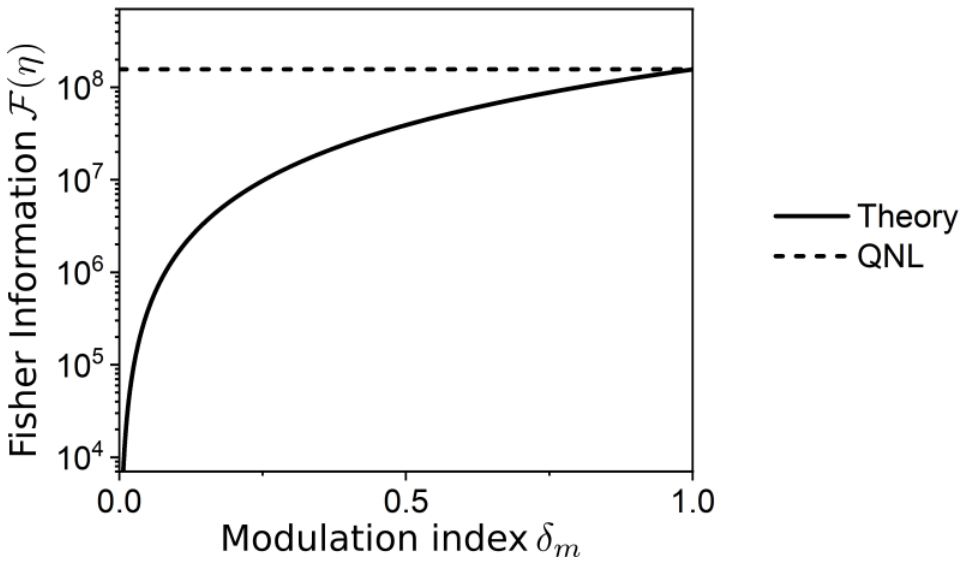

Figure 5.3: Theoretical model of the Fisher Information $\mathcal{F}(\eta)$ versus the applied modulation depth δ_m for shot noise limited laser light, for the measurement strategy described in Figure 5.2.

QNL is defined by $\mathcal{F}(\eta)_{QNL} = i_0/8qB$, i.e. the maximum value of $\mathcal{F}(\eta)$ for $\Phi = 1$. The best performance is achieved for $\delta_m = 1$ because the applied modulation determines the number of signal photons transferred to the measured sideband.

An equivalent strategy could be implemented by measuring the addition photocurrent of two photodiodes placed on each output port of PBS1, with the sample placed in the path to one of the photodiodes. This strategy is illustrated in Figure 5.4. This approach simplifies the optical arrangement, and the fewer optical components will mean that a lower total loss will be applied to the squeezed light. However, similarly to balanced detection, it would require careful balancing of the current generated by each photodiode. This challenge could be partially overcome by connecting the photodiodes in parallel, such that the addition of the photocurrents occurs before amplification. This would avoid the requirement of needing to balance the gain properties of separate amplifiers, as for balanced transimpedance-amplified photodetectors [95]. However, the efficiency of the two photodiodes would still need to be closely matched in order to achieve sufficient rejection of the common-mode signal. Therefore, the strategy illustrated in Figure 5.2 is used for the experimental demonstration here.

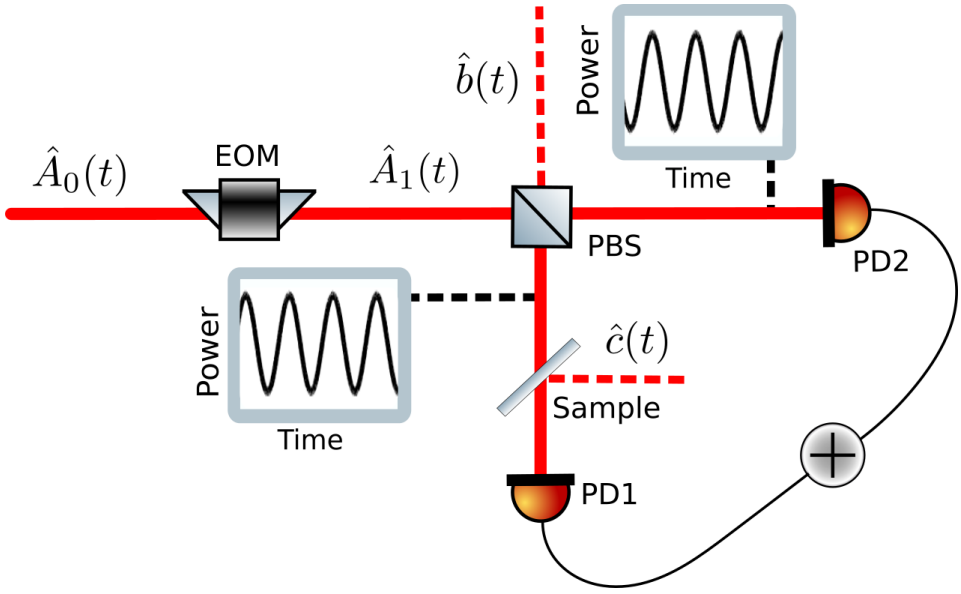

Figure 5.4: Alternative strategy for static loss estimation by measuring the addition photocurrent of amplitude modulated light on both output ports of PBS1. The presence of the sample before PD1 leads to a residual signal at the modulation frequency, which can be used to estimate the loss of the sample.

5.4 Experimental Implementation

5.4.1 Quantum Enhanced Loss Estimation

The form of Equation 5.17 is similar to that of Equation 4.13 for the detection of amplitude modulation. By comparing these equations, we expect that, for small values of loss, and large RBWs, a quantum advantage may be achieved with this measurement strategy using the source described in Chapter 3. A diagram of the experimental setup is shown in Figure 5.5. As before, the power of the amplitude squeezed light is 0.2 mW, generated using 14 m of PCF. In order to obtain optimal amplitude modulation ($\delta_m \approx 1$), the polarisation state of the incident light must be extremely pure, with a visibility $\sim 100\%$. A Thorlabs GT5-B Glan-Taylor (GT) polariser was used to achieve this. By placing a QWP on the output of the Sagnac interferometer (QWP1), the ellipticity in the polarisation of the squeezed light is largely removed. HWP3 then rotates axis of polarisation to align with the transmission port of the GT polariser. QWP1 and HWP3 therefore together minimise the loss on the light transmitted through the GT. Following the GT, QWP2 is used to generate circular polarisation. This reduces the voltage required to modulate between horizontal and vertical polarisation states, and means that full amplitude modulation can be observed on the output ports of PBS1 without applying a DC bias to the modulator. The EOM used is a custom Qubig AM7-NIR amplitude modulator, which is resonantly enhanced for modulation

at 10 MHz. A Thorlabs TED200C temperature controller is used to stabilise the modulation. An AR coated N-BK7 glass window with $\eta = 0.98 \pm 0.01$ is used to provide the optical loss, with the exact transmission dependent on its orientation. Due to the modulation, the average probe power incident on the sample is 0.1 mW, i.e. half of the power of the generated amplitude squeezing. The light is recombined by PBS2, and the amplitude modulation observed on the output of PBS2 will be proportional to the applied loss. This signal is detected by a single photodiode of the Thorlabs PDB440A(-AC) balanced detector, and the photocurrent is analysed by the Rohde & Schwarz FPC1000 spectrum analyser (SA).

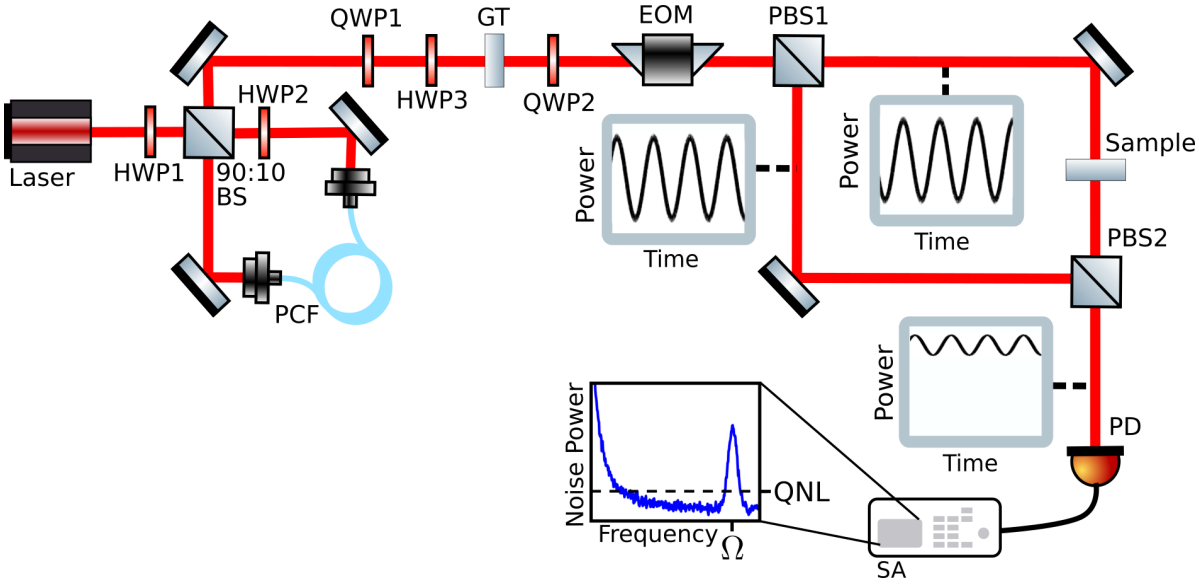

Figure 5.5: Schematic diagram of the loss estimation experiment. Pulsed laser light at 740 nm propagates into the Sagnac interferometer, generating 0.2 mW of amplitude squeezed light. The polarisation extinction of the probe light is optimised using a Glan-Taylor polariser (GT), and the transmission through the GT is maximised using QWP1 and HWP3. QWP2 is used to circularly polarise the light incident on the EOM. The light on each output port of the PBS is amplitude modulated with $\delta_m \approx 1$. A detector on the output port of PBS2 generates a photocurrent from the combined signal, which is analysed using an electronic spectrum analyser (SA).

As discussed in Section 5.3, the applied modulation must be $\delta_m \approx 1$ in order to saturate the quantum noise limit for this measurement strategy. To verify that sufficient modulation is provided by the EOM, a measurement of δ_m was made by blocking one port of PBS1, such that full amplitude modulation is observed on the output of PBS2. However, since this level of AC power is too high to be measured with the spectrum analyser, an oscilloscope was used for this measurement of δ_m. The results of this measurement are shown in Figure 5.6, and demonstrate the expected sinusoidal modulation predicted by Equation B.6 of Appendix B.1. The fitting curve gives an average voltage modulation am-

plitude of $V_{pk} = 0.918 \pm 0.001$ V. Using the quantum efficiency of $\eta_q = 0.84$ inferred from Figure 3.7, the quoted transimpedance gain of $G = 51 \times 10^3$ V/A, and the measured average power of $\langle P \rangle = 73.7$ μW, we infer a value of $\delta_m = 2V_{pk}\hbar\omega/\langle P \rangle Gq\eta_q = 0.976 \pm 0.001$. This value is sufficiently close to full amplitude modulation such that squeezing may allow for precision enhancement beyond the quantum noise limit.

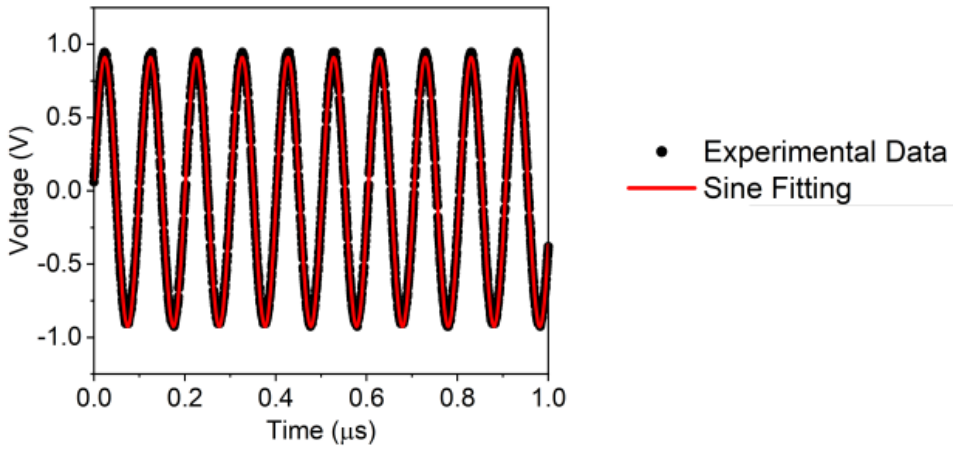

Figure 5.6: Trace of the detected voltage as a function of time, showing 10 MHz modulation. The red curve is a sine fitting, from which we infer a modulation depth of $\delta_m = 0.976 \pm 0.001$.

This was achieved by applying a sinusoidal voltage with an amplitude $V_p = 8.6$ V and an optimal frequency of 9.92 MHz to the modulator. A limitation of this measurement is that the voltage data was acquired using the AC coupled RF port of the detector. This means that inferring δ_m requires a reliable measurement of η_q. With a DC coupled detector, a relative voltage measurement could be used to determine δ_m with more accuracy.

To verify that the power spectrum of the detected light behaves as expected from Equation B.15 in Appendix B.1, a trace was measured with and without the presence of the N-BK7 loss sample, using a coherent state as a probe. This data is shown in Figure 5.7. This measurement was taken with a resolution bandwidth of $B = 1$ MHz. The red trace corresponds to the case with the sample in place, and gives rise to a peak in the power at $f = 10$ MHz, as expected from Equation B.15. The blue trace was measured without the sample in place, and the signal is significantly removed. However, a slight peak may still be observed in the blue trace at 10 MHz. This is because there is not complete cancellation of the modulation signal, since there will be a slight imbalancing due to time-dependent variations in the coupling of the two paths into the photodetector. This effect may be treated in a similar manner to common-mode rejection in balanced detection. The results shown in Figure 5.7 demonstrate a 58 dB suppression of the common-mode signal, which is comparable with purpose-built balanced detectors [97]. The bias in the measurement resulting from the incomplete common mode rejection is $\text{Bias}(\hat{\eta}) \approx 1 \times 10^{-6}$, which is 2 orders of magnitude

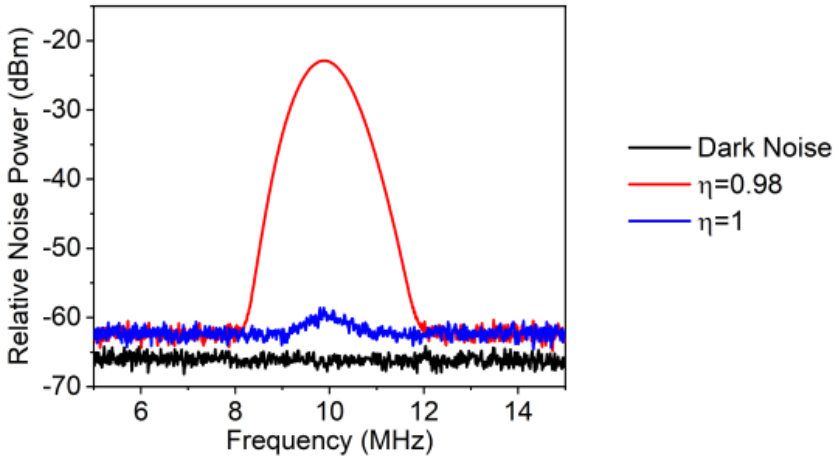

Figure 5.7: Trace of the detected noise power using the setup shown in Figure 5.5. The red trace was obtained using a transmission of $\eta = 0.98$, and the blue trace was measured without a sample in place. The black trace corresponds to the dark noise of the detector.

smaller than the error due to the shot noise contribution for 0.2 mW of detected power, according to Equation 5.20. The effect of the imbalancing is therefore not large enough to lead to a significant bias in the transmission estimation, although this bias will lead to a more significant error for smaller losses. However, it may result in an increase of the classical noise contribution to the variance of the measurement. This demonstrates that an improvement to this measurement strategy could be made by further increasing the resolution bandwidth, since this would reduce the effect of the imbalancing on the measurement bias and variance relative to the effect of quantum noise. However, because the frequency of the signal is fixed at the 10 MHz resonant frequency of the EOM, increasing the RBW beyond 1 MHz leads to distortion of the signal. Therefore for this experiment, the maximum RBW used was $B = 1$ MHz.

From Equation 5.21, it is expected that, with a RBW of $B = 1$ MHz, the variance of the transmission estimate will scale linearly with the squeezing parameter. A measurement of $\mathrm{Var}(\hat{\eta})$ as a function of the squeezing parameter Φ_{dB} is shown in Figure 5.8. This data was taken using RBW of $B = 1$ MHz and a VBW of $B_V = 100$ kHz. The average value of $\hat{\eta}$ observed across the range of squeezing values is $\hat{\eta} = 0.9816 \pm 0.0007$, which is in close agreement with the approximate $\eta = 0.98 \pm 0.01$ obtained using a powermeter. The black dashed line is a linear fitting from Equation 5.21, using the experimentally measured values and a single fitting parameter for $\mathrm{Var}(\Re[\mathcal{H}])$. This fitting gives $\mathrm{Var}(\Re[\mathcal{H}]) = 8.0 \pm 0.6 \times 10^{-6}$, which is consistent with the value of $\mathrm{Var}(\Re[\mathcal{H}]) = 7 \pm 1 \times 10^{-6}$ inferred from the amplitude modulation measurement in Chapter 4. The solid black curve corresponds to the CRB for this measurement strategy, i.e. the predicted variance for this measurement according to the bound given by Equation 5.20. Each measurement of $\hat{\eta}$ was taken from an average of 50

spectrum analyser measurements, and the error bars in Figures 5.8 and 5.9 indicate the standard deviations over 23 variance measurements. While the experimental results are

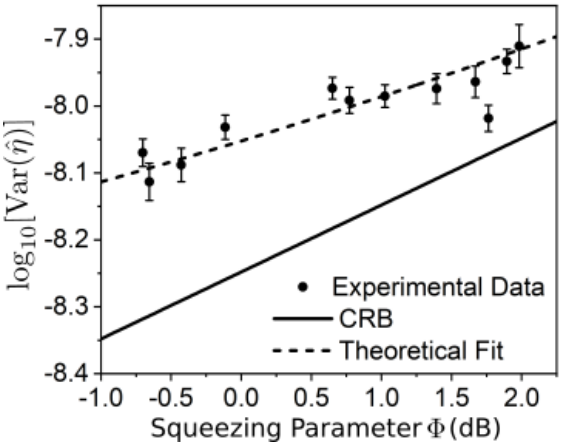

Figure 5.8: Experimentally measured $\mathrm{Var}(\hat{\eta})$ as a function of squeezing. The dashed line is a linear fitting and the solid black line corresponds to the CRB given by Equation 5.20.

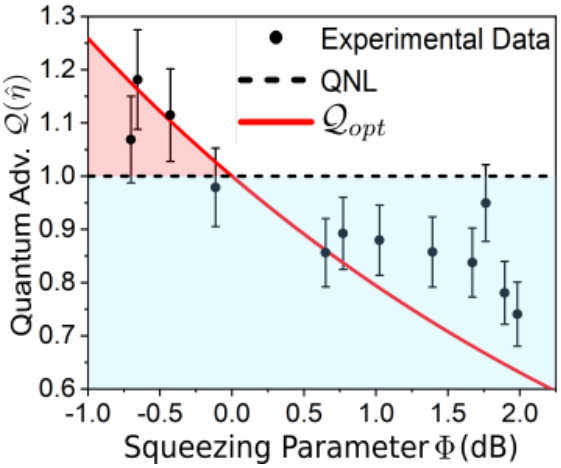

Figure 5.9: Experimentally measured quantum precision advantage as a function of squeezing. The red curve corresponds to $\mathcal{Q}_{opt}$.

close to the CRB, the small constant offset observed is characteristic of classical noise on the signal. Figure 5.9 shows the achieved quantum advantage as a function of squeezing for the same data as shown in Figure 5.8. The quantum advantage is defined as the ratio between the variance at $\Phi_{dB} = 0$ dB inferred from the linear fitting with the measured variance for squeezing parameter Φ:

$$\mathcal{Q}(\hat{\eta}) = \frac{\mathrm{Var}(\hat{\eta})_{QNL}}{\mathrm{Var}(\hat{\eta})_{\Phi}}. \tag{5.22}$$

The red curve indicates $\mathcal{Q}_{opt} = 1/\Phi$. While the experimental data shows a similar scaling with squeezing to $\mathcal{Q}_{opt}$, the observed divergence from this bound is due to the classical noise as shown in Figure 5.8. The effect of classical noise in Figure 5.9 is to flatten the linear trend of $\mathcal{Q}(\hat{\eta})$ with Φ, meaning that the data points are shifted closer to the QNL. Nonetheless, a maximum quantum advantage of $\mathcal{Q}(\hat{\eta}) = 1.2 \pm 0.1$ is observed with -0.7 dB of squeezing, and the scaling of $\mathcal{Q}(\hat{\eta})$ with the squeezing parameter demonstrates that this strategy provides an effective method of estimating a static optical loss with quantum enhanced precision. Furthermore, the proximity of the measured $\mathrm{Var}(\hat{\eta})$ to the CRB shows that this method is comparable to the fundamental bound for loss estimation using an amplitude squeezed probe of the same average power.

It is possible to further test the agreement with the theoretical model for $\mathrm{Var}(\hat{\eta})$ by measuring how $\mathcal{Q}(\hat{\eta})$ varies with RBW. Since there is a greater fraction of optical power

in the sideband than for the measurements of amplitude modulation in Chapter 4, it is expected that higher RBWs will be required to achieve significant quantum precision enhancement than for the measurements shown in Figure 4.13 in Chapter 4. The results for $\mathcal{Q}(\hat{\eta})$ as a function of B are shown in Figure 5.10, for an average squeezing parameter of $\Phi_{dB} = -1$ dB. The maximum quantum advantage at $B = 1$ MHz is $\mathcal{Q}(\hat{\eta}) = 1.18 \pm 0.05$. The

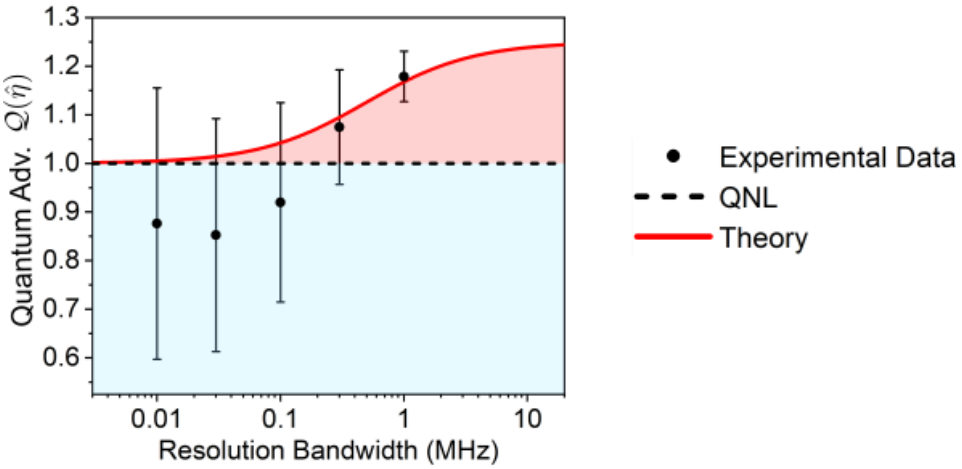

Figure 5.10: Inferred $\mathcal{Q}(\hat{\eta})$ from experimentally measured $\mathrm{Var}(\hat{\eta})$ as a function of RBW, for an average of $\Phi_{dB} = -1$ dB squeezing. The error bars were derived from the standard deviation over 23 separate fittings to the data, where each fitting corresponds to a single variance measurement.

red curve is a theoretical fitting, which infers a value for the classical amplitude noise of $\mathrm{Var}(\Re[\mathcal{H}]) = 2 \pm 1 \times 10^{-5}$. Due to the increased relative contribution of classical noise for low RBW, $B = 1$ MHz corresponds to the only RBW at which a significant quantum advantage is observed. The R squared value for this fitting is $R^2 = 0.75$. The fitting of this model to the data is therefore worse than the equivalent fitting shown Figure 4.13. However, this is expected due to the lower squeezing value achieved here, and also since the RBW is limited to a maximum value of $B = 1$ MHz. The error bars increase for smaller RBWs because the increased classical noise contribution means that the quantum precision enhancement is negligible compared to the measurement uncertainty. The results shown in Figures 5.8-5.10 indicate that the quantum advantage could be further improved by using a higher RBW, which would require increased detection bandwidth and higher frequency modulation. While further improvement in the confidence of this fitting could be obtained by using more narrowly spaced RBWs, heterodyne spectrum analysers typically only allow values of $B \in \{1, 3\} \times 10^n$Hz for integer n, meaning that these data points are therefore as closely spaced as possible. From Figure 5.10, we expect that the measurement would saturate $\mathcal{Q}_{opt}$ by using a RBW of $B = 10$ MHz. The lower average squeezing observed in this experiment is a direct result of the loss generated by the additional optical components required for static

loss estimation. The transmission measured between the output of the Sagnac interferometer and the detector is $\eta_{opt} = 0.71$, as compared to $\eta_{opt} = 0.81$ for the amplitude modulation experiment described in Chapter 4. Accounting for the detector efficiency of $\eta_q = 0.84$, this implies that the average level of generated amplitude squeezing is $\Phi_{dB} = -1.8$ dB. Despite the lower squeezing observed, these results demonstrate a significant quantum advantage in the estimation of η.

5.4.2 Towards Quantum Imaging with Bright Squeezed Light

Direct absorption imaging is a common application of transmission estimation [19, 146], and here we consider the potential applicability of the measurement strategy outlined in Section 5.3 to quantum enhanced imaging. This would involve raster scanning the sample across the path of the laser beam, and making a single transmission measurement at each sample position, as in [133]. Raster scanning is necessary since only a single spatial mode is squeezed: in order to directly observe quantum noise reduction across multiple pixels without raster scanning, it would be necessary to populate each independent spatial mode with quantum correlated photons [147]. To increase imaging resolution, a microscope arrangement could be used to focus the squeezed light on the sample.

Both sensitivity and precision determine the performance of such an imaging measurement. Sensitivity is characterised by the minimum detectable absorption due to the pixel noise floor. Image quality is therefore limited by sensitivity when the signal at a given pixel is comparable with the noise floor, such that the signal can become obscured by the noise floor. Precision in imaging is determined by the pixel error, and therefore limits image quality when the contrast between pixels is comparable with the pixel error due to fluctuations in the signal. In studies of quantum imaging using photon pair sources, the measurement is performed in the time domain, and therefore the pixel error typically corresponds directly to the pixel noise floor. Accordingly, both sensitivity [146] and precision [133] have been used to characterise the quantum image enhancement using such systems. However, the results of the present chapter and Chapter 4 have shown that for frequency domain measurements using bright squeezed light, sensitivity enhancement is not sufficient to imply precision enhancement. In Figure 5.11, the effect of sensitivity and precision enhancement on a noisy image of a cell is illustrated. Image (a) corresponds to the true image, with each pixel representing a transmission value $0 \leq \eta \leq 1$, which we want to estimate. In image (b) an error $\Delta\eta$ has been added to each pixel, such that the value of each pixel is given by $\hat{\eta} = \eta + \Delta\eta$. Additionally, we have defined a noise floor N, such that if $1-\eta < N$, the transmission value $\hat{\eta}$ is replaced by a random value according to the pixel error: $\hat{\eta} = \Delta\eta$. In image (c), a sensitivity enhancement is illustrated by reducing the noise floor by a factor: $N' = \sqrt{\Phi}N$. In image (d) both the precision and sensitivity have been enhanced, by reducing the noise floor according

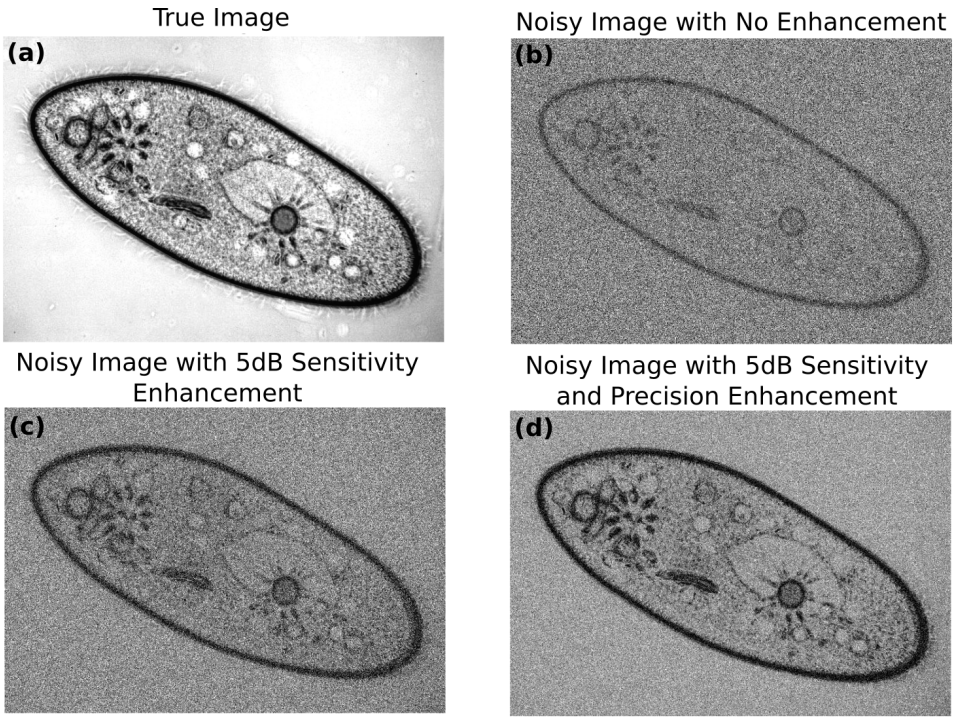

Figure 5.11: Simulation of an imaging measurement illustrating the effect of sensitivity and precision enhancement. (a) is the true image of the sample, and in (b), the effect of pixel error and a noise floor has been included. Image (c) corresponds to a 5dB sensitivity enhancement, and in (d), both sensitivity and precision have been enhanced by 5dB. These results are based on a simulation originally written by Euan Allen. The unprocessed image is taken from [3].

$N' = \sqrt{\Phi}N$, and reducing the pixel error according to: $\Delta\eta' = \sqrt{\Phi}\Delta\eta$. This simulation illustrates the additional improvement provided by a precision enhancement, compared with just enhancing the sensitivity.

For bright light microscopy, the power in the signal and the contrast between pixels is often sufficiently high for measurement precision and sensitivity not to limit the performance of the measurement. However, for measurements where the absorption of the sample, or the absorption contrast, is small, both precision and sensitivity can determine the quality of the image. We define the absorption contrast here as $C = (\eta_{max} - \eta_{min})/\eta_{max}$, where η_{max} and η_{min} are the maximum and minimum transmission parameters. In particular, if the absorption contrast is $C \sim \mathcal{O}(1/\sqrt{\langle N \rangle})$, for $\langle N \rangle$ detected photons, quantum noise in the probe beam may be a limiting factor in the image quality. For example, imaging of single molecules has been shown to be limited by optical shot noise [19].

For a quantum imaging measurement based on the scheme discussed in Section 5.4.1, squeezing would directly enhance the sensitivity of the measurement by reducing the noise floor of each pixel. However, for squeezing to increase the precision of the imaging measure-

ment, it is necessary that quantum noise dominates the variance on the timescales required to raster scan across the entire sample. This is because it is possible that the low frequency classical noise exhibits some nonstationary behaviour on such longer timescales. The signal power measured over a range of pixels will then have an additional noise contribution. Accordingly, a variance measurement taken over a longer duration may become dominated by classical noise, even when using $B = 1$ MHz. Therefore, it is necessary to measure the quantum advantage over a range of sweep times, T_s, in order to determine the longest measurement duration for which a quantum advantage may be achieved. The sweep time corresponds to $T_s = N f_s^{-1}$, where f_s is the sample rate and N is the number of samples. It is important to note that the sample rate can be chosen to be less than the resolution bandwidth. The sweep time therefore simply corresponds to the duration over which the data is collected. Results of $\mathcal{Q}(\hat{\eta})$ as a function of T_s are shown in Figure 5.12, for $B = 1$ MHz, and an average squeezing parameter of -1 dB. The optimal quantum advantage of $\mathcal{Q}(\hat{\eta}) = 1.2 \pm 0.1$ is observed for a sweep time of $T_s = 0.02$ s. However, the precision enhancement is reduced for long sweep times, and a significant quantum advantage is not observed from $T_s = 0.512$ s and above. This behaviour is in contrast to the results for measurements of amplitude mod-

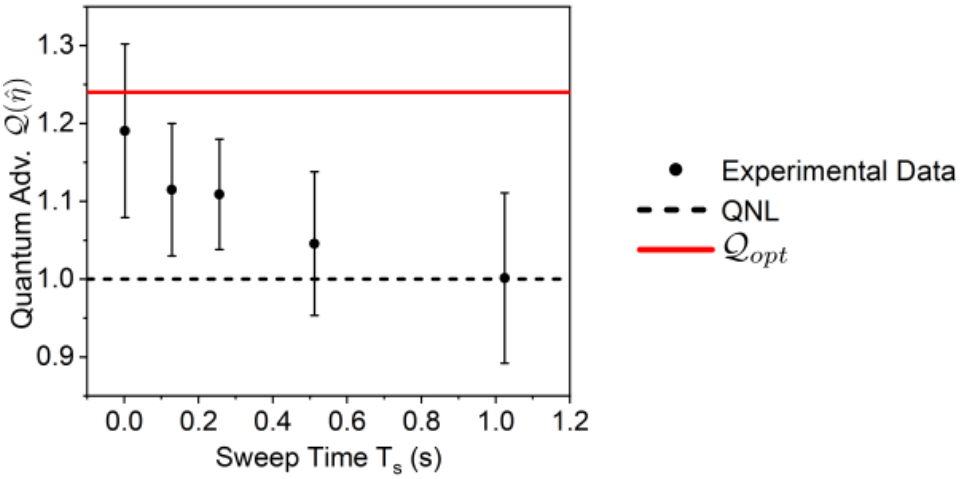

Figure 5.12: Inferred $\mathcal{Q}(\hat{\eta})$ from experimentally measured $\mathrm{Var}(\hat{\eta})$ as a function of sweep time, for an average of $\Phi_{dB} = -1$ dB squeezing. The error bars are derived from the standard deviations over 23 variance measurements. This shows that a quantum advantage in imaging may be achieved when the raster scan is performed over a short enough measurement duration.

ulation in Chapter 4, for which a constant sweep time of $T_s = 1$ s was used, with no observed degradation in the precision enhancement for long sweep times. The larger impact of using longer sweep times demonstrated by Figure 5.12 may be due to slight variations in the balancing of the coupling from the two paths into the photodetector over time. This presents a significant challenge in observing a quantum precision enhancement in imaging using this

setup, since the minimum sweep time for the spectrum analyser is $T_s = 0.002$ s. Completing the measurement within 0.02 s would therefore limit the image to 10 pixels. In order to overcome this limitation in sweep time, it may be necessary to further increase the RBW and modulation frequency. An alternative approach to overcoming this challenge would be to synchronise a spectrum analyser sweep at the modulation frequency with the raster scan, such that each pixel corresponds some subset of the data from a single sweep. This would enable an image to be acquired within a $T_s = 0.02$ s sweep of the spectrum analyser.

It is nonetheless possible to simulate the behaviour of a quantum imaging measurement using the model described in Section 5.3. These results are shown in Figure 5.13, for a probe beam generating a photocurrent of 0.1 mA, and with a RBW of $B = 1$ MHz. Image (a) represents the matrix of true transmission values η corresponding to the sample. The average absorption for this image is $\delta = 1 \times 10^{-3}$ and the contrast is $C = 1 \times 10^{-4}$. Image (b) corresponds to the measurement strategy for direct detection described in Section 5.2.1 for an integration time B^{-1}, in the presence of classical noise with $\mathrm{Var}(\Re[\mathcal{H}]) = 1 \times 10^{-5}$. Since the effect of classical noise for the DC measurement is much greater than the absorption contrast, no image of the sample can be observed with the DC measurement. Images (c)-(f) correspond to the measurement strategy described in Section 5.3. In the second row, images (c) and (d) respectively represent the case of $\Phi_{dB} = 0$ dB and $\Phi_{dB} = -5$ dB squeezing, with a classical noise contribution of $\mathrm{Var}(\Re[\mathcal{H}]) = 1 \times 10^{-3}$. Due to the high level of classical noise, squeezing does not improve the precision of the image. While the sensitivity of the image is improved by squeezing, this does not have a visible effect in this case, since the signal is typically sufficiently above the noise floor for each pixel. Images (e) and (f) are plotted for $\Phi_{dB} = 0$ dB and $\Phi_{dB} = -5$ dB respectively, and correspond to $\mathrm{Var}(\Re[\mathcal{H}]) = 1 \times 10^{-5}$, which approximates the level of classical noise observed experimentally. Here, squeezing is observed to reduce the effect of optical noise on the image, due to the improved precision of each transmission measurement. These simulations illustrate that the ability to improve imaging performance using bright squeezed light is highly dependent on the properties of the sample. Sensitivity enhancement can be observed when the signal for each pixel is comparable to the pixel noise floor, which for this strategy corresponds to samples with a low average absorption, $\delta \sim \mathcal{O}(1/\sqrt{\langle N \rangle})$, for $\langle N \rangle$ average photons. The effect of quantum precision enhancement can be observed for samples with low absorption contrast, $C \sim \mathcal{O}(1/\sqrt{\langle N \rangle})$, and when the pixel error is dominated by quantum noise. However, using realistic experimental parameters, an improvement in the image quality can be observed by applying squeezing. Furthermore, these simulations illustrate the effectiveness of this measurement strategy for reducing the impact of low frequency laser noise, which would prohibit the possibility of imaging such a low contrast sample using conventional bright light microscopy.

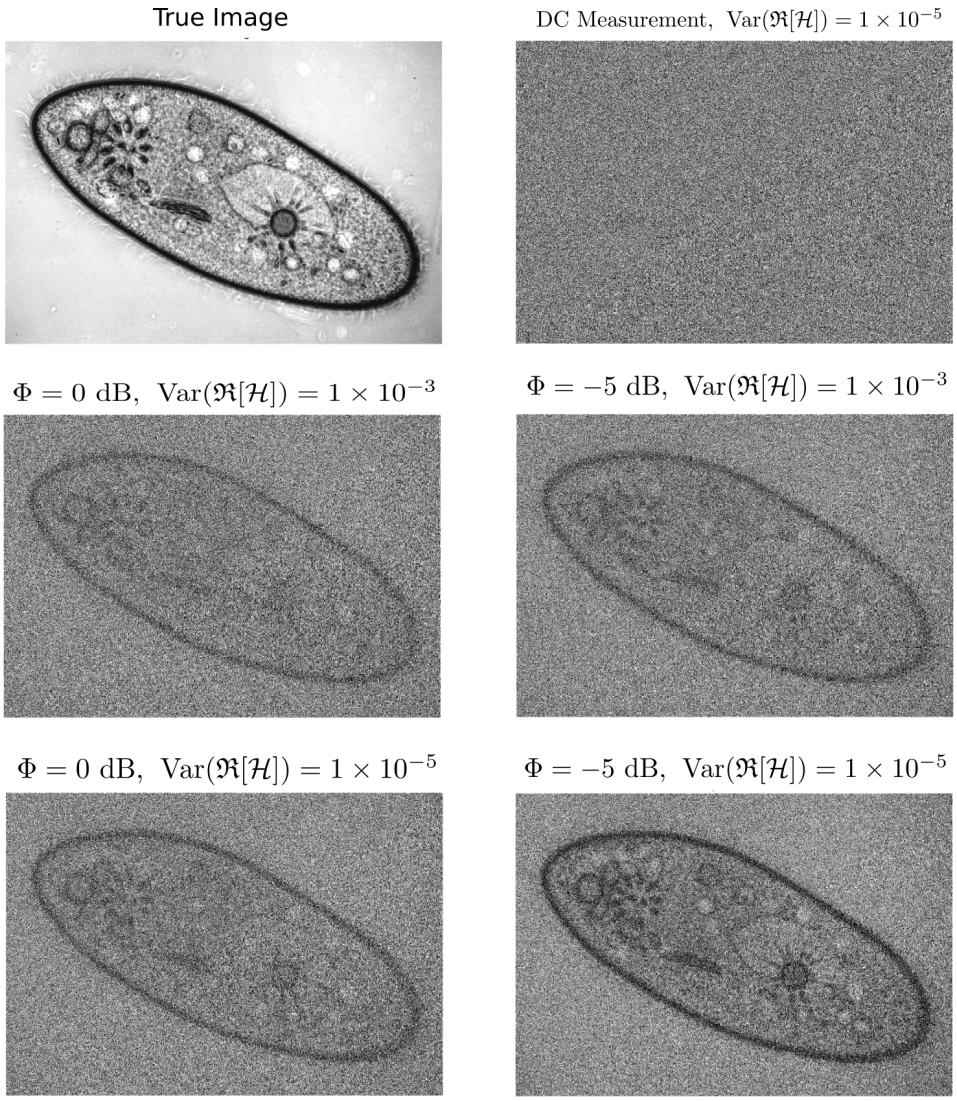

Figure 5.13: Simulation of absorption imaging for varied detection strategies and experimental parameters. (a) is the true image of the sample and (b) corresponds to direct detection of the DC photocurrent with $\mathrm{Var}(\Re[\mathcal{H}]) = 1 \times 10^{-5}$. (c)-(f) are plotted for the strategy outlined in Section 5.3, for varied levels of classical noise and squeezing.

5.5 Conclusion

In this chapter, a strategy for estimating optical transmission with bright squeezed light was demonstrated. Enhanced precision transmission estimation using quantum probes has been the focus of many theoretical and experimental studies [20, 21, 146, 22, 23, 133]. However, such demonstrations have been limited to picowatts of optical power, due to the significant low frequency excess noise observed on sources of high power amplitude squeezed light. In order to overcome the effect of low frequency excess noise, the strategy demon-

strated here applied path modulation of the amplitude squeezed light to transfer the signal to a shot noise limited bandwidth. The applicability of this scheme for quantum imaging was also studied.

Section 5.2 analysed the limits of precision in common measurement strategies for transmission estimation. Section 5.2.1 considered the case of direct detection, and analysed the Fisher information with and without the presence of excess low-frequency amplitude noise. It was shown that while direct detection of a coherent state saturates the quantum Crámer-Rao bound for transmission estimation, this no longer provides an optimal strategy in the presence of excess laser noise. The bound for the Fisher information using balanced detection is lower than that for direct detection of a coherent state. However, due to the cancellation of classical amplitude fluctuations, it was shown that balanced detection provides an optimal strategy for the estimation of a small optical absorption using laser light.

Section 5.3 provides an analysis of the measurement strategy proposed here, in which resonantly enhanced amplitude modulation is used to generate an absorption signal at the modulation frequency. Both the estimator and estimator variance are derived. This strategy is shown to provide a similar cancellation of excess laser noise for slight absorption as balanced detection. Unlike balanced detection, amplitude squeezing can be used with this approach to reduce the variance of the transmission measurement beyond the quantum noise limit.

In Section 5.4, an experimental demonstration of the proposed quantum enhanced transmission estimation measurement is presented. A quantum advantage of $\mathcal{Q}(\hat{\eta}) = 1.2 \pm 0.1$ is observed, and the experimental results agree quantitatively well with the variance predicted from the theoretical model. The average power of the amplitude squeezed light incident on the sample is 0.1 mW, which is 8 orders of magnitude above the power limitations of previous sub-QNL measurements of transmission [23, 22]. The measurement strategy demonstrated here could be directly applied to bright quantum imaging and spectroscopy, and the effectiveness of this scheme for quantum imaging is demonstrated by simulation. By providing a new means of achieving quantum limited precision in transmission estimation, this work may also find application in classical metrology, since it does not require shot noise limited behaviour at DC, or impose significant restrictions on the characteristics of the sample.

CHAPTER 6

CONCLUSION

For the last three decades, experiments with squeezed light have predominantly been oriented towards improving the sensitivity of optical measurements. In this thesis, we have focused on the precision advantage that can be obtained using bright squeezing, when accounting for the low frequency excess noise which is characteristic of laser light.

We began in Chapter 3 by presenting an experimental scheme for the generation of amplitude squeezed light, using an approach originally demonstrated in [1]. By using PCF, we achieved -1.3 dB of squeezing at 740 nm, therefore demonstrating the suitability of this approach to shorter wavelengths. The flexibility in the wavelength of the probe light with this method allows for a wide range of applicability. The results of the numerical simulations suggests the possibility for further improvements in the squeezing obtained with this setup. In particular, we anticipate that the measured squeezing may be improved by designing a PCF with lower third-order dispersion in order to minimise the pulse distortion. Additional improvement may be obtained by reducing optical loss. Nonetheless, the achieved squeezing was sufficient that this source could be used for the subsequent experiments presented in this thesis.

In Chapter 4, we investigated the precision advantage that may be obtained by using squeezed light to reduce optical noise in frequency domain measurements. While it is often assumed that an improvement in the signal-to-noise ratio will directly lead to a precision enhancement [127], we found that this is not necessarily the case, due to the low frequency optical noise transferred to the detected signal. The findings of our theoretical model were verified both by numerical simulation and experiment. For the experiment, the modulation index of an EOM was measured with a precision exceeding the quantum noise limit by 44%, using 0.2 mW of squeezed light. This was made possible by using the theoretical model to

find the conditions required for the variance of the signal to be limited by quantum noise. Although the detailed analysis was restricted to measurements of amplitude modulation, the theoretical model may be directly applied to similar frequency domain measurements such as Raman spectroscopy [134, 10], for which the performance may depend on both precision and sensitivity.

In Chapter 5, a novel method of estimating a static loss was proposed and experimentally demonstrated, which was shown to provide a quantum precision improvement by using a bright amplitude squeezed probe. The Fisher information for this measurement strategy was compared with other methods of classical loss estimation, and our approach was shown to provide a number of further advantages. For example, by employing path modulation to avoid low frequency classical noise, there is no requirement for shot noise limited behaviour at DC, and the only significant constraint on the sample is that the total absorption must be small. The average power of the probe was 0.1 mW, which is 8 orders of magnitude above the power limitations of previous demonstrations of loss estimation with quantum enhanced precision [23, 22]. Since the measured signal contains a significant fraction of the detected power, the effect of classical noise on the variance of the loss estimate could still be observed, which prevented the measurement from saturating the absolute theoretical bounds provided by the Fisher information calculations. However, this excess noise may be removed in future experiments by using classical noise reduction techniques. Alternatively, a higher frequency of modulation and detection would allow for an increased RBW, which would ensure that the measurement is limited by quantum noise. The scheme presented here may be directly applied to quantum imaging, as demonstrated by simulation. Additionally, it provides an alternative to FM spectroscopy, which may be advantageous in the case that an absorption feature is too broad to be detected by frequency modulation.

The work presented in this thesis represents an effort to enable quantum enhanced precision in measurements using high power squeezed light. While sensitivity enhancement has featured prominently in many demonstrations of bright squeezing [16, 10, 7, 8, 17], we show that considerations of the precision of such measurements will be important in facilitating the further development of quantum optical techniques in metrology. For example, the analysis of the variance of the signal power in Chapter 4 provided the groundwork for the realisation of the loss estimation measurement in Chapter 5. The focus on resource counting and the analysis of Fisher information closely resembles the approach taken in photon counting experiments, while including the effect of excess noise which is often encountered in measurements with bright laser light.

APPENDIX A

QUANTUM ENHANCED PRECISION ESTIMATION OF AMPLITUDE MODULATION

A.1 Calculation of the Signal-to-Noise Ratio

Here we derive the expected value of the electronic power p_Ω in the $\pm B/2$ frequency interval centered on the modulation frequency Ω, generated by the current $\hat{i}(t)$. We may write p_Ω as

$$p_\Omega = 2R|\hat{i}_\Omega|^2, \tag{A.1}$$

where R is the input resistance, $\hat{i}_\Omega = \int^\Omega \hat{i}(\nu)d\nu$ is the photocurrent in the frequency bin centered on Ω, using the notation $\int^\Omega \equiv \int_{\Omega-B/2}^{\Omega+B/2}$.

The amplitude of the optical field before modulation is applied may be written as $\hat{A}_0(t) = [1+\zeta(t)]\alpha_0 e^{i\theta} + \hat{a}(t)$, where θ is the phase of the classical field, $\hat{a}(t)$ describes the quantum amplitude fluctuations and $\zeta(t)$ is a stochastic noise function which corresponds to the low frequency classical noise of the laser. We have assumed a continuous-wave amplitude α_0 for simplicity. By making the assumption of large amplitude $\alpha \gg 1$ and small modulation $\Psi_m \ll 1$, the amplitude $\hat{A}(t)$ of the detected light after modulation may be written as

$$\hat{A}(t) \approx (\Psi_0 + \Psi_m \cos(2\pi\Omega t))[1+\zeta(t)]\alpha e^{i\theta} + \hat{a}(t) \equiv |\alpha(t)|e^{i\theta} + \hat{a}(t), \tag{A.2}$$

where Ψ_0 and Ψ_m are related to the modulation index by $\Psi_0 = 1-\delta_m/2$ and $\Psi_m = \delta_m/2$, and the detection efficiency η_q is modelled as an additional loss before detection, such that $\alpha = \sqrt{\eta_q}\alpha_0$. The effect of amplitude modulation on the quantum noise term has been neglected due to the small modulation assumption. The current at time t may then be written as

$$\hat{i}(t) = q\left(\hat{A}(t)^\dagger \hat{A}(t) + n_e(t)\right) = q\left(|\alpha(t)|^2 + \sqrt{2}|\alpha(t)|\hat{x}_\theta(t) + \hat{a}(t)^\dagger \hat{a}(t) + n_e(t)\right), \tag{A.3}$$

where we have defined the quadrature operator $\hat{x}_\theta(t) = \frac{1}{\sqrt{2}}[\hat{a}(t)e^{-i\theta} + \hat{a}(t)^\dagger e^{i\theta}]$ and the electronic noise term $n_e(t)$ corresponds to the number of electrons generated independently of the optical field. The component of the photocurrent at frequency ν is then given by

$$\hat{i}(\nu) = q\left[I(\nu) + \sqrt{2}\int \alpha(\mu)\hat{x}_\theta(\nu-\mu)d\mu + \int \hat{a}(-\mu)^\dagger \hat{a}(\nu-\mu)d\mu\right], \tag{A.4}$$

where $\int \equiv \int_{-\infty}^{\infty}$, and we have defined the unitary Fourier transforms

$$I(\nu) = \int \left(|\alpha(t)|^2 + n_e(t)\right)e^{-2\pi i\nu t}dt \tag{A.5}$$

and

$$\hat{x}_\theta(\nu) = \int \hat{x}_\theta(t)e^{-2\pi i\nu t}dt = \frac{1}{\sqrt{2}}\left[\hat{a}(-\nu)^\dagger e^{i\theta} + \hat{a}(\nu)e^{-i\theta}\right]. \tag{A.6}$$

We also define $\hat{a}(\nu)$ as the squeezed vacuum operator [26]

$$\hat{a}(\nu) = \hat{b}(\nu)\cosh r(\nu) - e^{2i\theta(\nu)}\hat{b}(-\nu)^\dagger \sinh r(\nu), \tag{A.7}$$

where $\hat{b}(\nu)$ and $\hat{b}(\nu)^\dagger$ are the bosonic creation and annihilation operators. The squeezing is defined such that $r(\nu) = r$ and $\theta(\nu) = \theta$ within the frequency bandwidth $-\Lambda/2 \le \nu \le \Lambda/2$ (where $\Lambda/2 > \Omega$) and $r(\nu) = 0$ outside of this frequency range. The 2θ phase factor then orients the squeezing in the amplitude direction. By defining $I_\Omega = \int^\Omega I(\nu)d\nu$ we can write p_Ω as

$$\begin{aligned} p_\Omega = 2q^2R\Bigg[& |I_\Omega|^2 + \sqrt{2}I_\Omega^*\int^\Omega\int \alpha(\mu)\hat{x}_\theta(\nu-\mu)d\mu d\nu + I_\Omega^*\int^\Omega\int \hat{a}(-\mu)^\dagger\hat{a}(\nu-\mu)d\mu d\nu \\ & + \sqrt{2}I_\Omega\int^\Omega\int \alpha(\mu)^*\hat{x}_\theta(\nu-\mu)^\dagger d\mu d\nu + 2\int^\Omega\int^\Omega\int\int \alpha(\mu)^*\alpha(\overline{\mu})\hat{x}_\theta(\nu-\mu)^\dagger\hat{x}_\theta(\overline{\nu}-\overline{\mu})d\mu d\overline{\mu}d\nu d\overline{\nu} \\ & + \sqrt{2}\int^\Omega\int^\Omega\int\int \alpha(\mu)^*\hat{x}_\theta(\nu-\mu)^\dagger\hat{a}(-\overline{\mu})^\dagger\hat{a}(\overline{\nu}-\overline{\mu})d\mu d\overline{\mu}d\nu d\overline{\nu} + I_\Omega\int^\Omega\int \hat{a}(\nu-\mu)^\dagger\hat{a}(-\mu)d\mu d\nu \\ & + \sqrt{2}\int^\Omega\int^\Omega\int\int \alpha(\mu)\hat{a}(\nu-\overline{\mu})^\dagger\hat{a}(-\overline{\mu})\hat{x}_\theta(\overline{\nu}-\mu)d\mu d\overline{\mu}d\nu d\overline{\nu} \\ & + \int^\Omega\int^\Omega\int\int \hat{a}(\nu-\mu)^\dagger\hat{a}(-\mu)\hat{a}(-\overline{\mu})^\dagger\hat{a}(\overline{\nu}-\overline{\mu})d\mu d\overline{\mu}d\nu d\overline{\nu}\Bigg], \end{aligned} \tag{A.8}$$

where $(\bullet)^*$ denotes the complex conjugate. From Equation A.2, we can find the frequency dependence of the classical field amplitude:

$$\alpha(\nu) = \int |\alpha(t)|e^{-2\pi i\nu t}dt = \alpha\left[\Psi_0(\delta(\nu)+h(\nu)) + \frac{\Psi_m}{2}(\delta(\nu-\Omega)+\delta(\nu+\Omega)+h(\nu-\Omega)+h(\nu+\Omega))\right], \tag{A.9}$$

where $h(\nu) = \int \zeta(t) e^{-2\pi i \nu t} dt$, and since classical noise is only observed at low frequencies ($\lesssim 2$ MHz), we can write for example $h(\Omega) = 0$. Equation A.2 allows us to define $I(\nu)$ as

$$
\begin{aligned}
(\text{A.10}) \quad I(\nu) = \alpha^2 \Bigg[\Psi_0^2 \Bigg(\delta(\nu) + 2h(\nu) + \int h(\mu) h(\nu-\mu) d\mu \Bigg) + \Psi_0 \Psi_m \Bigg(\delta(\Omega-\nu) + \delta(\Omega+\nu) \\
+ 2h(\nu-\Omega) + 2h(\nu+\Omega) + \int h(\mu) h(\nu-\mu-\Omega) d\mu + \int h(\mu) h(\nu-\mu+\Omega) d\mu \Bigg) + \\
+ \frac{\Psi_m^2}{4} \Bigg(\delta(\nu-2\Omega) + \delta(\nu+2\Omega) + 2\delta(\nu) + 2h(\nu-2\Omega) + 2h(\nu+2\Omega) + 4h(\nu) \\
+ \int h(\mu) h(\nu-\mu-2\Omega) d\mu + \int h(\mu) h(\nu-\mu+2\Omega) d\mu + 2 \int h(\mu) h(\nu-\mu) d\mu \Bigg) \Bigg] + n_e(\nu).
\end{aligned}
$$

We can then find the expectation $\langle p_\Omega \rangle$ with respect to the random variables $h(\nu)$, $n_e(\nu)$ and $\hat{a}(\nu)$. Since these variables are independent, the expectation value may be defined as $\langle \bullet \rangle \equiv \langle\langle\langle 0| \bullet |0\rangle\rangle_{h(\nu)}\rangle_{n_e(\nu)}$. To calculate this, we first compute

$$
\begin{aligned}
(\text{A.11}) \quad |I_\Omega|^2 = \Psi_0^2 \Psi_m^2 \alpha^4 \Bigg[1 + 4 \int^\Omega \Re[h(\nu-\Omega)] d\nu + 2 \int^\Omega \int \Re[h(\mu) h(\nu-\mu-\Omega)] d\mu d\nu \\
+ 4 \left| \int^\Omega h(\nu-\Omega) d\nu \right|^2 + 4 \int^\Omega \int^\Omega \int \Re[h(\nu-\Omega)^* h(\mu) h(\overline{\nu}-\mu-\Omega)] d\mu d\nu d\overline{\nu} \\
+ \left| \int^\Omega \int h(\mu) h(\nu-\mu-\Omega) d\mu d\nu \right|^2 \Bigg] + \Psi_0 \Psi_m \alpha^2 \Bigg[2 \int^\Omega \Re[n_e(\nu)] d\nu \\
+ 4 \int^\Omega \int^\Omega \Re[h(\nu-\Omega)^* n_e(\overline{\nu})] d\nu d\overline{\nu} + 2 \int^\Omega \int^\Omega \int \Re[h(\mu)^* h(\nu-\mu-\Omega)^* n_e(\overline{\nu})] d\mu d\nu d\overline{\nu} \Bigg] \\
+ \left| \int^\Omega n_e(\nu) d\nu \right|^2,
\end{aligned}
$$

where $\Re[\bullet]$ signifies the real part. Then, by evaluating the quantum part of the expectation value, we obtain the result:

$$
\begin{aligned}
(\text{A.12}) \quad \langle p_\Omega \rangle = 2q^2 R \left[\langle |I_\Omega|^2 \rangle + \Phi \int^\Omega \int^\Omega \int \langle \alpha(\mu)^* \alpha(\mu+\nu-\overline{\nu}) \rangle d\mu d\nu d\overline{\nu} + B\Lambda \left(\frac{\Phi^2}{8} + \frac{1}{8\Phi^2} - \frac{1}{4} \right) \right] \\
= 2q^2 R \Bigg[\alpha^4 \Bigg(\Psi_0^2 \Psi_m^2 + 2\Psi_0^2 \Psi_m^2 \int^\Omega \int \langle \Re[h(\mu) h(\nu-\mu-\Omega)] \rangle d\mu d\nu \\
+ 4\Psi_0^2 \Psi_m^2 \left\langle \left| \int^\Omega h(\nu-\Omega) d\nu \right|^2 \right\rangle + 4\Psi_0^2 \Psi_m^2 \int^\Omega \int^\Omega \int \langle \Re[h(\nu-\Omega)^* h(\mu) h(\overline{\nu}-\mu-\Omega)] \rangle d\mu d\nu d\overline{\nu} \\
+ \Psi_0^2 \Psi_m^2 \left\langle \left| \int^\Omega \int h(\mu) h(\nu-\mu-\Omega) d\mu d\nu \right|^2 \right\rangle \Bigg) + \alpha^2 \Bigg(\left(\Psi_0^2 + \frac{\Psi_m^2}{2} \right) \Phi B \\
+ \left(\Psi_0^2 + \frac{\Psi_m^2}{2} \right) \Phi \int^\Omega \int^\Omega \int \langle h(\mu)^* h(\mu+\nu-\overline{\nu}) \rangle d\mu d\nu d\overline{\nu} \Bigg) + \left\langle \left| \int^\Omega n_e(\nu) d\nu \right|^2 \right\rangle \\
+ B\Lambda \left(\frac{\Phi^2}{8} + \frac{1}{8\Phi^2} - \frac{1}{4} \right) \Bigg],
\end{aligned}
$$

for the squeezing parameter $\Phi = e^{-2r}$. In Equation A.12, we have neglected terms involving the expectation value of the product of an odd number of creation or annihilation operators, and terms outside the domain of $h(\nu)$. We have also used the fact that the expected amplitude of the classical noise terms $\langle h(\nu)\rangle = \langle n_e(\nu)\rangle = 0$, since the corresponding stochastic time-domain functions have a mean of zero. By observing that $\alpha \gg 1$, $\langle |\int h(\nu)d\nu|\rangle \ll 1$ and $\delta_m \ll 1$ for $i_0 \approx q\alpha^2$ we find

$$\langle p_\Omega\rangle \approx R\left(\frac{i_0^2\delta_m^2}{2} + 2qi_0\Phi B + 2q^2\left\langle\left|\int^\Omega n_e(\nu)d\nu\right|^2\right\rangle\right). \tag{A.13}$$

Similarly, at a small frequency interval Δf from Ω, we find that the electronic power of the optical noise floor and electronic noise floor are respectively

$$\langle p_N\rangle \approx R\left(2qi_0\Phi B + 2q^2\left\langle\left|\int^\Omega n_e(\nu)d\nu\right|^2\right\rangle\right) \quad \text{and} \quad \langle p_E\rangle = R\left(2q^2\left\langle\left|\int^\Omega n_e(\nu)d\nu\right|^2\right\rangle\right). \tag{A.14}$$

We then find that the optical signal-to-noise ratio δ_{SNR} may be expressed as

$$\delta_{SNR} = \frac{\langle p_\Omega\rangle - \langle p_N\rangle}{\langle p_N\rangle - \langle p_E\rangle} \approx \frac{i_0\delta_m^2}{4q\Phi B}. \tag{A.15}$$

A.2 Calculation of the Variance of the Sideband Power

In order to calculate the variance $\mathrm{Var}(p_\Omega) = \langle p_\Omega^2\rangle - \langle p_\Omega\rangle^2$, an expression for $\langle p_\Omega\rangle^2$ may be evaluated directly from Equation A.12 to give

$$\begin{aligned}\langle p_\Omega\rangle^2 = 4q^4R^2\Bigg[&\langle|I_\Omega|^2\rangle^2 + (2\Psi_0^2+\Psi_m^2)\langle|I_\Omega|^2\rangle\alpha^2\Bigg(\Phi B \\ &+ \Phi\int^\Omega\int^\Omega\int\langle h(\mu)^*h(\mu+\nu-\overline{\nu})\rangle d\mu d\nu d\overline{\nu}\Bigg) + \langle|I_\Omega|^2\rangle\Lambda B\left(\frac{\Phi^2}{4}+\frac{1}{4\Phi^2}-\frac{1}{2}\right) \\ &+\left(\Psi_0^4+\Psi_0^2\Psi_m^2+\frac{\Psi_m^4}{4}\right)\alpha^4\Bigg(\Phi^2B^2 + 2\Phi^2B\int^\Omega\int^\Omega\int\langle h(\mu)^*h(\mu+\nu-\overline{\nu})\rangle d\mu d\nu d\overline{\nu} \\ &+\Phi^2\int^\Omega\int^\Omega\int^\Omega\int^\Omega\int\int\langle h(\mu)^*h(\mu+\nu-\overline{\nu})\rangle\langle h(\overline{\mu})^*h(\overline{\mu}+\overline{\overline{\nu}}-\overline{\overline{\nu}})\rangle d\mu d\overline{\mu}d\nu d\overline{\nu}d\overline{\overline{\nu}}d\overline{\overline{\nu}}\Bigg) \\ &+(2\Psi_0^2+\Psi_m^2)\alpha^2\left(\frac{\Phi^2}{8}+\frac{1}{8\Phi^2}-\frac{1}{4}\right)\Bigg(\Phi\Lambda B^2 + \Phi\Lambda B\int^\Omega\int^\Omega\int\langle h(\mu)^*h(\mu+\nu-\overline{\nu})\rangle d\mu d\nu d\overline{\nu}\Bigg) \\ &+\Lambda^2B^2\left(\frac{\Phi^2}{8}+\frac{1}{8\Phi^2}-\frac{1}{4}\right)^2\Bigg].\end{aligned} \tag{A.16}$$

To find an expression for $\langle p_\Omega^2\rangle$, we can again neglect terms where the expectation value of the quadrature operators vanishes, giving

$$
\begin{aligned}
\text{(A.17)}\quad \langle p_\Omega^2 \rangle = 4q^4R^2 \Bigg\langle\ & |I_\Omega|^4 + 4|I_\Omega|^2 \int^\Omega \int^\Omega \int\int \alpha(\mu)^* \alpha(\overline{\mu}) \hat{x}_\theta(\nu-\mu)^\dagger \hat{x}_\theta(\overline{\nu}-\overline{\mu}) d\mu d\overline{\mu} d\nu d\overline{\nu} \\
& + 2I_\Omega^{*2} \int^\Omega \int^\Omega \int\int \alpha(\mu)\alpha(\overline{\mu}) \hat{x}_\theta(\nu-\mu)\hat{x}_\theta(\overline{\nu}-\overline{\mu}) d\mu d\overline{\mu} d\nu d\overline{\nu} \\
& + 2I_\Omega^{2} \int^\Omega \int^\Omega \int\int \alpha(\mu)^* \alpha(\overline{\mu})^* \hat{x}_\theta(\nu-\mu)^\dagger \hat{x}_\theta(\overline{\nu}-\overline{\mu})^\dagger d\mu d\overline{\mu} d\nu d\overline{\nu} \\
& + 4|I_\Omega|^2 \int^\Omega \int^\Omega \int\int \alpha(\mu)\alpha(\overline{\mu})^* \hat{x}_\theta(\nu-\mu)\hat{x}_\theta(\overline{\nu}-\overline{\mu})^\dagger d\mu d\overline{\mu} d\nu d\overline{\nu} \\
& + 3|I_\Omega|^2 \int^\Omega \int^\Omega \int\int \hat{a}(\nu-\mu)^\dagger \hat{a}(-\mu)\hat{a}(-\overline{\mu})^\dagger \hat{a}(\overline{\nu}-\overline{\mu}) d\mu d\overline{\mu} d\nu d\overline{\nu} \\
& + |I_\Omega|^2 \int^\Omega \int^\Omega \int\int \hat{a}(-\mu)^\dagger \hat{a}(\nu-\mu)\hat{a}(\overline{\nu}-\overline{\mu})^\dagger \hat{a}(-\overline{\mu}) d\mu d\overline{\mu} d\nu d\overline{\nu} \\
& + 2I_\Omega^* \int^\Omega \int^\Omega \int^\Omega \int\int\int \alpha(\mu)\alpha(\overline{\mu})^* \hat{x}_\theta(\nu-\mu)\hat{x}_\theta(\overline{\nu}-\overline{\mu})^\dagger \hat{a}(-\overline{\overline{\mu}})^\dagger \hat{a}(\overline{\overline{\nu}}-\overline{\overline{\mu}}) d\mu d\overline{\mu} d\overline{\overline{\mu}} d\nu d\overline{\nu} d\overline{\overline{\nu}} \\
& + 2I_\Omega^* \int^\Omega \int^\Omega \int^\Omega \int\int\int \alpha(\mu)\alpha(\overline{\mu})^* \hat{x}_\theta(\overline{\nu}-\overline{\mu})^\dagger \hat{a}(-\overline{\overline{\mu}})^\dagger \hat{a}(\overline{\overline{\nu}}-\overline{\overline{\mu}}) \hat{x}_\theta(\nu-\mu) d\mu d\overline{\mu} d\overline{\overline{\mu}} d\nu d\overline{\nu} d\overline{\overline{\nu}} \\
& + 2I_\Omega^* \int^\Omega \int^\Omega \int^\Omega \int\int\int \alpha(\mu)^*\alpha(\overline{\mu}) \hat{a}(-\overline{\overline{\mu}})^\dagger \hat{a}(\nu-\overline{\overline{\mu}}) \hat{x}_\theta(\overline{\nu}-\mu)^\dagger \hat{x}_\theta(\overline{\overline{\nu}}-\overline{\mu}) d\mu d\overline{\mu} d\overline{\overline{\mu}} d\nu d\overline{\nu} d\overline{\overline{\nu}} \\
& + 2I_\Omega^* \int^\Omega \int^\Omega \int^\Omega \int\int\int \alpha(\mu)^*\alpha(\overline{\mu}) \hat{x}_\theta(\overline{\nu}-\mu)^\dagger \hat{x}_\theta(\overline{\overline{\nu}}-\overline{\mu}) \hat{a}(-\overline{\overline{\mu}})^\dagger \hat{a}(\nu-\overline{\overline{\mu}}) d\mu d\overline{\mu} d\overline{\overline{\mu}} d\nu d\overline{\nu} d\overline{\overline{\nu}} \\
& + 2I_\Omega \int^\Omega \int^\Omega \int^\Omega \int\int\int \alpha(\mu)^*\alpha(\overline{\mu}) \hat{x}_\theta(\nu-\mu)^\dagger \hat{a}(\overline{\nu}-\overline{\overline{\mu}})^\dagger \hat{a}(-\overline{\overline{\mu}}) \hat{x}_\theta(\overline{\overline{\nu}}-\overline{\mu}) d\mu d\overline{\mu} d\overline{\overline{\mu}} d\nu d\overline{\nu} d\overline{\overline{\nu}} \\
& + 2I_\Omega \int^\Omega \int^\Omega \int^\Omega \int\int\int \alpha(\mu)^*\alpha(\overline{\mu}) \hat{a}(\overline{\nu}-\overline{\overline{\mu}})^\dagger \hat{a}(-\overline{\overline{\mu}}) \hat{x}_\theta(\overline{\overline{\nu}}-\overline{\mu}) \hat{x}_\theta(\nu-\mu)^\dagger d\mu d\overline{\mu} d\overline{\overline{\mu}} d\nu d\overline{\nu} d\overline{\overline{\nu}} \\
& + 2I_\Omega \int^\Omega \int^\Omega \int^\Omega \int\int\int \alpha(\mu)^*\alpha(\overline{\mu}) \hat{x}_\theta(\nu-\mu)^\dagger \hat{x}_\theta(\overline{\nu}-\overline{\mu}) \hat{a}(\overline{\overline{\nu}}-\overline{\overline{\mu}})^\dagger \hat{a}(-\overline{\overline{\mu}}) d\mu d\overline{\mu} d\overline{\overline{\mu}} d\nu d\overline{\nu} d\overline{\overline{\nu}} \\
& + 2I_\Omega \int^\Omega \int^\Omega \int^\Omega \int\int\int \alpha(\mu)^*\alpha(\overline{\mu}) \hat{a}(\overline{\overline{\nu}}-\overline{\overline{\mu}})^\dagger \hat{a}(-\overline{\overline{\mu}}) \hat{x}_\theta(\nu-\mu)^\dagger \hat{x}_\theta(\overline{\nu}-\overline{\mu}) d\mu d\overline{\mu} d\overline{\overline{\mu}} d\nu d\overline{\nu} d\overline{\overline{\nu}} \\
& + 2I_\Omega^* \int^\Omega \int^\Omega \int^\Omega \int\int\int \alpha(\mu)\alpha(\overline{\mu}) \hat{x}_\theta(\nu-\mu) \hat{a}(\overline{\nu}-\overline{\overline{\mu}})^\dagger \hat{a}(-\overline{\overline{\mu}}) \hat{x}_\theta(\overline{\overline{\nu}}-\overline{\mu}) d\mu d\overline{\mu} d\overline{\overline{\mu}} d\nu d\overline{\nu} d\overline{\overline{\nu}} \\
& + 2I_\Omega^* \int^\Omega \int^\Omega \int^\Omega \int\int\int \alpha(\mu)\alpha(\overline{\mu}) \hat{a}(\overline{\nu}-\overline{\overline{\mu}})^\dagger \hat{a}(-\overline{\overline{\mu}}) \hat{x}_\theta(\overline{\overline{\nu}}-\overline{\mu}) \hat{x}_\theta(\nu-\mu) d\mu d\overline{\mu} d\overline{\overline{\mu}} d\nu d\overline{\nu} d\overline{\overline{\nu}} \\
& + 2I_\Omega \int^\Omega \int^\Omega \int^\Omega \int\int\int \alpha(\mu)^*\alpha(\overline{\mu})^* \hat{x}_\theta(\nu-\mu)^\dagger \hat{x}_\theta(\overline{\nu}-\overline{\mu})^\dagger \hat{a}(-\overline{\overline{\mu}})^\dagger \hat{a}(\overline{\overline{\nu}}-\overline{\overline{\mu}}) d\mu d\overline{\mu} d\overline{\overline{\mu}} d\nu d\overline{\nu} d\overline{\overline{\nu}} \\
& + 2I_\Omega \int^\Omega \int^\Omega \int^\Omega \int\int\int \alpha(\mu)^*\alpha(\overline{\mu})^* \hat{x}_\theta(\overline{\nu}-\overline{\mu})^\dagger \hat{a}(-\overline{\overline{\mu}})^\dagger \hat{a}(\overline{\overline{\nu}}-\overline{\overline{\mu}}) \hat{x}_\theta(\nu-\mu)^\dagger d\mu d\overline{\mu} d\overline{\overline{\mu}} d\nu d\overline{\nu} d\overline{\overline{\nu}} \\
& + 4\Bigg[\int^\Omega \int^\Omega \int^\Omega \int^\Omega \int\int\int\int \alpha(\mu)^*\alpha(\overline{\mu})\alpha(\overline{\overline{\mu}})^*\alpha(\overline{\overline{\overline{\mu}}}) \times \\
& \hat{x}_\theta(\nu-\mu)^\dagger \hat{x}_\theta(\overline{\nu}-\overline{\mu}) \hat{x}_\theta(\overline{\overline{\nu}}-\overline{\overline{\mu}})^\dagger \hat{x}_\theta(\overline{\overline{\overline{\nu}}}-\overline{\overline{\overline{\mu}}}) d\mu d\overline{\mu} d\overline{\overline{\mu}} d\overline{\overline{\overline{\mu}}} d\nu d\overline{\nu} d\overline{\overline{\nu}} d\overline{\overline{\overline{\nu}}} \Bigg] \\
& + 2\Bigg[\int^\Omega \int^\Omega \int^\Omega \int^\Omega \int\int\int\int \alpha(\mu)^*\alpha(\overline{\mu}) \times
\end{aligned}
$$

$$\hat{x}_\theta(\nu-\mu)^\dagger\hat{x}_\theta(\overline{\nu}-\overline{\mu})\hat{a}(\overline{\overline{\nu}}-\overline{\overline{\mu}})^\dagger\hat{a}(-\overline{\overline{\mu}})\hat{a}(-\overline{\overline{\overline{\mu}}})^\dagger\hat{a}(\overline{\overline{\overline{\nu}}}-\overline{\overline{\overline{\mu}}})d\mu d\overline{\mu}d\overline{\overline{\mu}}d\overline{\overline{\overline{\mu}}}d\nu d\overline{\nu}d\overline{\overline{\nu}}d\overline{\overline{\overline{\nu}}}\Big]$$

$$+2\Big[\int^\Omega\int^\Omega\int^\Omega\int^\Omega\int\int\int\int\alpha(\mu)^*\alpha(\overline{\mu})\times$$

$$\hat{a}(\overline{\overline{\nu}}-\overline{\overline{\mu}})^\dagger\hat{a}(-\overline{\overline{\mu}})\hat{a}(-\overline{\overline{\overline{\mu}}})^\dagger\hat{a}(\overline{\overline{\overline{\nu}}}-\overline{\overline{\overline{\mu}}})\hat{x}_\theta(\nu-\mu)^\dagger\hat{x}_\theta(\overline{\nu}-\overline{\mu})d\mu d\overline{\mu}d\overline{\overline{\mu}}d\overline{\overline{\overline{\mu}}}d\nu d\overline{\nu}d\overline{\overline{\nu}}d\overline{\overline{\overline{\nu}}}\Big]$$

$$+2\Big[\int^\Omega\int^\Omega\int^\Omega\int^\Omega\int\int\int\int\alpha(\mu)^*\alpha(\overline{\mu})\times$$

$$\hat{x}_\theta(\nu-\mu)^\dagger\hat{a}(-\overline{\overline{\mu}})^\dagger\hat{a}(\overline{\nu}-\overline{\mu})\hat{a}(\overline{\overline{\nu}}-\overline{\overline{\mu}})^\dagger\hat{a}(-\overline{\overline{\overline{\mu}}})\hat{x}_\theta(\overline{\overline{\overline{\nu}}}-\overline{\mu})d\mu d\overline{\mu}d\overline{\overline{\mu}}d\overline{\overline{\overline{\mu}}}d\nu d\overline{\nu}d\overline{\overline{\nu}}d\overline{\overline{\overline{\nu}}}\Big]$$

$$+2\Big[\int^\Omega\int^\Omega\int^\Omega\int^\Omega\int\int\int\int\alpha(\mu)^*\alpha(\overline{\mu})\times$$

$$\hat{a}(\overline{\overline{\nu}}-\overline{\overline{\mu}})^\dagger\hat{a}(-\overline{\overline{\mu}})\hat{x}_\theta(\overline{\overline{\nu}}-\overline{\mu})\hat{x}_\theta(\nu-\mu)^\dagger\hat{a}(-\overline{\mu})^\dagger\hat{a}(\overline{\nu}-\overline{\mu})d\mu d\overline{\mu}d\overline{\overline{\mu}}d\overline{\overline{\overline{\mu}}}d\nu d\overline{\nu}d\overline{\overline{\nu}}d\overline{\overline{\overline{\nu}}}\Big]$$

$$+2\Big[\int^\Omega\int^\Omega\int^\Omega\int^\Omega\int\int\int\int\alpha(\mu)^*\alpha(\overline{\mu})^*\times$$

$$\hat{x}_\theta(\nu-\mu)^\dagger\hat{a}(-\overline{\mu})\hat{a}(\overline{\nu}-\overline{\mu})\hat{x}_\theta(\overline{\nu}-\mu)^\dagger\hat{a}(-\overline{\overline{\mu}})^\dagger\hat{a}(\overline{\overline{\nu}}-\overline{\overline{\mu}})d\mu d\overline{\mu}d\overline{\overline{\mu}}d\overline{\overline{\overline{\mu}}}d\nu d\overline{\nu}d\overline{\overline{\nu}}d\overline{\overline{\overline{\nu}}}\Big]$$

$$+2\Big[\int^\Omega\int^\Omega\int^\Omega\int^\Omega\int\int\int\int\alpha(\mu)\alpha(\overline{\mu})\times$$

$$\hat{a}(\nu-\overline{\overline{\mu}})^\dagger\hat{a}(-\overline{\overline{\mu}})\hat{x}_\theta(\overline{\nu}-\mu)\hat{a}(\overline{\overline{\nu}}-\overline{\overline{\mu}})^\dagger\hat{a}(-\overline{\overline{\overline{\mu}}})\hat{x}_\theta(\overline{\overline{\overline{\nu}}}-\overline{\mu})d\mu d\overline{\mu}d\overline{\overline{\mu}}d\overline{\overline{\overline{\mu}}}d\nu d\overline{\nu}d\overline{\overline{\nu}}d\overline{\overline{\overline{\nu}}}\Big]$$

$$+\Big[\int^\Omega\int^\Omega\int^\Omega\int^\Omega\int\int\int\int\hat{a}(\nu-\mu)^\dagger\hat{a}(-\mu)\hat{a}(-\overline{\mu})^\dagger\hat{a}(\overline{\nu}-\overline{\mu})\times$$

$$\hat{a}(\overline{\overline{\nu}}-\overline{\overline{\mu}})^\dagger\hat{a}(-\overline{\overline{\mu}})\hat{a}(-\overline{\overline{\overline{\mu}}})^\dagger\hat{a}(\overline{\overline{\overline{\nu}}}-\overline{\overline{\overline{\mu}}})d\mu d\overline{\mu}d\overline{\overline{\mu}}d\overline{\overline{\overline{\mu}}}d\nu d\overline{\nu}d\overline{\overline{\nu}}d\overline{\overline{\overline{\nu}}}\Big]\Big\rangle.$$

To explicitly evaluate $\langle p_\Omega^2\rangle$ in the following, we calculate the integrals in Equation A.17 separately, using Equation A.9 and the commutation relations of the Bose operators with the expectation value taken on the vacuum state. Terms 2-5 of Equation A.17 respectively give

$$\text{(A.18)}\quad \Big\langle 4|I_\Omega|^2\int^\Omega\int^\Omega\int\int\alpha(\mu)^*\alpha(\overline{\mu})\hat{x}_\theta(\nu-\mu)^\dagger\hat{x}_\theta(\overline{\nu}-\overline{\mu})d\mu d\overline{\mu}d\nu d\overline{\nu}\Big\rangle$$
$$=(2\Psi_0^2+\Psi_m^2)\alpha^2\Phi\Big(\langle|I_\Omega|^2\rangle B+2\int^\Omega\int^\Omega\langle|I_\Omega|^2\Re[h(\nu-\overline{\nu})]\rangle d\nu d\overline{\nu}$$
$$+\int^\Omega\int^\Omega\int\langle|I_\Omega|^2h(\mu)^*h(\mu+\nu-\overline{\nu})\rangle d\mu d\nu d\overline{\nu}\Big),$$

$$\text{(A.19)}\quad \Big\langle 2I_\Omega^{*2}\int^\Omega\int^\Omega\int\int\alpha(\mu)\alpha(\overline{\mu})\hat{x}_\theta(\nu-\mu)\hat{x}_\theta(\overline{\nu}-\overline{\mu})d\mu d\overline{\mu}d\nu d\overline{\nu}\Big\rangle$$
$$=\frac{\Psi_m^2}{4}\alpha^2\Phi\Big(\langle I_\Omega^{*2}\rangle B+2\int^\Omega\int^\Omega\langle I_\Omega^{*2}h(\nu+\overline{\nu}-2\Omega)\rangle d\nu d\overline{\nu}$$

$$+\int^{\Omega}\int^{\Omega}\int\langle I_{\Omega}^{*2}h(\mu-\Omega)h(\nu+\overline{\nu}-\mu-\Omega)\rangle d\mu d\nu d\overline{\nu}\Bigg),$$

$$\begin{aligned}(\text{A.20})\quad &\left\langle 2I_{\Omega}^{2}\int^{\Omega}\int^{\Omega}\int\int\alpha(\mu)^{*}\alpha(\overline{\mu})^{*}\hat{x}_{\theta}(\nu-\mu)^{\dagger}\hat{x}_{\theta}(\overline{\nu}-\overline{\mu})^{\dagger}d\mu d\overline{\mu}d\nu d\overline{\nu}\right\rangle\\ &=\frac{\Psi_{m}^{2}}{4}\alpha^{2}\Phi\Bigg(\langle I_{\Omega}^{2}\rangle B+2\int^{\Omega}\int^{\Omega}\langle I_{\Omega}^{2}h(\nu+\overline{\nu}-2\Omega)^{*}\rangle d\nu d\overline{\nu}\\ &\qquad+\int^{\Omega}\int^{\Omega}\int\langle I_{\Omega}^{2}h(\mu-\Omega)^{*}h(\nu+\overline{\nu}-\mu-\Omega)^{*}\rangle d\mu d\nu d\overline{\nu}\Bigg)\end{aligned}$$

and

$$\begin{aligned}(\text{A.21})\quad &\left\langle 4|I_{\Omega}|^{2}\int^{\Omega}\int^{\Omega}\int\int\alpha(\mu)\alpha(\overline{\mu})^{*}\hat{x}_{\theta}(\nu-\mu)\hat{x}_{\theta}(\overline{\nu}-\overline{\mu})^{\dagger}d\mu d\overline{\mu}d\nu d\overline{\nu}\right\rangle\\ &=(2\Psi_{0}^{2}+\Psi_{m}^{2})\alpha^{2}\Phi\Bigg(\langle|I_{\Omega}|^{2}\rangle B+2\int^{\Omega}\int^{\Omega}\langle|I_{\Omega}|^{2}\Re[h(\nu-\overline{\nu})]\rangle d\nu d\overline{\nu}\\ &\qquad+\int^{\Omega}\int^{\Omega}\int\langle|I_{\Omega}|^{2}h(\mu)^{*}h(\mu+\nu-\overline{\nu})\rangle d\mu d\nu d\overline{\nu}\Bigg).\end{aligned}$$

The summation of terms 6 and 7 of Equation A.17 gives

$$\begin{aligned}(\text{A.22})\quad &\left\langle 3|I_{\Omega}|^{2}\int^{\Omega}\int^{\Omega}\int\int\hat{a}(\nu-\mu)^{\dagger}\hat{a}(-\mu)\hat{a}(-\overline{\mu})^{\dagger}\hat{a}(\overline{\nu}-\overline{\mu})d\mu d\overline{\mu}d\overline{\nu}d\overline{\nu}\right\rangle\\ &+\left\langle|I_{\Omega}|^{2}\int^{\Omega}\int^{\Omega}\int\int\hat{a}(-\mu)^{\dagger}\hat{a}(\nu-\mu)\hat{a}(\overline{\nu}-\overline{\mu})^{\dagger}\hat{a}(-\overline{\mu})d\mu d\overline{\mu}d\nu d\overline{\nu}\right\rangle\\ &=\langle|I_{\Omega}|^{2}\rangle\Lambda B\left(\frac{\Phi^{2}}{2}+\frac{1}{2\Phi^{2}}-1\right).\end{aligned}$$

It is also possible to combine terms 8-15 of Equation A.17 as follows:

$$\begin{aligned}(\text{A.23})\quad &2\int^{\Omega}\int^{\Omega}\int^{\Omega}\int\int\int\Big[\langle I_{\Omega}^{*}\alpha(\mu)\alpha(\overline{\mu})^{*}\hat{x}_{\theta}(\nu-\mu)\hat{x}_{\theta}(\overline{\nu}-\overline{\mu})^{\dagger}\hat{a}(-\overline{\overline{\mu}})^{\dagger}\hat{a}(\overline{\overline{\nu}}-\overline{\overline{\mu}})\rangle\\ &\quad+\langle I_{\Omega}^{*}\alpha(\mu)\alpha(\overline{\mu})^{*}\hat{x}_{\theta}(\overline{\nu}-\overline{\mu})^{\dagger}\hat{a}(-\overline{\overline{\mu}})^{\dagger}\hat{a}(\overline{\overline{\nu}}-\overline{\overline{\mu}})\hat{x}_{\theta}(\nu-\mu)\rangle\\ &\quad+\langle I_{\Omega}^{*}\alpha(\mu)^{*}\alpha(\overline{\mu})\hat{a}(-\overline{\overline{\mu}})^{\dagger}\hat{a}(\nu-\overline{\overline{\mu}})\hat{x}_{\theta}(\overline{\nu}-\mu)^{\dagger}\hat{x}_{\theta}(\overline{\overline{\nu}}-\overline{\mu})\rangle\\ &\quad+\langle I_{\Omega}^{*}\alpha(\mu)^{*}\alpha(\overline{\mu})\hat{x}_{\theta}(\overline{\nu}-\mu)^{\dagger}\hat{x}_{\theta}(\overline{\overline{\nu}}-\overline{\mu})\hat{a}(-\overline{\overline{\mu}})^{\dagger}\hat{a}(\nu-\overline{\overline{\mu}})\rangle\\ &\quad+\langle I_{\Omega}\alpha(\mu)^{*}\alpha(\overline{\mu})\hat{x}_{\theta}(\nu-\mu)^{\dagger}\hat{a}(\overline{\nu}-\overline{\overline{\mu}})^{\dagger}\hat{a}(-\overline{\overline{\mu}})\hat{x}_{\theta}(\overline{\overline{\nu}}-\overline{\mu})\rangle\\ &\quad+\langle I_{\Omega}\alpha(\mu)^{*}\alpha(\overline{\mu})\hat{a}(\overline{\nu}-\overline{\overline{\mu}})^{\dagger}\hat{a}(-\overline{\overline{\mu}})\hat{x}_{\theta}(\overline{\overline{\nu}}-\overline{\mu})\hat{x}_{\theta}(\nu-\mu)^{\dagger}\rangle\\ &\quad+\langle I_{\Omega}\alpha(\mu)^{*}\alpha(\overline{\mu})\hat{x}_{\theta}(\nu-\mu)^{\dagger}\hat{x}_{\theta}(\overline{\nu}-\overline{\mu})\hat{a}(\overline{\overline{\nu}}-\overline{\overline{\mu}})^{\dagger}\hat{a}(-\overline{\overline{\mu}})\rangle\\ &+\langle I_{\Omega}\alpha(\mu)^{*}\alpha(\overline{\mu})\hat{a}(\overline{\overline{\nu}}-\overline{\overline{\mu}})^{\dagger}\hat{a}(-\overline{\overline{\mu}})\hat{x}_{\theta}(\nu-\mu)^{\dagger}\hat{x}_{\theta}(\overline{\nu}-\overline{\mu})\rangle\Big]d\mu d\overline{\mu}d\overline{\overline{\mu}}d\nu d\overline{\nu}d\overline{\overline{\nu}}\end{aligned}$$

$$= (4\Phi^2 - 2)\int^{\Omega}\int^{\Omega}\int^{\Omega}\int \langle \Re[I_\Omega]\alpha(\mu)\alpha(\mu+\nu-\overline{\nu}-\overline{\overline{\nu}})^*\rangle d\mu d\overline{\nu} d\overline{\overline{\nu}} d\overline{\overline{\overline{\nu}}}$$

$$= \Psi_0\Psi_m\alpha^2(4\Phi^2-2)\Bigg(\langle \Re[I_\Omega]\rangle B^2 + 2\int^{\Omega}\int^{\Omega}\int^{\Omega}\langle \Re[I_\Omega]\Re[h(\nu+\overline{\nu}-\overline{\overline{\nu}}-\Omega)]\rangle d\nu d\overline{\nu} d\overline{\overline{\nu}}$$
$$+ \int^{\Omega}\int^{\Omega}\int^{\Omega}\int \langle \Re[I_\Omega]h(\mu-\Omega)h(\mu+\nu-\overline{\nu}-\overline{\overline{\nu}})^*\rangle d\mu d\nu d\overline{\nu} d\overline{\overline{\nu}}\Bigg).$$

Similarly, we find that terms 16-19 of Equation A.17 simplify as

$$\begin{aligned}(\text{A.24})\quad & 2\int^{\Omega}\int^{\Omega}\int^{\Omega}\int\int\int\Big[\ \langle I_\Omega^*\alpha(\mu)\alpha(\overline{\mu})\hat{x}_\theta(\nu-\mu)\hat{a}(\overline{\nu}-\overline{\overline{\mu}})^\dagger\hat{a}(-\overline{\overline{\mu}})\hat{x}_\theta(\overline{\overline{\nu}}-\overline{\mu})\rangle \\ &+\langle I_\Omega^*\alpha(\mu)\alpha(\overline{\mu})\hat{a}(\overline{\nu}-\overline{\overline{\mu}})^\dagger\hat{a}(-\overline{\overline{\mu}})\hat{x}_\theta(\overline{\overline{\nu}}-\overline{\mu})\hat{x}_\theta(\nu-\mu)\rangle \\ &+\langle I_\Omega\alpha(\mu)^*\alpha(\overline{\mu})^*\hat{x}_\theta(\nu-\mu)^\dagger\hat{x}_\theta(\overline{\nu}-\overline{\mu})^\dagger\hat{a}(-\overline{\overline{\mu}})^\dagger\hat{a}(\overline{\overline{\nu}}-\overline{\overline{\mu}})\rangle \\ &+\langle I_\Omega\alpha(\mu)^*\alpha(\overline{\mu})^*\hat{x}_\theta(\overline{\nu}-\overline{\mu})^\dagger\hat{a}(-\overline{\overline{\mu}})^\dagger\hat{a}(\overline{\overline{\nu}}-\overline{\overline{\mu}})\hat{x}_\theta(\nu-\mu)^\dagger\rangle\ \Big] d\mu d\overline{\mu} d\overline{\overline{\mu}} d\nu d\overline{\nu} d\overline{\overline{\nu}} \\ &= \Phi^2\int^{\Omega}\int^{\Omega}\int^{\Omega}\int\langle I_\Omega^*\alpha(\mu)\alpha(\mu+\nu-\overline{\nu}-\overline{\overline{\nu}})\rangle d\mu d\overline{\nu} d\overline{\overline{\nu}} d\overline{\overline{\overline{\nu}}} \\ &+\Phi^2\int^{\Omega}\int^{\Omega}\int^{\Omega}\int\langle I_\Omega\alpha(\mu)^*\alpha(\mu+\nu-\overline{\nu}-\overline{\overline{\nu}})^*\rangle d\mu d\overline{\nu} d\overline{\overline{\nu}} d\overline{\overline{\overline{\nu}}} \\ &= 2\Psi_0\Psi_m\alpha^2\Phi^2\Bigg(\langle\Re[I_\Omega]\rangle B^2 + 2\int^{\Omega}\int^{\Omega}\int^{\Omega}\langle\Re[I_\Omega^*h(\nu+\overline{\nu}-\overline{\overline{\nu}}-\Omega)]\rangle d\nu d\overline{\nu} d\overline{\overline{\nu}} \\ &+\int^{\Omega}\int^{\Omega}\int^{\Omega}\int\langle\Re[I_\Omega^*h(\mu-\Omega)h(\mu+\nu-\overline{\nu}-\overline{\overline{\nu}})]\rangle d\mu d\nu d\overline{\nu} d\overline{\overline{\nu}}\Bigg).\end{aligned}$$

We can write term 20 of Equation A.17 as

$$\begin{aligned}(\text{A.25})\quad & 4\Big[\int^{\Omega}\int^{\Omega}\int^{\Omega}\int^{\Omega}\int\int\int\int\int \alpha(\mu)^*\alpha(\overline{\mu})\alpha(\overline{\overline{\mu}})^*\alpha(\overline{\overline{\overline{\mu}}})\times \\ &\hat{x}_\theta(\nu-\mu)^\dagger\hat{x}_\theta(\overline{\nu}-\overline{\mu})\hat{x}_\theta(\overline{\overline{\nu}}-\overline{\overline{\mu}})^\dagger\hat{x}_\theta(\overline{\overline{\overline{\nu}}}-\overline{\overline{\overline{\mu}}})d\mu d\overline{\mu} d\overline{\overline{\mu}} d\overline{\overline{\overline{\mu}}} d\nu d\overline{\nu} d\overline{\overline{\nu}} d\overline{\overline{\overline{\nu}}}\Big] \\ &= 4\left\langle\left|\int^{\Omega}\int\alpha(\mu)\hat{x}_\theta(\nu-\mu)d\mu d\nu\right|^4\right\rangle \\ &= 4\Bigg\langle\Bigg|\Psi_0\alpha\left(\int^{\Omega}\hat{x}_\theta(\nu)d\nu+\int^{\Omega}\int h(\mu)\hat{x}_\theta(\nu-\mu)d\mu d\nu\right)+\frac{\Psi_m\alpha}{2}\Bigg(\int^{\Omega}\hat{x}_\theta(\nu-\Omega)d\nu+\int^{\Omega}\hat{x}_\theta(\nu+\Omega)d\nu \\ &+\int^{\Omega}\int h(\mu-\Omega)\hat{x}_\theta(\nu-\mu)d\mu d\nu+\int^{\Omega}\int h(\mu+\Omega)\hat{x}_\theta(\nu-\mu)d\mu d\nu\Bigg)\Bigg|^4\Bigg\rangle.\end{aligned}$$

In the expansion of Equation A.25, many terms vanish due to both the restricted domain of $h(\nu)$ and the action of creation and annihilation operators on the vacuum. This allows

Equation A.25 to be significantly simplified, leading to the result:

$$
\begin{aligned}
(A.26)\quad & 4\Bigg[\int^{\Omega}\int^{\Omega}\int^{\Omega}\int^{\Omega}\int\int\int\int\langle\alpha(\mu)^*\alpha(\overline{\mu})\alpha(\overline{\overline{\mu}})^*\alpha(\overline{\overline{\overline{\mu}}})\times \\
&\qquad \hat{x}_\theta(\nu-\mu)^\dagger\hat{x}_\theta(\overline{\nu}-\overline{\mu})\hat{x}_\theta(\overline{\overline{\nu}}-\overline{\overline{\mu}})^\dagger\hat{x}_\theta(\overline{\overline{\overline{\nu}}}-\overline{\overline{\overline{\mu}}})\rangle d\mu d\overline{\mu}d\overline{\overline{\mu}}d\overline{\overline{\overline{\mu}}}d\nu d\overline{\nu}d\overline{\overline{\nu}}d\overline{\overline{\overline{\nu}}}\Bigg] \\
&= (4\Psi_0^4+4\Psi_0^2\Psi_m^2+\Psi_m^4)\alpha^4\Phi^2\Bigg(\frac{1}{2}B^2+\int^{\Omega}\int^{\Omega}\int^{\Omega}\int^{\Omega}\langle\Re[h(\overline{\nu}-\nu)h(\overline{\overline{\nu}}-\overline{\nu})]\rangle d\nu d\overline{\nu}d\overline{\overline{\nu}}d\overline{\overline{\overline{\nu}}} \\
&+\int^{\Omega}\int^{\Omega}\int^{\Omega}\int^{\Omega}\langle h(\overline{\nu}-\nu)^*h(\overline{\overline{\nu}}-\overline{\nu})\rangle d\nu d\overline{\nu}d\overline{\overline{\nu}}d\overline{\overline{\overline{\nu}}}+B\int^{\Omega}\int^{\Omega}\int\langle h(\mu)^*h(\mu+\nu-\overline{\nu})\rangle d\mu d\nu d\overline{\nu} \\
&\qquad +2\int^{\Omega}\int^{\Omega}\int^{\Omega}\int^{\Omega}\int\langle\Re[h(\mu)h(\mu+\nu-\overline{\nu})^*h(\overline{\overline{\nu}}-\overline{\nu})]\rangle d\mu d\nu d\overline{\nu}d\overline{\overline{\nu}}d\overline{\overline{\overline{\nu}}} \\
&\quad +\frac{1}{2}\int^{\Omega}\int^{\Omega}\int^{\Omega}\int^{\Omega}\int\int\langle h(\mu)^*h(\mu+\overline{\nu}-\nu)h(\overline{\mu})^*h(\overline{\mu}+\overline{\overline{\nu}}-\overline{\nu})\rangle d\mu d\overline{\mu}d\nu d\overline{\nu}d\overline{\overline{\nu}}d\overline{\overline{\overline{\nu}}}\Bigg) \\
&\qquad +\frac{\Psi_m^4}{8}\alpha^4\Phi^2\Bigg(\frac{1}{2}B^2+B\int^{\Omega}\int^{\Omega}\int\langle\Re[h(\mu-\Omega)h(\nu+\overline{\nu}-\mu-\Omega)]\rangle d\mu d\nu d\overline{\nu} \\
&\qquad\quad +2\int^{\Omega}\int^{\Omega}\int^{\Omega}\int^{\Omega}\langle h(\nu+\overline{\nu}-2\Omega)^*h(\overline{\nu}+\overline{\overline{\nu}}-2\Omega)\rangle d\nu d\overline{\nu}d\overline{\overline{\nu}}d\overline{\overline{\overline{\nu}}} \\
&\quad +2\int^{\Omega}\int^{\Omega}\int^{\Omega}\int^{\Omega}\int\langle\Re[h(\mu-\Omega)h(\nu+\overline{\nu}-2\Omega)^*h(\overline{\nu}+\overline{\overline{\nu}}-\mu-\Omega)]\rangle d\mu d\nu d\overline{\nu}d\overline{\overline{\nu}}d\overline{\overline{\overline{\nu}}} \\
&+\frac{1}{2}\int^{\Omega}\int^{\Omega}\int^{\Omega}\int^{\Omega}\int\int\langle h(\mu-\Omega)^*h(\overline{\mu}-\Omega)h(\nu+\overline{\nu}-\mu-\Omega)^*h(\overline{\nu}+\overline{\overline{\nu}}-\overline{\mu}-\Omega)\rangle d\mu d\overline{\mu}d\nu d\overline{\nu}d\overline{\overline{\nu}}d\overline{\overline{\overline{\nu}}}\Bigg).
\end{aligned}
$$

The summation of terms 21-24 of Equation A.17 can be written as

$$
\begin{aligned}
(A.27)\quad & 2\int^{\Omega}\int^{\Omega}\int^{\Omega}\int^{\Omega}\int\int\int\int\Bigg[\langle\alpha(\mu)^*\alpha(\overline{\mu})\hat{x}_\theta(\nu-\mu)^\dagger\hat{x}_\theta(\overline{\nu}-\overline{\mu})\hat{a}(\overline{\overline{\nu}}-\overline{\overline{\mu}})^\dagger\hat{a}(-\overline{\mu})\hat{a}(-\overline{\overline{\overline{\mu}}})^\dagger\hat{a}(\overline{\overline{\overline{\nu}}}-\overline{\overline{\overline{\mu}}})\rangle \\
&\qquad +\langle\alpha(\mu)^*\alpha(\overline{\mu})\hat{a}(\overline{\overline{\nu}}-\overline{\overline{\mu}})^\dagger\hat{a}(-\overline{\mu})\hat{a}(-\overline{\overline{\overline{\mu}}})^\dagger\hat{a}(\overline{\overline{\overline{\nu}}}-\overline{\overline{\overline{\mu}}})\hat{x}_\theta(\nu-\mu)^\dagger\hat{x}_\theta(\overline{\nu}-\overline{\mu})\rangle \\
&\qquad +\langle\alpha(\mu)^*\alpha(\overline{\mu})\hat{x}_\theta(\nu-\mu)^\dagger\hat{a}(-\overline{\mu})^\dagger\hat{a}(\overline{\nu}-\overline{\mu})\hat{a}(\overline{\nu}-\overline{\overline{\mu}})^\dagger\hat{a}(-\overline{\overline{\mu}})\hat{x}_\theta(\overline{\overline{\nu}}-\overline{\mu})\rangle \\
&\quad +\langle\alpha(\mu)^*\alpha(\overline{\mu})\hat{a}(\overline{\overline{\nu}}-\overline{\overline{\mu}})^\dagger\hat{a}(-\overline{\overline{\mu}})\hat{x}_\theta(\overline{\overline{\nu}}-\overline{\mu})\hat{x}_\theta(\nu-\mu)^\dagger\hat{a}(-\overline{\mu})^\dagger\hat{a}(\overline{\nu}-\overline{\mu})\rangle\Bigg]d\mu d\overline{\mu}d\overline{\overline{\mu}}d\overline{\overline{\overline{\mu}}}d\nu d\overline{\nu}d\overline{\overline{\nu}}d\overline{\overline{\overline{\nu}}} \\
&= \left(\frac{5\Phi^3}{2}-2\Phi+\frac{1}{2\Phi}\right)\int^{\Omega}\int^{\Omega}\int^{\Omega}\int^{\Omega}\int\langle\alpha(\mu)^*\alpha(\mu+\nu+\overline{\nu}-\overline{\overline{\nu}}-\overline{\overline{\overline{\nu}}})\rangle d\mu d\nu d\overline{\nu}d\overline{\overline{\nu}}d\overline{\overline{\overline{\nu}}} \\
&= (2\Psi_0^2+\Psi_m^2)\alpha^2\left(\frac{5\Phi^3}{2}-2\Phi+\frac{1}{2\Phi}\right)\Bigg(\frac{1}{2}B^3 \\
&\qquad +\frac{1}{2}\int^{\Omega}\int^{\Omega}\int^{\Omega}\int^{\Omega}\int\langle h(\mu)^*h(\mu+\nu+\overline{\nu}-\overline{\overline{\nu}}-\overline{\overline{\overline{\nu}}})\rangle d\mu d\nu d\overline{\nu}d\overline{\overline{\nu}}d\overline{\overline{\overline{\nu}}}\Bigg).
\end{aligned}
$$

Similarly, we can combine terms 25 and 26 of Equation A.17 to give

$$
\begin{aligned}
(A.28)\quad & 2\int^{\Omega}\int^{\Omega}\int^{\Omega}\int^{\Omega}\int\int\int\int\Bigg[\langle\alpha(\mu)^*\alpha(\overline{\mu})^*\hat{x}_\theta(\nu-\mu)^\dagger\hat{a}(-\overline{\mu})\hat{a}(\overline{\nu}-\overline{\mu})\hat{x}_\theta(\overline{\nu}-\overline{\mu})^\dagger\hat{a}(-\overline{\overline{\mu}})^\dagger\hat{a}(\overline{\overline{\nu}}-\overline{\overline{\mu}})\rangle
\end{aligned}
$$

$$+\langle\alpha(\mu)\alpha(\overline{\mu})\hat{a}(\nu-\overline{\overline{\mu}})^{\dagger}\hat{a}(-\overline{\mu})\hat{x}_{\theta}(\overline{\nu}-\mu)\hat{a}(\overline{\overline{\nu}}-\overline{\overline{\mu}})^{\dagger}\hat{a}(-\overline{\overline{\mu}})\hat{x}_{\theta}(\overline{\overline{\nu}}-\overline{\mu})\rangle\Big]\,d\mu d\overline{\mu}d\overline{\mu}d\overline{\overline{\mu}}d\nu d\overline{\nu}d\overline{\nu}d\overline{\overline{\nu}}$$

$$=(2\Psi_0^2+\Psi_m^2)\alpha^2\left(\Phi^3-\Phi\right)\Bigg(\frac{1}{2}B^3$$

$$+\frac{1}{2}\int^{\Omega}\int^{\Omega}\int^{\Omega}\int^{\Omega}\int\langle\Re[h(\mu)h(\mu+\nu+\overline{\nu}-\overline{\nu}-\overline{\overline{\nu}})]\rangle d\mu d\nu d\overline{\nu}d\overline{\nu}d\overline{\overline{\nu}}\Bigg).$$

The final term of Equation A.17 gives the result:

(A.29)
$$\int^{\Omega}\int^{\Omega}\int^{\Omega}\int^{\Omega}\int\int\int\int\langle\hat{a}(\nu-\mu)^{\dagger}\hat{a}(-\mu)\hat{a}(-\overline{\mu})^{\dagger}\hat{a}(\overline{\nu}-\overline{\mu})\times$$

$$\hat{a}(\overline{\overline{\nu}}-\overline{\overline{\mu}})^{\dagger}\hat{a}(-\overline{\overline{\mu}})\hat{a}(-\overline{\overline{\mu}})^{\dagger}\hat{a}(\overline{\overline{\nu}}-\overline{\overline{\mu}})\rangle d\mu d\overline{\mu}d\overline{\mu}d\overline{\overline{\mu}}d\nu d\overline{\nu}d\overline{\nu}d\overline{\overline{\nu}}$$

$$=B^3\Lambda\left(\frac{7\Phi^4}{32}-\frac{3\Phi^2}{8}+\frac{7}{32\Phi^4}-\frac{3}{8\Phi^2}+\frac{5}{16}\right).$$

By combining all the terms calculated for Equation A.17, we obtain the result for $\langle p_{\Omega}^2\rangle$:

(A.30)
$$\langle p_{\Omega}^2\rangle=4q^4R^2\Bigg[\langle|I_{\Omega}|^4\rangle+(4\Psi_0^2+2\Psi_m^2)\alpha^2\Phi\Bigg(\langle|I_{\Omega}|^2\rangle B+2\int^{\Omega}\int^{\Omega}\langle|I_{\Omega}|^2\Re[h(\nu-\overline{\nu})]\rangle d\nu d\overline{\nu}$$

$$+\int^{\Omega}\int^{\Omega}\int\langle|I_{\Omega}|^2h(\mu)^*h(\mu+\nu-\overline{\nu})\rangle d\mu d\nu d\overline{\nu}\Bigg)+\frac{\Psi_m^2}{2}\alpha^2\Phi\Bigg(\langle\Re[I_{\Omega}^{*2}]\rangle B$$

$$+2\int^{\Omega}\int^{\Omega}\langle\Re[I_{\Omega}^{*2}h(\nu+\overline{\nu}-2\Omega)]\rangle d\nu d\overline{\nu}$$

$$+\int^{\Omega}\int^{\Omega}\int\langle\Re[I_{\Omega}^{*2}h(\mu-\Omega)h(\nu+\overline{\nu}-\mu-\Omega)]\rangle d\mu d\nu d\overline{\nu}\Bigg)+\langle|I_{\Omega}|^2\rangle\Lambda B\left(\frac{\Phi^2}{2}+\frac{1}{2\Phi^2}-1\right)$$

$$+\Psi_0\Psi_m\alpha^2(4\Phi^2-2)\Bigg(\langle\Re[I_{\Omega}]\rangle B^2+2\int^{\Omega}\int^{\Omega}\int^{\Omega}\langle\Re[I_{\Omega}]\Re[h(\nu+\overline{\nu}-\overline{\overline{\nu}}-\Omega)]\rangle d\nu d\overline{\nu}d\overline{\overline{\nu}}$$

$$+\int^{\Omega}\int^{\Omega}\int^{\Omega}\int\langle\Re[I_{\Omega}]h(\mu-\Omega)h(\mu+\nu-\overline{\nu}-\overline{\overline{\nu}})^*\rangle d\mu d\nu d\overline{\nu}d\overline{\overline{\nu}}\Bigg)$$

$$+2\Psi_0\Psi_m\alpha^2\Phi^2\Bigg(\langle\Re[I_{\Omega}]\rangle B^2+2\int^{\Omega}\int^{\Omega}\int^{\Omega}\langle\Re[I_{\Omega}^*h(\nu+\overline{\nu}-\overline{\overline{\nu}}-\Omega)]\rangle d\nu d\overline{\nu}d\overline{\overline{\nu}}$$

$$+\int^{\Omega}\int^{\Omega}\int^{\Omega}\int\langle\Re[I_{\Omega}^*h(\mu-\Omega)h(\mu+\nu-\overline{\nu}-\overline{\overline{\nu}})]\rangle d\mu d\nu d\overline{\nu}d\overline{\overline{\nu}}\Bigg)$$

$$+(4\Psi_0^4+4\Psi_0^2\Psi_m^2+\Psi_m^4)\alpha^4\Phi^2\Bigg(\frac{1}{2}B^2+\int^{\Omega}\int^{\Omega}\int^{\Omega}\int^{\Omega}\langle\Re[h(\overline{\nu}-\nu)h(\overline{\overline{\nu}}-\overline{\nu})]\rangle d\nu d\overline{\nu}d\overline{\nu}d\overline{\overline{\nu}}$$

$$+\int^{\Omega}\int^{\Omega}\int^{\Omega}\int^{\Omega}\langle h(\overline{\nu}-\nu)^*h(\overline{\overline{\nu}}-\overline{\nu})\rangle d\nu d\overline{\nu}d\overline{\nu}d\overline{\overline{\nu}}+B\int^{\Omega}\int^{\Omega}\int\langle h(\mu)^*h(\mu+\nu-\overline{\nu})\rangle d\mu d\nu d\overline{\nu}$$

$$+2\int^{\Omega}\int^{\Omega}\int^{\Omega}\int^{\Omega}\int\langle\Re[h(\mu)h(\mu+\nu-\overline{\nu})^*h(\overline{\overline{\nu}}-\overline{\nu})]\rangle d\mu d\nu d\overline{\nu}d\overline{\nu}d\overline{\overline{\nu}}$$

$$+\frac{1}{2}\int^{\Omega}\int^{\Omega}\int^{\Omega}\int^{\Omega}\int\int\langle h(\mu)^*h(\mu+\overline{\nu}-\nu)h(\overline{\mu})^*h(\overline{\mu}+\overline{\overline{\nu}}-\overline{\nu})\rangle d\mu d\overline{\mu}d\nu d\overline{\nu}d\overline{\nu}d\overline{\overline{\nu}}\Bigg)$$

$$+\frac{\Psi_m^4}{8}\alpha^4\Phi^2\left(\frac{1}{2}B^2+B\int^{\Omega}\int^{\Omega}\int\langle\Re[h(\mu-\Omega)h(\nu+\overline{\nu}-\mu-\Omega)]\rangle d\mu d\nu d\overline{\nu}\right.$$
$$+2\int^{\Omega}\int^{\Omega}\int^{\Omega}\int^{\Omega}\langle h(\nu+\overline{\nu}-2\Omega)^* h(\overline{\overline{\nu}}+\overline{\overline{\nu}}-2\Omega)\rangle d\nu d\overline{\nu} d\overline{\overline{\nu}} d\overline{\overline{\nu}}$$
$$+2\int^{\Omega}\int^{\Omega}\int^{\Omega}\int^{\Omega}\int\langle\Re[h(\mu-\Omega)h(\nu+\overline{\nu}-2\Omega)^* h(\overline{\overline{\nu}}+\overline{\overline{\nu}}-\mu-\Omega)]\rangle d\mu d\nu d\overline{\nu} d\overline{\overline{\nu}} d\overline{\overline{\nu}}$$
$$\left.+\frac{1}{2}\int^{\Omega}\int^{\Omega}\int^{\Omega}\int^{\Omega}\int\int\langle h(\mu-\Omega)^* h(\overline{\mu}-\Omega)h(\nu+\overline{\nu}-\mu-\Omega)^* h(\overline{\overline{\nu}}+\overline{\overline{\nu}}-\overline{\mu}-\Omega)\rangle d\mu d\overline{\mu} d\nu d\overline{\nu} d\overline{\overline{\nu}} d\overline{\overline{\nu}}\right)$$
$$+(2\Psi_0^2+\Psi_m^2)\alpha^2\left(\frac{5\Phi^3}{2}-2\Phi+\frac{1}{2\Phi}\right)\left(\frac{1}{2}B^3\right.$$
$$\left.+\frac{1}{2}\int^{\Omega}\int^{\Omega}\int^{\Omega}\int^{\Omega}\int\langle h(\mu)^* h(\mu+\nu+\overline{\nu}-\overline{\overline{\nu}}-\overline{\overline{\nu}})\rangle d\mu d\nu d\overline{\nu} d\overline{\overline{\nu}} d\overline{\overline{\nu}}\right)$$
$$+(2\Psi_0^2+\Psi_m^2)\alpha^2\left(\Phi^3-\Phi\right)\left(\frac{1}{2}B^3\right.$$
$$\left.+\frac{1}{2}\int^{\Omega}\int^{\Omega}\int^{\Omega}\int^{\Omega}\int\langle\Re[h(\mu)h(\mu+\nu+\overline{\nu}-\overline{\overline{\nu}}-\overline{\overline{\nu}})]\rangle d\mu d\nu d\overline{\nu} d\overline{\overline{\nu}} d\overline{\overline{\nu}}\right)$$
$$\left.+B^3\Lambda\left(\frac{7\Phi^4}{32}-\frac{3\Phi^2}{8}+\frac{7}{32\Phi^4}-\frac{3}{8\Phi^2}+\frac{5}{16}\right)\right].$$

In the expression for $\mathrm{Var}(p_\Omega)=\langle p_\Omega^2\rangle-\langle p_\Omega\rangle^2$, there is significant cancellation between $\langle p_\Omega^2\rangle$ and $\langle p_\Omega\rangle^2$, and by taking the leading remaining terms we find that

$$\mathrm{Var}(p_\Omega)=\langle p_\Omega^2\rangle-\langle p_\Omega\rangle^2\approx 4q^4R^2\left[\langle|I_\Omega|^4\rangle-\langle|I_\Omega|^2\rangle^2+2\langle|I_\Omega|^2\rangle\Psi_0^2\alpha^2\Phi B\right] \tag{A.31}$$
$$\approx 4q^4R^2\left[\,16\Psi_0^4\Psi_m^4\alpha^8\int^{\Omega}\int^{\Omega}\langle\Re[h(\nu-\Omega)]\Re[h(\overline{\nu}-\Omega)]\rangle d\nu d\overline{\nu}\right.$$
$$\left.+4\Psi_0^2\Psi_m^2\alpha^4\int^{\Omega}\int^{\Omega}\langle\Re[n_e(\nu)]\Re[n_e(\overline{\nu})]\rangle d\nu d\overline{\nu}+2\Phi B\Psi_0^4\Psi_m^2\alpha^6\,\right].$$

By associating $\mathcal{H}=\int^{\Omega}h(\nu-\Omega)d\nu=\int_{-B/2}^{B/2}h(\nu)d\nu$ as the relative amplitude of the classical optical noise in the DC component, $\mathcal{N}=\int^{\Omega}n_e(\nu)d\nu$ as the amplitude of the electronic noise in the $\pm B/2$ frequency interval around Ω, and substituting $\Psi_0\approx 1$, $\Psi_m=\delta_m/2$ and $i_0\approx q\eta_q\alpha_0^2$, we find that for M spectral averages,

$$\mathrm{Var}(p_\Omega)\approx\frac{R^2}{M}\left[\,2q\delta_m^2 i_0^3\Phi B+4\delta_m^4 i_0^4\mathrm{Var}(\Re[\mathcal{H}])+4q^2\delta_m^2 i_0^2\mathrm{Var}(\Re[\mathcal{N}])\,\right]. \tag{A.32}$$

From Equation A.32, an improvement in precision beyond the quantum noise limit may be obtained in the case that squeezing ($\Phi<1$) provides a significant reduction in $\mathrm{Var}(p_\Omega)$.

A.3 Electro-optic Amplitude Modulation

Amplitude modulated light, as described by Equation A.2, provides a particularly convenient picture for analysing the behaviour of optical signals in the frequency domain. However, it is typically the case that modulation sidebands generated in real experiments can

only be approximately described in this way. In order to verify that Equation A.2 provides an accurate description of the state generated in this experiment, it is necessary to consider the evolution of the orthogonal polarisation components of the classical amplitude.

Since the PCF has some birefringence, there will be some ellipticity in the polarisation of the light collected from the output of the fibre. If the HWP on the output of the Sagnac interferometer rotates the polarisation of the light to align with the horizontal axis, the classical amplitude incident on the EOM may be written as

$$\begin{bmatrix} \alpha_H \\ \alpha_V \end{bmatrix} = \begin{bmatrix} \frac{\alpha_{in}}{2} + e^{-i\Theta}\frac{\alpha_{in}}{2} \\ \frac{\alpha_{in}}{2} - e^{-i\Theta}\frac{\alpha_{in}}{2} \end{bmatrix}, \tag{A.33}$$

which follows from the properties of the matrix defined in Equation 2.67. Here, α_H and α_V label the horizontal and vertical polarisation components, α_{in} is the mean classical amplitude of the light from the Sagnac interferometer, and Θ determines the ellipticity of the polarisation. For the squeezed light generated using the 14 m reel of fibre, the polarisation visibility of the light output from the Sagnac is $V = (P_{max} - P_{min})/(P_{max} + P_{min}) \approx 0.9$, where P_{max} and P_{min} are respectively the maximum and minimum powers transmitted through a linear polariser. Using Equation A.33, we obtain $\cos(\Theta) = 0.9$ and therefore $\Theta = 0.45$.

With the principle axes of the EOM oriented at 45° to the polarisation of the incident light, the transformed polarisation vector of the state on the output of the EOM can be given by [148]

$$\begin{aligned} \begin{bmatrix} \alpha'_H \\ \alpha'_V \end{bmatrix} &= \begin{bmatrix} \cos(\pi/4) & -\sin(\pi/4) \\ \sin(\pi/4) & \sin(\pi/4) \end{bmatrix} \begin{bmatrix} e^{-i\Gamma} \\ 1 \end{bmatrix} \begin{bmatrix} \cos(\pi/4) & \sin(\pi/4) \\ -\sin(\pi/4) & \sin(\pi/4) \end{bmatrix} \begin{bmatrix} \frac{\alpha_{in}}{2} + e^{-i\Theta}\frac{\alpha_{in}}{2} \\ \frac{\alpha_{in}}{2} - e^{-i\Theta}\frac{\alpha_{in}}{2} \end{bmatrix} \\ &= \begin{bmatrix} \frac{\alpha_{in}}{2} + e^{-i(\Theta+\Gamma)}\frac{\alpha_{in}}{2} \\ \frac{\alpha_{in}}{2} - e^{-i(\Theta+\Gamma)}\frac{\alpha_{in}}{2} \end{bmatrix}, \end{aligned} \tag{A.34}$$

where Γ is the phase shift imparted by the EOM. The resulting magnitude of the detected horizontal component after the PBS is then

$$|\alpha_H| = \sqrt{\frac{1}{2}\alpha_{in}^2 (1 + \cos(\Gamma + \Theta))}. \tag{A.35}$$

The phase Γ can be defined in terms of the voltage V applied to the EOM as $\Gamma = \pi V/V_\pi$, where V_π is the voltage required to achieve $\Gamma = \pi$, and is referred to as the half-wave voltage. Applying sinusoidal voltage modulation at frequency Ω, this may be written as

$$\Gamma(t) = -\pi \frac{V_0 \cos(2\pi\Omega t)}{V_\pi} = -\delta_{EOM} \cos(2\pi\Omega t), \tag{A.36}$$

where δ_{EOM} defines the modulation depth of the EOM. Making the assumption of small

modulation $\delta_{EOM} \ll 1$, the magnitude of the horizontal component can be approximated as

$$
\begin{aligned}
|\alpha'_H(t)| &= \sqrt{\frac{1}{2}\alpha_{in}^2(1+\cos(\Gamma(t))\cos(\Theta)-\sin(\Gamma(t))\sin(\Theta))} \\
&\approx \sqrt{\frac{1}{2}\alpha_{in}^2(1+\cos(\Theta)-\delta_{EOM}\cos(2\pi\Omega t)\sin(\Theta))} \\
&= \frac{1}{\sqrt{2}}\alpha_{in}\sqrt{1+\cos(\Theta)}\sqrt{1+\frac{\sin(\Theta)\delta_{EOM}\cos(2\pi\Omega t)}{1+\cos(\Theta)}} \\
&\approx \frac{1}{\sqrt{2}}\alpha_{in}\sqrt{1+\cos(\Theta)}\left(1+\frac{\sin(\Theta)\delta_{EOM}\cos(2\pi\Omega t)}{2+2\cos(\Theta)}\right).
\end{aligned} \tag{A.37}
$$

On the second line of Equation A.37, only the first term in the Taylor expansion of $\cos(\Gamma(t))$ has been kept, due to the assumption $\delta_{EOM} \ll 1$. Accordingly, the approximation made on the third line of Equation A.37 consists of taking only the first two terms of the Binomial expansion. In order to write this in the form of Equation A.2, we first reparameterise, by defining

$$
\begin{aligned}
&\alpha = \max\left(|\alpha'_H(t)|\right), \\
&A = \frac{1}{\sqrt{2}}\alpha_{in}\sqrt{1+\cos(\Theta)} \qquad \text{and} \\
&B = \frac{\alpha_{in}\sqrt{1+\cos(\Theta)}\sin(\Theta)}{2\sqrt{2}+2\sqrt{2}\cos(\Theta)}.
\end{aligned} \tag{A.38}
$$

From the definition of α, we can then write

$$
\begin{aligned}
|\alpha'_H(t)| &= \alpha(1-\Psi_m+\Psi_m\cos(2\pi\Omega t)) \\
&= (A+B\delta_{EOM})(1-\Psi_m+\Psi_m\cos(2\pi\Omega t)) = A+B\delta_{EOM}\cos(2\pi\Omega t).
\end{aligned} \tag{A.39}
$$

This leads to a valid solution for Ψ_m:

$$
\Psi_m = \frac{B\delta_{EOM}}{A+B\delta_{EOM}}. \tag{A.40}
$$

We note that, when the light incident on the EOM is circularly polarised, i.e. $\Theta = \pi/4$, the modulation depth is $\delta_{EOM} = \Psi_m/2 = \delta_m$, demonstrating the correspondence between the modulation depth of the voltage applied to EOM and the measured fractional amplitude modulation. While this equality does not hold for more general polarisation states, this analysis demonstrates that the amplitude modulation is well described by Equation A.39 when the light incident on the modulator has some degree of ellipticity, provided that the applied modulation is small. Therefore, the classical amplitude of the detected light is well described by a function oscillating sinusoidally by a fraction Ψ_m.

APPENDIX B

QUANTUM ENHANCED ESTIMATION OF STATIC LOSS WITH BRIGHT SQUEEZED LIGHT

B.1 Calculation of the Signal-to-Noise Ratio

Here we derive the signal-to-noise ratio for the loss estimation scheme described in Section 5.3. The quantum amplitude of the field before modulation is described by $\hat{A}^{in}(t) = [1+\zeta(t)]\alpha e^{i\theta} + \hat{a}(t)$. Since the amplitude modulation is generated by polarisation modulation from the EOM, we can define a vector which describes all spatial and polarisation modes of the system:

$$\vec{\hat{A}}^{in}(t) = \begin{bmatrix} |\alpha(t)|e^{i\theta} + \hat{a}_H(t) \\ \hat{b}_H(t) \\ \hat{c}_H(t) \\ \hat{a}_V(t) \\ \hat{b}_V(t) \\ \hat{c}_V(t) \end{bmatrix}, \tag{B.1}$$

where H denotes horizontal polarisation and V denotes vertical polarisation, and we have defined $|\alpha(t)| = [1+\zeta(t)]\alpha$. The different spatial modes are illustrated in Figure 5.2: $\hat{a}$ represents the spatial mode co-linear with the input beam, $\hat{b}$ represents the spatial mode co-linear with the reflection port of PBS1, and $\hat{c}$ corresponds to the vacuum port of the sample loss. The EOM then applies a relative phase shift of $\Gamma(t)$ to the polarisation components parallel to the birefringent axes of the EOM [148]. The EOM crystal is oriented such that its birefringent axes are aligned at 45° to the H and V axes. To compute the propagation of

the quantum state, we first define the following matrices:

$$R(\phi) = \begin{bmatrix} \cos(\phi) & 0 & 0 & -\sin(\phi) & 0 & 0 \\ 0 & \cos(\phi) & 0 & 0 & -\sin(\phi) & 0 \\ 0 & 0 & \cos(\phi) & 0 & 0 & -\sin(\phi) \\ \sin(\phi) & 0 & 0 & \cos(\phi) & 0 & 0 \\ 0 & \sin(\phi) & 0 & 0 & \cos(\phi) & 0 \\ 0 & 0 & \sin(\phi) & 0 & 0 & \cos(\phi) \end{bmatrix}, \tag{B.2}$$

$$M(\Gamma(t)) = \begin{bmatrix} e^{-i\Gamma(t)} & 0 & 0 & 0 & 0 & 0 \\ 0 & 1 & 0 & 0 & 0 & 0 \\ 0 & 0 & 1 & 0 & 0 & 0 \\ 0 & 0 & 0 & 1 & 0 & 0 \\ 0 & 0 & 0 & 0 & 1 & 0 \\ 0 & 0 & 0 & 0 & 0 & 1 \end{bmatrix}, \quad B = \begin{bmatrix} 1 & 0 & 0 & 0 & 0 & 0 \\ 0 & 1 & 0 & 0 & 0 & 0 \\ 0 & 0 & 1 & 0 & 0 & 0 \\ 0 & 0 & 0 & 0 & 1 & 0 \\ 0 & 0 & 0 & 1 & 0 & 0 \\ 0 & 0 & 0 & 0 & 0 & 1 \end{bmatrix} \quad \text{and}$$

$$\Lambda = \begin{bmatrix} \sqrt{\eta} & 0 & \sqrt{1-\eta} & 0 & 0 & 0 \\ 0 & 1 & 0 & 0 & 0 & 0 \\ -\sqrt{1-\eta} & 0 & \sqrt{\eta} & 0 & 0 & 0 \\ 0 & 0 & 0 & \sqrt{\eta} & 0 & \sqrt{1-\eta} \\ 0 & 0 & 0 & 0 & 1 & 0 \\ 0 & 0 & 0 & -\sqrt{1-\eta} & 0 & \sqrt{\eta} \end{bmatrix}.$$

The matrix $R(\phi)$ rotates the polarisation basis by ϕ radians, and is used to change into the basis corresponding to the birefringent axes of the EOM. $M(\Gamma(t))$ corresponds to the action of the EOM, B is the matrix corresponding to the polarising beamsplitters, and Λ applies the effect of the sample with transmission η. The action of the EOM on the input state can be calculated as

$$\begin{aligned} \vec{\hat{A}}^{mod}(t) &= R(-\pi/4)M(\Gamma(t))R(\pi/4)\vec{\hat{A}}^{in}(t) \\ &= \begin{bmatrix} \frac{1}{2}|\alpha(t)|e^{i\theta}(1+e^{-i\Gamma(t)}) + \frac{\hat{a}_H(t)}{2}(1+e^{-i\Gamma(t)}) + \frac{\hat{a}_V(t)}{2}(1-e^{-i\Gamma(t)}) \\ \hat{b}_H(t) \\ \hat{c}_H(t) \\ \frac{1}{2}|\alpha(t)|e^{i\theta}(1-e^{-i\Gamma(t)}) + \frac{\hat{a}_H(t)}{2}(1-e^{-i\Gamma(t)}) + \frac{\hat{a}_V(t)}{2}(1+e^{-i\Gamma(t)}) \\ \hat{b}_V(t) \\ \hat{c}_V(t) \end{bmatrix}. \end{aligned} \tag{B.3}$$

The state output from the second polarising beamsplitter is described by

$$\vec{\hat{A}}^{out}(t) = B\Lambda B\vec{\hat{A}}^{mod}(t) = \tag{B.4}$$

$$\begin{bmatrix} \frac{\sqrt{\eta}}{2}|\alpha(t)|e^{i\theta}(1+e^{-i\Gamma(t)}) + \frac{\sqrt{\eta}\hat{a}_H(t)}{2}(1+e^{-i\Gamma(t)}) + \frac{\sqrt{\eta}\hat{a}_V(t)}{2}(1-e^{-i\Gamma(t)}) + \sqrt{1-\eta}\hat{c}_H(t) \\ \hat{b}_H(t) \\ -\frac{\sqrt{1-\eta}}{2}|\alpha(t)|e^{i\theta}(1+e^{-i\Gamma(t)}) - \frac{\sqrt{1-\eta}\hat{a}_H(t)}{2}(1+e^{-i\Gamma(t)}) - \frac{\sqrt{1-\eta}\hat{a}_V(t)}{2}(1-e^{-i\Gamma(t)}) + \sqrt{\eta}\hat{c}_H(t) \\ \frac{1}{2}|\alpha(t)|e^{i\theta}(1-e^{-i\Gamma(t)}) + \frac{\hat{a}_H(t)}{2}(1-e^{-i\Gamma(t)}) + \frac{\hat{a}_V(t)}{2}(1+e^{-i\Gamma(t)}) \\ \sqrt{\eta}\hat{b}_V(t) + \sqrt{1-\eta}\hat{c}_V(t) \\ -\sqrt{1-\eta}\hat{b}_V(t) + \sqrt{\eta}\hat{c}_V(t) \end{bmatrix}.$$

The detected photocurrent is then the sum of the contributions to the spatial mode $\hat{a}$ from the horizontal and vertical polarisation modes:

$$\hat{i}(t) = q\left(\hat{A}_1^{out}(t)^\dagger \hat{A}_1^{out}(t) + \hat{A}_4^{out}(t)^\dagger \hat{A}_4^{out}(t) + n_e(t)\right), \tag{B.5}$$

where each component $\hat{A}_i^{out}(t)$ of the vector $\vec{\hat{A}}^{out}(t)$ has been labelled by the index i to indicate the corresponding spatial and polarisation mode, and the term $qn_e(t)$ again represents the dark current. Writing $\delta = 1-\eta$, this results in

$$\begin{aligned} \hat{i}(t) = {} & \frac{1}{2}q|\alpha(t)|^2\left(1+\eta-\delta\cos(\Gamma(t))\right) + \frac{1}{2}q|\alpha(t)|\left(1+\eta-\delta\cos(\Gamma(t))\right)\left(e^{i\theta}\hat{a}_H(t)^\dagger + e^{-i\theta}\hat{a}_H(t)\right) \\ & + \frac{1}{2}iq|\alpha(t)|\sin(\Gamma(t))\delta\left(e^{i\theta}\hat{a}_V(t)^\dagger - e^{-i\theta}\hat{a}_V(t)\right) + \frac{1}{2}q\hat{a}_H(t)^\dagger\hat{a}_H(t)\left(1+\eta-\delta\cos(\Gamma(t))\right) \\ & + \frac{1}{2}q\hat{a}_V(t)^\dagger\hat{a}_V(t)\left(1+\eta+\delta\cos(\Gamma(t))\right) \\ & + \frac{1}{2}q\sqrt{\eta(1-\eta)}|\alpha(t)|\left(e^{-i\theta}(1+e^{i\Gamma(t)})\hat{c}_H(t) + e^{i\theta}(1+e^{-i\Gamma(t)})\hat{c}_H(t)^\dagger\right) + (1-\eta)q\hat{c}_H(t)^\dagger\hat{c}_H(t) + qn_e(t). \end{aligned} \tag{B.6}$$

In the limit of small loss, the effect of the loss may be neglected from the quantum terms, and we can write

$$\hat{i}(t) \approx \frac{1}{2}q|\alpha(t)|^2\left(1+\eta-\delta\cos(\Gamma(t))\right) + \sqrt{2}q|\alpha(t)|\hat{x}_\theta(t) + q\hat{a}_H(t)^\dagger\hat{a}_H(t) + q\hat{a}_V(t)^\dagger\hat{a}_V(t) + qn_e(t), \tag{B.7}$$

where we have defined $\hat{x}_\theta(t) = \frac{1}{\sqrt{2}}\left(e^{i\theta}\hat{a}_H(t)^\dagger + e^{-i\theta}\hat{a}_H(t)\right)$. In order to calculate the power of the photocurrent at the frequency of the sideband, it is necessary to consider explicitly the time dependence of the modulation function $\Gamma(t)$. The EOM used in this experiment is capable of producing sinusoidal modulation at arbitrary modulation indices, and we can therefore assume a function of the form $\Gamma(t) = \frac{\pi}{2} - \arcsin(\delta_m\cos(2\pi\Omega t))$ for modulation frequency Ω, such that $\cos(\Gamma(t)) = \delta_m\cos(2\pi\Omega t)$, for modulation index δ_m. The constant bias of $\pi/2$ is obtained by placing a quarter-wave plate immediately before the EOM, such that the light incident on the modulator is circularly polarised [148]. The matrix $M(\Gamma(t))$ therefore describes the combined action of the QWP and the EOM. The spectral photocurrent is then

$$\hat{i}(\nu) = I(\nu) + \sqrt{2}\int \alpha(\nu)\hat{x}_\theta(\nu-\mu)d\mu + \int \hat{a}_H(-\mu)^\dagger\hat{a}_H(\nu-\mu)d\mu + \int \hat{a}_V(-\mu)^\dagger\hat{a}_V(\nu-\mu)d\mu, \tag{B.8}$$

for $\int \equiv \int_{-\infty}^{\infty}$, where $I(\nu)$ is the classical component of the spectral photocurrent, defined:

$$I(\nu) = \int \left(\frac{1}{2} |\alpha(t)|^2 \left(1 + \eta - \delta_m \delta \cos(2\pi\Omega t)\right) + n_e(t) \right) e^{-2\pi i \nu t} dt. \tag{B.9}$$

Also, if the input state is amplitude squeezed and horizontally polarised, as described by Equation B.1, the quantum fluctuation operator $\hat{a}_H(t)$ is defined as

$$\hat{a}_H(\nu) = \hat{d}_H(\nu) \cosh r(\nu) - e^{2i\theta(\nu)} \hat{d}_H(-\nu)^\dagger \sinh r(\nu), \tag{B.10}$$

where $\hat{d}_H(\nu)$ and $\hat{d}_H(\nu)^\dagger$ are bosonic creation and annihilation operators. As before, we can assume constant squeezing parameters $r(\nu)$ and $\theta(\nu)$ in the measurement bandwidth. It should be noted that the vacuum mode $\hat{a}_V(\nu)$ is not squeezed since it is in the orthogonal polarisation state to the amplitude squeezed light. Following the same approach as in Appendix A.1, the power in the sideband at frequency Ω is given by $p_\Omega = 2R|\hat{i}_\Omega|^2$, where $\hat{i}_\Omega = \int^\Omega \hat{i}(\nu) d\nu$, for $\int^\Omega \equiv \int_{\Omega - \frac{B}{2}}^{\Omega + \frac{B}{2}}$. This gives

$$\begin{aligned} p_\Omega = 2q^2 R \Bigg[& |I_\Omega|^2 + \sqrt{2} I_\Omega^* \int^\Omega \int \alpha(\mu) \hat{x}_\theta(\nu - \mu) d\mu d\nu + I_\Omega^* \int^\Omega \int \hat{a}_H(-\mu)^\dagger \hat{a}_H(\nu - \mu) d\mu d\nu \\ & + I_\Omega^* \int^\Omega \int \hat{a}_V(-\mu)^\dagger \hat{a}_V(\nu - \mu) d\mu d\nu + \sqrt{2} I_\Omega \int^\Omega \int \alpha(\mu)^* \hat{x}_\theta(\nu - \mu)^\dagger d\mu d\nu \\ & + 2 \int^\Omega \int^\Omega \int \int \alpha(\mu)^* \alpha(\overline{\mu}) \hat{x}_\theta(\nu - \mu)^\dagger \hat{x}_\theta(\overline{\nu} - \overline{\mu}) d\mu d\overline{\mu} d\nu d\overline{\nu} + I_\Omega \int^\Omega \int \hat{a}_H(\nu - \mu)^\dagger \hat{a}_H(-\mu) d\mu d\nu \\ & + I_\Omega \int^\Omega \int \hat{a}_V(\nu - \mu)^\dagger \hat{a}_V(-\mu) d\mu d\nu \Bigg], \end{aligned} \tag{B.11}$$

with $I_\Omega = \int^\Omega I(\nu) d\nu$. From the result of Appendix A.1, we have assumed here that terms smaller than $\mathcal{O}(\alpha^2)$ do not contribute significantly to the average power of the sideband. From Equation B.9, we find

$$\begin{aligned} I(\nu) = & \frac{1}{2}\alpha^2(1+\eta)\delta(\nu) + \alpha^2(1+\eta)h(\nu) + \frac{1}{2}\alpha^2(1+\eta) \int h(\mu) h(\nu - \mu) d\mu \\ & - \frac{1}{4}\alpha^2 \delta_m \delta \left[\delta(\nu - \mu) + \delta(\nu + \mu) \right] - \frac{1}{2}\alpha^2 \delta_m \delta \left[h(\nu - \Omega) + h(\nu + \Omega) \right] \\ & - \frac{1}{4}\alpha^2 \delta_m \delta \left[\int h(\mu) h(\nu - \Omega - \mu) d\mu + \int h(\mu) h(\nu + \Omega - \mu) d\mu \right] + n_e(\nu). \end{aligned} \tag{B.12}$$

From this, we can calculate

$$\begin{aligned} |I_\Omega|^2 = \delta_m^2 \delta^2 \alpha^4 \Bigg[& \frac{1}{16} + \frac{1}{4} \int^\Omega \Re[h(\nu - \Omega)] d\nu + \frac{1}{8} \int^\Omega \int \Re[h(\mu) h(\nu - \Omega - \mu)] d\mu d\nu \\ & + \frac{1}{4} \left| \int^\Omega h(\nu - \Omega) d\nu \right|^2 + \frac{1}{4} \int^\Omega \int^\Omega \int \Re[h(\mu) h(\nu - \Omega) h(\overline{\nu} - \Omega - \mu)] d\mu d\nu d\overline{\nu} \end{aligned} \tag{B.13}$$

$$+\frac{1}{16}\left|\int^{\Omega}\int h(\mu)h(\nu-\Omega-\mu)d\mu d\nu\right|^2\Bigg]-\delta_m\delta\alpha^2\Bigg[\frac{1}{2}\int^{\Omega}\Re[n_e(\nu)]d\nu$$
$$+\int^{\Omega}\int^{\Omega}\Re[h(\nu-\Omega)n_e(\overline{\nu})]d\nu d\overline{\nu}+\frac{1}{2}\int^{\Omega}\int^{\Omega}\int\Re[h(\mu)h(\nu-\Omega-\mu)n_e(\overline{\nu})^*]d\mu d\nu d\overline{\nu}\Bigg]$$
$$+\left|\int^{\Omega}n_e(\nu)d\nu\right|^2.$$

Taking the expectation value on Equation B.11, a result is obtained for the average power of the sideband:

$$\langle p_\Omega\rangle = 2q^2R\left[\langle|I_\Omega|^2\rangle+\Phi\int^{\Omega}\int^{\Omega}\int\langle\alpha(\mu)^*\alpha(\mu+\nu-\overline{\nu})\rangle d\mu d\nu d\overline{\nu}\right] \tag{B.14}$$
$$=2q^2R\Bigg[\alpha^4\Bigg(\frac{1}{16}\delta_m^2\delta^2+\frac{1}{8}\delta_m^2\delta^2\int^{\Omega}\int\langle\Re[h(\mu)h(\nu-\Omega-\mu)]\rangle d\mu d\nu$$
$$+\frac{1}{4}\delta_m^2\delta^2\left\langle\left|\int^{\Omega}h(\nu-\Omega)d\nu\right|^2\right\rangle+\frac{1}{4}\delta_m^2\delta^2\int^{\Omega}\int^{\Omega}\int\langle\Re[h(\mu)h(\nu-\Omega)h(\overline{\nu}-\Omega-\mu)]\rangle d\mu d\nu d\overline{\nu}$$
$$+\frac{1}{16}\delta_m^2\delta^2\left\langle\left|\int^{\Omega}\int h(\mu)h(\nu-\Omega-\mu)d\mu d\nu\right|^2\right\rangle\Bigg)$$
$$+\alpha^2\left(\Phi B+\Phi\int^{\Omega}\int^{\Omega}\int\langle h(\mu)^*h(\mu+\nu-\overline{\nu})\rangle d\mu d\nu d\overline{\nu}\right)+\left\langle\left|\int^{\Omega}n_e(\nu)d\nu\right|^2\right\rangle\Bigg],$$

for squeezing parameter Φ. By considering that $\delta\ll 1$, $\int|h(\nu)|d\nu\ll 1$, and writing $i_0=q\alpha^2$, the average power of the signal can be approximated as

$$\langle p_\Omega\rangle\approx R\left(\frac{1}{8}i_0^2\delta_m^2\delta^2+2qi_0\Phi B+2q^2\left\langle\left|\int^{\Omega}n_e(\nu)d\nu\right|^2\right\rangle\right). \tag{B.15}$$

The power of the optical noise floor and electronic noise floor are found to be identical to those for the case of amplitude modulation:

(B.16)
$$\langle p_N\rangle\approx R\left(2qi_0\Phi B+2q^2\left\langle\left|\int^{\Omega}n_e(\nu)d\nu\right|^2\right\rangle\right)\quad\text{and}\quad\langle p_E\rangle=R\left(2q^2\left\langle\left|\int^{\Omega}n_e(\nu)d\nu\right|^2\right\rangle\right).$$

The resulting signal-to-noise ratio δ_{SNR} for this measurement is therefore

$$\delta_{SNR}=\frac{\langle p_\Omega\rangle-\langle p_N\rangle}{\langle p_N\rangle-\langle p_E\rangle}\approx\frac{i_0\delta_m^2\delta^2}{16q\Phi B}. \tag{B.17}$$

B.2 Calculation of the Variance of the Sideband Power

The calculation of the variance of the signal power is significantly simplified here, since, assuming a similar result to Appendix A.2, we anticipate that terms smaller than $\mathcal{O}(\alpha^6)$

will not significantly contribute to $\mathrm{Var}(p_\Omega)$. Using Equation B.14, we can therefore write

(B.18)
$$\langle p_\Omega\rangle^2 = 4q^4R^2\left[\langle|I_\Omega|^2\rangle^2 + 2\langle|I_\Omega|^2\rangle\alpha^2\Phi B + 2\langle|I_\Omega|^2\rangle\alpha^2\Phi\int^\Omega\int^\Omega\int\langle h(\mu)^* h(\mu+\nu-\overline{\nu})\rangle d\mu d\nu d\overline{\nu}\right].$$

Using Equation B.11, $\langle p_\Omega^2\rangle$ can be written as

(B.19)
$$\begin{aligned}
&4q^4R^2\left[\langle|I_\Omega|^4\rangle + 6\left\langle|I_\Omega|^2\int^\Omega\int^\Omega\int\int\alpha(\mu)^*\alpha(\overline{\mu})\hat{x}_\theta(\nu-\mu)^\dagger\hat{x}_\theta(\overline{\nu}-\overline{\mu})d\mu d\overline{\mu}d\nu d\overline{\nu}\right\rangle\right.\\
&\qquad\left.+2\left\langle|I_\Omega|^2\int^\Omega\int^\Omega\int\int\alpha(\mu)\alpha(\overline{\mu})^*\hat{x}_\theta(\nu-\mu)\hat{x}_\theta(\overline{\nu}-\overline{\mu})^\dagger d\mu d\overline{\mu}d\nu d\overline{\nu}\right\rangle\right]\\
&=4q^4R^2\left[\langle|I_\Omega|^4\rangle + 4\langle|I_\Omega|^2\rangle\alpha^2\Phi B + 8\alpha^2\Phi\int^\Omega\int^\Omega\langle|I_\Omega|^2\Re[h(\nu-\overline{\nu})]\rangle d\nu d\overline{\nu}\right.\\
&\qquad\left.+4\alpha^2\Phi\int^\Omega\int^\Omega\int\langle|I_\Omega|^2 h(\mu)^* h(\mu+\nu-\overline{\nu})\rangle d\mu d\nu d\overline{\nu}\right].
\end{aligned}$$

Here, only terms of order $\mathcal{O}(\alpha^6)$ and above have been kept, and further simplification was made by neglecting terms for which the quantum expectation value vanishes. This leads to a result for the variance of the sideband power given by

(B.20)
$$\begin{aligned}
\mathrm{Var}(p_\Omega) &= \langle p_\Omega^2\rangle - \langle p_\Omega\rangle^2 \approx 4q^4R^2[\langle|I_\Omega|^4\rangle - \langle|I_\Omega|^2\rangle^2 + 2\langle|I_\Omega|^2\rangle\alpha^2\Phi B]\\
&\approx 4q^4R^2\left[\frac{1}{16}\delta_m^4\delta^4\alpha^8\int^\Omega\int^\Omega\langle\Re[h(\nu-\Omega)]\Re[h(\overline{\nu}-\Omega)]\rangle d\nu d\overline{\nu}\right.\\
&\qquad\left.+\frac{1}{4}\delta_m^2\delta^2\alpha^4\int^\Omega\int^\Omega\langle\Re[n_e(\nu)]\Re[n_e(\overline{\nu})]\rangle d\nu d\overline{\nu} + \frac{1}{8}\delta_m^2\delta^2\alpha^6\Phi B\right].
\end{aligned}$$

Using the notation $\mathcal{H} = \int_{-\frac{B}{2}}^{\frac{B}{2}} h(\nu)d\nu$ and $\mathcal{N} = \int^\Omega n_e(\nu)d\nu$ as before, with $\delta = 1-\eta$ and for M spectral averages, this gives

(B.21)
$$\mathrm{Var}(p_\Omega) = \frac{R^2}{M}\left[\frac{1}{2}q\delta_m^2(1-\eta)^2 i_0^3\Phi B + \frac{1}{4}\delta_m^4(1-\eta)^4 i_0^4\mathrm{Var}(\Re[\mathcal{H}]) + q^2\delta_m^2(1-\eta)^2 i_0^2\mathrm{Var}(\Re[\mathcal{N}])\right].$$

For $\eta \approx 1$ and $\delta_m \approx 1$, the contribution of classical noise relative to quantum noise is similar to the result for the detection of small amplitude modulation given by Equation A.32. Therefore, it is expected that squeezing should provide a precision advantage for static transmission estimation for a small optical loss.

BIBLIOGRAPHY

[1] D. Krylov and K. Bergman, "Amplitude-squeezed solitons from an asymmetric fiber interferometer," *Optics letters*, vol. 23, no. 17, pp. 1390–1392, 1998.

[2] H. Vahlbruch, M. Mehmet, K. Danzmann, and R. Schnabel, "Detection of 15 db squeezed states of light and their application for the absolute calibration of photoelectric quantum efficiency," *Physical review letters*, vol. 117, no. 11, p. 110801, 2016.

[3] R. L. Howey, "How to look at a pair of mecia: Part ii," 2001. `http://www.microscopy-uk.org.uk/mag/indexmag.html?http://www.microscopy-uk.org.uk/mag/artjun01/rhparam2.html`, Last accessed 01-08-2021.

[4] V. Giovannetti, S. Lloyd, and L. Maccone, "Advances in quantum metrology," *Nature photonics*, vol. 5, no. 4, pp. 222–229, 2011.

[5] Z. Ou, S. F. Pereira, H. Kimble, and K. Peng, "Realization of the einstein-podolsky-rosen paradox for continuous variables," *Physical Review Letters*, vol. 68, no. 25, p. 3663, 1992.

[6] V. Giovannetti, S. Lloyd, and L. Maccone, "Quantum metrology," *Physical review letters*, vol. 96, no. 1, p. 010401, 2006.

[7] M. Tse et al., "Quantum-enhanced advanced ligo detectors in the era of gravitational-wave astronomy," *Phys. Rev. Lett.*, vol. 123, p. 231107, 2019.

[8] F. Acernese et al., "Increasing the astrophysical reach of the advanced virgo detector via the application of squeezed vacuum states of light," *Phys. Rev. Lett.*, vol. 123, p. 231108, 2019.

[9] M. A. Taylor, J. Janousek, V. Daria, J. Knittel, B. Hage, H.-A. Bachor, and W. P. Bowen, "Biological measurement beyond the quantum limit," *Nature Photonics*, vol. 7, no. 3, p. 229, 2013.

[10] C. A. Casacio, L. S. Madsen, A. Terrasson, M. Waleed, K. Barnscheidt, B. Hage, M. A. Taylor, and W. P. Bowen, "Quantum-enhanced nonlinear microscopy," *Nature*, vol. 594, no. 7862, pp. 201–206, 2021.

[11] M. W. Mitchell, "Number-unconstrained quantum sensing," *Quantum Science and Technology*, vol. 2, no. 4, p. 044005, 2017.

[12] S. Lorenz, C. Silberhorn, N. Korolkova, R. Windeler, and G. Leuchs, "Squeezed light from microstructured fibres: towards free-space quantum cryptography," *Applied Physics B*, vol. 73, no. 8, pp. 855–859, 2001.

[13] K. Hirosawa, H. Furumochi, A. Tada, F. Kannari, M. Takeoka, and M. Sasaki, "Photon number squeezing of ultrabroadband laser pulses generated by microstructure fibers," *Physical review letters*, vol. 94, no. 20, p. 203601, 2005.

[14] M. Zwierz, C. A. Pérez-Delgado, and P. Kok, "General optimality of the heisenberg limit for quantum metrology," *Physical review letters*, vol. 105, no. 18, p. 180402, 2010.

[15] J. Minkoff, *Signal processing fundamentals and applications for communications and sensing systems*.
Artech House, 2002.

[16] E. Polzik, J. Carri, and H. Kimble, "Spectroscopy with squeezed light," *Physical review letters*, vol. 68, no. 20, p. 3020, 1992.

[17] F. Wolfgramm, A. Cere, F. A. Beduini, A. Predojević, M. Koschorreck, and M. W. Mitchell, "Squeezed-light optical magnetometry," *Physical review letters*, vol. 105, no. 5, p. 053601, 2010.

[18] G. C. Bjorklund, "Frequency-modulation spectroscopy: a new method for measuring weak absorptions and dispersions," *Optics letters*, vol. 5, no. 1, pp. 15–17, 1980.

[19] M. Celebrano, P. Kukura, A. Renn, and V. Sandoghdar, "Single-molecule imaging by optical absorption," *Nature Photonics*, vol. 5, no. 2, pp. 95–98, 2011.

[20] A. Monras and M. G. Paris, "Optimal quantum estimation of loss in bosonic channels," *Physical review letters*, vol. 98, no. 16, p. 160401, 2007.

[21] T. S. Woodworth, K. W. C. Chan, C. Hermann-Avigliano, and A. M. Marino, "Transmission estimation at the cramér-rao bound for squeezed states of light in the presence of loss and imperfect detection," *Physical Review A*, vol. 102, no. 5, p. 052603, 2020.

[22] E. Losero, I. Ruo-Berchera, A. Meda, A. Avella, and M. Genovese, "Unbiased estimation of an optical loss at the ultimate quantum limit with twin-beams," *Scientific reports*, vol. 8, no. 1, pp. 1–11, 2018.

[23] J. Sabines-Chesterking, R. Whittaker, S. Joshi, P. Birchall, P.-A. Moreau, A. McMillan, H. Cable, J. O'Brien, J. Rarity, and J. Matthews, "Sub-shot-noise transmission

measurement enabled by active feed-forward of heralded single photons," *Physical Review Applied*, vol. 8, no. 1, p. 014016, 2017.

[24] D. J. Griffiths, *Introduction to electrodynamics*.
American Association of Physics Teachers, 2005.

[25] L. W. Davis and G. Patsakos, "Tm and te electromagnetic beams in free space," *Optics Letters*, vol. 6, no. 1, pp. 22–23, 1981.

[26] R. Loudon, *The quantum theory of light*.
OUP Oxford, 2000.

[27] U. Leonhardt, *Essential quantum optics: from quantum measurements to black holes*.
Cambridge University Press, 2010.

[28] G. Grynberg, A. Aspect, and C. Fabre, *Introduction to quantum optics: from the semi-classical approach to quantized light*.
Cambridge university press, 2010.

[29] K. Shimoda, *Introduction to laser physics*, vol. 44.
Springer, 2013.

[30] C. Fabre and N. Treps, "Modes and states in quantum optics," *Reviews of Modern Physics*, vol. 92, no. 3, p. 035005, 2020.

[31] A. Kenfack and K. Życzkowski, "Negativity of the wigner function as an indicator of non-classicality," *Journal of Optics B: Quantum and Semiclassical Optics*, vol. 6, no. 10, p. 396, 2004.

[32] D. F. Walls and G. J. Milburn, *Quantum optics*.
Springer Science & Business Media, 2007.

[33] R. Lewis-Swan, M. Olsen, and K. Kheruntsyan, "Approximate particle number distribution from direct stochastic sampling of the wigner function," *Physical Review A*, vol. 94, no. 3, p. 033814, 2016.

[34] L. Mandel and E. Wolf, *Optical coherence and quantum optics*.
Cambridge university press, 1995.

[35] M. G. Raymer and I. A. Walmsley, "Temporal modes in quantum optics: then and now," *Physica Scripta*, vol. 95, no. 6, p. 064002, 2020.

[36] H.-A. Bachor, T. C. Ralph, S. Lucia, and T. C. Ralph, *A guide to experiments in quantum optics*, vol. 1.
Wiley Online Library, 2004.

[37] S. Donati, *Photodetectors: devices, circuits and applications*.
John Wiley & Sons, 2021.

[38] H. P. Yuen and V. W. Chan, "Noise in homodyne and heterodyne detection," *Optics letters*, vol. 8, no. 3, pp. 177–179, 1983.

[39] B. L. Schumaker, "Noise in homodyne detection," *Optics letters*, vol. 9, no. 5, pp. 189–191, 1984.

[40] D. Smithey, M. Beck, J. Cooper, M. Raymer, and A. Faridani, "Complete experimental characterization of the quantum state of a light mode via the wigner function and the density matrix: application to quantum phase distributions of vacuum and squeezed-vacuum states," *Physica Scripta*, vol. 1993, no. T48, p. 35, 1993.

[41] R. Kumar, E. Barrios, A. MacRae, E. Cairns, E. Huntington, and A. Lvovsky, "Versatile wideband balanced detector for quantum optical homodyne tomography," *Optics Communications*, vol. 285, no. 24, pp. 5259–5267, 2012.

[42] A. Zavatta, M. Bellini, P. L. Ramazza, F. Marin, and F. T. Arecchi, "Time-domain analysis of quantum states of light: noise characterization and homodyne tomography," *JOSA B*, vol. 19, no. 5, pp. 1189–1194, 2002.

[43] C. Rauscher, V. Janssen, and R. Minihold, *Fundamentals of spectrum analysis*. Rohde & Schwarz, 2007.

[44] A. Technologies, "Spectrum and signal analyzer measurements and noise," 2011.

[45] M. T. Hunter, A. G. Kourtellis, C. D. Ziomek, and W. B. Mikhael, "Fundamentals of modern spectral analysis," in *2010 IEEE AUTOTESTCON*, pp. 1–5, IEEE, 2010.

[46] K. Blow, R. Loudon, S. J. Phoenix, and T. Shepherd, "Continuum fields in quantum optics," *Physical Review A*, vol. 42, no. 7, p. 4102, 1990.

[47] R. W. Boyd, *Nonlinear optics*. Academic press, 2020.

[48] B. Yurke, "Squeezed-coherent-state generation via four-wave mixers and detection via homodyne detectors," *Physical Review A*, vol. 32, no. 1, p. 300, 1985.

[49] A. I. Lvovsky, "Squeezed light," *Photonics: Scientific Foundations, Technology and Applications*, vol. 1, pp. 121–163, 2015.

[50] U. Leonhardt, "Quantum physics of simple optical instruments," *Reports on Progress in Physics*, vol. 66, no. 7, p. 1207, 2003.

[51] V. Händchen, T. Eberle, S. Steinlechner, A. Samblowski, T. Franz, R. F. Werner, and R. Schnabel, "Observation of one-way einstein–podolsky–rosen steering," *Nature Photonics*, vol. 6, no. 9, pp. 596–599, 2012.

[52] M. V. Larsen, X. Guo, C. R. Breum, J. S. Neergaard-Nielsen, and U. L. Andersen, "Deterministic generation of a two-dimensional cluster state," *Science*, vol. 366, no. 6463, pp. 369–372, 2019.

[53] W. Asavanant, Y. Shiozawa, S. Yokoyama, B. Charoensombutamon, H. Emura, R. N. Alexander, S. Takeda, J.-i. Yoshikawa, N. C. Menicucci, H. Yonezawa, *et al.*, "Generation of time-domain-multiplexed two-dimensional cluster state," *Science*, vol. 366, no. 6463, pp. 373–376, 2019.

[54] K. Fukui, W. Asavanant, and A. Furusawa, "Temporal-mode continuous-variable three-dimensional cluster state for topologically protected measurement-based quantum computation," *Physical Review A*, vol. 102, no. 3, p. 032614, 2020.

[55] J. Aasi, J. Abadie, B. Abbott, R. Abbott, T. Abbott, M. Abernathy, C. Adams, T. Adams, P. Addesso, R. Adhikari, *et al.*, "Enhanced sensitivity of the ligo gravitational wave detector by using squeezed states of light," *Nature Photonics*, vol. 7, no. 8, p. 613, 2013.

[56] U. L. Andersen, T. Gehring, C. Marquardt, and G. Leuchs, "30 years of squeezed light generation," *Physica Scripta*, vol. 91, no. 5, p. 053001, 2016.

[57] C. McCormick, A. M. Marino, V. Boyer, and P. D. Lett, "Strong low-frequency quantum correlations from a four-wave-mixing amplifier," *Physical Review A*, vol. 78, no. 4, p. 043816, 2008.

[58] A. Hosaka, K. Hirosawa, R. Sawada, and F. Kannari, "Generation of photon-number squeezed states with a fiber-optic symmetric interferometer," *Optics express*, vol. 23, no. 15, pp. 18850–18863, 2015.

[59] M. Rosenbluh and R. Shelby, "Squeezed optical solitons," *Physical review letters*, vol. 66, no. 2, p. 153, 1991.

[60] K. Bergman and H. Haus, "Squeezing in fibers with optical pulses," *Optics letters*, vol. 16, no. 9, pp. 663–665, 1991.

[61] S. Schmitt, J. Ficker, M. Wolff, F. König, A. Sizmann, and G. Leuchs, "Photon-number squeezed solitons from an asymmetric fiber-optic sagnac interferometer," *Physical review letters*, vol. 81, no. 12, p. 2446, 1998.

[62] K. Bergman, H. Haus, E. Ippen, and M. Shirasaki, "Squeezing in a fiber interferometer with a gigahertz pump," *Optics letters*, vol. 19, no. 4, pp. 290–292, 1994.

[63] C. Yu, H. Haus, and E. Ippen, "Soliton squeezing at the gigahertz rate in a sagnac loop," *Optics letters*, vol. 26, no. 10, pp. 669–671, 2001.

[64] M. Fiorentino, J. E. Sharping, P. Kumar, and A. Porzio, "Amplitude squeezing in a mach-zehnder fiber interferometer: Numerical analysis of experiments with microstructure fiber," *Optics express*, vol. 10, no. 2, pp. 128–138, 2002.

[65] M. Fiorentino, J. E. Sharping, P. Kumar, A. Porzio, and R. S. Windeler, "Soliton squeezing in microstructure fiber," *Optics letters*, vol. 27, no. 8, pp. 649–651, 2002.

[66] S. Sawai and S. Sassa, "800 nm vacuum squeezed pulse generation experiment using a photonic crystal fiber nonlinear polarization interferometer,"

[67] J. Milanović, M. Lassen, U. L. Andersen, and G. Leuchs, "A novel method for polarization squeezing with photonic crystal fibers," *Optics express*, vol. 18, no. 2, pp. 1521–1527, 2010.

[68] K. Thorn, "A quick guide to light microscopy in cell biology," *Molecular biology of the cell*, vol. 27, no. 2, pp. 219–222, 2016.

[69] S. Wäldchen, J. Lehmann, T. Klein, S. Van De Linde, and M. Sauer, "Light-induced cell damage in live-cell super-resolution microscopy," *Scientific reports*, vol. 5, no. 1, pp. 1–12, 2015.

[70] A. Mecozzi and P. Kumar, "Linearized quantum-fluctuation theory of spectrally filtered optical solitons," *Optics letters*, vol. 22, no. 16, pp. 1232–1234, 1997.

[71] G. P. Agrawal, "Nonlinear fiber optics," in *Nonlinear Science at the Dawn of the 21st Century*, pp. 195–211, Springer, 2000.

[72] R. Stolen and C. Lin, "Self-phase-modulation in silica optical fibers," *Physical Review A*, vol. 17, no. 4, p. 1448, 1978.

[73] R. R. Alfano *et al.*, *The supercontinuum laser source*.
Springer, 1989.

[74] P. N. Butcher and D. Cotter, *The elements of nonlinear optics*.
No. 9, Cambridge university press, 1990.

[75] C. C. Gerry and R. Grobe, "Statistical properties of squeezed kerr states," *Physical Review A*, vol. 49, no. 3, p. 2033, 1994.

[76] A. Wilson-Gordon, V. Buek, and P. Knight, "Statistical and phase properties of displaced kerr states," *Physical Review A*, vol. 44, no. 11, p. 7647, 1991.

[77] L.-Y. Hu, Z.-L. Duan, X.-X. Xu, and Z.-S. Wang, "Wigner function evolution in a self-kerr medium derived by entangled state representation," *Journal of Physics A: Mathematical and Theoretical*, vol. 44, no. 19, p. 195304, 2011.

[78] M. Ismail and P. Simeonov, "Complex hermite polynomials: their combinatorics and integral operators," *Proceedings of the American Mathematical Society*, vol. 143, no. 4, pp. 1397–1410, 2015.

[79] K. Blow, R. Loudon, and S. J. Phoenix, "Graphical representation of self-phase modulation noise," *Journal of Modern Optics*, vol. 40, no. 12, pp. 2515–2524, 1993.

[80] R. Loudon, "Graphical representation of squeezed-state variances," *Optics communications*, vol. 70, no. 2, pp. 109–114, 1989.

[81] M. Shirasaki and H. A. Haus, "Squeezing of pulses in a nonlinear interferometer," *JOSA B*, vol. 7, no. 1, pp. 30–34, 1990.

[82] S. Friberg, S. Machida, M. Werner, A. Levanon, and T. Mukai, "Observation of optical soliton photon-number squeezing," *Physical review letters*, vol. 77, no. 18, p. 3775, 1996.

[83] S. Spaelter, M. Burk, U. Stroessner, A. Sizmann, and G. Leuchs, "Propagation of quantum properties of sub-picosecond solitons in a fiber," *Optics Express*, vol. 2, no. 3, pp. 77–83, 1998.

[84] M. Kitagawa and Y. Yamamoto, "Number-phase minimum-uncertainty state with reduced number uncertainty in a kerr nonlinear interferometer," *Physical Review A*, vol. 34, no. 5, p. 3974, 1986.

[85] M. Fiorentino, J. E. Sharping, P. Kumar, D. Levandovsky, and M. Vasilyev, "Soliton squeezing in a mach-zehnder fiber interferometer," *Phys. Rev. A*, vol. 64, p. 031801, 2001.

[86] J. Milanovic, J. Heersink, C. Marquardt, A. Huck, U. L. Andersen, and G. Leuchs, "Polarization squeezing with photonic crystal fibers," *Laser Physics*, vol. 17, no. 4, pp. 559–566, 2007.

[87] R. Shelby, M. Levenson, S. Perlmutter, R. DeVoe, and D. Walls, "Broad-band parametric deamplification of quantum noise in an optical fiber," *Physical review letters*, vol. 57, no. 6, p. 691, 1986.

[88] C. Doerr, M. Shirasaki, and F. Khatri, "Simulation of pulsed squeezing in optical fiber with chromatic dispersion," *JOSA B*, vol. 11, no. 1, pp. 143–149, 1994.

[89] R. Fork, O. Martinez, and J. Gordon, "Negative dispersion using pairs of prisms," *Optics letters*, vol. 9, no. 5, pp. 150–152, 1984.

[90] M. Meissner, C. Marquardt, J. Heersink, T. Gaber, A. Wietfeld, G. Leuchs, and U. L. Andersen, "All-fibre source of amplitude squeezed light pulses," *Journal of Optics B: Quantum and Semiclassical Optics*, vol. 6, no. 8, p. S652, 2004.

[91] F. Kärtner, D. Dougherty, H. A. Haus, and E. P. Ippen, "Raman noise and soliton squeezing," *JOSA B*, vol. 11, no. 7, pp. 1267–1276, 1994.

[92] H. A. Haus and Y. Lai, "Quantum theory of soliton squeezing: a linearized approach," *JOSA B*, vol. 7, no. 3, pp. 386–392, 1990.

[93] M. Tateda, N. Shibata, and S. Seikai, "Interferometric method for chromatic dispersion measurement in a single-mode optical fiber," *IEEE Journal of Quantum Electronics*, vol. 17, no. 3, pp. 404–407, 1981.

[94] E. Rosencher and B. Vinter, *Optoelectronics*.
Cambridge University Press, 2002.

[95] A. Masalov, A. Kuzhamuratov, and A. Lvovsky, "Noise spectra in balanced optical detectors based on transimpedance amplifiers," *Review of Scientific Instruments*, vol. 88, no. 11, p. 113109, 2017.

[96] O. Svelto and D. C. Hanna, *Principles of lasers*, vol. 1.
Springer, 2010.

[97] P. Kukura, M. Celebrano, A. Renn, and V. Sandoghdar, "Single-molecule sensitivity in optical absorption at room temperature," *The Journal of Physical Chemistry Letters*, vol. 1, no. 23, pp. 3323–3327, 2010.

[98] C. Gardiner, P. Zoller, and P. Zoller, *Quantum noise: a handbook of Markovian and non-Markovian quantum stochastic methods with applications to quantum optics*, vol. 56.
Springer Science & Business Media, 2004.

[99] B. Higgins et al., "Entanglement-free heisenberg-limited phase estimation," *Nature*, vol. 450, p. 393–396, 2007.

[100] P. M. Birchall, J. L. O'Brien, J. C. Matthews, and H. Cable, "Quantum-classical boundary for precision optical phase estimation," *Physical Review A*, vol. 96, no. 6, p. 062109, 2017.

[101] E. J. Allen, J. Sabines-Chesterking, A. R. McMillan, S. K. Joshi, P. S. Turner, and J. C. Matthews, "Approaching the quantum limit of precision in absorbance estimation using classical resources," *Physical Review Research*, vol. 2, no. 3, p. 033243, 2020.

[102] R. Cole, "Live-cell imaging: The cell's perspective," *Cell adhesion & migration*, vol. 8, no. 5, pp. 452–459, 2014.

[103] P. Berthold, S. P. Tsunoda, O. P. Ernst, W. Mages, D. Gradmann, and P. Hegemann, "Channelrhodopsin-1 initiates phototaxis and photophobic responses in chlamydomonas by immediate light-induced depolarization," *The Plant Cell*, vol. 20, no. 6, pp. 1665–1677, 2008.

[104] M. Xiao, L.-A. Wu, and H. J. Kimble, "Precision measurement beyond the shot-noise limit," *Physical review letters*, vol. 59, no. 3, p. 278, 1987.

[105] D. F. Walls, "Squeezed states of light," *nature*, vol. 306, no. 5939, p. 141, 1983.

[106] S. Kasapi, S. Lathi, and Y. Yamamoto, "Amplitude-squeezed, frequency-modulated, tunable, diode-laser-based source for sub-shot-noise fm spectroscopy," *Optics letters*, vol. 22, no. 7, pp. 478–480, 1997.

[107] P. S. Ribeiro, C. Schwob, A. Maître, and C. Fabre, "Sub-shot-noise high-sensitivity spectroscopy with optical parametric oscillator twin beams," *Optics letters*, vol. 22, no. 24, pp. 1893–1895, 1997.

[108] D. Kilper, A. Schaefer, J. Erland, and D. Steel, "Coherent nonlinear optical spectroscopy using photon-number squeezed light," *Physical Review A*, vol. 54, no. 3, p. R1785, 1996.

[109] F. Marin, A. Bramati, V. Jost, and E. Giacobino, "Demonstration of high sensitivity spectroscopy with squeezed semiconductor lasers," *Optics communications*, vol. 140, no. 1-3, pp. 146–157, 1997.

[110] G. Triginer Garces, H. M. Chrzanowski, S. Daryanoosh, V. Thiel, A. L. Marchant, R. B. Patel, P. C. Humphreys, A. Datta, and I. A. Walmsley, "Quantum-enhanced stimulated emission detection for label-free microscopy," *Applied Physics Letters*, vol. 117, no. 2, p. 024002, 2020.

[111] J. L. Sørensen, J. Hald, and E. Polzik, "Quantum noise of an atomic spin polarization measurement," *Physical review letters*, vol. 80, no. 16, p. 3487, 1998.

[112] P. Grangier, R. Slusher, B. Yurke, and A. LaPorta, "Squeezed-light–enhanced polarization interferometer," *Physical review letters*, vol. 59, no. 19, p. 2153, 1987.

[113] Y.-q. Li, P. Lynam, M. Xiao, and P. J. Edwards, "Sub-shot-noise laser doppler anemometry with amplitude-squeezed light," *Physical review letters*, vol. 78, no. 16, p. 3105, 1997.

[114] R. C. Pooser and B. Lawrie, "Ultrasensitive measurement of microcantilever displacement below the shot-noise limit," *Optica*, vol. 2, no. 5, pp. 393–399, 2015.

[115] S. Slussarenko, M. M. Weston, H. M. Chrzanowski, L. K. Shalm, V. B. Verma, S. W. Nam, and G. J. Pryde, "Unconditional violation of the shot-noise limit in photonic quantum metrology," *Nature Photonics*, vol. 11, no. 11, p. 700, 2017.

[116] S. M. Kay, *Fundamentals of statistical signal processing*.
Prentice Hall PTR, 1993.

[117] J. V. Beck and K. J. Arnold, *Parameter estimation in engineering and science*.
James Beck, 1977.

[118] M. H. Quenouille, "Notes on bias in estimation," *Biometrika*, vol. 43, no. 3/4, pp. 353–360, 1956.

[119] J. Combes, C. Ferrie, Z. Jiang, and C. M. Caves, "Quantum limits on postselected, probabilistic quantum metrology," *Physical Review A*, vol. 89, no. 5, p. 052117, 2014.

[120] H. V. Poor, *An introduction to signal detection and estimation*.
Springer Science & Business Media, 2013.

[121] S. L. Braunstein and C. M. Caves, "Statistical distance and the geometry of quantum states," *Physical Review Letters*, vol. 72, no. 22, p. 3439, 1994.

[122] M. A. Nielsen and I. Chuang, *Quantum computation and quantum information*.
American Association of Physics Teachers, 2002.

[123] B. Escher, R. de Matos Filho, and L. Davidovich, "General framework for estimating the ultimate precision limit in noisy quantum-enhanced metrology," *Nature Physics*, vol. 7, no. 5, pp. 406–411, 2011.

[124] L. J. Fiderer, J. M. Fraïsse, and D. Braun, "Maximal quantum fisher information for mixed states," *Physical review letters*, vol. 123, no. 25, p. 250502, 2019.

[125] A. Yariv and P. Yeh, *Nonlinear Waves in Crystals*.
Wiley, New York, 1984.

[126] M. Gehrtz, G. C. Bjorklund, and E. A. Whittaker, "Quantum-limited laser frequency-modulation spectroscopy," *JOSA B*, vol. 2, no. 9, pp. 1510–1526, 1985.

[127] M. Xiao, L.-A. Wu, and H. Kimble, "Detection of amplitude modulation with squeezed light for sensitivity beyond the shot-noise limit," *Optics letters*, vol. 13, no. 6, pp. 476–478, 1988.

[128] O. Pinel, P. Jian, N. Treps, C. Fabre, and D. Braun, "Quantum parameter estimation using general single-mode gaussian states," *Physical Review A*, vol. 88, no. 4, p. 040102, 2013.

[129] E. L. Lehmann and G. Casella, *Theory of point estimation*.
Springer Science & Business Media, 2006.

[130] A. A. Berni, T. Gehring, B. M. Nielsen, V. Händchen, M. G. Paris, and U. L. Andersen, "Ab initio quantum-enhanced optical phase estimation using real-time feedback control," *Nature Photonics*, vol. 9, no. 9, p. 577, 2015.

[131] H. Yonezawa, D. Nakane, T. A. Wheatley, K. Iwasawa, S. Takeda, H. Arao, K. Ohki, K. Tsumura, D. W. Berry, T. C. Ralph, *et al.*, "Quantum-enhanced optical-phase tracking," *Science*, vol. 337, no. 6101, pp. 1514–1517, 2012.

[132] R. Whittaker, C. Erven, A. Neville, M. Berry, J. O'Brien, H. Cable, and J. Matthews, "Absorption spectroscopy at the ultimate quantum limit from single-photon states," *New Journal of Physics*, vol. 19, no. 2, p. 023013, 2017.

[133] J. Sabines-Chesterking, A. McMillan, P. Moreau, S. Joshi, S. Knauer, E. Johnston, J. Rarity, and J. Matthews, "Twin-beam sub-shot-noise raster-scanning microscope," *Optics express*, vol. 27, no. 21, pp. 30810–30818, 2019.

[134] R. B. de Andrade, H. Kerdoncuff, K. Berg-Sørensen, T. Gehring, M. Lassen, and U. L. Andersen, "Quantum-enhanced continuous-wave stimulated raman scattering spectroscopy," *Optica*, vol. 7, no. 5, pp. 470–475, 2020.

[135] G. Zonios, A. Dimou, I. Bassukas, D. Galaris, A. Tsolakidis, and E. Kaxiras, "Melanin absorption spectroscopy: new method for noninvasive skin investigation and melanoma detection," *Journal of biomedical optics*, vol. 13, no. 1, p. 014017, 2008.

[136] H. Schiff, G. Mackay, and J. Bechara, "The use of tunable diode laser absorption spectroscopy for atmospheric measurements," *Research on chemical intermediates*, vol. 20, no. 3, pp. 525–556, 1994.

[137] J. C. Hebden, S. R. Arridge, and D. T. Delpy, "Optical imaging in medicine: I. experimental techniques," *Physics in Medicine & Biology*, vol. 42, no. 5, p. 825, 1997.

[138] J. M. Dawlaty, S. Shivaraman, J. Strait, P. George, M. Chandrashekhar, F. Rana, M. G. Spencer, D. Veksler, and Y. Chen, "Measurement of the optical absorption spectra of epitaxial graphene from terahertz to visible," *Applied Physics Letters*, vol. 93, no. 13, p. 131905, 2008.

[139] L. Goris, A. Poruba, L. Hod'Ákova, M. Vaněček, K. Haenen, M. Nesládek, P. Wagner, D. Vanderzande, L. De Schepper, and J. Manca, "Observation of the subgap optical absorption in polymer-fullerene blend solar cells," *Applied physics letters*, vol. 88, no. 5, p. 052113, 2006.

[140] G. Zhao, W. Tan, M. Jia, J. Hou, W. Ma, L. Dong, L. Zhang, X. Feng, X. Wu, W. Yin, *et al.*, "Intensity-stabilized fast-scanned direct absorption spectroscopy instrumentation based on a distributed feedback laser with detection sensitivity down to 4×10^{-6}," *Sensors*, vol. 16, no. 9, p. 1544, 2016.

[141] M. G. Allen, K. L. Carleton, S. J. Davis, W. J. Kessler, C. E. Otis, D. A. Palombo, and D. M. Sonnenfroh, "Ultrasensitive dual-beam absorption and gain spectroscopy: applications for near-infrared and visible diode laser sensors," *Applied Optics*, vol. 34, no. 18, pp. 3240–3249, 1995.

[142] A. Arbouet, D. Christofilos, N. Del Fatti, F. Vallée, J. Huntzinger, L. Arnaud, P. Billaud, and M. Broyer, "Direct measurement of the single-metal-cluster optical absorption," *Physical review letters*, vol. 93, no. 12, p. 127401, 2004.

[143] M. McDonald, F. Vietmeyer, D. Aleksiuk, and M. Kuno, "Supercontinuum spatial modulation spectroscopy: detection and noise limitations," *Review of Scientific Instruments*, vol. 84, no. 11, p. 113104, 2013.

[144] P. Billaud, S. Marhaba, N. Grillet, E. Cottancin, C. Bonnet, J. Lermé, J.-L. Vialle, M. Broyer, and M. Pellarin, "Absolute optical extinction measurements of single

nano-objects by spatial modulation spectroscopy using a white lamp," *Review of Scientific Instruments*, vol. 81, no. 4, p. 043101, 2010.

[145] G. D. Houser and E. Garmire, "Balanced detection technique to measure small changes in transmission," *Applied optics*, vol. 33, no. 6, pp. 1059–1062, 1994.

[146] G. Brida, M. Genovese, and I. R. Berchera, "Experimental realization of sub-shot-noise quantum imaging," *Nature Photonics*, vol. 4, no. 4, pp. 227–230, 2010.

[147] M. A. Taylor and W. P. Bowen, "Quantum metrology and its application in biology," *Physics Reports*, vol. 615, pp. 1–59, 2016.

[148] A. Yariv, *Optical electronics*.
Saunders College Publishing, 1991.